Universitat
de les Illes Balears

DOCTORAL THESIS
2019

NONLINEAR AND CHAOTIC BEHAVIOR IN CMOS-MEMS RESONATORS

Joan Barceló Aguiló

Universitat
de les Illes Balears

DOCTORAL THESIS
2019

Doctoral Degree in Electronic Engineering

NONLINEAR AND CHAOTIC BEHAVIOR IN CMOS-MEMS RESONATORS

Joan Barceló Aguiló

Thesis Supervisor: Jaume Verd Martorell
Thesis tutor: Jaume Verd Martorell

Doctor by the Universitat de les Illes Balears

Universitat de les Illes Balears

Dr Jaume Verd Martorell, of the Universitat de les Illes Balears

I DECLARE:

That the thesis titles *Nonlinear and chaotic behavior in CMOS- MEMS resonators* presented by Joan Barceló Aguiló to obtain a doctoral degree, has been completed under my supervision and meets the requirements to opt for an International Doctorate.

For all intents and purposes, I hereby sign this document.

Signature

Palma de Mallorca, 29 November 2018

This work has been supported by the Spanish Ministry of Economy and Competitiveness under projects TEC2009-07254-E and TEC2014-52878-R, by the European FEDER fund, and by Erasmus Mundus Action 2 EUROWEB Scholarship Program.

EUROWEB
European Research and Education Collaboration with Western Balkan

MINISTERIO DE ECONOMÍA Y COMPETITIVIDAD

FEDER
Fondo Europeo de Desarrollo Regional

Lluitar constant i vèncer, regnar sobre l'altura
i alimentar-se i viure de cel i de llum pura...
Oh vida! Oh noble sort!
Miquel Costa i Llobera (1854-1922)

Abstract

Microelectromechanical Systems (MEMS) are relevant components for the diversification and integration of functionalities into a single heterogeneous chip or package in the known More than Moore approach. This thesis contributes to this field by exploiting the possibilities of mature CMOS technologies to develop chaotic CMOS-MEMS resonators with higher performance than obtained until now and supporting its potential application in compact chaos-based secure communication systems. Specifically, this work deals with the analysis, design and experimental demonstration of chaotic electrical signal generation using simple MEMS structures with a high degree of integration and scalability in CMOS technologies and others.

The work analyzes from a practical perspective the geometric and electrical conditions for sustained chaotic motion in electrostatically actuated beam-shaped resonators. Practical applications require reasonable and wide enough range of system parameters to assure a feasible functionality in current technologies. An exhaustive analysis and numerical study of the system features indicates the need for cross-well chaotic motion that implies a bistable performance of the MEMS device. Such conditions involve, in contrast to typical MEMS resonators applications (sensors or RF oscillators), a relatively large gap between the resonator and electrodes making the readout method a key issue. The on-chip CMOS capacitive readout circuit allows the detection of the resonator motion with a high signal-to-noise ratio.

A nonlinear electromechanical model for capacitive clamped-clamped beam (cc-beam) resonators have been developed and implemented in an analog hardware description language (AHDL) enabling system level electrical simulations. The model accounts for nonlinearities from variable resonator-electrode gap, thermal effect, residual fabrication stress, fringing field effect as well as an accurate resonator deflection profile in contrast to par-

allel plate approximations. Accurate analytical expressions of the design conditions for bistability have been derived from the model and validated through FEM simulations and experimental data.

The results reached in this thesis goes beyond the merely numerical or analytical approaches stated up to now for beam-shaped resonators. Experimental measurements of extensive homoclinic chaotic motion have been reported for the first time in a straight and non-axially forced bistable cc-beam resonator operating, in addition, in the MHz range. The pioneer results on such simple and highly scalable structures represents a breakthrough for the development of a compact and low-cost platform for the study of potential applications of bistability and chaotic signal generation with added values beyond the use of purely electronic circuits.

Resum en català

El Sistemes Microelectromecànics (MEMS) són components rellevants en la diversificació i integració de diferents funcionalitats dins un únic xip o encapsulat heterogeni, el que es coneix com aproximació More than Moore. Aquesta tesi contribueix en aquest camp mitjanant l'explotació de tecnologies CMOS madures en el desenvolupament de ressonadors CMOS-MEMS caòtics amb millors prestacions que les obtingudes fins el moment i que refermen la seva potencial aplicació en sistemes compactes de comunicacions segures basades en caos. En concret, aquest treball tracta sobre l'anàlisi, disseny i demostració experimental de generadors elèctrics de senyal caòtic emprant estructures MEMS simples amb un alt grau d'integració i escalabilitat en tecnologies CMOS i d'altres.

El treball analitza des d'una perspectiva pràctica les condicions geomètriques i elèctriques necessàries per obtenir moviment caòtic sostingut en ressonadors de tipus biga amb actuació electrostàtica. Les aplicacions pràctiques requereixen d'un rang raonable i suficientment ampli de paràmetres que garanteixin la funcionalitat adequada del sistema amb les tecnologies actuals. Un anàlisi exhaustiu i numèric de les característiques del sistema evidencia la necessitat de treballar amb moviment caòtic de pou creuat (cross-well), fet que implica un comportament biestable del dispositiu MEMS. Aquest comportament requereix, al contrari que en aplicacions típiques dels ressonadors MEMS (sensors i oscil·ladors de radiofreqüència), d'una distància relativament elevada entre el ressonador i els elèctrodes fent que el mètode de lectura emprat sigui un punt clau. El circuit CMOS de lectura capacitiva integrat monolíticament sobre el xip permet la detecció del moviment del ressonador amb una elevada relació senyal/soroll.

S'ha desenvolupat un model electromecànic no-lineal per ressonadors de tipus pont (cc-beams) implementat en un llenguatge de descripció de hardware analògic (AHDL) que permet la realització de simulacions elèctriques a nivell de sistema. El model considera les

no-linealitats originades per la distància variable entre el ressonador i l'elèctrode, l'efecte tèrmic, l'estrès residual, els camps elèctrics marginals així com un perfil acurat de la deflexió del ressonador a diferència de les aproximacions de pla paral·lel. A partir d'aquest model s'han obtingut expressions analítiques acurades de disseny per a la condició de bistabilitat que han estat validades a partir de simulacions FEM i de dades experimentals.

Els resultats assolits en aquesta tesi sobrepassen els enfocs merament numèrics o analítics reportats fins el moment per a ressonadors de tipus biga. Per primer cop s'han obtingut mesures experimentals de moviment caòtic homoclínic i sostingut en un ressonador biestable tipus pont, recte i no forçat axialment, i que a més opera en el rang dels MHz. Aquests resultats pioners amb estructures simples i totalment escalables representen un avenç en el desenvolupament d'una plataforma compacta i de baix cost per l'estudi d'aplicacions de la biestabilitat i la generació de senyals caòtics amb valors afegits respecte a la utilització de circuits estrictament electrònics.

Resumen en castellano

Los Sistemas Microelectromecánicos (MEMS) son componentes relevantes en la diversificación e integración de diferentes funcionalidades dentro de un único chip o encapsulado heterogéneo, lo que se conoce como aproximación More than Moore. Esta tesis contribuye en este campo mediante la explotación de tecnologías CMOS maduras en el desarrollo de resonadores CMOS-MEMS caóticos con mejores prestaciones que las obtenidas hasta el momento y que afianzan su potencial aplicación en sistemas compactos de comunicaciones seguras basadas en caos. En concreto, este trabajo trata sobre el análisis, diseño y demostración experimental de generadores eléctricos de señal caótica utilizando estructuras MEMS simples con un alto grado de integración y escalabilidad en tecnologías CMOS y otras.

El trabajo analiza desde una perspectiva práctica las condiciones geométricas y eléctricas necesarias para obtener movimiento caótico sostenido en resonadores de tipo viga con actuación electrostática. Las aplicaciones prácticas requieren un rango razonable y suficientemente amplio de parámetros que garanticen la funcionalidad adecuada del sistema con las tecnologías actuales. Un análisis exhaustivo y numérico de las características del sistema evidencia la necesidad de trabajar con movimiento caótico de pozo cruzado (cross-well), hecho que implica un comportamiento biestable del dispositivo MEMS. Este comportamiento requiere, al contrario que en aplicaciones típicas de los resonadores MEMS (sensores y osciladores de radiofreqüencia), una distancia relativamente elevada entre el resonador i los electrodos haciendo que el método de lectura utilizado sea un punto clave. El circuito CMOS de lectura capacitiva integrado monolíticamente sobre el chip permite la detección del movimiento del resonador con una elevada relación señal/ruido.

Se ha desarrollado un modelo electromecánico no-lineal para resonadores de tipo puente (cc-beams) implementado en un lenguaje de descripción de hardware analógico (AHDL) que

permite la realización de simulaciones eléctricas a nivel de sistema. El modelo considera las no-linealidades originadas por la distancia variable entre el resonador y el electrodo, el efecto térmico, el estrés residual, los campos eléctricos marginales así como un perfil preciso de la deflexión del resonador a diferencia de las aproximaciones de plano paralelo. A partir de este modelo se han obtenido expresiones analíticas precisas de diseño para la condición de biestabilidad que han sido validadas a partir de simulaciones FEM y de datos experimentales.

Los resultados alcanzados en esta tesis sobrepasan los enfoques meramente numéricos o analíticos reportados hasta el momento para resonadores de tipo viga. Por primera vez se han obtenido medidas experimentales de movimiento caótico homoclínico y sostenido en un resonador biestable de tipo puente, recto, no forzado axialmente y que, además, opera en el rango de los MHz. Estos resultados pioneros con estructuras simples y totalmente escalables representan un avance en el desarrollo de una plataforma compacta y de bajo coste para el estudio de aplicaciones de la biestabilidad y la generación de señales caóticas con valores añadidos respecto a la utilización de circuitos estrictamente electrónicos.

Acronyms

AFM Atomic Force Microscopy

AHDL Analog Hardware Description Language

AMS Austria Micro Systems

ANN Artificial Neural Network

BEOL Back End of Line

BW Bandwidth

CMOS Complementary Metal Oxide Semiconductor

FDM Finite Difference Method

FEM Finite Element Method

FEOL Front end of Line

FOX Field Oxide

FPGA Field Programmable Gate Array

GND Ground

HMS Home-Made hydrofluoric Solution

IC Integrated Circuit

ITRS International Technology Roadmap for Semiconductors

MEMS Micro-Electromechanical System

RF-MEMS Radio Frequency Micro-Electromechanical System

NEMS Nano-Electromechanical System

OT Operating Temperature

PECVD Plasma-Enhanced Chemical Vapor Deposition

PSS Periodic Steady State

RT Room Temperature

SA Spectrum Analyzer

SEM Scanning Electron Microscope

SiP System in Package

SoC System on Chip

TIA Transimpedance Amplifier

VHF Very High Frequency

1DOF One Degree of Freedom

1WP One/Single-Well Potential

2WP Two/Double-Well Potential

Contributions of the author

The results of this thesis have been partially published as articles in the following international specialized journals:

- **J. Barceló**, I. De Paúl, S. Bota, J. Segura and J. Verd, "Cross-well chaotic motion in an electrostatically actuated CMOS microbeam resonator", *In preparation.*
- **J. Barceló**, S. Bota, J. Segura, and J. Verd, "Nonlinear cc-beam microresonator model for system level electrical simulations: Application to bistable behavior analysis", *Sensors and Actuators, A: Physical*, vol. 272, pp. 33-41, 2018.
- **J. Barceló**, J.L. Rosselló, S. Bota, J. Segura and J. Verd, "Electrostatically actuated microbeam resonators as chaotic signal generators: A practical perspective", *Communications In Nonlinear Science And Numerical Simulation*, n. 30, pp. 316 - 327. 2016.
- **J. Barceló**, Z. Marinković, V. Marković and J. Verd, " Fuzzy Control for chaotic response improvement in MEMS resonators", *Microwave Review*, vol.21, no.1, pp. 23-28. IEEE, 2015.

and as communications in the following international conferences and symposiums:

- **J. Barceló**, I. De Paúl, S. Bota, J. Segura and J. Verd, "Chaotic Signal Generation in the MHz Range with a Monolithic CMOS-MEMS Microbeam Resonator", *32st IEEE International Conference on Micro Electro Mechanical Systems (MEMS)*, Coex, Seoul (Korea) 2019.
- **J. Barceló**, S. Bota, J. Segura and J. Verd, "Development of a Bistable CMOS-MEMS Microbeam Resonator with Electrostatic Actuation", *31st IEEE International*

Conference on Micro Electro Mechanical Systems (MEMS), Belfast (United Kingdom) 2018.

- **J. Barceló**, I. De Paúl, S. Bota, J. Segura and J. Verd, "Bistability in a CMOS-MEMS Thermally Tuned Microbeam Resonator", *International Symposium on Circuits and Systems (ISCAS)*, Florence (Italy) 2018.

- **J. Barceló**, I. De Paúl, S. Bota , J. Segura and J. Verd, "Experimental validation of bistability in an electrostatically actuated microbeam resonator with thermal tuning", *28th Micromechanics and Microsystems Europe workshop (MME)*, Uppsala (Sweden) 2017.

- **J. Barceló**, I. De Paúl, S. Bota , J. Segura and J. Verd, "Thermal Tuning and Design Conditions for Bistability in Electrostatically Actuated Microbeam Resonators", *32th Design of Circuits and Integrated Systems Conference (DCIS)*, Barcelona (Spain) 2017.

- **J. Barceló**, S. Bota, J. Segura and J. Verd, "Accurate Model for Designing cc-beam Resonators with Bistable Behavior", *27th Micromechanics and Microsystems Europe workshop (MME)*, Cork (Ireland) 2016.

- **J. Barceló**, J. Segura, S. Bota and J. Verd, "Nonlinear CC-beam Resonator Model for System Level Electrical Simulations", *31th Design of Circuits and Integrated Systems Conference (DCIS)*, Granada (Spain) 2016.

- **J. Barceló**, Z. Marinković, V. Marković and J. Verd, "Improvement of the Chaotic Response in MEMS with Fuzzy Control Implemented by ANN", *12th International Conference on Advanced Technologies, Systems and Services in Telecommunications (TELSIKS)*, Niš (Serbia) 2015.

- **J. Barceló**, S. Bota, J. Segura and J. Verd, "Towards an On-Chip MEMS Chaotic Generator in a Commercial 0.35-Micron CMOS Technology", *26th Micromechanics and Microsystems Europe workshop (MME)*, Toledo (Spain) 2015.

- **J. Barceló**, J. Segura, S. Bota and J. Verd, "Design of a monolithic CMOS-MEMS resonator as chaotic signal generator", *29th Conference on Design of Circuits and Integrated Systems (DCIS)*, Madrid (Spain) 2014.

Contents

List of Figures

List of Tables

Chapter 1

Introduction and motivation

This first chapter gives a brief overview of the thesis, which is mainly proposed as the exploiting of mature CMOS technologies to develop chaotic CMOS-MEMS resonators with higher performance than obtained until now. MEMS devices are framed in the More than Moore era and the bistability and chaos behavior in such devices are introduced in the state of the art context. The CRIPTOMEMS and KEYNEMS research projects, which constitutes the framework of this thesis, are also presented. Finally, the structure of this dissertation is described and enumerated.

1.1 MEMS in the More than Moore era

MEMS acronym stands for micro-electromechanical system, and consists usually in a device in the size of microns, containing mechanical moving parts whose movement is electrically excited and/or sensed. In this way, the system relates the mechanical and the electrical domains, performing a transduction from one domain to the other, or in both senses. MEMS represent one of the elements for the functionality diversification sought after in the More than Moore paradigm (see figure 1-1). This new domain, besides the continuous scaling-down in IC technologies following the Moore law (or even beyond it), is driving interest in new devices for information processing and memory, new technologies for heterogeneous integration of multiple functions, and new paradigms for system architecture [1].

The interest for the micro and nano technology was announced in 1959 by the Richard Feynman's famous lecture entitled "There's Plenty of Room at the Bottom" and pronounced in the American Physical Society meeting at Caltech [2]. In it, Feynman exposes the enor-

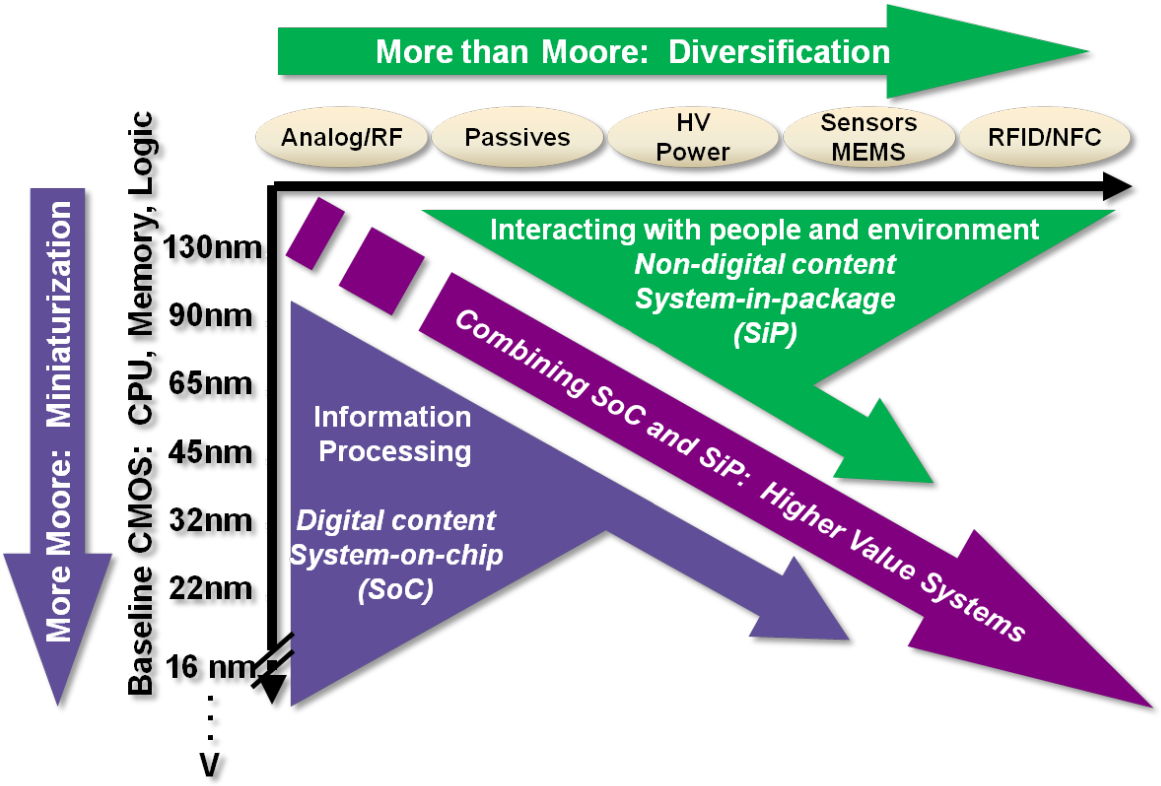

Figure 1-1: Dual trend for the integrated systems, projected by ITRS: miniaturization of the digital functions (More Moore) and functional diversification (More than Moore) [1].

mous potential of the field of science that allows the manipulation, control and measurement of particles and elements of the order of atomic magnitude. As of then, the study of micro and nanotechnology has undergone a great intensification that has affected a large spectrum of technical areas of application. Nowadays, the digital era in which society is immersed has been reached thanks to the development and miniaturization of the IC technology. This process offers a wide variety of interesting opportunities as well as numerous challenges that must be faced with new designs, technologies and approaches.

The development of MEMS has been possible by the innovation of silicon based fabrication techniques; the MEMS technology uses a variety of materials and processes from the IC industry, like, for instance, the surface micromachining and the bulk micromachining. The first MEMS resonator (a transistor with a resonating gate, whose resonance frequency was 5 kHz and its quality factor was 500) was released in 1967 [3]. From this moment, industry and research have developed several design solutions, with the aim of improve the MEMS features, mainly quantified as the resonance frequency, the quality factor, the mo-

tional impedance and the power-handling (the maximum power which can be invested in the resonator movement before the appearance of the nonlinear regime) parameters. The first MEMS with a comb-drive structure (with a resonance frequency of about 50 kHz and a quality factor of 100) was fabricated by the University of Berkeley (California) in 1989 [4], and in 1998 the first polysilicon made comb-drive was released [5]. In order to overcome the frequency limitation of the comb-drive MEMS, the beam shaped resonators (cantilevers and cc-beams) were introduced [6], as well as other geometries like disk resonators, which provide a model in 2003 with a resonance frequency in the order of GHz and a quality factor upper than 1500 at room conditions, keeping also low the motional impedance.

The current and potential future applications of MEMS include microsensors (e.g. gyroscopes and accelerometers [7]) biomedical applications (e.g. instruments for analysis, implants and drug delivery [8]), microactuators and RF-MEMS (e.g. tunable micromachined capacitors, integrated high Q inductors, low-loss micromechanical switches [9], [10], [11]). In particular those RF-MEMS devices arouse great interest because of their amenability to on-chip integration alongside transistors, which might enable a single-chip RF front-end, reducing size and power consumption and raising robustness against interferences [12].

1.2 Nonlinear dynamics and chaos

A dynamical system is a set of possible states that present a temporal evolution, together with a rule or law which defines the present state in terms of previous states [13]. On the other hand, state is defined as all the necessary information to know the behavior and the evolution of the system. In a nonlinear dynamical system described from dynamical variables with bounded values, the chaotic regime is defined as the nonperiodic but bounded movement, with great sensitive dependence on initial conditions, unpredictable (without knowing the rule governing the system, only knowing the values of the dynamical variables along the whole time, it is impossible to predict the values of these dynamical variables in future time), with noise shape but, in contrast to noise, deterministic (given the same conditions, the response dynamics will be identical no matter the number of repetitions). Formally, chaotic behavior appears when confinement in the phase space (for bounded values of the dynamical variables) and exponential divergence of initially near trajectories (a consequence of the sensitive dependence on initial condition) take place simultaneously.

This notion of exponential divergence is quantified by the Lyapunov exponents [14] [15].

At the same time, attractor is defined as the subset of the phase space where trajectories converge after a long enough time lapse, in a way that an attractor is never abandoned by trajectories even if they are perturbed [16]. The bounded and non chaotic dynamic systems can converge in a point (equilibrium point), or in a set of states that are repeated periodically (limit cycle). The chaotic dynamics is characterized by a third kind of attractors (called strange attractors), whose more interesting feature is that they present a fractal (non integer) dimension [14], [17].

1.3 Nonlinear dynamics and chaos in MEMS, state of the art

The behavior of electrostatically actuated MEMS resonators is inherently nonlinear due to the nonlinear electrostatic force and the mechanical resonator nonlinear properties that can be exploited to display chaotic motion under specific operating conditions. In spite of its considerable potential in several applications, the chaotic behavior of such MEMS devices constitutes an exotic field, with very few reported experimental results.

1.3.1 Chaotic behavior in MEMS resonators

In 1998, Y. Wang et al. reported for the first time experimental chaotic behavior from a MEMS (fabricated at Cornell University in 1996) [18]. The MEMS structure, a nonoverlapping comb drive, was fabricated using the single-crystal reactive etching and metalization process [19], and monolithically integrated with the electronic circuitry. The operation of this system was performed by means of electrostatic actuation (which depends on the position of the resonator, i.e what is called parametric forcing) provided by electrodes parallel to the beams structures, and the mechanical stiffness is obtained from the restoring springs that hold the structure, which will be susceptible to the induced resonant movement figure (1-2). The application of a bias voltage to the structure results in a symmetric stiffness in the electrical domain which tunes the effective stiffness of the system and, in consequence, provokes a reduction of the resonance frequency. From this tuning procedure, the system is made to be bistable, and with a proper AC excitation the chaotic behavior arises, as a reconstruction of the two-well potential Duffing attractor and can be experimentally measured. The proposed structure in [18] has a size of approximately 1.5×0.75mm, resonates

with a natural frequency of ≈ 6 kHz, and typical values of 32.6V of bias voltage and 1.37 V of excitation amplitude are needed. The movement of the structure resonance is given in the parallel direction to the electrodes (or in the perpendicular direction to the "fingers"); the movement in another direction is prevented by the structural design of the resonator, and this fact prevents the system from collapsing because of the pull in effect. The disposition of the fingers increases the coupling area and, in this way, relatively low voltages are needed. Finally reference [18] experimentally demonstrated the autosynchronization capability of pairs of identical devices.

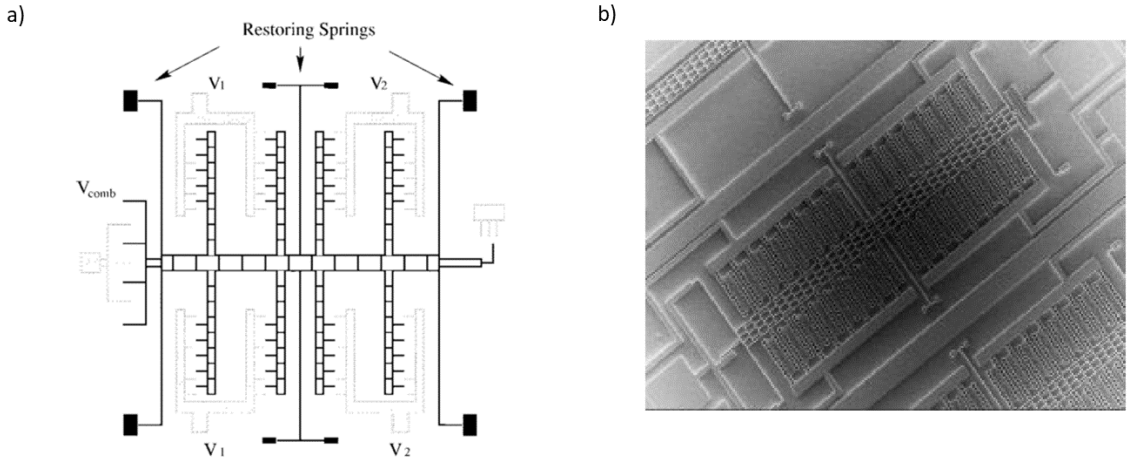

Figure 1-2: a) Schematic representation and b) SEM image of the electromechanical system reported in [18].

References [20] and [21] introduces a theoretical prediction of the chaotic behavior in a comb drive shaped MEMS (depicted in figure 1-3) by means of the analytical Melnikov method [22]. In these references, the electromechanical system was modeled with a version of the Mathieu equation, and the natural frequency of the fabricated device was ≈ 10 kHz. The procedure to attain chaotic behavior consists in tuning the mechanical stiffness by means of DC voltage until the two-well potential distribution is reached, and then an AC excitation with the proper frequency and amplitude was applied. The numerical simulations and experimental results agreed in the reproduction of the chaotic attractor for a set of parameters (bias voltage, excitation amplitude and frequency) for which the Melinkov criterion predicts chaotic behavior. The homoclinic structure is found to be indispensable for the Melnikov analysis, and essential for the chaotic behavior attainment.

The adoption of these relative large and complex structures increases the resonator mass,

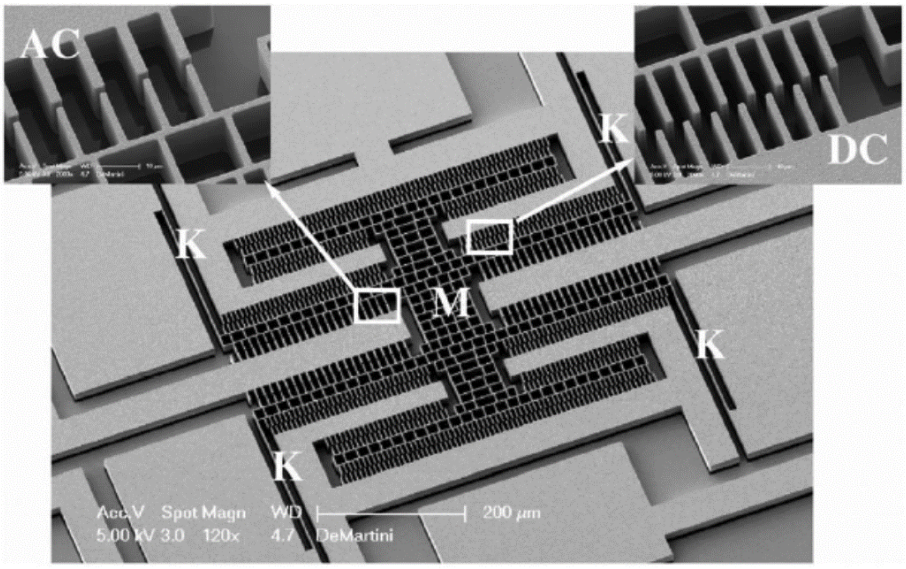

Figure 1-3: SEM image of the fabricated device reported in [20] and [21].

reducing its resonance frequency, and adds constraints in terms of fabrication reliability. As a consequence, the very few experimental results reported in the literature have been obtained with MEMS resonators working in the kHz range [18], [20], [21]. On the other hand, the consideration of simple resonant structures, as a cantilever (clamped beam) or a bridge (cc-beam) resonator, provides significant benefits in terms of integration feasibility and scalability to nanometer dimensions (NEMS resonators) enabling both high sensitivity and high operating frequency. In [23], authors proposed the analysis of the nonlinear dynamics of a cantilever shaped MEMS oscillator from Poincare maps. Using a closed loop configuration a bistable system was attained, and nonlinear effects like period doubling bifurcation and ultimately chaotic behavor were numerically obtained.

In [24] and [25], authors provide a procedure to follow the period-doubling route to chaos with an electrostatically actuated microstructure. The application of high DC voltages is needed to bring the device into a nonlinear state, which can be observed as a breaking of the symmetry in the acceleration-velocity phase state plots. By applying upper DC values than the "DC-symmetry-breaking", an applied growing AC amplitude provoke a symmetry breaking in the velocity-position phase plot (called "AC-symmetry-breaking" by [25]). The symmetry-breakings are a prerequisite for the period-doubling route to chaos [17]. On further increasing the AC amplitude, and under superharmonic frequencies the period doubling sequence takes place and interesting chaotic transition (banded chaos) is

observed during it.

In [26], numerical studies (leaded by the Melnikov criterion) are performed to establish the conditions for homoclinic chaos in cc-beam mircoresonators. Extensive chaotic behavior is obtained by numerical simulations. Moreover a robust adaptive control based on fuzzy and sliding-mode control is applied to stabilize the MEMS resonator in a high-amplitude oscillation state, suppressing the chaotic response. References [27], [28] and [29] continued the analysis performed in [26] providing wider perspectives or proposing improvements to the chaotic predictive method based on the Melnikov theory. In [27] an analytical and numerical analysis of the homoclinic and heteroclinic chaotic behavior based on the three-well potential distribution (made possible by the presence of the quintic term of the nonlinear stiffness) is introduced: the parameter criteria to allow such a potential distribution are set, and the approximate analytical prediction for chaotic response is addressed. On the other hand, references [28] and [29], developed a new criterion for chaotic behavior prediction with is claimed to be more accurate than the Melnikov analysis.

In [30] the symmetry-breaking route to chaos has been found, and extensive chaotic motion is numerically predicted and experimentally measured to appear in nonplanar motion performed by a fabricated nanowire resonator. This paper reports that in the nonplanar regime, the chaotic behavior can be rather common, this fact converts the non-planar movement into one of the strategies to seek the chaotic response in resonators. Reference [30] states that dynamical phenomenon of crisis can occur where two symmetry-broken chaotic attractors can collide simultaneously with their basin boundaries to form a much larger, single chaotic attractor possessing the full symmetry of the system.

Experimental chaotic motion has also been measured in microcantilevers used for atomic force microscopy (AFM), as reported in [31] and [32]. In these applications the microcantilevers are subjected to a variety of short and long range forces, van der Waals, capilarity, Pauli repulsion, nanoscale contact and elastic forces amongst others. Period doublig sequences under these conditions have been found for both asymmetric single well and asymmetric double well potential.

Potential application is secure communication purposes

Prospective applications of chaotic MEMS/NEMS resonators at VHF (very high frequency) range and higher include random number generators or signal encryption system in chaotic

based secure communications systems as proposed in [18], [21], [30]. Until now, traditionally the security in communication systems has been based on software techniques and protocols for data encryption. However, the need for high speed in data transmission has motivated an increase in the interest of hardware schemes for real time data cryptography. The feature of autosynchronization presented by chaotic systems, demonstrated in the pioneer work [33] for the Lorenz system, and physically implemented in electronic circuits and experimentally corroborated by [34] has immediate application in the field of secure communications. In [34], authors encrypted useful information by means of a widebanded chaotic carrier signal (the output of the sender), and recovered it after a synchronization of the chaotic signal in the receptor. Reference [18] experimentally observed for the first time the synchronization between a pair of identical MEMS resonators, and proposed immediately their scheme to be used in secure communications purposes. Nevertheless, despite this promising work, [18] is, still nowadays, the only work where synchronization between chaotic MEMS is proposed. Up to now, it seems that the scientific community has preferred to focus in the research of chaotic optical devices for its use in secure communication systems as the alternative option to the use of electronic or electromechanic chaotic systems [35], [36], [37].

1.3.2 Bistability in MEMS

Bistability in MEMS, because of its several potential applications, has sparked the interest of researchers and developers, but in spite of that, until now, just analytical and numerical studies about bistable simple clamped-clamped microbeams are reported in literature. For instance, in [38] and [29], the different regions of parameter space are set to imply a classification of the resonator dynamics. On the other hand the existing experimental works refer to comb-drive MEMS in the range of the KHz [39], arched beams [40] and axially loaded bridges [41], where buckling is given by an applied mechanical axial forcing. However, reference [42] reports an interesting work, including experimental results, where a bistable behavior of a microcantilever (with a frequency in the range of the kHz) is achieved by means of the interaction of fringing field effects with electrostatic and mechanical (restoring) forces.

Amongst their numerous applications, bistable MEMS have been found to be useful as threshold switches, mechanical memories, micro-relays, band-pass filters, and energy harvesters [39]. For instance, the bistable microcantilever reported in [42] was used as

pressure sensor in [43]. Finally, bistability (two-well potential distribution) can be seen as the first step to attain chaotic behavior in MEMS resonators, since it has revealed to be the easiest and (by far) most reported strategy to obtain chaotic response in a resonator, as it allows an assimilation to the well know Duffing Ueda chaotic system.

1.4 Objectives: CRIPTOMEMS and KEYNEMS projects

The thesis objectives are completely framed within the projects CRIPTOMEMS (TEC2009-07254-E) and KEYNEMS (TEC2014-52878-R). Starting from the intrinsic nonlinearities previously observed in beam resonators, the CRIPTOMEMS project was conceived as a first exploration of the feasibility in obtaining chaotic signal generators based on beam-shaped CMOS-MEMS resonators for a potential application in cryptographic schemes. The project proposed, as an added value of MEMS resonators (instead of purely integrated circuits), the use as encryption key of a physical parameter of the device that cannot be measured. In this sense the MEMS-based device becomes a physically unclonable device. From the theoretical and numerical results obtained from this project, the main line of the next KEYNEMS project was devised for the practical implementation of clamped-clamped microbeams resonators as nonlinear and chaotic CMOS-MEMS devices using mature CMOS technologies.

In this context, the main objective of this thesis work is the analysis, design and experimental demonstration of generation of chaotic electrical signals by using simple microelectromechanical structures with a high degree of integrability and scalability in commercial CMOS technologies. The CMOS-MEMS fabrication approach, detailed in chapter 3, exhibits interesting features for the achievement and development of MEMS based bistable and chaotic systems:

- The scaling down of the MEMS dimensions to the submicrometric range allows the fabrication of resonators with relative high frequencies. The increase of the chaotic resonator frequency allows a wider bandwidth and a higher velocity in potential applications of data transmission.

- The monolithic integration (MEMS resonator and CMOS circuitry fabricated into a single CMOS die) improves the signal to noise ratio and in consequence the quality

of the output signal. Moreover, the monolithic integration allows its immediate application in smart microsystems as a transmission module component, providing, in this way, compact, economical and reliable systems.

- The use of electrostatic transduction implies a direct dealing with electric signals without the need of additional transduction elements. In this way an improvement of the energetic efficiency is expected in comparison with optical based systems.

- The use of capacitive readout allows an easy and direct monolithic integration of such MEMS/NEMS devices with electronics enabling the exploitation of their practical applications [44], [45], [46], [47].

1.4.1 Why cc-beam MEMS?

The aim of the present work is to study and evaluate the potentialities of nonlinear behavior in MEMS resonators, establish their operating limits and propose design rules to optimize their operation. Hardware-based designs are claimed to provide high performance solutions for several fields in engineering, and amongst them, the wide potential applications of MEMS devices make them highlight. MEM systems allow a high level of scalability, which implies an increase of the operating frequency and the bandwidth, and they are compatible with CMOS technology. Specifically, the use of simple structures (like cantilevers or cc-beams) as resonators is optimal, because, for the same stiffness, they present the least mass, allowing a higher frequency, and higher sensitivity. Simple structures are compatible with top-down and bottom-up fabrication approaches and, in addition, they provide benefits in terms of fabrication reliability and scalability down to nanometric dimensions.

The approach proposed in this work is to exploit the electromechanical nonlinearities inherent in doubly clamped beams (cc-beams) for interesting nonlinear behaviors, like the bistability, and eventually chaotic motion. The strategy for the chaotic behavior attainment is the reproduction of the Duffing Ueda strange chaotic attractor with two-well potential. Consequently, bistability is seen as the first step to achieve extensive, robust and nontransient chaotic response. As it has been mentioned, bistability itself presents several uses and applications, and the mere achievement of two-well potential distribution (bistable behavior) itself represents an objective. This bistability is sought in an in-plane operation, without adding curvature to the beams, or applying axial loads; this fact provides more

simplicity and reliability to the current approach. Moreover, the in-plane operation provides facilities to the capacitive readout, unlike the out-of-plane operation. However, the need of bistability (namely, a homoclinic structure) prevents the cantilever-based designs from being considered, because the two-well potential distribution requires a non negligible nonlinear mechanical stiffness while in the cantilever (because of its smaller hyperstaticity order with respect to the cc-beam) this condition is not fulfilled (notice that the bistable behavior of the cantilevers reported in [42] and [43] relies on a not in-plane fringing field-based forcing). On the other hand, the way proposed in [27] to achieve the chaotic regime in a MEMS resonator, based on the quintic nonlinear stiffness term (which would allow the heteroclinic-based chaos) is not considered in this work, since it has been proved that the quintic stiffness term has a negligible influence on the static and dynamic behavior of the systems under study.

In summary, the development of this thesis has been focused on submicrometric cc-beam designs, with non-linear behavior, fabricated in commercial CMOS technologies, whose in-plane operation is based on electrostatic actuation and capacitive readout. It is important to remark that there are no previous experimental results of such resonators exhibiting either bistability or chaos, and some of the numerical simulations reported up to now exhibit mostly unclear results. In some simulation studies chaos is only obtained for extremely narrow range of actuation voltages [25], making practical implementations unfeasible due to inherent fabrication tolerances. In other numerical works, extended and sustained chaotic behavior is reported but assuming impractical system parameters [26], [27].

1.5 Thesis outline

The structure of this dissertation has been disposed with the aim of allow, as much as possible, a fairly comprehension of the effectuated work. After this introductory chapter, the document has been distributed amongst seven chapters and four additional appendices, with the following structure:

- Chapter 2: In this chapter, the mathematical approaches and tools used for the static and dynamic features description of nonlinear resonators are summarized.
- Chapter 3: The MEMS generalities theory and the fabrication approaches of the MEMS devices is explained in this chapter.

- Chapter 4: This chapter explores the design and operating conditions for the two-well potential distribution and homoclininc chaos in beam-shaped MEMS, using a 1DOF model based on the parallel plate assumption.

- Chapter 5: In this chapter, an accurate nonlinear model considering realistic conditions of MEMS cc-beams (near real deflection profile, and nonlinear second order parameters) is developed. The conclusions provided by chapter 4 are adapted to this accurate model.

- Chapter 6: This chapter presents the experimental results of bistable behavior and chaotic response. These results prove the conclusions mainly exposed in previous chapters, and the accuracy of the model presented in chapter 5.

- Chapter 7: In this chapter, the main conclusions of the thesis are exposed as well as the proposed future work to continue with the advances provided by this thesis.

- Appendix A: In this appendix, a control method based on fuzzy logic and implemented with artificial neural networks is proposed to be used to improve the chaotic response of a MEMS system within the homoclinic region.

- Appendix B: This appendix presents the implementation of the model developed in chapter 5 in an analog hardware description language (AHDL) and its utility for the bistable analysis.

- Appendix C: This appendix is a list of the different generations of chips designed and fabricated during this thesis.

- Appendix D: This appendix summarizes the main approaches to the application of chaotic behavior to the field of critpography and secure communications.

Chapter 2

Mathematical model of nonlinear and chaotic resonators

This chapter summarizes the mathematical tools and approaches used to model the static and dynamic features and behavior of nonlinear resonators. The models for the MEMS resonator behavior (exposed in further chapters) can be assimilated to the Duffing equation which has been used to observe (by means of analytical and numerical studies) the nonlinear response of such systems. The features of the Duffing equation are explored from the analytical and numerical point of view, and analytical and numerical methods for chaotic behavior prediction and detection are introduced.

2.1 One degree of freedom model

A reduced-order model, with one degree of freedom (1DOF), for a doubly clamped beam (figure 2-1) under electrostatic actuation (see section 3.1.5 for details) is obtained, and assimilated to the classical Duffing equation. The Galerkin method, a powerful and computationally efficient weighted-residual method, capable of handling nonconservative and nonlinear systems has been used [48]. Next, a brief illustration of this method is presented.

2.1.1 The Galerkin discretization and order-reduction method

Following the theoretical development explained in [48], consider a system with an equation and boundary condition expressed as

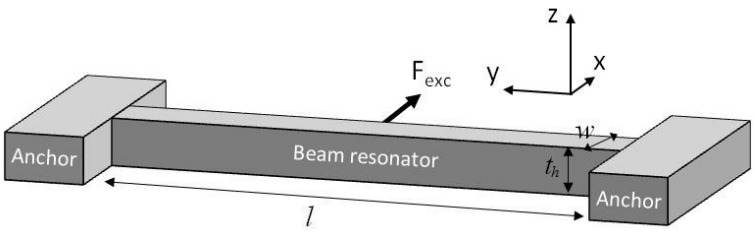

Figure 2-1: Representation of a clamped-clamped beam resonator (where the electrostatic actuation is applied) with its dimensional variables.

$$A(z) = F$$
$$B_1(z) = z_{1,0} \quad B_2(z) = z_{2,0} \tag{2.1}$$

with $z(x,t)$ being a parameter that depends on space and time variables, A a linear or nonlinear differential operator in space and time, F the forcing function, B_1 and B_2 are boundary operators and $z_{1,0}$ and $z_{2,0}$ the boundary constants (nontime varying). Based on the method of separation of variables, an approximate solution of the system (2.1) is assumed to have the form of

$$z(x,t) = \phi_0(x) + \sum_{i=1}^{n} u_i(t)\,\phi_i(x) \tag{2.2}$$

where $\phi_0(x)$, the particular static solution of the system, satisfies the inhomogeneous boundary conditions of equation (2.1), every $u_i(t)$ is an unknown function of time, and every $\phi_i(x)$ correspond to an approximate or trial function, which should fulfll the following conditions:

- Satisfy the homogeneous form of all the boundary conditions of the problem.
- Be as many times differentiable as the order of the differential equation of the system
- Form or belong to a complete set of linearly independent functions, otherwise the series of equation (2.2) will not converge to the exact solution as $n \to \infty$

The approximated solution (2.2) is substituted into the system (2.1), and the error R is generated:

$$A\left[\phi_0(x)+\sum_{i=1}^{n}u_i(t)\,\phi_i(x)\right]-F=R. \tag{2.3}$$

Following the procedure of the weighted residual methods, the error R is made to converge to 0 by requiring it to be orthogonal to every weighting function (chosen to be the $\phi_i(x)$ functions, in the case of the Galerkin method). Multiplying equation (2.3) by $\phi_j(x)$ and integrating the whole equation over the domain Γ of the problem the following expression is obtained:

$$\int_\Gamma \phi_j(x)\left(A\left[\phi_0(x)+\sum_{i=1}^{n}u_i(t)\,\phi_i(x)\right]-F\right)dx=\int_\Gamma \phi_j R dx=0 \tag{2.4}$$

The result of this procedure is a set of n differential equations in time ($u_i(t)$), which can be numerically integrated using Runge-Kutta techniques. The total response is given by substituting these integrated functions into equation (2.2).

2.1.2 1DOF model formulation

Starting from the Bernouilli-Euler-based equation, provided in [49], which governs the deflection $\omega(y,t)$ of beams with uniform geometry and material properties, a 1DOF macromodel (reduced-order model) can be obtained from applying the Galerkin method [48]. Following [49], the deflection of each position y of the beam span of a clamped-clamped microbeam is given by :

$$\begin{aligned} EI\frac{\partial^4\omega}{\partial y^4}+\rho w t_h\frac{\partial^2\omega}{\partial t^2}+c_1\frac{\partial\omega}{\partial t} &= \left(N_1+\frac{Ewt_h}{2l}\int_0^l\left(\frac{\partial\omega}{\partial y}\right)^2dy\right)\frac{\partial^2\omega}{\partial y^2} \\ &\quad+\frac{\epsilon t_h v(t)^2}{2(s-\omega)^2} \end{aligned} \tag{2.5}$$

where l,w,and t_h are the dimensions of the beam (length, width and thickness respectively), s is the gap between the beam and the electrode, y is the position along the beam length, t time, E the Young modulus, I the moment of inertia of the cross section, ρ the material density, ϵ the dielectric constant, c_1 is the damping factor per unit length and N_1 the axial load. The term added to N_1 parameter corresponds to the mid-plane stretching effect that, as will be seen in the development of the method, causes the non-linear behavior of the

system [50]. The voltage parameter $v(t)$ is defined as

$$v(t) = V_{DC} + V_{AC}\cos(\Omega t) \tag{2.6}$$

and the boundary conditions are

$$\omega(0,t) = \omega(l,t) = 0, \quad \frac{\partial\omega(0,t)}{\partial y} = \frac{\partial\omega(l,t)}{\partial y} = 0 \tag{2.7}$$

For simplicity, non-dimensional parameters (denoted by hats) are commonly used:

$$\hat{y} = \frac{y}{l}, \quad \hat{\omega} = \frac{\omega}{s}, \quad \hat{t} = \frac{t}{T}. \tag{2.8}$$

where T is a time scale defined as [48]:

$$T = \sqrt{\frac{\rho w t_h l^4}{EI}} \tag{2.9}$$

From these definitions the following relations are obtained

$$\frac{\partial^n\omega}{\partial y^n} = \frac{s}{l^n}\frac{\partial^n\hat{\omega}}{\partial\hat{y}^n}, \quad \frac{\partial^n\omega}{\partial t^n} = \frac{s}{T^n}\frac{\partial^n\hat{\omega}}{\partial\hat{t}^n} \tag{2.10}$$

and substituting these relations into equation (2.5) leads to

$$\begin{aligned} EI\frac{s}{l^4}\frac{\partial^4\hat{\omega}}{\partial\hat{y}^4} + \rho w t_h\frac{s}{T^2}\frac{\partial^2\hat{\omega}}{\partial\hat{t}^2} + c_1\frac{s}{T}\frac{\partial\hat{\omega}}{\partial\hat{t}} &= \left(N_1 + \frac{E w t_h}{2l}\int_0^1\left(\frac{s}{l}\frac{\partial\hat{\omega}}{\partial\hat{y}}\right)^2 l d\hat{y}\right)\frac{s}{l^2}\frac{\partial^2\hat{\omega}}{\partial\hat{y}^2} \\ &\quad + \frac{\epsilon t_h v(t)^2}{2s^2(1-\hat{\omega})^2} \end{aligned} \tag{2.11}$$

Finally, the nondimensional equation (2.12) is obtained. From now, the hats of the nondimensional parameters have been removed for simplicity.

$$\frac{\partial^4\omega}{\partial y^4} + \frac{\partial^2\omega}{\partial t^2} + c\frac{\partial\omega}{\partial t} = \left(N + \alpha_1\int_0^1\left(\frac{\partial\omega}{\partial y}\right)^2 dy\right)\frac{\partial^2\omega}{\partial y^2} + \alpha_2\frac{v(t)^2}{(1-\omega)^2} \tag{2.12}$$

where $c = \dfrac{c_1 l^4}{EIT}$, $N = \dfrac{N_1 l^2}{EI}$, $\alpha_1 = 6\left(\dfrac{s}{w}\right)^2$, and $\alpha_2 = \dfrac{\epsilon t_h l^4}{2s^3 EI}$, and having defined the cross section moment of inertia (I) as $I = \dfrac{t_h w^3}{12}$. Based on the method of separation of variables, the solution of equation (2.12) can be written in the form

$$\omega(y,t) = \sum_{i=1}^{n} u_i(t)\,\phi_i(y) \tag{2.13}$$

with $\phi_i(y)$ being the i-th mode shape of the clamped-clamped beam. The mode shapes are orthogonal between them. By substituting this equation into equation (2.12), multiplying each term by the j-nth mode shape and integrating all over the beam domain from 0 to 1, the following expression is obtained:

$$\begin{aligned}
&\int_0^1 \phi_j(y)\left(\sum_{i=1}^{n} u_i(t)\,\frac{\partial^4\phi_i(y)}{\partial y^4} + \sum_{i=1}^{n}\frac{\partial^2 u_i(t)}{\partial t^2}\phi_i(y)\right)dy \\
&+c\int_0^1 \phi_j(y)\left(\sum_{i=1}^{n}\frac{\partial u_i(t)}{\partial t}\phi_i(y)\right)dy \\
&-\int_0^1 \phi_j(y)\left(\alpha_1\int_0^1\left(\sum_{i=1}^{n} u_i(t)\,\frac{\partial\phi_i(y)}{\partial y}\right)^2 dy + N\right)\left(\sum_{i=1}^{n} u_i(t)\,\frac{\partial^2\phi_i(y)}{\partial y^2}\right)dy \\
&= \alpha_2 v(t)^2\int_0^1\left(\frac{\phi_j(y)}{\left(1-\sum_{i=1}^{n} u_i(t)\,\phi_i(y)\right)^2}\right)dy
\end{aligned} \tag{2.14}$$

The ortogonality between the mode shapes implies that

$$\int_0^1 \phi_i\phi_j = \delta_{i,j} \tag{2.15}$$

where $\delta_{i,j}$ is the Kronecker Delta, namely 1 if $i = j$ and 0 otherwise. Considering only the first term of the Galerkin expansion ($\omega(y,t) = u_1(t)\,\phi_1(y)$):

$$\begin{aligned}
&\int_0^1 \phi_1(y)\,u_1(t)\,\frac{\partial^4\phi_1(y)}{\partial y^4}dy + \frac{\partial^2 u_1(t)}{\partial t^2} + c\frac{\partial u_1(t)}{\partial t} \\
&-\int_0^1 \phi_1(y)\left(\alpha_1\int_0^1\left(u_1(t)\,\frac{\partial\phi_1(y)}{\partial y}\right)^2 dy + N\right)\left(u_1(t)\,\frac{\partial^2\phi_1(y)}{\partial y^2}\right)dy \\
&= \alpha_2 v(t)^2\int_0^1\left(\frac{\phi_1(y)}{\left(1-u_1(t)\,\phi_1(y)\right)^2}\right)dy
\end{aligned} \tag{2.16}$$

and, by regrouping terms:

$$\frac{\partial^2 u_1(t)}{\partial t^2} + c\frac{\partial u_1(t)}{\partial t} + u_1(t)\overbrace{\left(\int_0^1 \phi_1(y)\frac{\partial^4 \phi_1(y)}{\partial y^4}dy - N\int_0^1 \phi_1(y)\frac{\partial^2 \phi_1(y)}{\partial y^2}dy\right)}^{\kappa_1}$$
$$-u_1(y)^3\underbrace{\alpha_1\int_0^1 \phi_1(y)\frac{\partial^2 \phi_1(y)}{\partial y^2}dy\int_0^1\left(\frac{\partial \phi_1(y)}{\partial y}\right)^2 dy}_{\kappa_3}$$
$$=\underbrace{\alpha_2 v(t)^2\int_0^1\left(\frac{\phi_1(y)}{(1-u_1(t)\phi_1(y))^2}\right)dy}_{F(y,t,v(t))} \tag{2.17}$$

Changing the notation $\dot{} = \dfrac{\partial}{\partial t}$, $' = \dfrac{\partial}{\partial y}$ and denoting respectively by u_i and ϕ_i the functions $u_i(t)$ and $\phi_i(y)$, equation (2.17) can be expressed as [50]:

$$\ddot{u} + c\dot{u} + \kappa_1 u + \kappa_3 u^3 = F. \tag{2.18}$$

However, the integral of the forcing term ($F(y,t,v(t))$) can not be easily solved, and a Taylor expansion in power series, without retaining a sufficient number of terms would make the method wield inaccurate results. A reliable and efficient method (proposed in [49]) to overcome this issue consists in multiplying both sides of equation (2.12) by $(1-\omega)^2$ (being ω the the nondimensional parameter) and then applying the Galerkin method. If the following relation between axial force and the mode shape is used:

$$\phi_i'''' - N\phi_i'' - \omega_{n0i}^2\phi_i = 0 \tag{2.19}$$

with ω_{n0i} being the natural frequency corresponding to the i-th mode shape, expressed with respect to the time scale T, the development of the Galerkin method provides:

$$
\begin{aligned}
& \int_0^1 \phi_j \left(1-\sum_{m=1}^{n} u_m\phi_m\right)^2 \left(\sum_{i=1}^{n} u_i\omega_{n0i}^2\phi_i + \sum_{i=1}^{n} \ddot{u}_i\phi_i\right) dy \\
+ \quad & c\int_0^1 \phi_j \left(1-\sum_{m=1}^{n} u_m\phi_m\right)^2 \left(\sum_{i=1}^{n} \dot{u}_i\phi_i\right) dy \\
- \quad & \alpha_1\int_0^1 \phi_j \left(1-\sum_{m=1}^{n} u_m\phi_m\right)^2 \left(\int_0^1 \left(\sum_{i=1}^{n} u_i\phi_i'\right)^2 dy\right)\left(\sum_{i=1}^{n} u_i\phi_i''\right) dy \\
= \quad & \alpha_2 v(t)^2 \int_0^1 \phi_j dy
\end{aligned} \tag{2.20}
$$

Only one term in the Galerkin expansion is considered now:

$$
\begin{aligned}
& \int_0^1 \phi_1 \left(u_1\omega_{n0i}^2\phi_1\right)(1-u_1\phi_1)^2 dy + \int_0^1 \ddot{u}_1\phi_1^2(1-u_1\phi_1)^2 dy \\
+ \quad & c\int_0^1 \dot{u}_1\phi_1^2(1-u_1\phi_1)^2 dy - \alpha_1\int_0^1 \phi_1\left(u_1\phi_1''\int_0^1 \left(u_1\phi_1'\right)^2 dy\right)(1-u_1\phi_1)^2 dy \\
= \quad & \alpha_2 v(t)^2 \int_0^1 \phi_1 dy
\end{aligned} \tag{2.21}
$$

Finally the reduced order model provided by the Galerkin method (equation (2.22)), after executing the spatial integrals (easier to solve than in equation (2.17)), can be numerically integrated in time for dynamic simulations.

$$
\begin{aligned}
& \ddot{u}_1 + u_1\omega_{n0i}^2 + c\dot{u}_1 - \alpha_1 \frac{\int_0^1 \phi_1'^2 dy \left(u_1^3\int_0^1 \phi_1\phi_1'' dy - 2u_1^4\int_0^1 \phi_1^2\phi_1'' dy + u_1^5\int_0^1 \phi_1^3\phi_1'' dy\right)}{\left(1-2u_1\int_0^1 \phi_1^3 dy + u_1^2\int_0^1 \phi_1^4 dy\right)} \\
= \quad & \alpha_2 v(t)^2 \frac{\int_0^1 \phi_1 dy}{\left(1-2u_1\int_0^1 \phi_1^3 dy + u_1^2\int_0^1 \phi_1^4 dy\right)}
\end{aligned} \tag{2.22}
$$

2.2 Analytical approach to the Duffing equation

In 1918, Georg Duffing introduced an equation for a nonlinear oscillator with a cubic stiffness term to describe the hardening spring effect observed in many mechanical problems [22]. The Duffing equation governs the behavior of an oscillator subjected to structural nonlinear stiffness, to viscosity damping, and to a sinusoidal excitation [51]. Many years later, Holmes and Moon experimentally observed chaotic behavior with a metallic cantilever beam placed

symmetrically between two clamped magnets, which perform temporally periodic forcing to the cantilever [52]. P. Holmes and F. Moon described the motion of the tip of a cantilever beam by means of a version of the Duffing equation with a negative linear stiffness. The Duffing equation represents, together with the Van der Pol equation the most common examples of chaotic oscillators [22]. From the generic form of the Duffing equation (2.23), an analysis of the fixed points and their stability is performed.

$$\ddot{x} + \alpha x^3 + \beta x + \delta \dot{x} = \Phi cos\left(\omega t\right) \tag{2.23}$$

where α corresponds to the nonlinear stiffness, β to the linear stiffness, δ to the damping parameter and Φ to the excitation amplitude. The equation (2.23) can be rewritten as a system with:

$$\begin{aligned} \dot{x}_1 &= x_2 \\ \dot{x}_2 &= -\alpha x_1^3 - \beta x_1 + \epsilon\left(-\bar{\delta} x_2 + \bar{\Phi}\cos\left(\omega t\right)\right) \end{aligned} \tag{2.24}$$

where $x_1 = x$,$x_2 = \dot{x}$, $\delta = \epsilon\bar{\delta}$, $\Phi = \epsilon\bar{\Phi}$, and ϵ being a small perturbation parameter. The unperturbed case is a Hamiltonian system [53]. The system (2.24) may be expressed as a matrix $\dot{X} = F\left(X\right)$, were

$$X = \begin{pmatrix} x_1 \\ x_2 \end{pmatrix}; F\left(X\right) = \begin{pmatrix} f_1\left(x_1, x_2\right) \\ f_2\left(x_1, x_2\right) \end{pmatrix} \tag{2.25}$$

Considering the non forced case $\Phi = 0$ the fixed points (denoted by $(x_{1st},\ x_{2st})$) are obtained from imposing $\dot{x}_1 = \dot{x}_2 = 0$, namely

$$\begin{aligned} 0 &= x_{2st} \\ 0 &= -\alpha x_{1st}^3 - \beta x_{1st} - \epsilon\bar{\delta} x_{2st} \end{aligned} \tag{2.26}$$

In this way, the signs of the linear and nonlinear stiffness coefficients (α, β) determine the nature of the fixed points. In the case of $\alpha\beta > 0$ only the trivial fixed point exists $(x_{1st}, x_{2st}) = (0, 0)$. In contrast, for $\alpha\beta < 0$, besides the trivial fixed point, there are two

nontrivial fixed points, given by $(x_{1st}, x_{2st}) = \left(\pm\sqrt{-\frac{\beta}{\alpha}}, 0\right)$. Following the procedure shown in [17], the stability of the fixed point is examined by performing local analysis. Now the variables y_1 and y_2 and their temporal derivatives are defined as

$$\begin{aligned} y_1 &= x_{1st} + \Delta x_1(t) \\ y_2 &= x_{2st} + \Delta x_2(t) \\ \dot{y_1} &= \Delta \dot{x_1}(t) \\ \dot{y_2} &= \Delta \dot{x_2}(t) \end{aligned} \tag{2.27}$$

where $|\Delta x_1(t)|, |\Delta x_1(t)| << 1$. Introducing these variables into the matrix Duffing equation (2.24), the following system is obtained

$$\begin{aligned} \Delta \dot{x_1}(t) &= f_1(y_1, y_2) = y_2 \\ \Delta \dot{x_2}(t) &= f_2(y_1, y_2) = -\alpha y_1^3 - \beta y_1 - \epsilon\bar{\delta} y_2 \end{aligned} \tag{2.28}$$

Undoing the change of variable, neglecting the powers of the terms $\Delta x_1(t)$, $\Delta x_1(t)$ and taking into account the equilibrium equations (2.26), leads to the following matrix equation:

$$\begin{pmatrix} \Delta \dot{x_1} \\ \Delta \dot{x_2} \end{pmatrix} = \begin{pmatrix} 0 & 1 \\ -\left(\beta + 3\alpha x_{1st}^2\right) & -\epsilon\bar{\delta} \end{pmatrix} \begin{pmatrix} \Delta x_1 \\ \Delta x_2 \end{pmatrix} \tag{2.29}$$

which is equivalent to the expression $\frac{d\Delta X}{dt} = J_F \Delta X$ evaluated over the fixed points, where J_F is the Jacobian matrix of $F(X)$. The eigenvalues of the matrix J_F can be obtained from its characteristic equation

$$\lambda^2 + \epsilon\bar{\delta}\lambda + \left(\beta + 3\alpha x_{1st}^2\right) = 0 \tag{2.30}$$

namely

$$\lambda = \frac{-\epsilon\bar{\delta} + \sqrt{\left(\epsilon\bar{\delta}\right)^2 - 4\left(\beta + 3\alpha x_{1st}^2\right)}}{2} \tag{2.31}$$

The signs of the eigenvalues and, consequently, the stability of the fixed points depend on

the values of the parameters of the characteristic equation. In the cases under consideration, the damping term always opposes the movement, thus a negative sign for the δ parameter is considered. The cases given by the sign combinations for the α and β parameters are analyzed.

- **Case 1** $\alpha, \beta > 0$. In this case, only the trivial fixed point exists, $(x_{1st}, x_{2st}) = (0, 0)$, thus the expression of the eigenvalues is given by

$$\lambda = \frac{-\epsilon\bar{\delta} \pm \sqrt{\left(\epsilon\bar{\delta}\right)^2 - 4\beta}}{2} \tag{2.32}$$

  and some subcases may be considered

  * $4\beta > (\epsilon\delta)^2$. The eigenvalues are complex conjugate values with negative real part, thus the trivial fixed point is a stable focus.
  * $4\beta = (\epsilon\delta)^2$. There is only one eigenvalue, which is real and negative.
  * $4\beta < (\epsilon\delta)^2$. There are two real and negative eigenvalues. The trivial fixed point is a stable node.

- **Case 2** $\alpha, \beta < 0$. In this case, the only fixed point is the trivial one, thus the eigenvalues are obtained from equation (2.32). There will be a positive and a negative eigenvalue, regardless the damping term. In consequence, the trivial fixed point will be a saddle point.

- **Case 3** $\alpha < 0, \beta > 0$. For this situation, besides the trivial fixed point, there are two nontrivial fixed points given by $(x_{1st}, x_{2st}) = \left(\pm\sqrt{-\frac{\beta}{\alpha}}, 0\right)$. The eigenvalues of the jacobian matrix evaluated over the nontrivial fixed points are given by

$$\lambda = \frac{-\epsilon\bar{\delta} \pm \sqrt{\left(\epsilon\bar{\delta}\right)^2 + 8\beta}}{2} \tag{2.33}$$

  thus, regardless the value of the damping factor, the nontrivial fixed points will be always saddle points. In contrast, the nature of the trivial fixed point depends on the relative value of the damping factor and the linear stiffness term following three subcases, the same subcases than in case 1.

- **Case 4** $\alpha > 0, \beta < 0$. With this situation, the nature of the nontrivial fixed points follow diffent subcases:

  * $|8\beta| > (\epsilon\delta)^2$. The eigenvalues are complex conjugate, with negative real part, thus both nontrivial points are stable focus.
  * $|8\beta| = (\epsilon\delta)^2$. There is only one eigenvalue, which is real and negative.
  * $|8\beta| < (\epsilon\delta)^2$. The eigenvalues are real and negative. The nontrivial fixed points are stable nodes.

  On the other hand, the trivial fixed point will be always a saddle point, which can be deduced from the eigenvalues of the jacobian matrix evaluated over this point, namely a real positive and a real negative eigenvalues.

2.2.1 Analysis of the case 4: $\alpha > 0$, $\beta < 0$

If the conservative situation is considered (namely, neglecting the damping and forcing terms) [54], the resulting equation is given by

$$\ddot{x} + \beta x + \alpha x^3 = 0. \tag{2.34}$$

The equilibrium or fixed points are known to be $(x_{1st}, x_{2st}) = (0, 0)$, which is a saddle point, and $(x_{1st}, x_{2st}) = \left(\pm\sqrt{\frac{-\beta}{\alpha}}, 0\right)$, which for the conservative case are two centers. Equation (2.34) represents an integrable Hamiltonian system with total energy [55]:

$$H = T(\dot{x}) + U(x) = \frac{1}{2}\dot{x}^2 + \frac{1}{2}\beta x^2 + \frac{1}{4}\alpha x^4 \tag{2.35}$$

where the potential function is

$$U(x) = \beta\frac{1}{2}x^2 + \alpha\frac{1}{4}x^4 \tag{2.36}$$

This potential function presents a local maximum in $x = 0$ and two local minima in $x = \pm\sqrt{\frac{-\beta}{\alpha}}$. The minimum value of the potential function in these local minima is $U_{\min} = U\left(\pm\sqrt{\frac{-\beta}{\alpha}}\right) = \frac{-\beta^2}{4\alpha}$. The potential function $U(x)$ for different values of the parameters is depicted in figure 2-2:

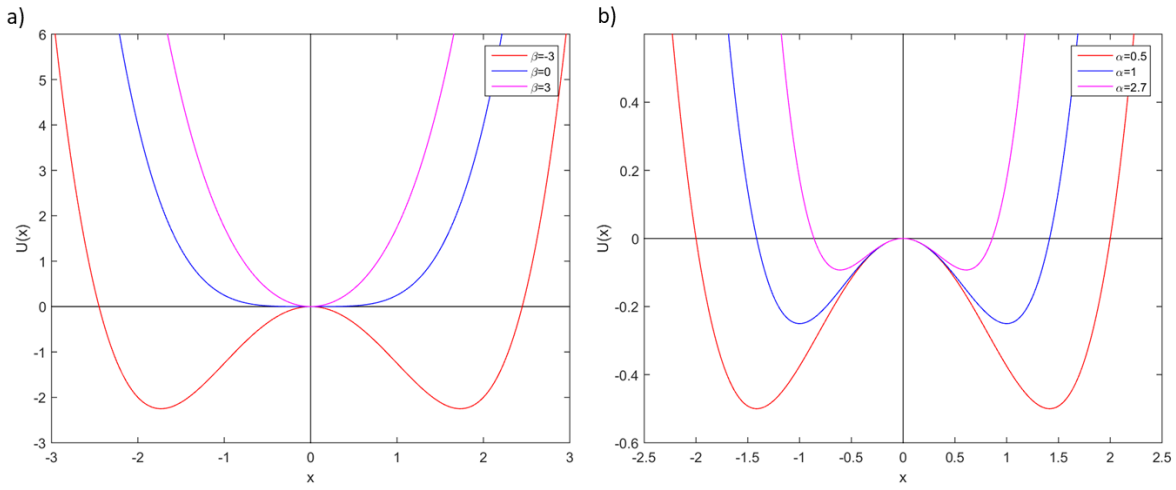

Figure 2-2: Representation of the pontential function for a) $\alpha = 1$ and different values of β and b) $\beta = -1$ and different values of α.

The time derivative of the total energy of the system provided by equation (2.35) is $\dot{H} = \dot{x}\left(\ddot{x} + \beta x + \alpha x^3\right)$. The definition of the system (2.34) implies $\dot{H} = 0$ and, consequently, the total energy has a constant value along the whole orbit (which is consistent with its conservative essence) [54]. The value of the constant energy for each orbit is determined from the initial values of position and velocity $(x_0, \dot{x}_0)$ as $H_0 = \frac{1}{2}\dot{x}_0^2 + \frac{1}{2}\beta x_0^2 + \frac{1}{4}\alpha x_0^4$. In this way for each value of energy, the velocity can be written and plot as a function of the position as [54]:

$$\dot{x}\left(x\right) = \pm\sqrt{2\left(H_0 - U\left(x\right)\right)}. \tag{2.37}$$

The orbits corresponding to each value of initial energy are plotted in figure 2-3, and the maximum velocity in each orbit is obtained from its minimum value of the potential function as $\dot{x}_{\max} = \sqrt{2\left(H_0 - U_{\min}\left(x\right)\right)} = \sqrt{2H_0 + \frac{\beta^2}{2\alpha}}$.

The symmetric orbits corresponding to the $H_0 = 0$ level of energy for the conservative case are called homoclinic orbits. The equation of the homoclinic orbits is found to be [55]:

$$\Gamma_{\pm}^{0}\left(t\right) = \left(\pm\sqrt{\frac{-2\beta}{\alpha}}\,\mathrm{sech}\left(\sqrt{-\beta}t\right), \mp\sqrt{\frac{2\beta^2}{\alpha}}\tanh\left(\sqrt{-\beta}t\right)\mathrm{sech}\left(\sqrt{-\beta}t\right)\right) \tag{2.38}$$

Beside the homoclinic orbits, from sign of the constant energy level, two different kind of movements can be observed: the in-well low-amplitude oscillations with a energy level

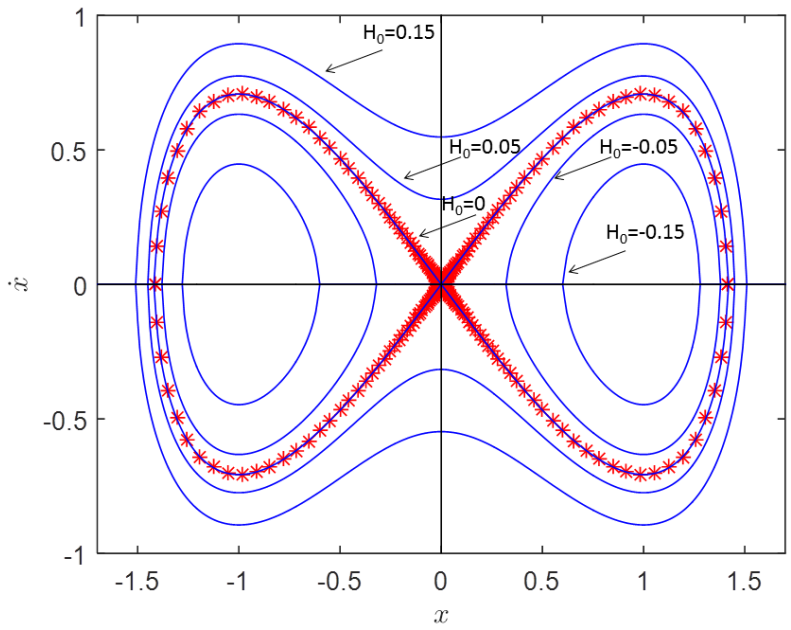

Figure 2-3: Phase portrait of the conservative orbits for different levels of constant energy (H_0). The homoclinic orbits are highlighted with red asterisks.

placed in $U_{\min} < H_0 < 0$, which turn around the nontrivial fixed points, and the cross-well motion, with a positive level of energy. The homoclinic orbits, also called separatrix, represent the boundary between these two movements.

If the damping term is introduced in equation (2.34), the system is no longer conservative, and given that $\dot{H} = \dot{x}\left(\ddot{x} - x + \alpha x^3\right) = \delta\dot{x}^2 < 0$ the energy decreases along the orbits, except over the axis $\dot{x} = 0$ where the energy remains constant [54]. The two nontrivial fixed point are no longer centers, instead of that they behave as stable focus. The trivial fixed point keeps being a saddle point, but the homoclinic orbit is broken: the stable manifold has no longer its origin in the unstable manifold like in the conservative case, but it comes from upper levels of energy.

Finally, if the forcing term $\Phi\cos(\omega t)$ is also included, the system presents a far richer dynamical behavior. First of all it cannot be known if the system loses or wins energy along the orbits: $\dot{H} = \dot{x}\left(\ddot{x} - x + \alpha x^3\right) = \delta\dot{x}^2 + \dot{x}\Phi\cos(\omega t)$. However, the energy keep being constant over the axis $\dot{x} = 0$. On the other hand the fixed point are no longer independent of the time:the solutions of the system $\dot{x} = x = 0$ present a dynamic evolution. Finally, the introduction of forcing term implies an increase from 2 to 3 of the dynamical dimension of

the system; accordingly to Poincare-Bendixon theorerm [22], it is this third dimension that allows for chaotic behavior.

2.2.2 Duffing equation solutions based on Jacobi elliptic functions

Taking the undamped and unforced Duffing system, accordingly to [56], the differential equation $\ddot{z} + az + bz^3 = 0$ with initial conditions $z(0) = z_0$ and $\dot{z}(0) = \dot{z}_0$ has an exact analytical solution in the form of the Jacobi elliptic function $z = Zcn(\omega t + \theta)$, where $\omega t + \theta$ is the argument of the elliptic function (cn), k^2 is the modulus and Z is the amplitude given by

$$Z = \sqrt{\left(-\frac{a}{b} + \frac{a + bz_0^2}{b}\sqrt{1 + \frac{2\dot{z}_0^2 b}{a}}\right)} \tag{2.39}$$

The frequency of vibration (denoted by Ω) for a phase angle of 2π is found to be a generalization of the resonant frequency equation for the case on non-negligible nonlinear stiffness.

$$\Omega = \frac{\pi\sqrt{a + bZ^2}}{2K\left(\dfrac{bZ^2}{2\left(a + bZ^2\right)}\right)} \tag{2.40}$$

with $K(\cdot)$ being the compete elliptic integral of the first kind, defined with the arbitrary variable κ as:

$$K(\kappa) = \frac{\pi}{2}\left(1 + \frac{1}{4}\kappa^2 + \frac{9}{64}\kappa^4 + \frac{25}{256}\kappa^6 + \ldots\right) \tag{2.41}$$

The adjustment between this analytical solution for the Duffing equation and the numerically obtained solutions can be proven either in time or in frequency domain. Since the differential equation is undamped, the initial amplitude remains as the stationary oscillation amplitude. Thus, equation (2.40) shows the influence of the nonlinear stiffness (as a function of the oscillation amplitude) in the system resonance frequency, observed as the spring hardening effect caused by the mechanic nonlinearity. This effect is in agreement with the amplitude-dependent peak resonant frequency obtained by L.D.Landau and E.M Lifshitz in [57], which is briefly summarized in section 2.2.3.

2.2.3 Amplitude-dependent resonance frequency: Landau analysis

Accordingly to [57] and [58], the dumped mass-spring equation ca be assimilated to te mass-spring equation with a generic nonlinear stiffness function (F_k), given by:

$$F_k = k_1 x + k_2 x^2 + k_3 x^3 + \sigma x^n \tag{2.42}$$

with σx^n representing the higher order terms, which are assumed to be negligible. If the undamped and unforced case is considered:

$$m\frac{\partial^2 x}{\partial^2 t} + k_1 x + k_2 x^2 + k_3 x^3 = 0 \tag{2.43}$$

where m represents the mass, an oscillation at the natural frequency ω_0 (given by $\omega_0 = \sqrt{\frac{k_1}{m}}$) is expected. However, the nonlinear terms changes the oscillation frequency to ω_0'. To obtain an approximation for such new frequency, a perturbation analysis around the linear natural frequency is performed, by considering

$$\begin{aligned} \omega_0' &= \omega_0 + \epsilon\omega_1 + \epsilon^2\omega_2 \\ x &= x_0 + \epsilon x_1 + \epsilon^2 x_2 \end{aligned} \tag{2.44}$$

with ϵ being a small and positive perturbation parameter. The nonlinear stiffness parameters are defined as $k_2 = \epsilon\kappa_2 m$ and $k_3 = \epsilon\kappa_3 m$, and a new time variable $\tau = \omega_0 t$ is introduced. The derivatives with respect to the original time variable t are related to the derivatives with respect to the new time variable τ as following: $\frac{\partial}{\partial t} = \frac{\partial}{\partial \tau}\frac{\partial \tau}{\partial t}$. Introducing the expressions (2.44) into equation (2.43):

$$\begin{aligned} \left(\omega_0 + \epsilon\omega_1 + \epsilon^2\omega_2\right)^2 \left(\frac{\partial^2 x_0}{\partial \tau^2} + \epsilon\frac{\partial^2 x_1}{\partial \tau^2} + \epsilon^2\frac{\partial^2 x_2}{\partial \tau^2}\right) + \omega_0^2\left(x_0 + \epsilon x_1 + \epsilon^2 x_2\right) \\ +\epsilon\kappa_2\left(x_0 + \epsilon x_1 + \epsilon^2 x_2\right)^2 + \epsilon^2\kappa_3\left(x_0 + \epsilon x_1 + \epsilon^2 x_2\right)^3 = 0 \end{aligned} \tag{2.45}$$

and grouping terms in powers of ϵ (ϵ^0, ϵ^1, and ϵ^2) next three equations are obtained:

$$\omega_0^2 \frac{\partial^2 x_0}{\partial \tau^2} + \omega_0^2 x_0 = 0$$

$$2\omega_1\omega_0 \frac{\partial^2 x_0}{\partial \tau^2} + \omega_0^2 \frac{\partial^2 x_1}{\partial \tau^2} + \omega_0^2 x_1 + \kappa_2 x_0^2 = 0$$

$$\omega_0^2 \frac{\partial^2 x_2}{\partial \tau^2} + \omega_1^2 \frac{\partial^2 x_0}{\partial \tau^2} + \omega_0^2 x_2 + 2\kappa_2 x_0 x_1 + \kappa_3 x_0^3 + 2\omega_0\omega_2 \frac{\partial^2 x_0}{\partial \tau^2} + 2\omega_0\omega_1 \frac{\partial^2 x_1}{\partial \tau^2} = 0 \quad (2.46)$$

The first equation, corresponding to the terms in ϵ^0, provides a solution in the form of $x_0 = X_0 \cos(\tau)$ and by substituting it into the second equation, corresponding to the terms in ϵ^1, the following expression is obtained:

$$\omega_0^2 \frac{\partial^2 x_1}{\partial \tau^2} + \omega_0^2 x_1 = -\kappa_2 \left(X_0 \cos(\tau)\right)^2 - 2\omega_1\omega_0 X_0 \cos(\tau) \quad (2.47)$$

where the secular term $2\omega_1\omega_0 X_0 \cos(\tau)$ would imply an infinite growing of x_1 in time, thus needs to be equaled to zero, which imply $\omega_1 = 0$. Then a solution for the equation (2.47) is found as

$$x_1 = X_0^2 \frac{\kappa_2}{6\omega_0^2} \cos(2\tau) - X_0^2 \frac{\kappa_2}{2\omega_0^2} \quad (2.48)$$

Repeating the process and substituting the found expressions for x_0 and x_1 into the equation in terms of ϵ^3 provides

$$\omega_0^2 \frac{\partial^2 x_2}{\partial \tau^2} + \omega_0^2 x_2 = -\left(\frac{3\kappa_3}{4} X_0^3 - \frac{5\kappa_2^2}{6\omega_0^2} X_0^3 - 2\omega_0\omega_2 X_0\right) \cos(\tau) - \left(\frac{\kappa_2^2}{6\omega_0^2} X_0^3 + \frac{\kappa_3}{4} X_0^3\right) \cos(3\tau) \quad (2.49)$$

where, again, the secular term $\left(\frac{3\kappa_3}{4} X_0^3 - \frac{5\kappa_2^2}{6\omega_0^2} X_0^3 - 2\omega_0\omega_2 X_0\right)$ must be set to zero, thus

$$\omega_2 = \left(-\frac{5\kappa_2^2}{12\omega_0^3} + \frac{3\kappa_3}{8\omega_0}\right) X_0^2 \quad (2.50)$$

and now, the equation in terms ϵ^3 can be solved, providing the expression of x_2. At this point the value of the oscillation frequency affected by the nonlinear terms can be obtained:

$$\omega_0' = \omega_0 + \epsilon^2 \left(-\frac{5\kappa_2^2}{12\omega_0^3} + \frac{3\kappa_3}{8\omega_0}\right) X_0^2 \quad (2.51)$$

which implies (in agreement with [59] and [60]) the amplitude dependence of the resonance frequency in terms of the Landau successive approximations method:

$$\omega_0' = \omega_0 + \omega_0 \left(\frac{3k_3}{8k_1} - \frac{5k_2^2}{12k_1^2} \right) X_0^2 \tag{2.52}$$

The nonlinearity is most apparent around the resonance frequency since nonlinear spring provokes that the resonance frequency depends on the oscillation amplitude.

2.3 Numerical approach to the Duffing equation

A wider knowledge of the nonlinear and chaotic features of the Duffing equation requires numerical computation. The goal of this approach is to numerically bound the regions of the parameters space that provide chaotic behavior for a further extrapolation to the equation of the MEMS under study.

2.3.1 Duffing system with double-well potential (2WP)

The typical chaotic strange attractor of the Duffing system with two-well potential distribution corresponds to snap-trough oscillations in the form of a cross-well chaotic motion: a bounded non-periodic and, apparently, erratic jumps between the potential wells through the potential barrier placed in the trivial fixed point $x = 0$ [61]. A complete view of the dynamics of the Duffing system with two potential wells is provided in [62]. The main interest regarding to the system's behavior is located to the surroundings of the principal resonance. In [62] all the attractors governing the nonlinear resonance phenomenon are related and a map of the parameter space regions (where the boundaries for the nonlinear effects and the robust chaotic motion are set) is shown. Chaotic behavior can be obtained from the reproduction of the strange chaotic attractor, or as the culmination of the period-doubling process (also known as Feigenbaum route), a process of nonlinear effects which provoke the progressive appearance of new frequencies until the chaotic response is reached.

Figure 2-4 depicts the numerically obtained bifurcation diagrams of the two potential well Duffing system, from a variation of a parameter while the other parameters are keep constant. For each value of the control parameters (β in figure 2-4a) and Φ in figure 2-4b)) the equation is numerically solved and the positions of the Poincare[1] points are plotted. Notice that the Poincare map is enforced to depict only the stationary response, while the

[1]The Poincare map is known as the stroboscopic plot of the phase space, obtained from the intersection of the trajectories with a subspace (called Poincare section), transversal to the flow, which implies a discrete time mapping with a regular sampling period [63].

transient response has been removed. Extensive chaotic behavior for a wide range of the control parameters can be observed from these numerical simulations.

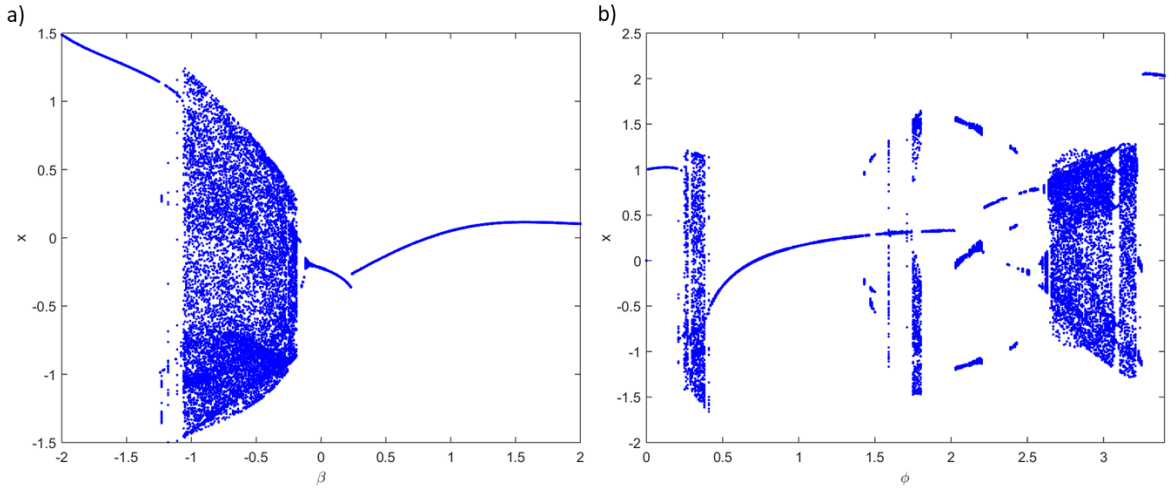

Figure 2-4: Bifurcation diagrams based on the positions of the Poincare points: a) variation of the β parameter under constant values of the $\alpha = 1$, $\delta = 0.2$, $\Phi = 0.3$ and $\omega = 1$ parameters and b) variation of the ϕ parameter under constant values of the $\alpha = 1$, $\beta = -1$, $\delta = 0.2$ and $\omega = 1$ parameters.

Robust and sustained chaotic behavior, as reported in [52], is obtained in the regions predicted by the bifurcation diagrams and its time series, phase map, Poincare map and periodogram are shown in figures 2-5 and 2-6.

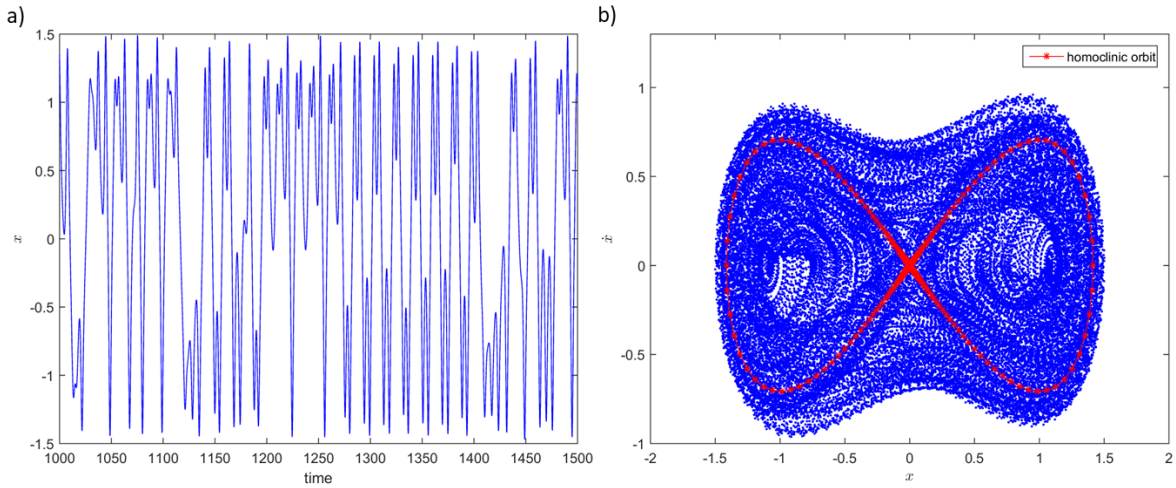

Figure 2-5: a) Chaotic time series and b) phase map with highlighted homoclinic orbits for the two-well potential Duffing equation with parameters $\alpha = 1$, $\beta = -1$, $\delta = 0.2$, $\Phi = 0.3$ and $\omega = 1$.

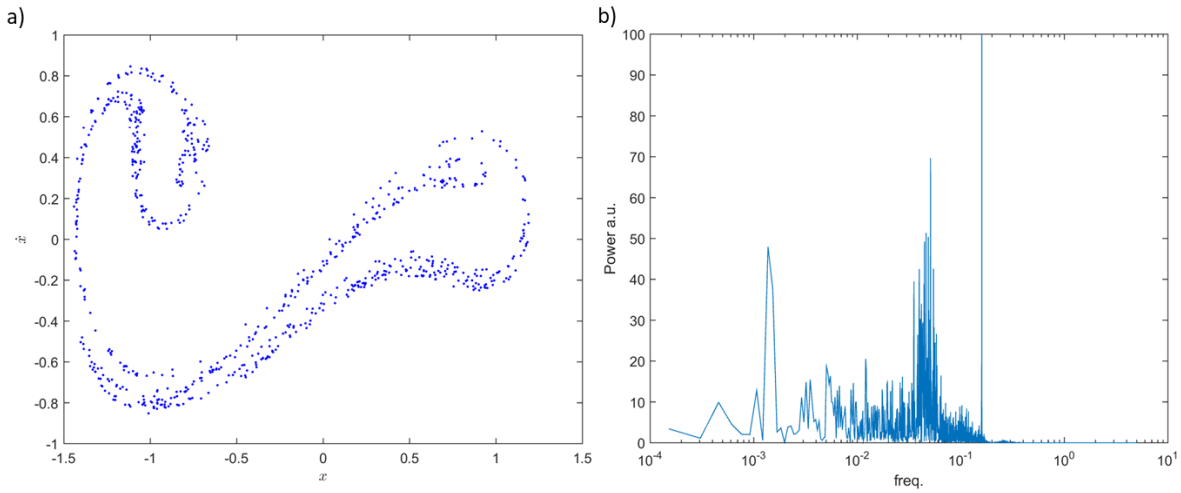

Figure 2-6: a) Chaotic Poincare map and b) periodogram for the two-well potential Duffing equation with parameters $\alpha = 1$, $\beta = -1$, $\delta = 0.2$, $\Phi = 0.3$ and $\omega = 1$.

2.3.2 Duffing system with single-well potential (1WP)

Nonlinear and even chaotic behavior have been reported from the Duffing system with a single potential well [64]. The Duffing system is defined by a symmetrical vector field, and this fact generates symmetrical trajectories with respect to the origin [65]. The bifurcation caused by symmetry breaking imply the presence of nonlinear behaviors which may lead, to period-doubling bifurcation and, ultimately, to chaotic behavior [25]. Only the orbits which have reached a symmetry breaking can follow the period-doubling route. In reference [65] regions of the parameters space with nonlinear and chaotic motion of the Duffing equation with a single potential well are represented. In the same way as in figure 2-4, a bifurcation diagram based on the Poincare points is depicted in figure 2-7a). The chaotic behavior predicted in this bifurcation diagram is numerically obtained and represented in 2-7b) and 2-8.

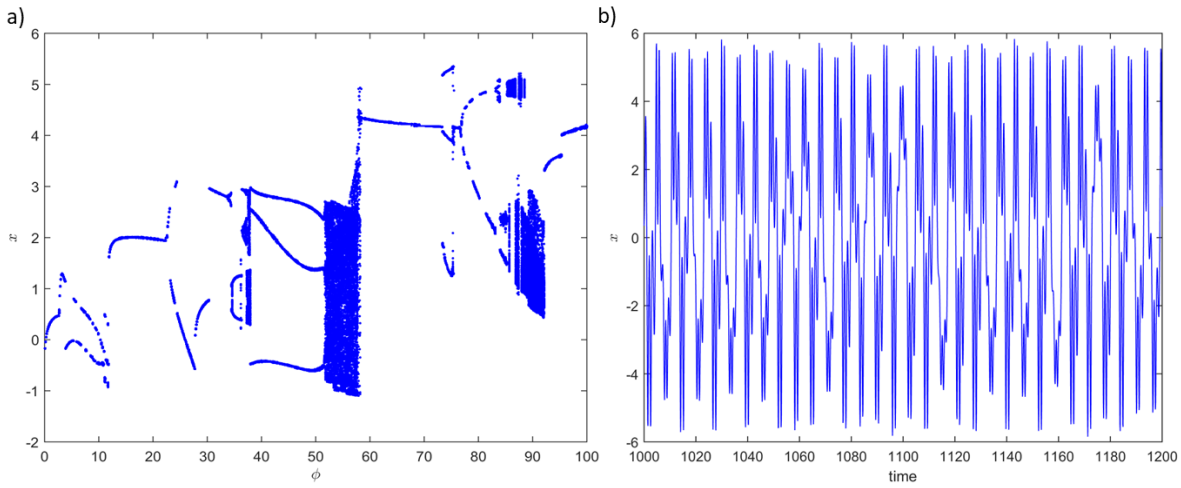

Figure 2-7: a) Bifurcation diagrams based on the positions of the Poincare points:variation of the ϕ parameter under constant values of $\alpha = \beta = \omega = 1$, $\delta = 0.2$. b) Chaotic time series in a single potential well distribution for $\alpha = \beta = \omega = 1$, $\delta = 0.2$ and $\Phi = 57$.

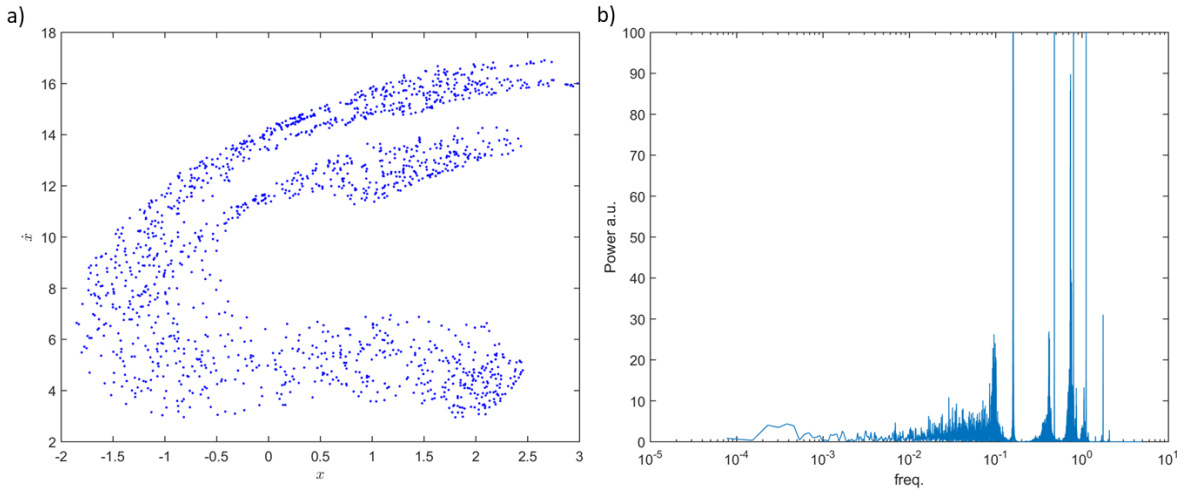

Figure 2-8: a) Chaotic Poincare map and b) periodogram for the single-well potential Duffing equation with parameters $\alpha = \beta = \omega = 1$, $\delta = 0.2$ and $\Phi = 57$.

As a conclusion, chaotic behavior can be also reached with a single potential well distribution, however the required excitation amplitudes are far greater than the ones needed in the double-well potential Duffing system. Moreover, the chaotic behavior obtained as the culmination of the period doubling route in a single potential well system is considered "weak" in comparison with the "robust" chaotic behavior corresponding to the "cross-well" attractor [54], [62]. The weakness of the chaotic motion of the single well potential system can be seen from its frequency bandwidth when the position time series is represented in

the frequency domain and compared with the bandwidth for the "cross well" case (figures 2-6b) and 2-8b)).

2.4 Melnikov method and chaos

The Melnikov method is an analytical technique which can be used to predict the presence of chaos in a dynamical system [66], [22]. For a generic one degree of freedom system as

$$\dot{u} = f(u) + \epsilon g(u,t) \tag{2.53}$$

and considering the vectors $u = \begin{pmatrix} x \\ y \end{pmatrix}$ $f = \begin{pmatrix} f_0(x,y) \\ f_1(x,y) \end{pmatrix}$, and $g = \begin{pmatrix} g_0(x,y,t) \\ g_1(x,y,t) \end{pmatrix}$, the system can be expressed as

$$\begin{aligned} \dot{x} &= f_0(x,y) + \epsilon g_0(x,y,t) = \frac{\partial H}{\partial y} + \epsilon g_0(x,y,t) \\ \dot{y} &= f_1(x,y) + \epsilon g_1(x,y,t) = -\frac{\partial H}{\partial x} + \epsilon g_1(x,y,t) \end{aligned} \tag{2.54}$$

where ϵ is a small perturbation parameter, g is a periodic function in t function with period T, and H is a real Hamiltonian function. Assume that the unperturbed system ($\epsilon = 0$) is an integrable Hamiltonian system which possesses a fixed hyperbolic saddle point u_0 with overlapping stable and unstable manifolds, and an homoclinic orbit $\Gamma_{\pm}^{0}(t)$ [55] [66]. If a small perturbation is applied ($\epsilon \neq 0$), a periodic orbit close to the saddle point exists (and represents a fixed point in the Poincare map) [66]. In agreement with Moser theorem and the Smale Birkhoff homoclinic theorem, if the the stable and unstable manifolds intersect transversely then the systems dynamics will contain a horseshoe map [66]. The existence of a horseshoe map implies that there are a countable infinity of periodic orbits, that there are an uncountable number of aperiodic orbits, and that there is a dense orbit which comes arbitrarily close to every point in the invariant set of the horseshoe map. In summary a chaotic set may exists in the system when a transverse intersection of the manifolds occurs [22], [66]. The Melnikov function, defined as

$$M(t_0) = \int_{-\infty}^{\infty} f\left(\Gamma_{+}^{0}(t)\right) \wedge g\left(\Gamma_{+}^{0}(t), t + t_0\right) dt \tag{2.55}$$

(where $\Gamma_+^0(t) = \Gamma_+^0(x(t), y(t))$ is the homoclinic orbit) gives a measure of distance between the stable and unstable manifolds in the perturbed case (when $\epsilon \neq 0$ and can be used to tell when the stable and unstable manifolds intersect transversely. If for some t_0 and some set of parameters $M(t_0) = 0$ and $M'(t_0) \neq 0$ (with M' being the time derivative of the Melnikov function), the stable and unstable manifolds have a transverse intersection, horseshoe map exists, and chaos may occur [22], [66].

2.5 Lyapunov exponents

The aperiodic long-term behavior of a bounded deterministic system with a high sensitivity to initial conditions may be taken as a commonly accepted description of chaotic motion [14]. While it is relatively easy to establish when a system is deterministic (described by equations without random variables), aperiodic and bounded, at least for the time-scales over which numerical computations are feasible, the sensitive dependence on initial conditions is far more difficult to establish [14]. Lyapunov exponents quantify the exponential divergence of initially close state-space trajectories and estimate the amount of chaos in a system [15].

The Lyapunov spectrum (a system with n dimensions has n Lyapunov exponents) is closely related to the eigenvalues of the system. Both quantities are determined from the Jacobian matrix assuming linear local dynamics. However, unlike the eigenvalues, Lyapunov exponents are always real numbers, their associated directions are mutually orthogonal and each Lyapunov exponent is a global quantity (averaged along the orbit or trajectory) [14].

An striking feature of chaotic systems is the unpredictability of their future states despite a deterministic time evolution [67]. This instability is a consequence of the inherent instability of the solutions, reflected by the sensitive dependence on initial conditions. While in linear or periodic systems the divergence between initially close trajectories is very slow, in chaotic systems such divergence is given at exponential rate. The properly averaged exponent of this exponential rate is characteristic for the system underlying the data and quantifies the strength of chaos [67]. From the Lyapunov spectrum, the most significant exponent is the maximal one. Several developed algorithms restrict themselves to determine the maximal Lyapunov exponent. As an abstract analysis, let $\bar{s}_{n1}$ and $\bar{s}_{n2}$ be two points in phase space with small distance between them $\|\bar{s}_{n1} - \bar{s}_{n2}\| = \delta_0 \ll 1$, while $\delta_{\Delta n}$ denotes the distance at time n between the two trajectories emerging from these points,

$\delta_{\Delta n} = \|\bar{s}_{n1+\Delta n} - \bar{s}_{n2+\Delta n}\|$. Then, the maximal Lyapunov exponent λ verifies approximately the relation

$$\delta_{\Delta n} \approx \delta_0 e^{\lambda \Delta n} \tag{2.56}$$

Two trajectories cannot separate further than the size of the attractor, thus the law (2.56) is only valid during times Δn for which $\delta_{\Delta n}$ remains small. In addition, a mathematically more rigorous definition must involve two limits: $\delta_0 \to 0$ and $\Delta n \to \infty$. More specifically the first limit must be implemented firstly in order to avoid the second one (where the Lyapunov exponent λ becomes a well-defined and invariant quantity) to provide always infinite results [67]. Considering the previous observations, the dynamic behavior of the system can be classified from the value of λ provided by the equation(2.56).

- A negative value of the maximal Lyapunov exponent means an exponential rhythm approximation of the trajectories, which implies the existence of a stable fixed point.
- A zero value of the maximal Lyapunov exponent implies a conservation of the distance between two trajectories, for instance a marginally stable motion.
- A positive but finite value of the maximal Lyapunov exponent reveals an exponentially growing divergence between the trajectories. This fact is assimilated to the sensitive dependence to initial conditions, which characterizes the chaotic systems
- An infinite value of the maximal Lyapunov exponent corresponds to random noise.

The Lyapunov exponents are a characteristic quantity, invariant under transformations as phase space reconstructions, variable changes, and rescalings, as long as these transformations are smooth. The Lyapunov exponents carry the units of an inverse time and give a typical time scale for the divergence or convergence of nearby trajectories [67].

Given the definition of the Lyapunov spectrum $(\lambda_1, \lambda_2, \ldots, \lambda_n)$, where n is the number of equations (or, equivalently the number of state variables), the sum of the positive exponents, equals the Kolmogorov entropy K (equation (2.57)). This is a mean rate of the information gain [68], [15].

$$K = \sum_{\lambda_i > 0} \lambda_i \tag{2.57}$$

2.5.1 Lyapunov exponents in unidimensional dynamic systems

Let an unidimensional map[2] be defined as [14]:

$$x_{n+1} = f(x_n) \tag{2.58}$$

Consider two nearby initial points, x_0, $x_0 + \Delta x_0$, with $\Delta x_0 \ll 1$. After an iteration of the map, these points are separated by

$$\Delta x_1 = f(x_0 + \Delta x_0) - f(x_0) \tag{2.59}$$

Being, by definition

$$f'(x_0) = \left.\frac{df}{dx}\right|_{x_0} = \lim_{\Delta x_0 \to 0} \frac{f(x_0 + \Delta x_0) - f(x_0)}{\Delta x_0} \tag{2.60}$$

equation (2.58) can be approximated to

$$\Delta x_1 \approx \Delta x_0 f'(x_0) \tag{2.61}$$

Now the local Lyapunov exponent can be calculated as the λ which verifies $e^{\lambda} = \left|\frac{\Delta x_1}{\Delta x_0}\right|$, namely

$$\lambda = \ln \left|\frac{\Delta x_1}{\Delta x_0}\right| \approx \ln |f'(x_0)| \tag{2.62}$$

The global Lyapunov exponent is defined as the average of the local ones (exponents given by equation (2.62)) over many iterations [14]:

$$\lambda = \lim_{N \to \infty} \frac{1}{N} \sum_{n=0}^{N-1} \ln |f'(x_n)| \tag{2.63}$$

Besides the average exponential rate of separation of two nearby initial conditions, the global Lyapunov exponent quantifies as well the average stretching of the phase space. However, it is important to understand that the value of the local Lyapunov may oscillate widely with respect to the global value of the system, and it is possible the presence of transient chaotic behavior or even periodic behavior for a long time before eventually sampling a different

[2]Discrete sequence of state vectors or scalars which constitute a dynamic system described in discrete time [69]

region dominated by an strange attractor. In such cases, long computations are required to avoid incorrect results, and even under this assumption, no matter how long the calculation lasts, a complete dependability of the result would never be reached [14].

Let now a one-dimensional flow defined by $\dot{x} = f(x)$ [14]. To calculate the Lyapunov exponent, two initial points close enough to each other (x_0 and $x_0 + \Delta x_0$) are considered, and a small time delay Δt

$$\Delta x_1 = \Delta x_0 + [f(x_0 + \Delta x_0) - f(x_0)]\,\Delta t \approx \Delta x_0 \left[1 + f'(x_0)\,\Delta t\right] \tag{2.64}$$

In the same way as in the discrete case (map), the local Lyapunov exponent is defined as the λ that verifies [14]:

$$e^{\lambda \Delta t} = \frac{\Delta x_1}{\Delta x_0} = 1 + f'(x_0)\,\Delta t \tag{2.65}$$

and, in order to obtain the global value of the Lyapunov exponent, the average value along the trajectory is calculated, as it is done in the discrete case with the equation (2.63). In the case of continuous unidimensional systems, the trajectories can only be attracted towards fixed points or the infinite. A trajectory attracted towards a fixed point will provide a negative Lyapunov exponent; in this case the Lyapunov exponent quantifies the rhythm at which the points of the neighborhood of the fixed point collapse towards it. On the other hand, it must be understood that a trajectory attracted toward the infinite will present a positive Lyapunov exponent without chaotic movement, but in this case a positive Lyapunov exponent does not mean a chaotic behavior because the movement is not bounded [14]. Actually, since in a deterministic system trajectories are not allowed to intersect, a continuous system (described by autonomous differential equations) cannot be chaotic in less than 3 dimensions [67] (in agreement with the Poincare-Bendixson theorem [13], [22]).

The Lyapunov exponents of a unidimensional discrete system (map) are nondimensional, while for a continuous system they have the units corresponding to t^{-1}. The inverse of the Lyapunov exponent can be understood as the measure in temporal domain of the divergence or convergence of the trajectories corresponding to the initial conditions in a neighborhood (keeping in mind the great oscillation that the local Lyapunov exponent may present)[14].

2.5.2 Phase space reconstruction by Delay Method

Consider a dynamic system where each state depend on N dynamic variables which constitute the phase state. However, the available information provided by an experiment is not a phase space, but a time series, commonly a scalar sequence of measurements of some quantity which depends on the current state of the system, taken at a sampling time [67]:

$$s_n = s\left(\bar{x}\left(n\Delta t\right)\right) + \mu_n \tag{2.66}$$

where s is the sampling function, and μ_n the measurement noise. Fortunately, from a time series, the reconstruction of the phase space is possible. Such a reconstruction is really needed, given the importance of the phase space in further calculations of the system dynamics. The phase state, reconstructed by delays in m dimensions is constituted by vectors $\bar{s}_n$ in the form of:

$$\bar{s}_n = \left(s_n, s_{n+\nu}, \ldots, s_{n+(m-2)\nu}, s_{n+(m-1)\nu}\right) \tag{2.67}$$

where each component of the vector is a value of the time series, separated from the next one and the previous one by a temporary margin. This temporary margin, expressed as number of samples (ν) or in temporary units ($\nu\Delta t$) is known as "delay". Each point of the trajectory expressed with the reconstructed phase space has m components, one component for each delay in the original time series. An important question now is under what assumptions a trajectory expressed with the reconstructed phase space is equivalent to the trajectory in the original phase space.

Takens' theorem determines when the obtained representation of the state vectors in the original phase state in $\mathbb{R}^n$ is equivalent[3] to the the representation given by the vectors $\bar{s}_n$ in $\mathbb{R}^m$, corresponding to the reconstructed phase space by delays [69]. Before the formulation of the Takens' theorem, some concepts are introduced.

An attractor is defined as the set of points or the subspace in phase space dense of solution trajectories after the evanescence of the initial transient solutions [14]. Equilibrium points, limit cycles or toroidal surfaces (for quasiperiodic motions) are examples of nonchaotic attractors. However chaotic orbits move around strange attractors, which are

[3] An equivalence is a homeomorphism, namely a bijective continuous function between two topological sets, and with continuous inverse function [69].

constituted by a set in phase space with fractal dimension [16]. Examples of attractors are depicted in figure 2-9. Formally, an attractor A is a set of points, with null volume, belonging to the phase space, which verifies the following conditions [69], [16]:

- A is an invariant set: all the trajectories that start from A, remain in A for all time.
- A attracts a set of initial conditions (basins of attraction of A). There is a set $U \supset A$ such as $x_0 \in U$, the distance between $x(t)$ and A tends to zero when t tends to ∞. A attracts all the trajectories starting from U. The greatest U that satisfies this condition is called basis of the attractor.
- A is minimal: there is no subset of A which verifies these two previous conditions

Note that for the existence of an attractor, the overall dynamics must be dissipative, i.e., globally stable, and the total rate of contraction must outweigh the total rate of expansion [15]. A dynamic system is dissipative if the volume of any set in the phase space decreases along the time. Formally, let S_0 be a set of points which occupies a volume V_0 in the phase space. Let's consider these points as initial conditions of trajectories that, after a time T will become the set of points $S_T = f_T(S_0)$ which will occupy a volume V_T in phase space. If the condition $V_T < V_0 \forall (T, S_0)$ is verified , then the system is dissipative. Eventually a null volume (namely, the attractor) will be reached.

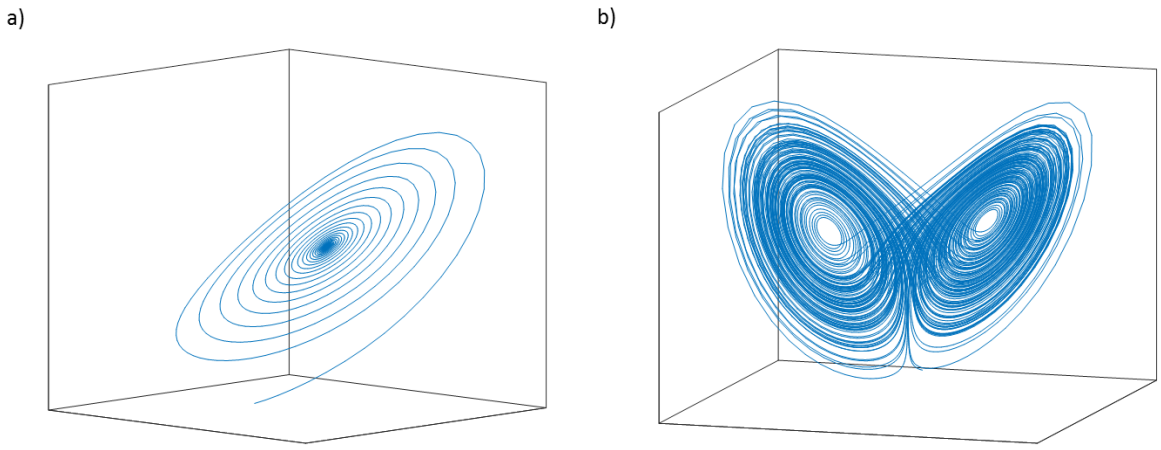

Figure 2-9: a) Nonchaotic attractor obtained from Lorenz equation. b) Lorenz strange chaotic attractor.

The Minkowski-Bouligand (or "box-counting") dimension is a parameter that characterizes the dimension of a fractal set [14]. Given a fractal set located into a n-dimensional

space, let's define a a set of n-dimensional cubes or "boxes" with edge L. The number of needed cubes to cover all the fractal set depends on the edge L. More specifically, if the object that is covered by "boxes" was a line, one would expect that $N \propto \frac{1}{L}$, and if it was a surface, one would expect that $N \propto \frac{1}{L^2}$, etc. In the same way, for a set of a fractal dimension D_0 the verification of $N \propto \frac{1}{L^{D_0}}$ is expected, thus the Minkowski-Bouligand dimension is defined as [70]:

$$D_0 = \lim_{L \to 0} \frac{\ln(N)}{\ln\left(\frac{1}{L}\right)} \tag{2.68}$$

Another method to determine the dimension of the attractor consists in, given a point in the space, build around it a topological sphere with variable radius r, and quantify the number of points of the attractor inside the topological sphere as a function of the radius (and let's call this function $b(r)$). The exponent of the growth of the number of points inside the topological sphere as a function of the radius is good approximation of the attractor dimension (d), which may be not an integer [14], [70]. This exponent is known as the correlation dimension:

$$b(r) = kr^d \tag{2.69}$$

At this point the Takens' theorem can be enunciated:

Theorem 1. *Let M be a compact manifold of dimension m. For pairs (ϕ, y), with $\phi \in Diff^2(M)$, $y \in C^2(M, \mathbb{R})$, it is a generic property that the map $\Phi_{\phi,y} : M \to \mathbb{R}^{2m+1}$, defined by*

$$\Phi_{(\phi,y)}(x) = \left(y(x), y(\phi(x)), \ldots, y\left(\phi^{2m}(x)\right)\right)$$

is an embedding[4] [71].

Takens' theorem establishes that, as a generic property, a map built by means of the delay method ("delay map") of dimension $m = 2D + 1$ is an embedding of a compact manifold A of dimension D if the measurement function $s : A \to \mathbb{R}$ is class C^2 and includes all the degrees of freedom. As a consequence of this enunciate, if the dimension (m) of the reconstructed phase space is greater than twice the attractor 's dimension, an attractor

[4]Continuous and injective application between topological spaces (differentiable manifolds, in this case) which implies a homeomorphism between image and inverse image [71].

generated in the reconstructed space will be equivalent to the existing one in the original phase space [67].

If a dimension m provides a good reconstruction of the phase space, reconstructions with dimensions $m' > m$ will be also good. However, it must be taken into account that an excessively big value of the reconstructed space dimension adds redundancies that may generate for instance, a degradation in the performance of the algorithms for the Lyapunov exponent calculation. A way to estimate the optimal dimensions for the reconstructed phase space is the false neighbors method. The main idea of this method is to measure the euclidean distance between a given point and its closest neighbor in the reconstructed phase space while the dimension m of the reconstructed phase space is being increased. If the increase of m implies an increase in the distance, it can be deduced that the previous dimension m was insufficient and the points seemed to be closer than what they really are because they were in a projection of a space with more dimensions. Otherwise, it can be deduced that the increase of the dimension m is unnecessary. Let a generic point p defined in a reconstructed space with $m-1$ dimensions : $p = \left(s_k, s_{k+\nu}, \ldots, s_{k+(m-3)\nu}, s_{k+(m-2)\nu}\right)$, and let the point p_{NN} be its closer neighbor, the square of the euclidean distance between them can be expressed as

$$R_{m-1}^2 = \left[s_k - s_{NN}\right]^2 + \cdots + \left[s_{k+(m-3)\nu} - s_{NN+(m-3)\nu}\right]^2 + \left[s_{k+(m-2)\nu} - s_{NN+(m-2)\nu}\right]^2 \tag{2.70}$$

while the square of the euclidean distance between those two points when another dimension is added to the reconstructed space state is

$$R_m^2 = R_{m-1}^2 + \left[s_{k+(m-1)\nu} - s_{NN+(m-1)\nu}\right]^2 \tag{2.71}$$

Using a threshold value R_T for the ratio between the increase in the euclidean distance when the additional dimension is added and the euclidean distance in the original dimension, a criterion to decide whether the original dimension of the reconstructed phase space is enough is established as

$$R_T < \frac{\left|s_{k+(m-1)\nu} - s_{NN+(m-1)\nu}\right|}{R_m} \tag{2.72}$$

In practice, values of R_T between 10 and 50 are found to be appropriated for most situations [72]. The problem in determining the temporary delay (or lag) is still an open issue. In agreement with [15] a delay value that would provide good results is the one that makes the autocorrelation function drop to $1 - \frac{1}{e}$ of its initial value. The autocorrelation function is the measure of the similarity of a signal with respect to itself after a time delay [14], [67]. It allows to quantify the repetition patterns and the periodicities of a signal. For discrete cases (such as a time series), and for a generic delay ν, the autocorrelation function is defined as:

$$r_\nu = \sum_{n=1}^{N} (x_n - \mu)(x_{n+\nu} - \mu) \tag{2.73}$$

being μ the expected value of the signal. Then, is agreement with [15], a delay which implies an approximate relation given by

$$\frac{r_\nu}{r_0} \approx 1 - \frac{1}{e} \tag{2.74}$$

is needed. It means that the delay makes the components of the reconstructed phase space points be away enough to not present similarities.

Once the phase space is reconstructed, it is possible to reconstruct the attractor of the original system. The proper relation between the values of the attractor dimension and the reconstructed phase space dimensions, is obtained, in summary, from next theorems [14]:

- A generic d-dimensional curved space can be represented into a cartesian space with dimensions of $2d + 1$ dimension, fulfilling the requirement of no intersection of trajectories (Whitney's theorem) [14], [73].

- The anounced Takens' theorem, besides proving that the delay-constructed variables allow to reconstruct the phase space in order to host the dynamic system (provided the measured variable is smooth and couples to all the other variables), states the needed number of delays in the phase space reconstruction is $2d + 1$ [14].

- Sauer et.al. generalize the theorems of Whitney and Takens for attractors of fractal dimension D_F. The dimensions of the needed phase space to host an attractor with fractal dimension D_F must be simply greater than $2D_F$ [74].

In this way, a phase space reconstruction (called time-delay embedding space) with the minimum dimensions needed to reproduce and keep all the dynamic and topological

conditions of the original system can be reached. In most of the cases, this minimum dimension ("embedding dimension") is the nearest integer greater than $2D_F$.

The dimension of the phase space will influence on the kind of attractors. For example, a bounded solution of an autonomous differential equation on a curve must converge in a point (attractive equilibrium point), while for autonomous differential equations over the plane the bounded solutions may converge either to an equilibrium point or closed curve (periodic orbit or limit cycle). In systems of 3 dimensions or more dynamics are richer and more diverse [69]. In agreement with the theorem of Poincare-Bendixson[5], in systems with dimension equal o greater than 3 described by continuous differential equations, the presence of a positive Lyapunov exponent is an indicator of the presence of an strange attractor and chaotic behavior. In contrast of maps, a system described by autonomous equations cannot be chaotic in less than three dimensions. Since the trajectories are not allowed to intersect in a deterministic system, either the phase space or the attractor must be more than 2-dimensional. Notice that strange attractors with fractal dimensions are typical of chaotic systems [67].

The presence of a positive Lyapunov exponent is sufficient for diagnosing chaos and represents local instability in a particular direction. As mentioned before, the presence of an attractor makes the overall dynamics be dissipative [15]. Thus, even when there are several positive Lyapunov exponents, the sum across the entire spectrum is negative [15]. Actually, a theoretical consequence of the work of E.Lorenz [76] is that one of the causes of the strange attractors is the presence of dissipative terms, thus in absence of these terms the strange attractor disappears and a limit cycle appears.

2.5.3 Measuring the maximal Lyapunov exponent from data

One of the main goals of the dynamic systems analysis is to obtain the maximal Lyapunov exponent from a time series generated by the system. For this purpose, several algorithms have been implemented: Wolf et.al (1985), Sano and Sawada (1986) and Rosenstein el.al. (1993). These methods have in common the main numerical procedure for the calculation of the maximal Lyapunov exponent from a time series. A reconstruction of the phase space and the test of the exponential divergence of nearby trajectories by means of an average

[5]The bounded orbits corresponding to a C^1 class differential equation over the plane are periodic orbits, or (asymptotically) tend to periodic orbits or end in a fixed point [75].

value of those divergence along the whole data set.

Given a time series with values $\{x_1, x_2, \ldots, x_n\}$, the trajectory is expressed in the phase space reconstructed by delays as a matrix X with dimension $M \times m$:

$$X = \begin{bmatrix} X_1 \\ X_2 \\ \vdots \\ X_M \end{bmatrix} = \begin{bmatrix} x_1 & x_{1+\nu} & \cdots & x_{1+(m-1)\nu} \\ x_2 & x_{2+\nu} & \cdots & x_{2+(m-1)\nu} \\ \vdots & \vdots & \cdots & \vdots \\ x_M & x_{M+\nu} & \cdots & x_{M+(m-1)\nu} \end{bmatrix} \tag{2.75}$$

with m being the optimal dimension for the phase space reconstructed by delays or embedding space, M the number of initial points that belong to the first delay interval (as shown in figure 2-10) and ν the temporary delay nondimensionalized with the sampling period of the original time series (if J is the value of the time delay, and f_s is the sampling frequency of the time series, the relation $\nu = J \cdot f_s$ is verified). In order to build the matrix, it is necessary to consider a duration of the time series as a number N of points such as N is multiple of the optimal dimension of the reconstructed phase space. In this way the relation $N = M \times m$ is verified.

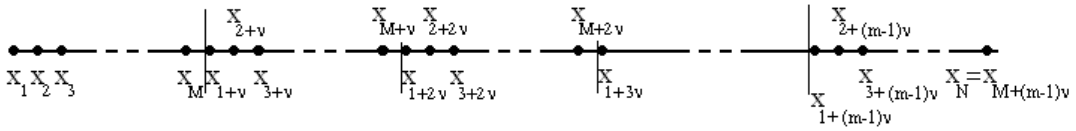

Figure 2-10: Representation of the time series points and their correspondence with the elements of the matrix M, equation (2.75).

Only with the time series, the whole state of the system is defined: e.g. in the $i-th$ discrete time, the system state is given by

$$X_i = \left[x_i, x_{i+\nu}, \ldots, x_{i+(m-1)\nu}\right] \tag{2.76}$$

Notice that every vector-row belonging to the trajectory matrix is a point in the reconstructed phase space. The numerical method for the maximal Lyapunov exponent calculation consists in taking one of these points X_{n0} as a reference, selecting all the points in a sphere of radius ϵ centered in X_{n0}, and computing the average of the distances between

the point X_{n0} and all these nearby points as a function of the relative time (expressed as a delay multiple). The logarithm of the averaged value of the ratio between the distance from the reference point to each point in the sphere and that distance in the initial time is a measure that contains all the deterministic fluctuations due to either the projection over the reconstructed phase space or the inherent dynamics of the system. Finally, an average of those logarithmic values must be done by taking as reference X_{n0} the other points (an arbitrary set of N points) of the time series. The values of last average depend on the discrete time Δn of the time series:

$$\lambda_1(\Delta n) = \frac{1}{N}\sum_{n_0=1}^{N} \ln\left(\frac{1}{|U(X_{n0})|}\sum_{X_n \in U(X_{n0})}\left|\frac{d_{X_n}(\Delta n)}{d_{X_n}(0)}\right|\right) \tag{2.77}$$

where $U(X_{n0})$ is the set of points X_n belonging to the the sphere of radius ϵ centered in the reference point X_{n0}, $d_{X_n}(0)$ is the euclidean distance in the initial time between the reference point X_{n0} and the generic point X_n belonging to $U(X_{n0})$, and $d_{X_n}(\Delta n)$ is the distance between these two generic points after a time lapse Δn (note that this time lapse implies a displacement of number of points Δn in the reconstructed-by-delays matrix of the system). λ_1 represents an estimation of the maximal Lyapunov exponent. From this basic procedure each algorithm introduces slight variations to improve the convergence of the numerical method, and to make it more robust and reliable.

A priori, the optimal value of the radius ϵ is unknown, and the problem of the presence of noise in the time series data must be considered. If the noise level is higher than the radius ϵ some points may be falsely considered to belong to the topological sphere. On the other hand, if the considered dimension m for the reconstructed phase space is big enough to avoid the intersection of trajectories, small variations of m wont affect the result.

An improved version of the Wolf algorithm implemented in Matlab is used in this thesis to perform the estimations of the maximal Lyapunov exponent, as a way to explore the presence of chaotic behavior in the generated time series. The main feature of the Wolf algorithm is the that a single neighbor is followed and repeatedly replaced when its separation from the reference trajectory grows beyond a certain limit [15], [77]. To corroborate its proper performance, several time series, obtained from the numerical resolution of the Duffing equation, have been used to test the algorithm, and its results have been compared with those provided by the Govorukhin algorithm. The Govorukhin algorithm, developed

by V. Govorukhin is a free source code which provides the Lyapunov spectrum from the ODE -system instead of the time-series. For each set of parameters corresponding to the equation parameters, the Govorukhin algorithm obtains the evolution of the three Lyapunov exponents of the Duffing system. The good agreement between both methods, the improved and Matlab-implemented Wolf algorithm and the Govorukhin algorithm (shown in figures 2-11 and 2-12, for either linear and chaotic Duffing systems), proves the accuracy of the first one, which can be used for time-series obtained from any source. The comparison is performed between the maximal Lyapunov exponent provided by the Govorukhin method and the Lyapunov value (corresponding to the maximal exponent) given by the Wolf algorithm.

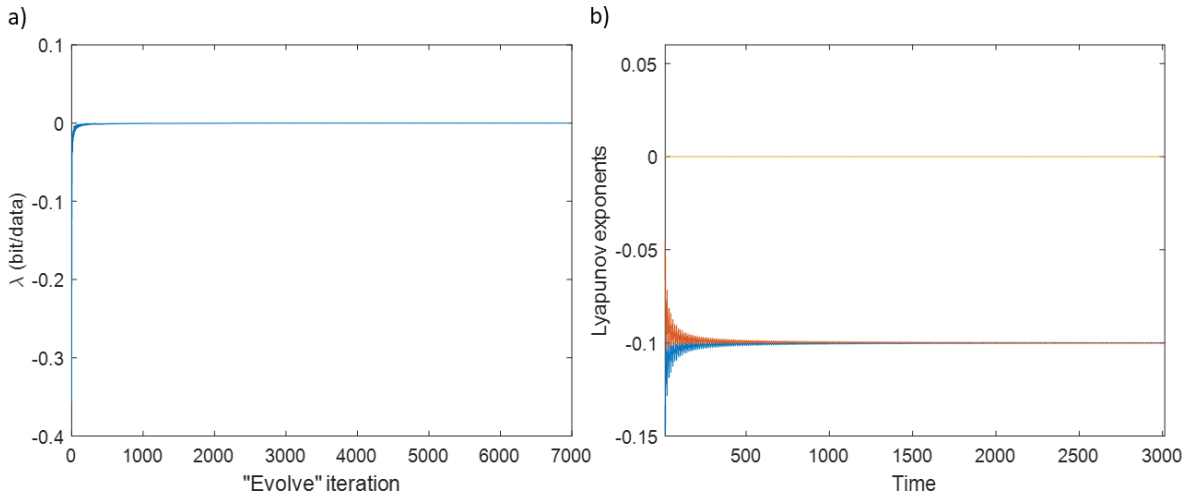

Figure 2-11: Lyapunov exponent of a Duffing linear system obtained from a) its time series with Wolf algorithm and b) its ODE system with Govorukhin algorithm.

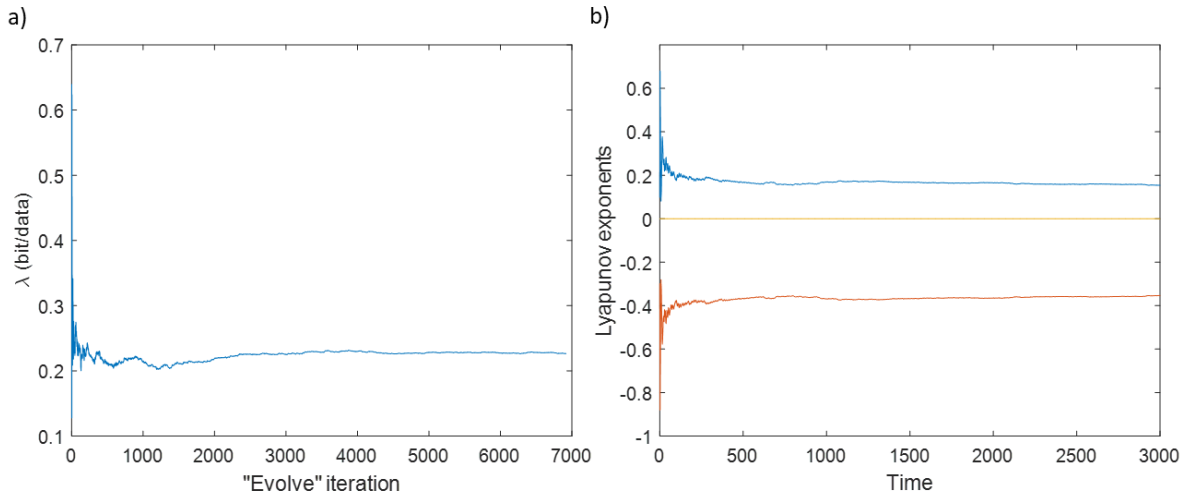

Figure 2-12: Lyapunov exponent of a Duffing chaotic system obtained from a) its time series with Wolf algorithm and b) its ODE system with Govorukhin algorithm.

Chapter 3

MEMS resonators: theory and fabrication

In this chapter, the operating principles and the fundamental parameters of electrostatically actuated cc-beam resonators with capacitive readout are described. The used analytical approach is the one degree of freedom (1DOF), obtained from the Galerkin discretization and order-reduction method. Taking this approach as starting point, an equation that govern the dynamical behavior of a generic cc-beam is obtained and all its terms are modeled with analytical expressions. In the same way, the electrostatic actuation and the capacitive readout principles are exposed and their influence over the MEMS performance is analyzed. The second part of this chapter relates the used fabrication and integration techniques and approaches in the framework of CMOS technologies, considered in this work.

3.1 MEMS modeling

The electromechanical system under consideration consists in a clamped-clamped beam placed symmetrically and in plane between two electrodes in which electrostatic actuation and capacitive readout may be respectively performed. Figure 3-1 depicts the scheme of the system and shows its geometrical parameters.

3.1.1 Resonance frequencies and modes

Given the one dimensional Bernouilli-Euler differential equation for the homogeneous beam (2.5), if the undamped and unforced case is considered and if the axial force and the mid-

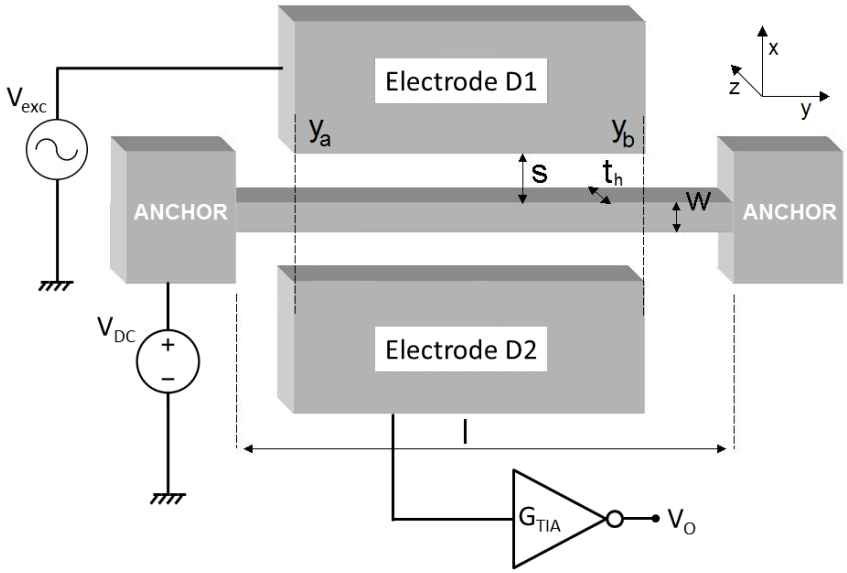

Figure 3-1: Schematics of the electromechanical system with one of the possible topologies, showing the parameters length (l), width (w), thickness dimension (t_h) and beam-driver gap distance (s). The in-plane vibration takes place in the x-direction.

plane stretching terms are set equal to zero, accordingly to [48] it can be expressed as

$$\frac{\partial^4 \psi(y,t)}{\partial y^4} + \frac{\rho A}{EI}\frac{\partial^2 \psi(y,t)}{\partial t^2} = 0, \tag{3.1}$$

where the deflection of the beam is denoted as $\psi(y,t)$, A is the cross section area ($A = wt_h$) and all the other parameters are defined in section 2.1.2. A solution in the form of $\psi(y,t) = x(y)\sin(\omega_n t + \theta)$ is supposed, where ω_n is the resonant frequency of the n mode of vibration and θ is an arbitrary phase; then the differential equation (3.1) becomes

$$\frac{\partial^4 x(y)}{\partial y^4} - \frac{\rho A}{EI}\omega_n^2 x(y) = 0 \tag{3.2}$$

If a solution in the form of $x(y) = e^{\lambda y}$ is considered, the characteristic equation is found to be

$$\lambda^4 - \frac{\rho A}{EI}\omega_n^2 = 0 \tag{3.3}$$

calling $q^4 = \frac{\rho A}{EI}\omega_n^2$, the roots of the characteristic equations are $\lambda = \pm q$,$\lambda = \pm iq$, thus the general solution has the form $x(y) = C_1 e^{qy} + C_2 e^{-qy} + C_3 e^{iqy} + C_4 e^{-iqy}$. In this way the

general solution can be written as

$$x(y) = A_1 \sinh(qy) + A_2 \cosh(qy) + A_3 \sin(qy) + A_4 \cos(qy), \tag{3.4}$$

and its y-derivative function is

$$\frac{dx(y)}{dy} = q\left[A_1 \cosh(qy) + A_2 \sinh(qy) + A_3 \cos(qy) - A_4 \sin(qy)\right] \tag{3.5}$$

From the boundary conditions (namely, $x(0) = x(l) = 0$ and $\frac{dx(0)}{dy} = \frac{dx(l)}{dy} = 0$ for the cc-beam), the following transcendental equation is obtained

$$\left(\sinh(ql)^2 - \sin(ql)^2\right) - \left(\cosh(ql) - \cos(ql)\right)^2 = 0 \tag{3.6}$$

whose solutions (4.7300, 7.8532, 10.9956, 14.1372, ...) are the eigenvalues k_n for the different in-plane vibration modes of the cc-beam.

3.1.2 Beam under punctual load

As a first approximation, the dynamical behavior of the resonators is conceived as a lumped mass-spring system. The mass is assumed to be concentrated an the middle point of the beam span ($y = l/2$ in figure 3-1) and all the forcing is supposed to be punctual over this point. Under these assumptions, the system dynamics is described analytically with a single degree of freedom equation in the x-direction (figure 3-2). Consider the undamped case, whose dynamic equation can be written as:

$$m_{\text{eff}}\ddot{x} + k_1 x = 0 \tag{3.7}$$

The beam deflection under a punctual force in such direction (F_x) applied at the center is [78]:

$$\omega_F(y) = \frac{F_x y^2}{4EI}\left(\frac{y}{3} - \frac{l}{4}\right) \tag{3.8}$$

for beam length values between 0 and $l/2$. The displacement of the middle point $y = l/2$ is taken as the reference displacement x and the linear stiffness constant, for the beam under punctual load, according to the Hooke law is:

$$k_1 = \frac{16Et_h w^3}{l^3} \tag{3.9}$$

In a cc-beam, the cubic nonlinear stiffness (k_3) cannot be neglected, especially for large deformations. As seen in section 2.1.2 and specifically in equation (2.17), the main source of the nonlinear stiffness is the mid-plane stretching generated because of the hyperstaticity of the cc-beam . In [59], an approximate analysis of the nonlinear additional anharmonic force caused by large deformations is used to estimate the nonlinear stiffness of a cc-beam accordingly to equation (3.10), an expression quite similar to that reported in [79], [80] [81], and which has been validated from FEM simulations.

$$k_3 = 0.767\frac{k_1}{w^2} = \frac{12.272Et_h w}{l^3} \tag{3.10}$$

In contrast to cc-beam resonators, for a cantilever beam the geometric and inertia nonlinearities can be considered negligible [48]. Finally, the expression for the system effective mass, which is considered to be concentrated in the middle point of the cc-beam span ($y = l/2$) is found to be:

$$m_{\text{eff}} = \frac{192\rho w t_h l}{k_n^4} \tag{3.11}$$

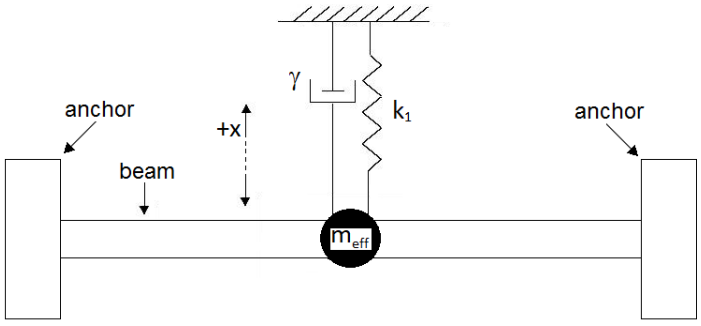

Figure 3-2: Schematics representation of the damped mass-spring system.

3.1.3 Beam under uniformly distributed load

In the case that the load applied to the beam is uniformly distributed along the beam span, the deformation is lower (and smaller displacement of the middle point) than in the

case of a punctual force concentrated at the middle. For the same value of the force, if it is distributed, the beam presents more stiffness. The elastic profile curve of a cc-beam subjected to a uniformly distributed load is found ([78]) to follow equation:

$$\omega_q(y) = \frac{q}{EI}\left(-\frac{l}{12}y^3 + \frac{1}{24}y^4 + \frac{l^2}{24}y^2\right) \tag{3.12}$$

where q is defined as the load per length unit, and the total force applied to the beam is $F = q \cdot l$. In the same way as in section 3.1.2, the displacement of the middle point of the beam span ($\omega_q(l/2)$) is identified with the x variable, and accordingly to the Hooke law, from equation (3.12), the linear stiffness in this case is obtained ([82]) as

$$k_1 = \frac{32Et_hw^3}{l^3} \tag{3.13}$$

The ratio between the linear and the nonlinear stiffness keeps the same constant value (for a given w parameter) as in the mass-spring model [59]:

$$k_3 = 0.767\frac{k_1}{w^2} = \frac{2 \cdot 12.272Et_hw}{l^3} \tag{3.14}$$

Nevertheless, the natural frequency, given by equation (3.16) is know to be an intrinsic feature of the beam, which does not depend on how it is loaded or forced. In this way, the effective mass in the case of uniformly loaded beam results to be [83]:

$$m_{\text{eff}} = \frac{2 \cdot 192\rho w t_h l}{k_n^4} \tag{3.15}$$

For large deformations, the punctual load model is a-priori considered more realistic than the uniform load model because, given the strong dependence of the force on the position, the deformed cc-beam shape implies a far bigger concentration of the force in the middle zone of the beam span.

3.1.4 Damping term

The natural frequency of the mass-spring system can be obtained from the general solution ($x(t) = a\cos(\omega_0 t + \theta)$) of the homogeneous differential equation of the undamped and unforced spring-mass system (3.7):

$$\omega_0 = \sqrt{\frac{k_1}{m_{\text{eff}}}} \tag{3.16}$$

If the dissipation of energy , caused by several sources,is considered in the mathematical model, the damping term must be included in the differential equation, thus it results to be

$$m_{\text{eff}}\ddot{x} + \gamma\dot{x} + k_1 x = 0. \tag{3.17}$$

Let the solutions of this equation be in the form of $x(t) = ae^{r\cdot t}$, the characteristic equation is given by $m_{\text{eff}}r^2 + \gamma r + k_1 = 0$. Being $r = \dfrac{-\gamma \pm \sqrt{\gamma^2 - 4k_1 m_{\text{eff}}}}{2m_{\text{eff}}}$, the critical value of the damping term is defined as

$$\gamma_{\text{cr}} = 2\sqrt{k_1 m_{\text{eff}}} \tag{3.18}$$

if the damping parameter has a smaller value than the critical value, the r parameter is complex and the general solution will be oscillatory. By defining the parameter ζ as the ratio between the actual damping term and the critical one

$$\zeta = \frac{\gamma}{\gamma_{\text{cr}}} = \frac{\gamma}{2\sqrt{k_1 m_{\text{eff}}}} \tag{3.19}$$

ζ is nondimensional damping parameter which depends on the fluid where the oscillation takes place, and the shape of the oscillator. The quality factor Q is defined as the dimensionless parameter that relates the value of the total energy stored in the system with the energy that dissipates in each cycle. The value of the quality factor is the sum of the contributions of all the dissipation mechanisms [84]:

$$\frac{1}{Q} = \frac{1}{Q_{\text{air}}} + \frac{1}{Q_{\text{anchor}}} + \frac{1}{Q_{\text{surface}}} + \frac{1}{Q_{\text{TED}}} + \frac{1}{Q_{\text{others}}} \tag{3.20}$$

namely the air-squeezing, anchor loses, the surface contribution, the thermoelastic damping (TED), and others. Specifically the quality factor Q depends on the pressure of the gas surrounding the resonator following the shape shown in figure 3-3, and is related with the ζ parameter as

$$Q = \frac{1}{2\zeta} \tag{3.21}$$

thus the quality factor Q describes how undamped the system is. Then the r parameters can be expressed as

$$r = \frac{-\zeta\gamma_{\text{cr}} \pm \sqrt{(\zeta\gamma_{\text{cr}})^2 - 4k_1 m_{\text{ eff}}}}{2m_{\text{eff}}} \tag{3.22}$$

and, by developing this equation with the definition of the critical damping parameter γ_{cr} given in equation (3.18), the following expression is obtained:

$$r = -\zeta\omega_0 \pm i\omega_0\sqrt{1-\zeta^2} \tag{3.23}$$

On the other hand, the damping term γ can be written as

$$\gamma = 2\zeta m_{\text{eff}}\omega_0 = \frac{m_{\text{eff}}\omega_0}{Q} \tag{3.24}$$

The general solution for the differential equation of the unforced and damped mass-spring system $m_{\text{eff}}\ddot{x} + 2\zeta m_{\text{eff}}\omega_0\dot{x} + k_1 = 0$ would be in the form of

$$x(t) = \lambda_1 e^{r_1 t} + \lambda_2 e^{r_2 t} \tag{3.25}$$

being $e^{r_1 t} = e^{-\zeta\omega_0 t}\left(\cos\left(\omega_0\sqrt{1-\zeta^2}t\right) + i\sin\left(\omega_0\sqrt{1-\zeta^2}t\right)\right)$, and
$e^{r_2 t} = e^{-\zeta\omega_0 t}\left(\cos\left(\omega_0\sqrt{1-\zeta^2}t\right) - i\sin\left(\omega_0\sqrt{1-\zeta^2}t\right)\right)$, then

$$x(t) = e^{-\zeta\omega_0 t}\left(C_1\cos\left(\omega_0\sqrt{1-\zeta^2}t\right) + C_2\sin\left(\omega_0\sqrt{1-\zeta^2}t\right)\right) \tag{3.26}$$

where $C_1 = (\lambda_1 + \lambda_2)$ and $C_2 = i(\lambda_1 - \lambda_2)$, constants which may be determined from the initial conditions. If the initial conditions $x(0) = x_0$ and $\dot{x}(0) = \dot{x}_0$ are imposed, the general solution becomes

$$x(t) = e^{-\zeta\omega_0 t}\left(x_0\cos\left(\omega_0\sqrt{1-\zeta^2}t\right) + \frac{\zeta\omega_0 x_0 + \dot{x}_0}{\omega_0\sqrt{1-\zeta^2}}\sin\left(\omega_0\sqrt{1-\zeta^2}t\right)\right) \tag{3.27}$$

This general solution, shown in figure 3-4 a) for its underdamped case ($\gamma < \gamma_{\text{cr}}$), has a perfect agreement with the numerical obtained solution of the damped and unforced mass-spring system (3.17). The resonance frequency of the damped system can be deduced to be

$$\omega_a = \omega_0 \sqrt{1 - \zeta^2} \tag{3.28}$$

while the amplitude presents an exponential decrease (also depicted in figure 3-4 a)), whose exponent is a multiple of the natural frequency of the undamped spring-mass system. Figure 3-4b) represents the variation of the resonance frequency in terms of the Q factor.

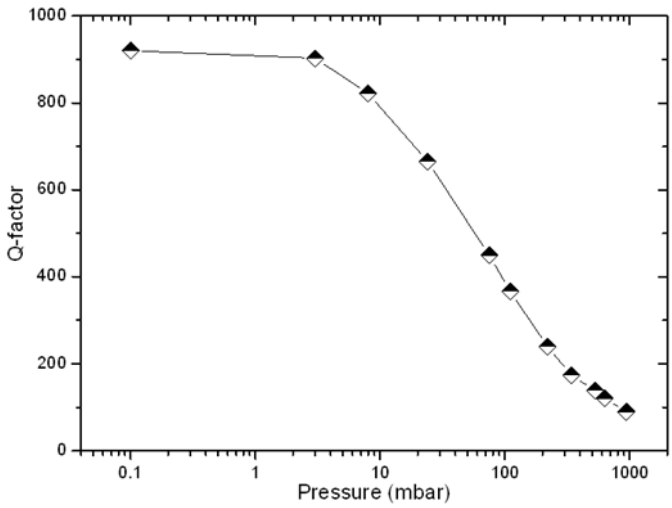

Figure 3-3: Dependence of the quality factor Q on the pressure [86].

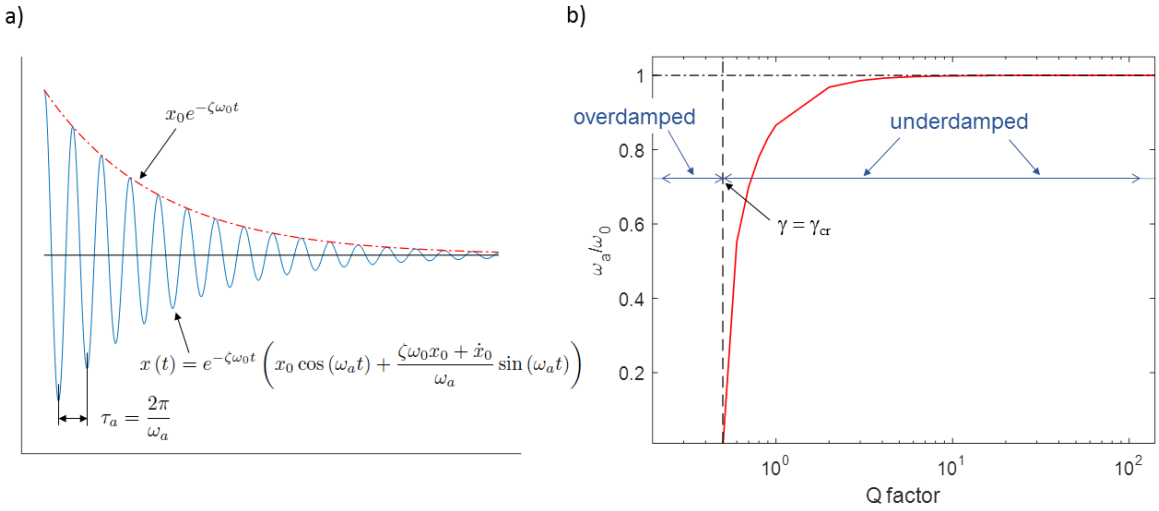

Figure 3-4: a) Representation of the sinusoidal response of an unforced and underdamped resonator. b) Resonance frequency variation caused by the damping effect, normalized with the undamped natural frequency.

3.1.5 Electrostatic actuation

When using electrical conductors as structural layers, the beam resonator and an electrode constitute a capacitor. The capacitance between the plates of a parallel plate capacitor is given by

$$C_0 = \frac{\epsilon_0 l t_h}{s} \tag{3.29}$$

being ϵ the vacuum permittivity with an approximate value of $\epsilon_0 \approx 8.854\ F/m$. Knowing that the electrostatic energy and the electric charge stored between the plates of the capacitor are respectively

$$W_C = \frac{1}{2} C V^2, \tag{3.30}$$

and

$$Q_C = CV, \tag{3.31}$$

the relations between the differential variations of energy and charge in the capacitor from differential variations of capacitance can be established: $dW_C = \frac{1}{2} V^2 dC$ and $dQ_C = V dC$. Considering that this charge is provided by a voltage supply; the supply charge (Q_V) varies as $dQ_V = -dQ_C$ and the total stored electrical energy change is given by $dW_e = dW_C - V dQ_C = -\frac{1}{2} V^2 dC$ [58]. If the 1 DOF. parallel plate model approximation is considered, the capacitance constituted by the beam and each electrode depends on the displacement of the moving resonator:

$$C = \frac{\epsilon_0 t_h l}{s - x} \tag{3.32}$$

The force acting on the capacitor is the negative gradient of the total energy and, given that only movement in x-direction is considered, the expression of the electrostatic force can be expressed as [58]:

$$F_e = -\frac{dW_e}{dx} = \frac{1}{2} V^2 \frac{\partial C}{\partial x} = \frac{V^2 \epsilon_0 l t_h}{2\,(s - x)^2} \tag{3.33}$$

Accordingly to last equation , the capacitive electrostatic force is positive for a positive $\frac{dC}{dx}$, which means that the electrostatic force has the same sign as the the displacement

that provokes an increase of the capacitance [58]. On the other hand, the electrostatic force is proportional to the square of the voltage, thus it is independent on the sign of such voltage. In the general case, V is considered as the contributions of the AC and DC voltages, resulting

$$F_e = \frac{\left(V_{DC}^2 + V_{AC}^2 \left(\cos\left(\omega t\right)\right)^2 + 2V_{DC}V_{AC}\cos\left(\omega t\right)\right)\epsilon_0 l t_h}{2\left(s-x\right)^2} \tag{3.34}$$

and expanding

$$F_e = \frac{\left(V_{DC}^2 + \frac{1}{2}V_{AC}^2 + \frac{1}{2}V_{AC}^2\cos\left(2\omega t\right) + 2V_{DC}V_{AC}\cos\left(\omega t\right)\right)\epsilon_0 l t_h}{2\left(s-x\right)^2} \tag{3.35}$$

it can be seen that the electrostatic force has frequency components at frequencies zero, ω and 2ω. The component of the generated electrostatic force at the frequency ω is

$$F_{e\omega}\left(t\right) = V_{DC}V_{AC}\cos\left(\omega t\right)\frac{\partial C}{\partial x} \tag{3.36}$$

Given the damped and forced linear mass-spring system equation,

$$m_{\text{eff}}\ddot{x}\left(t\right) + \gamma\dot{x}\left(t\right) + k_1 x\left(t\right) = F_e\left(t\right) \tag{3.37}$$

the Laplace transform provides the transfer function between the input (forcing) and the output (position) [85]:

$$H\left(s\right)) = \frac{X\left(s\right)}{F_e\left(s\right)} = \frac{1}{m_{\text{eff}}}\frac{1}{s^2 + \frac{\omega_0}{Q}s + \omega_0^2} \tag{3.38}$$

where the projection over the $j\omega$ axis results $\frac{X\left(\omega\right)}{F_e\left(\omega\right)} = \frac{1}{k_1}\left[\frac{1}{1-\left(\frac{\omega}{\omega_0}\right)^2 + \frac{j\omega}{Q\omega_0}}\right]$. An underdamped system presents a resonant peak that increases in amplitude with greater quality factor Q values. Finally the position response at the resonance frequency is given by [85]:

$$x\left(\omega=\omega_0\right)=\frac{F_{e\omega}}{k_1}\left[\frac{1}{1-\left(\frac{\omega}{\omega_0}\right)^2+\frac{j\omega}{Q\omega_0}}\right]_{\omega=\omega_0}=-j\frac{Q}{k_1}F_{e\omega}=-j\frac{Q}{k_1}V_{DC}V_{AC}\frac{dC}{dx} \tag{3.39}$$

3.1.6 Capacitive readout

One of the important issues to solve in the submicrometer and nanometer scale resonators is the transduction of the movement into an electrical signal. The approach used in this work is the use of capacitive readout principle. Since the charge between the plates of a capacitor is given by the capacitance times the voltage between such plates ($Q=CV$) and given that the current is, by definition, the time derivative of the charge ($I_c=\frac{\partial Q}{\partial t}$), the capacitive current generated by the resonant beam subjected to bias voltage and AC excitation can be expressed as [86]:

$$I_c=\frac{\partial\left(C\cdot V\right)}{\partial t}=C\frac{\partial\left(V_{AC}\cos\left(\omega t\right)\right)}{\partial t}+\left(V_{DC}+V_{AC}\cos\left(\omega t\right)\right)\frac{\partial C}{\partial t} \tag{3.40}$$

assuming that $V_{AC}\ll V_{DC}$ (which is the most habitual case), equation (3.40) can be approximated to

$$I_c\approx -C\omega V_{AC}\sin\left(\omega t\right)+V_{DC}\frac{\partial C}{\partial t}=I_P+I_M \tag{3.41}$$

with I_P being the parasitic current generated by the sinusoidal essence of the V_{AC} voltage (and thus does no reflect the movement of the oscillator) and I_M the motional current, proportional to the variation of the capacitance between the resonator and the electrode. From equation (3.32) it is known that, since either permittivity (ϵ_0) or coupling area ($l\cdot t_h$) are constants, thus the variation of the capacity, which generates I_M is due to the variation of the position. With the aim of analyze the motional current term, the movement of the moving resonator is assumed to be sinusoidal. In this way

$$I_M\approx V_{DC}\frac{\partial C}{\partial t}=V_{DC}\frac{\partial C}{\partial x}\frac{\partial\left(x_0\sin\left(\omega t\right)\right)}{\partial t}=\eta\omega x_0\cos\left(\omega t\right) \tag{3.42}$$

with η being the electromechanical coupling factor. This is an important factor that expresses the ratio between the applied AC voltage and the component of the generated

electrostatic force at the frequency ω:

$$\eta = \frac{F_{e\omega}}{V_{AC}\cos(\omega t)} = V_{DC}\frac{dC}{dx} \tag{3.43}$$

with $F_{e\omega}$ given by equation (3.36) [86]. The derivative function of the capacitance between the oscillator and the electrode with respect to the position x is $\frac{dC}{dx} = \frac{d\left(\frac{\epsilon_0 t_h l}{(s-x)}\right)}{dx} = \frac{\epsilon_0 t_h l}{(s-x)^2} = \frac{C_0 s}{(s-x)^2}$, which for small amplitude oscillations can be approximated to $\frac{C_0}{s}$. In this way, the electromechanical coupling factor can be written as:

$$\eta \approx V_{DC}\frac{C_0}{s} \tag{3.44}$$

Thus the motional generated current (I_M) depends on the applied DC voltage, on the oscillation amplitude, on the frequency and on the coupling area.

From equation (3.39) it can be observed that when the AC excitation is applied in a frequency corresponding to the natural frequency of the resonator, the effect of the force is multiplied by the quality factor Q, defined in (3.21), which is specific for each resonator system. For the usual high-Q resonators, the approximate expression $QF_e = k_1 x$ can be considered [86], and in this way, the oscillation amplitude in this case can be approximated to

$$x_r = Q\frac{\eta V_{AC}}{k_1} \approx \frac{Q}{k_1}V_{DC}V_{AC}\frac{C_0}{s} \tag{3.45}$$

which is consistent with the expression provided in (3.39) and the motional current term can now be written to depend on the electromechanical coupling factor as

$$I_{Mr} = Q\frac{\eta^2 V_{AC}\omega}{k_1} \approx Q\frac{C_0^2 V_{DC}^2 V_{AC}\omega}{s^2 k_1} \tag{3.46}$$

Finally, the parasitic current is defined as

$$I_P = C_P\frac{\partial V}{\partial t} = -C_P\omega V_{AC}\sin(\omega t) \tag{3.47}$$

where C_P is defined, in general, as the coupling capacitance between the readout electrode and the electrode or structure where the AC excitation is applied. The motional current

is magnified at the resonance frequency, however out-of-resonance the parasitic term of the current dominates over the motional term.

3.1.7 Equivalent electric circuit for MEMS resonators

The electrical performance of the MEMS system in its linear regime can be assimilated to a RLC (figure 3-5) circuit corresponding to the motional impedances in series with a transformer, and all in parallel with the capacitance corresponding to the parasitic current, given by equation (3.47) [87]. A relation between the applied AC excitation and the generated capacitive current for the readout can be obtained. At this point two different capacitances must be distinguished: C_E is the capacitance formed by the resonator and the electrode between which the AC excitation takes place, and C_R is the capacitance between the resonator and the readout electrode. The sign of time derivatives of these capacitances determines if the generated motional current at the resonance and AC excitation are in the same phase or in the opposite phase. However, since the resonator is placed symmetrically between the electrodes, in any case the value of these capacitances for the zero displacement is the same: C_0. In this way, given the approximation $\frac{dC}{dx} \approx \frac{C_0}{s}$ introduced in section (3.1.6), equation (3.36) results:

$$F_{e\omega}(t) = V_{DC} V_{AC} \cos(\omega t) \frac{C_0}{s}, \tag{3.48}$$

and the motional current can be approximated to

$$I_M(t) = V_{DC} \frac{C_0}{s} \dot{x}(t) \tag{3.49}$$

which implies $\dot{x}(t) = \frac{s I_M(t)}{V_{DC} C_0}$. Knowing the expression for $\dot{x}(t)$, equations for $\ddot{x}(t)$ and $x(t)$ may be obtained as

$$x(t) = \frac{s}{V_{DC} C_0} \int_0^t I_M(t)\, dt \tag{3.50}$$

and

$$\ddot{x}(t) = \frac{s}{V_{DC} C_0} \frac{dI_M(t)}{dt} \tag{3.51}$$

By substituting these expression into the equation of the linear damped mass-spring equation (3.37)

$$m_{\text{eff}}\frac{s}{V_{DC}C_0}\frac{dI_M(t)}{dt}+\gamma\frac{sI_M(t)}{V_{DC}C_0}+k_1\frac{s}{V_{DC}C_0}\int_0^t I_M(t)\,dt=V_{DC}V_{AC}\cos(\omega t)\frac{C_0}{s} \tag{3.52}$$

Last equation can be assimilated to the RLC circuit differential equation:

$$L_M\frac{di}{dt}+R_Mi+\frac{1}{C_M}\int_0^t idt=V_{AC}\cos(\omega t) \tag{3.53}$$

and given the expressions for the electromechanical coupling factor (η), the damping term (γ) and the qualilty factor (Q) provided respectively by equations (3.44), (3.24) and (3.21), the motional RLC constants of the equivalent circuit are found to be

- Motional inductance: $L_M=m_{\text{eff}}\left(\frac{s}{V_{DC}C_0}\right)^2=\frac{m_{\text{eff}}}{\eta^2}$ (3.54)

- Motional resistance: $R_M=\gamma\left(\frac{s}{V_{DC}C_0}\right)^2=\frac{\sqrt{k_1m_{\text{eff}}}}{Q\eta^2}$ (3.55)

- Motional capacitance: $C_M=\frac{1}{k_1}\left(\frac{V_{DC}C_0}{s}\right)^2=\frac{\eta^2}{k_1}$ (3.56)

while the parasitic capacitance C_P is defined in section 3.1.6. On the other hand, following the definition of the electromechanical coupling factor (η) in equation (3.44), η_E and η_R are defined respectively as $\eta_E=V_{DC}\frac{dC_E}{dx}$ and $\eta_R=V_{DC}\frac{dC_R}{dx}$. The motional current given in equation (3.46) can be expressed as

$$I_{Mr}=-\frac{Q}{k_1}\frac{dC_E}{dt}\frac{dC_R}{dt}V_{AC}\omega \tag{3.57}$$

The sign of the electromechanical coupling factors determines the phase of the motional current, defining the transformer factor as [88]:

$$\Phi_M = \frac{\eta_E}{\eta_R} \tag{3.58}$$

Given the symmetrical position of the beam with respect to the electrodes the defined capacitances verify $\left|\frac{dC_E}{dt}\right| = \left|\frac{dC_R}{dt}\right| \approx \frac{C_0}{s}$. Thus the value of Φ_M is 1 or -1.

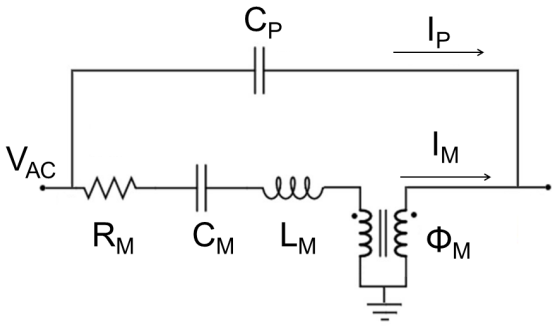

Figure 3-5: Equivalent electric circuit for the resonator.

3.1.8 One driver versus two drivers configurations

In the one driver configuration, the electrostatic and readout capacitances (C_E and C_R) are defined between the resonator and the same electrode, thus their time derivatives verify $\frac{dC_E}{dt} = \frac{dC_R}{dt}$. With this circumstance the phase inversion effect appears and the antiresonance occurs at lower frequency than the resonance (figure 3-6a)). The main drawback of this configuration is that there is a direct coupling of the electrostatic capacitance C_E in the readout electrode, and given that both parasitic and motional current oscillate at the same frequency, the parasitic current can mask the motional current. This problem is overcome by using different electrodes for driving and readout, this is the two-driver configuration. In this case a growing C_E implies a decreasing C_R and vice versa, this is to say $\frac{dC_E}{dt} = -\frac{dC_R}{dt}$. In this case there is no phase inversion, and the resonance precedes the antiresonance in the frequency sweep (figure 3-6b)).

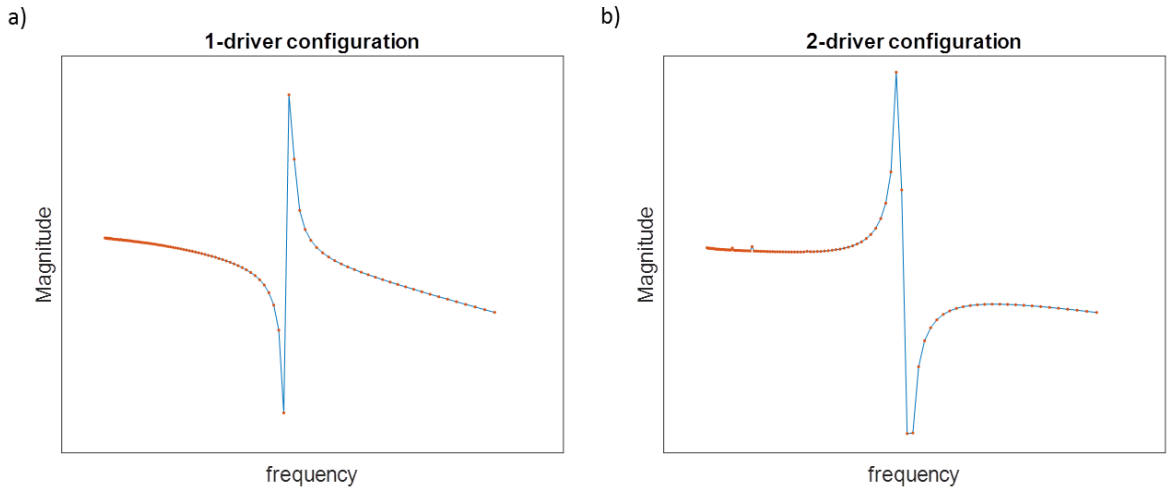

Figure 3-6: Numerical simulations of the frequency response of the electromechanical system in a) one-driver configuration (where phase is inverted) and b) two-driver configuration (where phase is not inverted).

3.1.9 Complete dynamic equation

The mechanical nonlinear behavior is modeled by the nonlinear (cubic) stiffness term, provided in sections 3.1.2 and 3.1.3. Higher order stiffness terms are neglected in the vast majority of references in literature, since they has been found to be unnecessary. Figure 3-7 compares, for two different resonator dimensions, the force vs deflection chart obtained by FEM simulations and from the polynomial equation ($F(x) = k_1 x + k_3 x^3 + \dots$) till the third degree and till the fifth degree. For the usual values of the displacement the use of higher order stiffness terms provides no appreciable benefits in terms of accuracy.

Once all the terms and parameters that have influence on the dynamic behavior corresponding to the flexure resonance of biased (by a DC voltage) and electrostatically actuated (by an AC excitation) clamped clamped beams are defined, the one degree of freedom equation to model the dynamics is found to be

$$m_{\text{eff}}\ddot{x} + \gamma\dot{x} + k_1 x + k_3 x^3 = \frac{C_0 s}{2}\frac{\left(V_{DC} + V_{AC}\cos(\omega t)\right)^2}{(s-x)^2} \tag{3.59}$$

Developing the forcing term

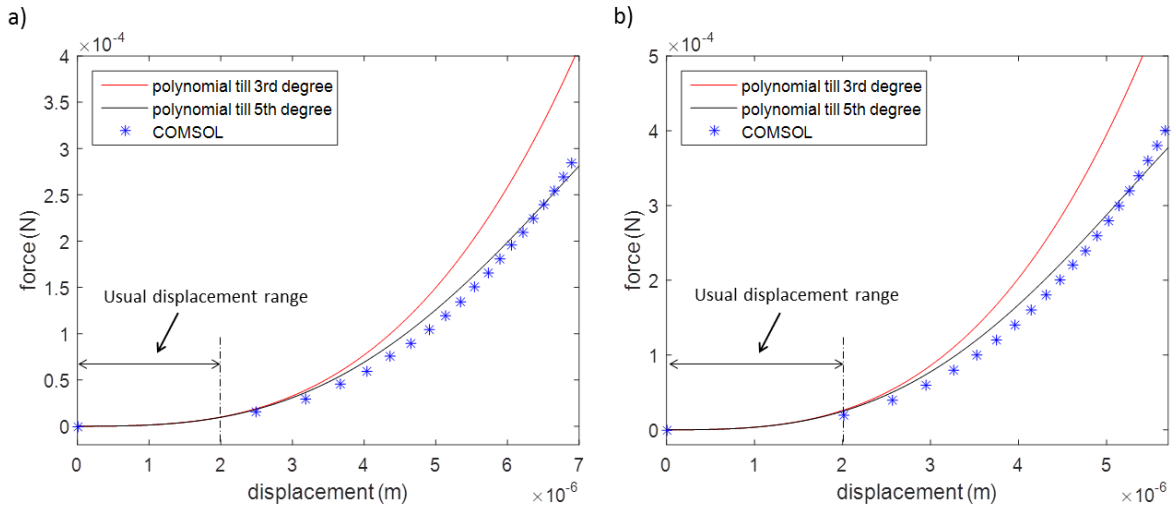

Figure 3-7: FEM (COMSOL) and analytical force-displacement plots using the dimensions of polysilicon resonators corresponding to a) AMS 035 technology with dimensions l=54.6 μm, w=350 nm, th=282 nm and b) UMC 018 technology with dimensions l=43.6 μm, w=280 nm, th=580 nm.

$$m_{\text{eff}}\ddot{x} + \gamma\dot{x} + k_1 x + k_3 x^3 = \frac{C_0 s}{2\,(s-x)^2}\left(V_{DC}^2 + 2V_{DC}V_{AC}\cos(\omega t) + (V_{AC}\cos(\omega t))^2\right) \quad (3.60)$$

assuming that the bias voltage is far greater than the excitation amplitude ($V_{AC} << V_{DC}$), and that the oscillation amplitude of the beam is really small in comparison with the gap parameter ($x << s$), the forcing term in V_{AC}^2 can be neglected and the complete dynamic equation can be assimilated to the Duffing equation (2.23). In this way, the Duffing equation can be used as a first approximation to study and understand the behavior of nonlinear resonators susceptible to present chaotic response. However, it must be taken into account that the dependence of the forcing on the position (x) introduces nonlinearity and complexity that cannot be neglected. In fact, the electrostatic force involves a parametric excitation.

3.1.10 Nonlinearities in frequency response

The nonlinear effects on the electrostatically actuated cc-beam resonators have their origin either in the mechanical domain or in the electrical domain. The nonlinearities in the electrical domain are caused by the nonlinear essence of the electrostatic coupling, and

provokes a bending towards lower frequencies of the frequency peak (spring softening). On the other hand, the mechanical nonlinearity, which is modeled with the nonlinear stiffness term, generates a bending of the frequency peak toward upper frequencies (spring hardening). When experimental measurements are performed (instead of numerically obtained plots), the phenomena of spring hardening and softening are observed as hysteresis (shown in figure 3-8), and they are magnified by a growing value of the Q factor [59].

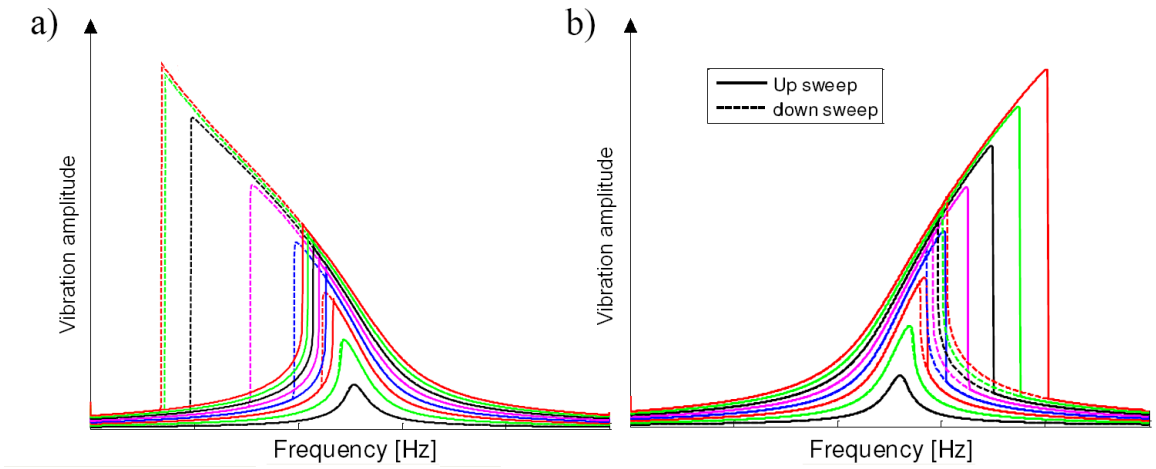

Figure 3-8: Illustration of a) the spring softening effect caused by a dominant presence of the electrostatic nonlinearity and of b) the spring hardening caused by a dominant presence of the mechanical nonlinearity.

3.2 MEMS Fabrication

This section introduces a brief summary of the fabrication methods and approaches of MEM and NEM systems, the use of CMOS technologies for this purpose and especially the features of a specific technology for MEMS fabrication. The application of this technology to the design and fabrication of monolithic MEMS resonators in previous works is taken as a starting point for the present study.

3.2.1 Scaling-Down

A scaling-down of the mechanical transducer size into the submicrometer and nanometer range provides important advantages but, at the same time, some challenges [86], [89], [90]. Table 3.1 summarizes the effect of a uniform scaling-down on the different parameters of the electromechanical systems. The way how the scaling down proper to CMOS technologies

(where the thickness dimension does not scale in terms of λ) affects these parameters is also shown . A scaling factor of λ^n in a magnitude means that, for a decrease of a factor λ in the 3 dimensions of the beam, this magnitude decreases a factor λ^n , while a scaling factor of λ^{-n} means that it increases a factor λ^n. The scaling-down of the resonator dimensions implies an increase of the operating frequency and the bandwidth, highly desirable for RF applications. On the other hand it makes the beam more nonlinear, with richer dynamical response and several potential applications. Moreover, the effect of the miniaturization provides benefits in terms of energy efficiency and response time. However, as shown in table 3.1 the main drawbacks of the scaling-down are a decrease of the electrostatic coupling and force, which may eventually compromise the actuation and the capacitive readout.

Table 3.1: Scaling factor for the different magnitudes, assuming an uniform scaling λ in all dimensions, and assuming the scaling proper to CMOS technologies (the thickness parameter (t_h) is assumed not to scale in terms of λ).

Parameter	Scaling Factor	Scaling Factor in CMOS technologies
Mass (m)	λ^3	λ^2
Linear stiffness (k_1)	λ	1
Nonlinear stiffness (k_3)	λ^{-1}	λ^{-2}
Nonlinearity strength (k_1/k_3)	λ^{-2}	λ^{-2}
Resonance frequency (f_0)	λ^{-1}	λ^{-1}
Electrostatic coupling (C_0)	λ	1
Electrostatic force (F_E)	1	λ^{-1}
Response time (τ)	λ	λ
Capacitive current (I_C)	λ	1

3.2.2 CMOS-MEMS fabrication and system integration

The fabrication process of MEMS and NEMS fabrication is known to follow two basic techniques [86]:

- bulk micromachining: refers to all techniques used to remove significant amounts of the substrate (bulk) material, in such a way that the bulk is part of structural material of the micromachined movable structure. The silicon etching can be performed using

wet etchants or etchants in vapor and plasma states (dry etching), both in an isotropic or anisotropic way.

- surface micromachining: involves the deposition of thin films on the wafer surface and the selective removal of one or more of these layers (sacrificial layers) to release the movable structures.

The progressive miniaturization of microsensors and microactuators fabricated using IC technologies and materials achieved over the past years has allowed the integration of those devices and the interface circuit on the same chip (monolithic integration) or in the same package (hybrid integration), with important advantage in terms of cost of fabrication, size and reliability [86]. Specifically with the monolithic integration, the whole electromechanical system is fabricated with an optimized process for IC and some compatible post-processing steps. Using this approach, the parasitics due to the interconnection between the actuators and the interface circuit are minimized (which is compulsory with the submicrometer range fabricate devices in oder to allow operative sensor readout), the system assembly is simple and does not depend on the number of connections; finally the use of the same technology allows a good matching between the actuator and the interface circuit.

In general, the fabrication process of CMOS MEMS is done with a regular CMOS process sequence in combination with compatible micromachining and film deposition [91]. In this sense, three main approaches can be distinguished [92]:

- Pre-CMOS or MEMS-first approach: The MEMS structures are totally or partially formed before the CMOS process. The IC is not affected by the micromachining process, but the structure must be protected during the CMOS process [93], [94].

- Intra-CMOS or Intermediate-CMOS approach: The microstructures are fabricated by micromachining the CMOS metalization stack during an interruption of the CMOS process sequence [95], [96]. Inserting the micromachining process steps before the backend interconnect metalization ensures process compatibility with the polysilicon deposition and anneal. As in the pre-CMOS approach, MEMS structures have to be protected during the CMOS process.

- Post-CMOS or MEMS-last approach: All micromachining process is performed once the CMOS process is finished. This approach implies a limitation of the available

temperature for the MEMS process, but also the advantage of allowing the vertical stacking of microstructures on top of the electronics, which reduces the die size and can improve performance through reduced interconnect parasitic resistance and capacitance [92]. Two strategies may be distinguished within this approach. In the first strategy, the MEMS structures are completely built on top of a finished CMOS substrate, leaving the CMOS layers untouched. The microstructures are released by etching a CMOS sacrificial layer [97]. In the second strategy, the MEMS are obtained machining the CMOS layers using CMOS-compatible bulk and surface micromachining techniques [98].

Following references [99] and [92], the term CMOS-MEMS refers the intra-CMOS process (in which the MEMS is defined using one or more layers of the CMOS back-end-of-line[1] materials, available in the standard CMOS technologies), while the pre-CMOS and post-CMOS approaches, since they require special technological processes (not available in a standard CMOS technology), are considered non standard approaches.

The intra CMOS approach takes advantage of the benefits provided by the CMOS technologies: fast turnaround fabrication time, reproducibility, yield, reliable MEMS dimensions definition due to the strict CMOS technology tolerance and good matching with the interfacing circuitry, minimizing the parasitic effects and optimizing the signal-to-noise ratio. On the other hand, some limitations come from the design rules established by the standard CMOS IC process and the properties of the back-end-of-line materials which exhibit higher energy losses [99]. The releasing of the MEMS resonator to obtain the movable mechanical MEMS device is performed using isotropic wet etching, anisotropic dry etching or a combination of these etchings.

3.2.3 Fabrication approach

The current approach used in the framework of this thesis consists in the design and fabrication of monolithically integrated MEMS with an intra-CMOS process, defining standard BEOL CMOS layers as structural MEMS layers and a post CMOS wet etching without additional mask [100]. The purpose of this wet etching is the release of the resonant struc-

[1]Back end of line (BEOL) is the set of layers deposited over the semiconductor where the individual devices (transistors, capacitors, resistors, etc.) are patterned (namely the front end of line or FEOL). Within BEOL, metalization layers have interconnection functions between FEOL elements.

tures by means of the removal of the SiO_2 sacrificial layer. The used commercial CMOS technology is the AMS 0.35 μm from "Austria Micro Systems". This technology, commonly abbreviated as AMS 035, provides a set of CMOS processes with a common core, called C35. This core includes a p-type substrate, a polysilicon capacitor module, four metal layers with their interconnection VIAS, and a bias voltage of 3.3V [85], [101]. The passivation layer is enough to protect the CMOS circuitry during the etching procedure allowing the process to be mask-less [99]. A low cost standard intra-CMOS process is followed, after which the mechanical resonators are completely mechanized without any additional micro/nano-mechanization techniques. A standard CMOS layer is used as structural layer and the different silicon dioxide underlying layers are used as sacrificial layers. To allow a direct postprocessing of the MEMS, a pad cut has been defined over the resonator area. In this way, the resonator structure is kept free of the addition of any other layer over it. The rest of the chip area is covered by the passivation layer which protects the circuitry during the postprocess. The fabrication area for the resonators is designed specifically allowing a very fast etching of the sacrificial layers, which does not cause any damage to the CMOS and does not need any additional protection mask [86]. In last decade a wide variety of devices have been fabricated using the AMS 035 CMOS technology: resonators [102], oscillators [103], sensors [45], relays [104], etc. A similar strategy of CMOS MEMS fabrication was developed at the Carnegie Mellon University (USA) by the group of G.K. Fedder [46], [97] and, more recently, at the National Tsing Hua University (Taiwan) using TSMC 0.35 μm and TSMC 0.18 μm technologies [47], [105]. The cross-section of the AMS 035 CMOS technology is shown in figure 3-9, and the dimensional and mechanical parameters each layer are shown in table 3.2.

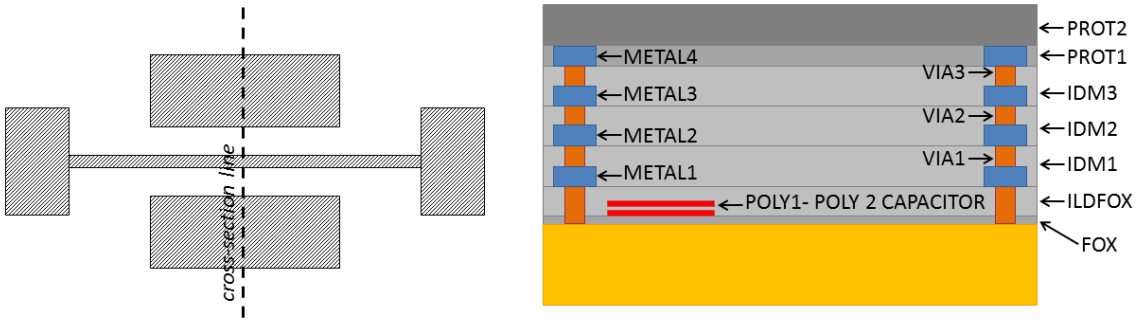

Figure 3-9: Cross-section of the AMS 0.35μm CMOS technology.

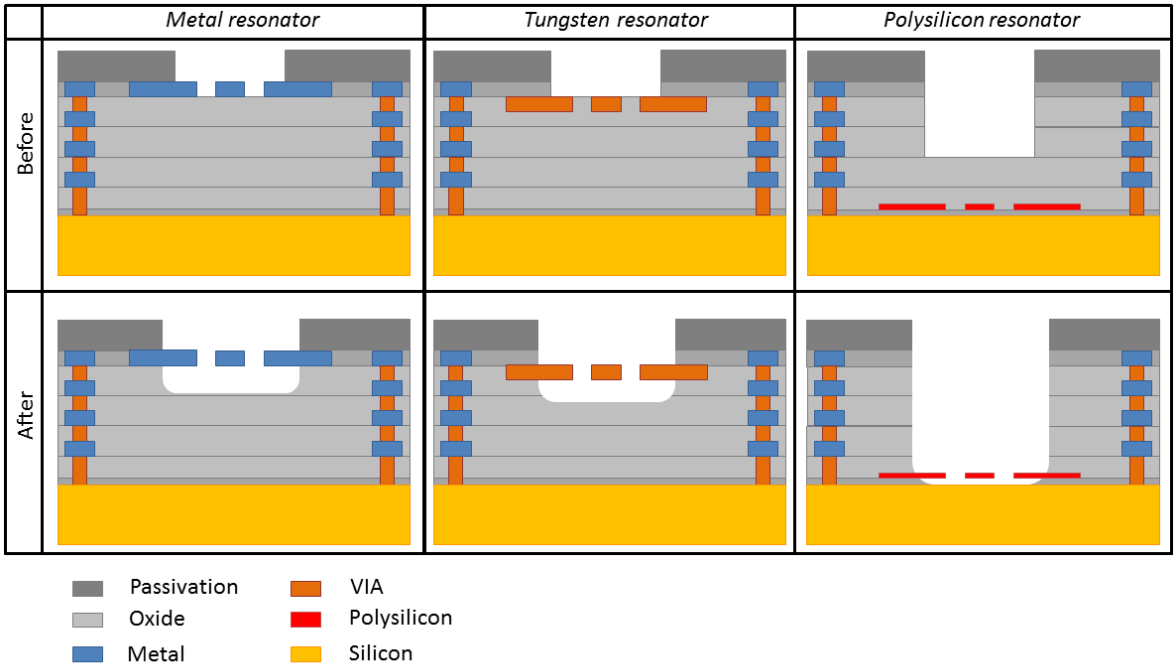

Figure 3-10: Cross-section of the AMS 0.35μm CMOS technology when using different available standard CMOS layers as structural layer, before and after the wet etching.

Table 3.2: Dimensions and mechanical parameters corresponding to the different layers of AMS 0.35μm CMOS technology [85], [101].

	Poly 1	Metal 1..3	VIA	Metal 4
Material	Polysilicon	TiN-Al-TiN	W	TiN-Al
t_h (nm)	282	640	1000	850
Min. gap (nm)	450	450	450	600
Min. width (nm)	350	600	500	600
Density (kg/m^3)	2330	3000	19300	3000
Young's modulus (GPa)	160	131	410	131

Releasing process

When the CMOS process is finished, the resonator is buried into the silicon dioxide (SiO_2), dielectric material which is working as sacrificial material. In this way a post-process to release the structure and allow its movement is needed. This releasing process is the only process which is made out-foundry, and consist in a post CMOS one-step maskless wet etching with a hydrofluoric solution (HF) [100]. One of the used HF solutions is the commercial Silox Vapox III (from Transene Company, Inc.) which contains ammonium fluoride, glacial

acetic acid, aluminum corrosion inhibitor, surfactant and DI water, and presents a theoretical etch rate of 960 $\mathring{A}$/min for the silicon dioxide [105]. The hydrofluoric acid attacks the silicon dioxide, but (in spite of the presence of aluminum corrosion inhibitor) since it is a highly corrosive acid, it attacks also the aluminum (to a lesser extent). Experimental measurements (reported in [105]) effectuated with Silox Vapox III revealed an etch rate of about 29 $\mathring{A}$/min. In this way the selectivity Silox Vapox III of between silicon dioxide and aluminum is approximately 33:1. Another used commercial HF solution is ALPAD Etch 639 (also from Transene Company, Inc.), an oxide etchant designed to minimize attack on aluminum pads or other aluminum structures and on silicon surfaces. The formulation of ALPAD Etch 639 includes a surfactant to ensure wetout over high surface energy substrates. The last used wet etchant is a home-made a reproduction of the commercial HF solutions. The wet etching has a low effect on the passivation: for example the selectivity between silicon dioxide and silicon nitride of the Silox Vapox III is approximately 96:1. The releasing process follows four steps:

- In the etching step, the chip is submerged into the hydrofluoric solution (HF) along a period of time which depends on how deep the structure is placed.
- After the etching step, the sample is submerged in deionized water, maintaining a constant flow, to remove the reactive agent.
- The sample is submerged into isopropyl alcohol (isopropanol) bath, to remove the water which may be accumulated in the nooks of the chip.
- Finally, the sample is put into an oven, under a temperature of 100°C, to dry it and to eliminate all the isopropyl alcohol from the chip.

After these four steps the structure is released and ready for operation or scanning electron microscope (SEM) imaging. Figure 3-10 represents the etching process for the different available structural layers.

Metal devices

While using the top metal layer or a deeper metal layer available in the technology as structural layer, the CMOS circuitry and the resonator are designed together. Mainly, the material corresponding to the metal layers is aluminum, stacked between thin layers

of titanium nitride. The sacrificial layer is the underlying stack of silicon dioxide layers corresponding to the different inter-metal oxides (i.e.IMD3, IMD2, and IMD1), metal1-poly oxide (ILDFOX), and field oxide (FOX) [99]. As usual, a pad window is defined over the resonator area to allow a direct post-processing of the MEMS and the rest of the chip area (except the electrical contact pads) is covered by the passivation layer: a silicon nitride film (Si_3N_4) deposited by plasma-enhanced chemical vapor deposition (PECVD) which protects the circuitry during the post-CMOS process [86]. The structures are completely mechanized at the end of the standard CMOS process, and the sacrificial layer is only present under the resonator enabling a simple etching of the silicon dioxide. Whit this approach, the minimum width of the resonator as well as the gap spacing to the electrodes is limited by the design rules of the technology (in the case of AMS 035 technology, MET4 design rules limit the resonator width and the gap both to 600 nm). The mask-less HF solution-based etching process is the only processing step outside the foundry. As it is an isotropic process, the etching time depends on the MEMS dimensions and the quantity of oxide over the structure [99].

One of the developed options for the AMS 035 technology is to use the top metal layer as the structural material for the resonators. This metal layer is constituted by a titanium nitride (TiN) layer of 100 nm below an aluminum (Al) layer of 750 nm. An averaging process provided the mechanical properties of this double layer, namely a density of 3000 Kg/m^3 and a Young's modulus of 131 GPa [85].

Polysilicon devices

Mechanical structures fabricated with the polysilicon capacitor module are available in the AMS 035 technology. This module is constituted by two polysilicon layers: Poly1 is the bottom layer (282 nm) and Poly2 is the top layer (200 nm). This two polysilicon layers are separated by a 41 nm thick silicon oxide layer [86].

The usual is to use the Poly1 layer as structural layer to fabricate both the resonator and the electrodes. In this case, the sacrificial layer is the underlying field oxide layer (FOX of 290nm). To allow the direct post-processing without any additional mask, a hole through the silicon dioxide is also opened over the resonator area in order to fasten the releasing process. This hole is defined in the AMS 035 technology by using a stack of three layers: PAD layer (pad cut), VIA3 layer, and VIA2 layer. In this way, in contrast to the metal

approach, the resonator structure remains still protected by IMD1 and ILDFOX layers to avoid damages during the rest of the CMOS process (metal deposition and etchings). The rest of the chip area is covered by passivation layer in the same way that in the metal approach. In order to release the resonator, the same post-CMOS process that in the metal approach is performed. In this case, since several oxide layers above the resonator have also to be removed, the post-process time must be increased [86].

Tungsten devices

The VIA layers, from VIA 1 to VIA 3, made of tungsten (W) work as connectors between metal layers. In the deposition process of the tungsten, a 20 nm layer of TiN is deposited to protect the lateral walls of the whole in the SiO_2; however given its relative thinness, its influence over the mechanical properties of the VIA has been neglected [85] [106]. When the VIA is defined between two metal layers, its thickness correspond to the distance between these metal layers, but when there is no defined metal layer below the VIA it can occupy the thickness of this missing metal layer. When no metal layer is defined either above or below the VIA it has a minimum and a maximum thickness values. Since the only limit for the VIA layers length is the aspect ratio allowed by the technology, the VIA layers can be used as the structural layers for MEMS devices. Experimental measurements of torsional relays fabricated with tungsten VIA 3 of AMS 035 CMOS technology are reported in [106], [104] and [107]. Specifically, this thesis reports fabricated resonators using the VIA3 and their experimental measurements (see chapter 6 for details).

Chapter 4

Limits of electrostatically actuated microbeam resonators as chaotic signal generators: a first approximation

The biasing requirements to obtain cross-well chaotic motion for in-plane electrostatically driven beam-shaped MEMS resonators are investigated in this chapter for typical actuation/readout topologies. Practical applications such as chaotic signal generators require reasonable and wide enough range of voltages (DC and AC) to assure a feasible control in current CMOS or nanotechnologies. In this chapter, these conditions are found when enabling cross-well motion operation in stead of in-well operation. As a first approximation, from the 1DOF model, parallel plate assumptions are used in the derivation of electrostatic force term, neglecting the effect of the fringing field at this stage, as well as other nonlinear second order effects. The parallel plate approximation, based on the mass-spring model (see section 3.1.2) assumes the beam displacement in the x-direction (denoted by the variable x) as a non deformable solid. Under these assumptions, and considering the scaling in the dimensional parameters down to the submicrometer range, this chapter tackles with the conditions and limits for two-well potential distribution and chaos in nonlinear cc-beam resonators when considering typical parameter values from various fabrication approaches.

4.1 Electromechanical system analysis

As seen in chapter 2, it is possible to obtain chaotic behavior from a recreation of the chaotic Duffing attractor with two-well potential or even with one-well potential distributions. The nonlinear essence of the physical system allows the appearance of nonlinear behavior such as Period Doubling bifurcation or the reproduction of strange attractors, which ultimately may lead to chaotic motion.

Chaotic behavior generated from recreation of the strange attractor of the Duffing system with two-potential well arises in a sustained, robust and nontransient form, for a wide range of system parameters and for a wide bandwidth in the frequency domain (see section 2.3.1). Moreover, cross-well chaos, arisen from the two-well potential Duffing system is more widely reported in literature (see section (1.3.1)) than the single potential well chaos. For these reasons, the first approach to MEMS resonators chaotic behavior is based on the two-well potential Duffing strange attractor.

For instance, references [108] and [21] claim that the main way to obtain chaotic motion with a resonator is the reproduction of the two-well potential distribution in the Duffing system. In addition, as stated in section 2.4, the application of the Melnikov method requires the presence of more than one potential minimum to generate the homoclinic (or heteroclinic [27]) trajectory for the unperturbed case.

4.2 Two-well potential distribution in a cc-beam resonator

The design and operating conditions to achieve a two-well potential distribution are analyzed using the parallel plate approximation (where the whole beam is identified with the mass-spring model explained in section 3.1.2). Three topologies are typically used in the literature to perform both the electrostatic actuation and readout of the capacitive current $I_c(t)$ generated at the resonator-driver interface [45],[109]. A DC voltage and an AC voltage source (V_{AC} and V_{DC} respectively) are used to bias and excite the resonator using some of the three schemes depicted in figure 4-1. Topology I uses two electrodes, in addition to the beam resonator, for electrostatic actuation (upper electrode) by means of an AC voltage source (with an amplitude V_{AC} at a frequency ω), and capacitive readout (bottom electrode) respectively. The resonator is biased at a DC voltage (V_{DC}) to obtain a capacitive current (due to the resonator motion) that is sensed by the readout electrode. The capacitive current

$I_c(t)$ has mainly two components (motional and parasitic) as stated in section 3.1.6. The whole expression for the capacitive current, as a function of time, is

$$\begin{aligned} I_c(t) &= \frac{d(CV)}{dt} = V(t)\frac{dC(t)}{dt} + C(t)\frac{dV(t)}{dt} \\ &\approx V_{DC}\frac{\partial C(t)}{\partial x(t)}\frac{\partial x(t)}{\partial t} + C_p(t)\frac{\partial V_{AC}(t)}{\partial t} = I_M(t) + I_P(t) \end{aligned} \tag{4.1}$$

where $C_p(t)$, defined as the parasitic capacitance, is the capacitance the AC application place and the readout electrode. In (4.1) it is assumed (like in most applications) that $V_{DC} \gg V_{AC}$. It is important to note that Topology I exhibits some benefits with respect to the other two topologies also found in the literature and shown in figure 4-1(b and c). The use of independent AC and DC voltages is more suitable for operating as a self-sustained oscillator [45]. The AC signal can be generated by a sustaining circuit and feed to the excitation electrode to get a closed-loop configuration, eliminating the need for integration of bulky passive elements as ac-coupling capacitors or inductors. On the other hand, in terms of capacitive readout, the parasitic feedthrough current is minimized when using specific electrodes for the electrostatic actuation and capacitive readout as pointed in section 3.1.8. Both Topologies I and II have no direct capacitive coupling between the actuation electrode (V_{AC}) and the readout electrode, thus getting a theoretically null C_p in contrast to the single-electrode topology (figure 4-1c), which corresponds to one-driver configuration. In any case, in practical applications, there is always a non-zero parasitic current due to the effects like coupling through the substrate, and especially the fringing field effect. Next, the electrostatic force term in the motional equation is analyzed for these three topologies.

4.2.1 Topology I

The lumped equation to describe the resonator dynamics with the topology I (figure 4-1a)) where the AC signal is connected to the driving electrode and the bias voltage is applied to the beam, can be approximated to

$$m_{\text{eff}}\ddot{x} + \gamma\dot{x} + k_1 x + k_3 x^3 = \frac{C_0 s}{2}\left(\frac{(V_{AC}\cos(\omega t) - V_{DC})^2}{(s-x)^2} - \frac{V_{DC}^2}{(s+x)^2}\right) \tag{4.2}$$

Expanding the expression of the actuation force F_{exc} (right side of the equation)

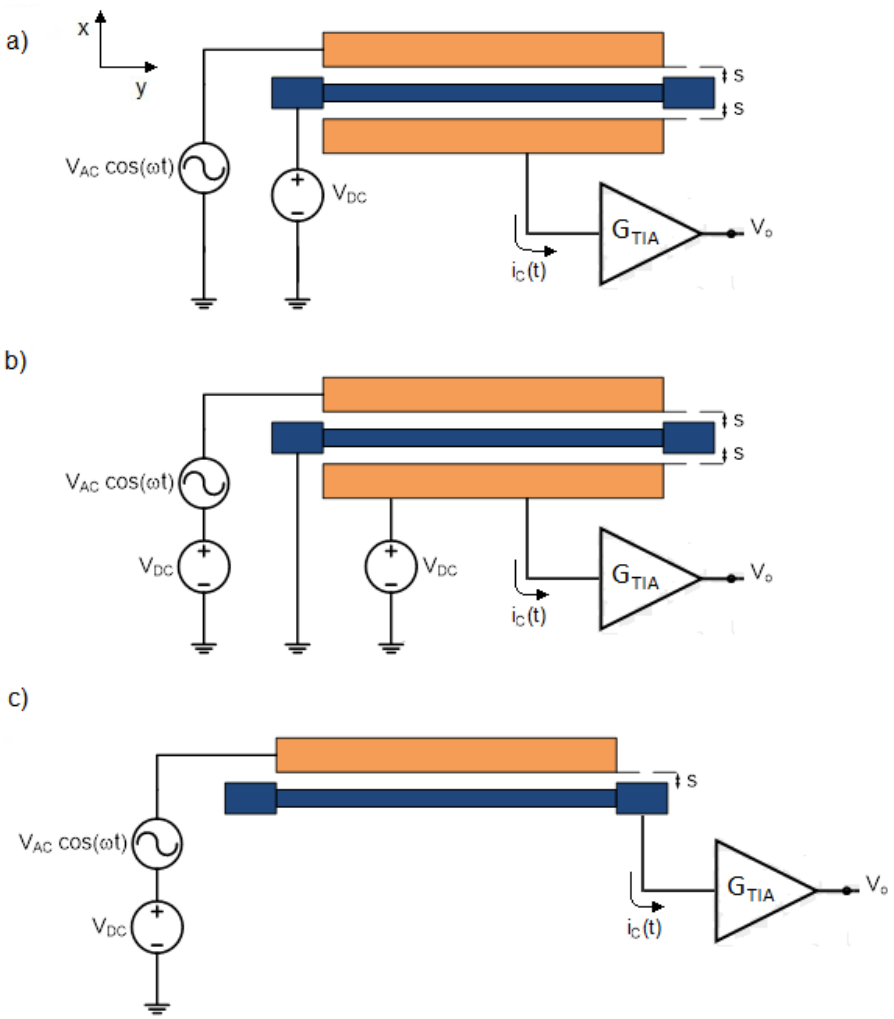

Figure 4-1: Schematic representations of driven beam resonators: a) Topology I. b) Topology II. c) Topology III.

$$F_{exc} = \frac{C_0 s}{2}\left(\frac{(V_{AC}\cos(\omega t))^2 - 2V_{DC}V_{AC}\cos(\omega t)}{(s-x)^2}\right) + \frac{C_0 s}{2}V_{DC}^2\left(\frac{1}{(s-x)^2} - \frac{1}{(s+x)^2}\right) \tag{4.3}$$

and by developing the second term power in series, the actuation force is found to be

$$F_{exc} = \frac{C_0 s}{2}\left(\frac{(V_{AC}\cos(\omega t))^2 - 2V_{DC}V_{AC}\cos(\omega t)}{(s-x)^2}\right) + \frac{C_0 s}{2}\frac{V_{DC}^2}{s^2}\left(\frac{4x}{s} + \frac{8x^3}{s^3} + \sigma\left(x^n\right)\right) \tag{4.4}$$

Due to the symmetry of the DC electrostatic force in this topology, since the bias voltage is applied to the beam resonator, the even power coefficients cancel each other and do not

appear in the motional equation. In equation (4.4), $\sigma\left(x^n\right)$ denotes higher-order terms. After this development, equation (4.2) can be assimilated to the Duffing equation (2.23) which describes the response of a periodically excited oscillator [54],[110] as experimentally demonstrated in [109]. Therefore, the system motion equation is given by

$$\begin{aligned} & \ddot{x}+\left(\frac{k_3}{m_{\text{eff}}}-\frac{4C_0V_{DC}^2}{m_{\text{eff}}s^4}\right)x^3+\left(\frac{k_1}{m_{\text{eff}}}-\frac{2C_0V_{DC}^2}{m_{\text{eff}}s^2}\right)x+\left(\frac{\gamma}{m_{\text{eff}}}\right)\dot{x} \\ = & \frac{C_0 s}{2m_{\text{eff}}}\left(\frac{\left(V_{AC}\cos\left(\omega t\right)\right)^2-2V_{DC}V_{AC}\cos\left(\omega t\right)}{\left(s-x\right)^2}\right)+\frac{C_0 s}{2}\frac{V_{DC}^2}{s^2}\sigma\left(x^n\right) \end{aligned} \tag{4.5}$$

Note how the bias voltage V_{DC} tunes the effective linear and nonlinear beam stiffness modulating the nonlinear behavior (i.e. spring softening and spring hardening)[111]. Neglecting the higher-order terms ($\sigma\left(x^n\right)$), the main difference between the MEMS system model and the Duffing oscillator is the parametric excitation amplitude (i.e. the electrostatic force depends on the resonator position) that causes the pull-in effect [112].

At this point, the design and biasing conditions required to create a double-well potential for the electrostatically actuated MEMS with the current topology are derived. Given the Duffing system described by equation (2.24), and its potential function provided by equation (2.36), the local maximum and minimum positions of the potential function are $x=0$ and $x=\pm\sqrt{-\frac{\beta}{\alpha}}$; as explained in section 2.2.1, $\beta\alpha<0$ is required to have a nontrivial real solution. The Duffing system exhibits a two-well potential distribution when $\beta<0$ and $\alpha>0$. The nontrivial positions correspond to minumums of the potential function (namely, the potential wells) [54], which can be corroborated from the sign of the second derivative of the potential function ($U''\left(\sqrt{-\frac{\beta}{\alpha}}\right)=\beta+3\alpha\left(-\frac{\beta}{\alpha}\right)=-2\beta>0$ so local minima, and $U''\left(0\right)=\beta<0$ so local maximum). Consequently a negative linear stiffness and a positive cubic stiffness are required.For small oscillation amplitudes relative to the gap (i.e. $x/s\ll 1$), Taylor series to the third power approximation of the electrostatic force is acceptable to estimate the MEMS behavior. Thus, equation (4.5) is suitable for the system analysis without taking into account higher order terms. The Duffing-like equation shows a two-well potential distribution when following inequalities are satisfied:

$$\frac{k_1}{m_{\text{eff}}}-\frac{2C_0V_{DC}^2}{m_{\text{eff}}s^2}<0 \quad \text{and} \quad \frac{k_3}{m_{\text{eff}}}-\frac{4C_0V_{DC}^2}{m_{\text{eff}}s^4}>0 \tag{4.6}$$

The last equation establishes that double-well potential cannot be attained in this way for a cantilever structure since its k_3 parameter is almost zero. On the other hand, for a cc-beam structure, the V_{DC} values must verify the following inequalities:

$$\sqrt{\frac{k_1 s^2}{2C_0}} < V_{DC} < \sqrt{\frac{k_3 s^4}{4C_0}} \tag{4.7}$$

It is evident that, to allow the existence of a set of DC values that verify these conditions, the following inequation must be met:

$$\sqrt{\frac{k_1 s^2}{2C_0}} < \sqrt{\frac{k_3 s^4}{4C_0}} \tag{4.8}$$

Given the definitions of the parameters k_1 and k_3 given respectively in equations (3.9) and (3.10) the design condition required to enable cross-well operation for the cc-beam resonator width w in terms of the gap distance s is easily derived:

$$s > \sqrt{2\frac{k_1}{k_3}} = 1.615w \tag{4.9}$$

Notice that, since it is given as a ratio between the linear and nonlinear stiffness, this geometric design condition is also valid when the beam is considered to be under an uniformly distributed force (with k_1 and k_3 respectively defined in equations (3.13) and (3.14)). Seeking the biasing conditions to achieve a two-well potential (2WP) distribution, the static force equation along the position x is given in equation (4.10). The AC voltage term in cos^2 implies a bias component that affects the static balance; however, given that V_{AC} is considered to be far smaller than V_{DC}, the small bias term generated by the AC voltage can be neglected, and in this way:

$$F\left(x, V_{DC}\right) = -\left(k_1 x + k_3 x^3\right) + \frac{s V_{DC}^2 C_0}{2}\left(\frac{1}{(s-x)^2} - \frac{1}{(s+x)^2}\right) \tag{4.10}$$

while the whole potential energy function along the position x can be expressed as

$$\begin{aligned} & U\left(x, V_{DC}\right) = U_{\text{elastic}}\left(x\right) + U_{\text{electric}}\left(x, V_{DC}\right) \\ = \; & \frac{1}{2}k_1 x^2 + \frac{1}{4}k_3 x^4 - \frac{s V_{DC}^2 C_0}{2}\left(\frac{1}{(s-x)} + \frac{1}{(s+x)}\right) \end{aligned} \tag{4.11}$$

The equilibrium points of the system and their stability features can be found respec-

tively from the roots of the first and second potential function derivative ($\frac{\partial U\left(x,V_{DC}\right)}{\partial x}=0$, $\frac{\partial^2 U\left(x,V_{DC}\right)}{\partial x^2}=0$). Assuming for simplicity only positive bias voltages and solving both equations concurrently, the solutions of type (x,V_{DC}) that represent equilibrium points and bias stability boundaries are found. The first couple of solutions is

$$\left(x_{pi0},V_{pi0}\right)=\left(0,\sqrt{\frac{k_1 s^2}{2C_0}}\right), \tag{4.12}$$

where V_{pi0} is the lower limit value in inequations (4.7). This expression for the V_{pi0} is well-known in the literature as the pull-in voltage, that is, the bias voltage causing the collapse onto the electrode driver. This effect is only valid for gap values when the design condition in (4.9) is not satisfied (figure 4-2a). A second couple of real solutions is found to be

$$\left(x_{piw},V_{piw}\right)=\left(\pm\sqrt{\frac{k_3 s^2-2k_1}{3k_3}},\sqrt{\frac{2\left(k_3 s^2+k_1\right)^3}{27C_0 s^2 k_3^2}}\right), \tag{4.13}$$

which only exists if the design condition for 2WP (4.9) is fulfilled (figure 4-2b).

For the case when the design condition for 2WP is attained ($s > 1.615\cdot w$), $x=0$ represents an equilibrium point for any V_{DC}. For $V_{DC}<V_{pi0}$, $x=0$ is an stable equilibrium point. V_{pi0} is, in this case, the bias voltage value at which this point becomes unstable and for $V_{pi0}<V_{DC}<V_{piw}$, and the position x tends to the nearest stable equilibrium points (now the bottom of the potential wells). The static collapse onto the driver takes place in this case for bias voltages higher than V_{piw} that can be defined as the true pull-in voltage when working with a double-well potential.

In the case when the design condition is not verified ($s < 1.615\cdot w$), the only stable point $x=0$ becomes unstable when the bias voltage reaches the value of V_{pi0}, and then the system is subjected to the pull-in effect. With the aim of illustrate the positions and the stability of the equilibrium points in both cases, they are calculated using the parameter values corresponding to a 1MHz-designed polysilicon cc-beam for the AMS 035 CMOS technology (given in the first row of table 4.2) , and depicted in figure 4-2. Using the same parameter values, the force and potential functions along all the possible deformed positions x are calculated for different values of the bias voltage when the design condition (equation (4.9)) is fulfilled (and the two-well potential is allowed), and represented in figure 4-3. In this case, the roots of force function in figure 4-3 a) correspond to the equilibrium points

of the supercritical Pitchfork bifurcation diagram (figure 4-2b) at the different bias values. Notice that the situation of two-well potential distribution implies 5 roots of the static force function.

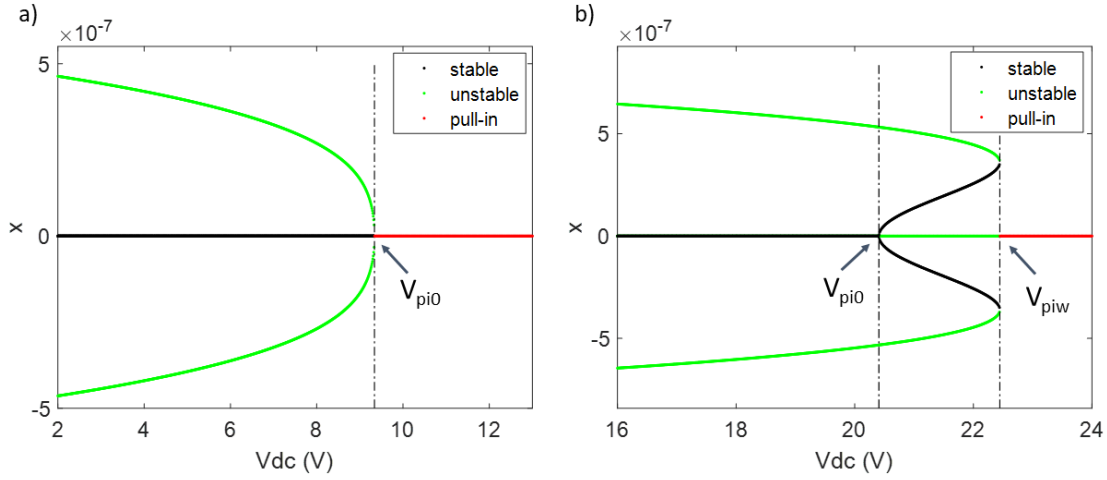

Figure 4-2: Bifurcation diagram showing the resonator equilibrium points and their stability as a function of the DC bias voltage in case of a) not verifying (for $s = 1.439w$, subcritical Pitchfork bifurcation) and b) verifying (for $s = 2.41w$, supercritical Pitchfork bifurcation) the design condition for double-well potential.

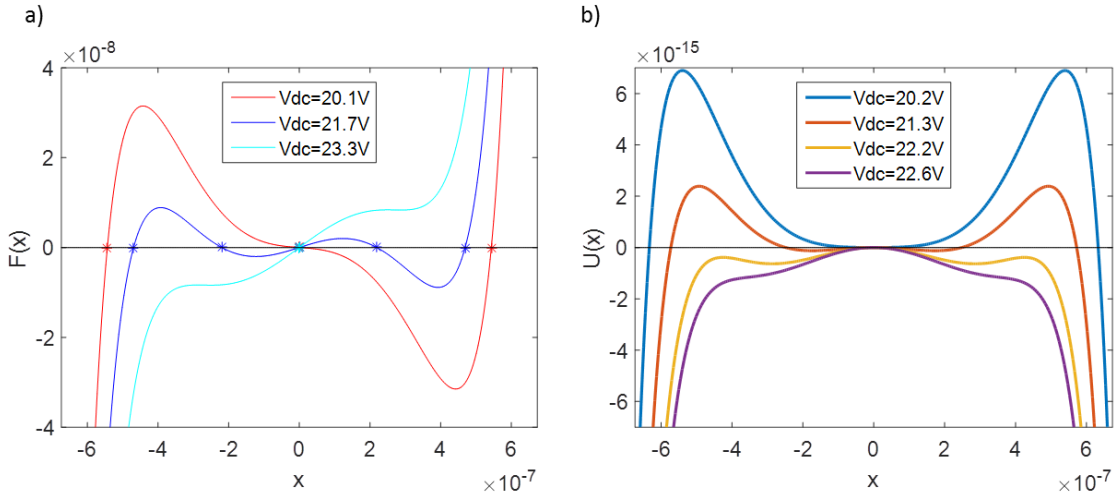

Figure 4-3: a) force and b)potential b) distribution along the deformation position for different biasing conditions, verifying ($s = 2.41w$) the design condition for double-well potential.

Once a double-well potential distribution has been reached, another important operating condition is that the potential barrier between potential wells must be lower than the

potential barriers that separate the potential valleys to the pull-in regions. If the potential values of the nontrivial unstable equilibrium points (corresponding to the potential maxima at deformed positions) are lower that the potential value at the trivial unstable equilibrium point $U(0)$, the snap-in (or cross-well) movement wont be able to take place, because the beam will collapse instead of it.

4.2.2 Topology II

In the second topology (figure 4-1b) the bias voltage is also applied symmetrically at both electrodes, as a result the same considerations than the previous scheme are used for the power series development of the actuation force. In this case, the system motional equation and the Duffing-like equation are

$$m_{\text{eff}}\ddot{x} + \gamma\dot{x} + k_1 x + k_3 x^3 = \frac{C_0 s}{2}\left(\frac{\left(V_{AC}cos\left(\omega t\right) + V_{DC}\right)^2}{\left(s-x\right)^2} - \frac{V_{DC}^2}{\left(s+x\right)^2}\right) \tag{4.14}$$

and

$$\begin{aligned} &\ddot{x} + \left(\frac{k_3}{m_{\text{eff}}} - \frac{4C_0V_{DC}^2}{m_{\text{eff}}s^4}\right)x^3 + \left(\frac{k_1}{m_{\text{eff}}} - \frac{2C_0V_{DC}^2}{m_{\text{eff}}s^2}\right)x + \left(\frac{\gamma}{m_{\text{eff}}}\right)\dot{x} \\ = \;& \frac{C_0 s}{2m_{\text{eff}}}\left(\frac{\left(V_{AC}\cos\left(\omega t\right)\right)^2 + 2V_{DC}V_{AC}\cos\left(\omega t\right)}{\left(s-x\right)^2}\right) + \frac{C_0 s}{2}\frac{V_{DC}^2}{s^2}\sigma\left(x^n\right) \end{aligned} \tag{4.15}$$

respectively. The analysis and conclusions of the potential function characteristics developed for the topology I are also valid for this topology, since both topologies have the same layout and are governed by the same static potential function (equation (4.11)).

4.2.3 Topology III

The topology in figure 4-1c) uses one single electrode for both biasing and actuation purposes. In this case, the dynamics of the MEMS is governed by:

$$m_{\text{eff}}\ddot{x} + \gamma\dot{x} + k_1 x + k_3 x^3 = \frac{C_0 s}{2}\left(\frac{\left(V_{AC}\cos\left(\omega t\right) + V_{DC}\right)^2}{\left(s-x\right)^2}\right) \tag{4.16}$$

Since the DC bias voltage is not applied symmetrically in this topology, the position $x = 0$ is no longer an equilibrium point and the even powers in Taylor expansion do not cancel

each other. The potential energy function (having considered again that $V_{DC} \gg V_{AC}$ and, thus, neglected the small bias term generated by the $\cos^2$ term) can be written as

$$U\left(x, V_{DC}\right) = \frac{1}{2}k_1 x^2 + \frac{1}{4}k_3 x^4 - \frac{sV_{DC}^2 C_0}{2}\left(\frac{1}{(s-x)}\right) \tag{4.17}$$

Given that parameters k_1, k_3, C_0 and s are positive, the existence of more than two roots for $|x| < s$ is not possible, making a double-well potential distribution unfeasible. Thus, for small V_{DC} values there is an stable equilibrium point that becomes unstable for values exceeding the pull-in voltage and unavoidably cause the resonator collapse to the electrode. An expression of the pull-in voltage for a one-driver topology has been widely reported in the literature [58], [82], providing $V_{pi0} = \sqrt{\frac{8k_1 s^2}{27C_0}}$ for a position of $x_{pi0} = s/3$, however these results correpond to the approximation in which the nonlinear stiffness has been neglected.

4.3 Design for 2WP with cc-beams

In previous sections, the impossibility of obtaining a double-well potential energy distribution, neither for cantilevers structures nor cc-beams arranged as in topology III have been demonstrated. In this section, the considerations required to design an electrostatically actuated cc-beam resonator exhibiting a double-well potential in the equivalent topologies I and II are analyzed. For a given technology, characterized mainly by the minimum width w that can be fabricated and the mechanical properties of the resonator structural layer (Young's modulus (E) and density (ρ)), the desired operating frequency determines the length of the beam resonator according to

$$l = \sqrt[4]{\frac{16Ew^2k_n^4}{192\rho\left(2\pi f_0\right)^2}} \tag{4.18}$$

where k_n is the first eigenvalue, taking the value 4.73 for an in-plane cc-beam resonator. To create a double-well potential, the design condition (4.9) sets the minimum gap s and therefore the needed bias voltage. To provide a reasonable range of DC voltages between V_{pi0} and V_{piw} that allow the operation in a two-well potential, the gap s which sets the voltage range is chosen to be higher than the minimum imposed by equation (4.9). A margin of 10% voltage range (between the upper and lower bias boundary values) is considered to be reasonable, thus the proper gap is obtained by solving:

$$1.1\sqrt{\frac{k_1 s^2}{2C_0}} = \sqrt{\frac{2\left(k_3 s^2 + k_1\right)^3}{27 C_0 s^2 k_3^2}} \tag{4.19}$$

from the next expansion of this equation

$$(1.1)^2 \frac{27}{4} \frac{k_1 s^2}{C_0} = \frac{\left(k_3 s^2 + k_1\right)^3}{C_0 s^2 k_3^2} \tag{4.20}$$

it is found to be independent on the C_0 parameter; even more, calling $\mu_{10} = \dfrac{27\,(1.1)^2}{4}$, equation (4.20) leads to

$$k_3 s^6 + (3 - \mu_{10})\, k_3^2 k_1 s^4 + 3 k_3 k_1^2 s^2 + k_1^3 = 0 \tag{4.21}$$

by substituting the expressions of k_1 and k_3 (either for the mass-spring model or for the uniformly loaded beam) in equation (4.21), it results to be also independent on all the parameters (E, l, t_h) except on the gap/width ratio:

$$(12.272)^3 \left(\frac{s}{w}\right)^6 + (3 - \mu_{10})\,(12.272)^2\, 16 \left(\frac{s}{w}\right)^4 + 3 \cdot 12.272\,(16)^2 \left(\frac{s}{w}\right)^2 + 16^3 = 0 \tag{4.22}$$

In conclusion, the margin percentage (pc) between the upper and lower voltage boundary values depend only on the s/w ratio. Calling $\mu = \dfrac{27\,(1 + pc/100)^2}{4}$, the figure 4-4a) represents the required value of the s/w ratio to allow each margin percentage. Notice that the value of the ratio corresponding to the 0% of the margin is exactly 1.615, the minimum s/w ratio to enable the presence of the nontrivial stable equilibrium points.

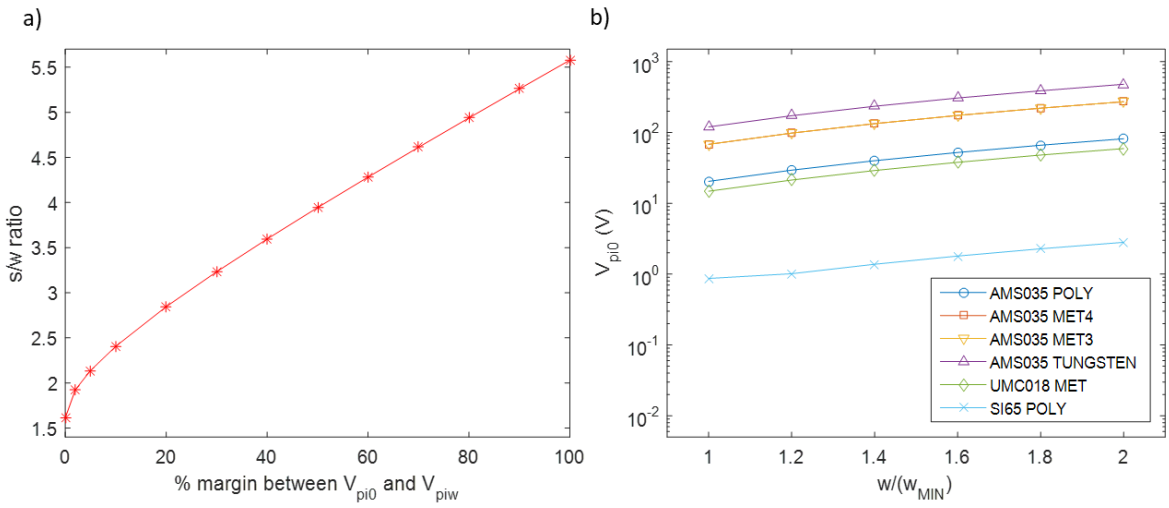

Figure 4-4: a) Ratio between s and w to enable each margin percentage between V_{pi0} and V_{piw}. b) Lower bias boundary value for two potential well distribution, at a frequency of 1MHz, as function of the normalized width parameter for the technologies considered in table 4.2.

The main cc-beam resonator characteristics from a practical perspective are its resonance frequency and the minimum DC bias voltage that enables 2WP (V_{pi0}). Such parameters are related according to

$$V_{pi0} = 2\pi f_0 \sqrt{\frac{96\rho w s^3}{\epsilon_0 k_n^4}} \tag{4.23}$$

assuming the case of punctual load applied to the middle point of the beam span, and to

$$V\mathrm{q}_{pi0} = 2\pi f_0 \sqrt{\frac{192\rho w s^3}{\epsilon_0 k_n^4}} \tag{4.24}$$

for the uniformly distributed forcing along the beam span. Two important conclusions can be stated from equations (4.19), (4.23) and (4.24):

- The minimum V_{pi0} value is achieved by minimizing the resonator width w (limited by the technology), as can be seen in figure 4-4b).
- The required bias voltage scales linearly with the desired natural frequency. Thus, an increase $\times 10$ of the desired natural frequency implies an increase $\times 10$ of the needed bias voltage to achieve 2WP, as shown in figure 4-5a).

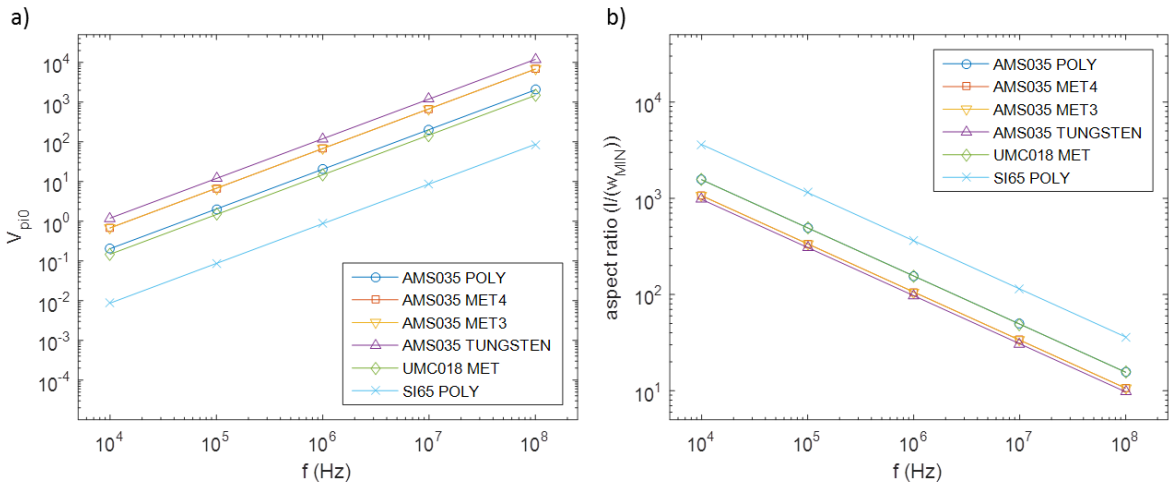

Figure 4-5: a) Bias voltage needed and b) aspect ratio (length/width) required at the desired operation frequency of the MEMS resonator for the technologies considered in table 4.2.

Another important consideration for practical applications of cc-beam resonators as chaotic generators is related to the magnitude of the motional current obtained. In contrast to linear applications, where the gap distance is designed to be as small as possible to maximize the electromechanical coupling, here, a large gap is required to enable cross-well motion. In this sense, the electromechanical coupling factor (4.25) allows a quantification of the capability to generate such current in terms of only the DC bias voltage and geometric parameters [44].

$$\eta \approx \frac{V_{DC} C_0}{s} \propto t_h \tag{4.25}$$

Once the desired frequency is set, the DC voltage range, the gap distance and the resonator length remain as fixed parameters. Therefore, as derived from (4.25) given the definition of the coupling capacitance at the non-deformed position (C_0), the only way to enhance the electromechanical coupling is by fabricating the resonator with its thickness (t_h) as large as possible. Note that the parameters length (l) (4.18), bias boundary values (V_{pi0}, V_{pi0}) (4.12) (4.13) and gap of 10% of margin between bias boundary values ($s_{10\%}$) (4.19) for a given frequency does not depend on the thickness parameter (t_h), in consequence the t_h can be modified without affecting them. In any case, the maximum aspect ratio (t_h/w) that can be fabricated is limited by the available technologies.

On the other hand, the need of reducing the resonator width to maintain appropriated

DC voltage ranges while working at relative high frequency is also illustrated in figure 4-5. In contrast, it is important to remark that for low frequencies (i.e. less than 100 kHz) the use of too narrow beams may become a handicap. Thus, the aspect ratio between the length and the resonator width can be unfeasible from a fabrication perspective. In fact, the maximum aspect ratio (l/w) reported in the literature regarding fabricated cc-beam resonators is lower than 400 [113]. In this case, the use of wider beams or even larger structures like nonoverlapping comb drives would be preferred.

In past sections we have omitted the fringing field effects on the electrostatic force calculation. In practice such effect can be considered as an increase of the effective coupling capacitance C_0 [114]. Since there is not any impact on mechanical parameters (i.e. k_1 and k_3), the design condition given by the inequation (4.9) remains unchanged. In any case, the increase of the electrostatic force reduces the value of lower and upper limits of V_{DC} that induce the double-well potential. However, the ratio of such new limits V^*_{pi0} andV^*_{piw} remain unchanged since such ratio (4.26) does not depend on electrical parameters.

$$\frac{V^*_{piw}}{V^*_{pi0}} = \sqrt{\frac{4\left(k_3 s^2 + k_1\right)^3}{27 s^4 k_3^2 k_1}} \tag{4.26}$$

Up to now we have assumed a fully symmetry in the device (i.e. gap distance between the resonator to the electrodes) obtaining a symmetric electrostatic force and double-well potential. In practice, fabrication tolerances may induce gap mismatch in the device. A detailed analysis of last terms in equation (4.2) reveals that a double-well potential is possible at the expenses of increasing the gap distance and the polarization voltage requirements. This effect is illustrated in figure 4-6 for a 10-MHz resonator considering the technologies in table 4.2. The exponential dependence of both the bias voltage and gap value as a function of the gap mismatch can be clearly observed. Thus, for a gap mismatch below 2% the obtained values are quite similar to the ideal case (figure 4-5). On the other hand, for a 10% mismatch the bias voltage required is much higher. As an example of this situation, the potential and force distribution along the possible positions (x), for different gap values, are depicted in figures 4-7 and 4-8 (using the parameter values given in table 4.2 for1MHz polysilicon resonators with AMS 035 technology) to compare their shapes when a mismatch of 10% affect one of the two gaps and when there is a total symmetry. The point to prove is that the two potential well distribution (which implies 5 roots of the force function) can

only be reached if the gap is increased. Note that, an increasing gap means an increase of the needed voltage, thus in order to perform the comparison, a DC voltage with the same proportion of V_{pi0} and V_{piw} is considered in each case : $V_{DC} = 0.1 \cdot V_{pi0} + 0.9 \cdot V_{piw}$. While for a nominal gap of $1\mu m$ (figure 4-7) the two-well potential distribution cannot be reached, it arises for a gap of $1.5\mu m$ (figure 4-8). However, if the potential barrier ($U(x)$) between the potential wells is higher than one of the nontrivial potential maximums, the cross-well motion wont be able to take place, and the system will collapse by the the pull-in effect.

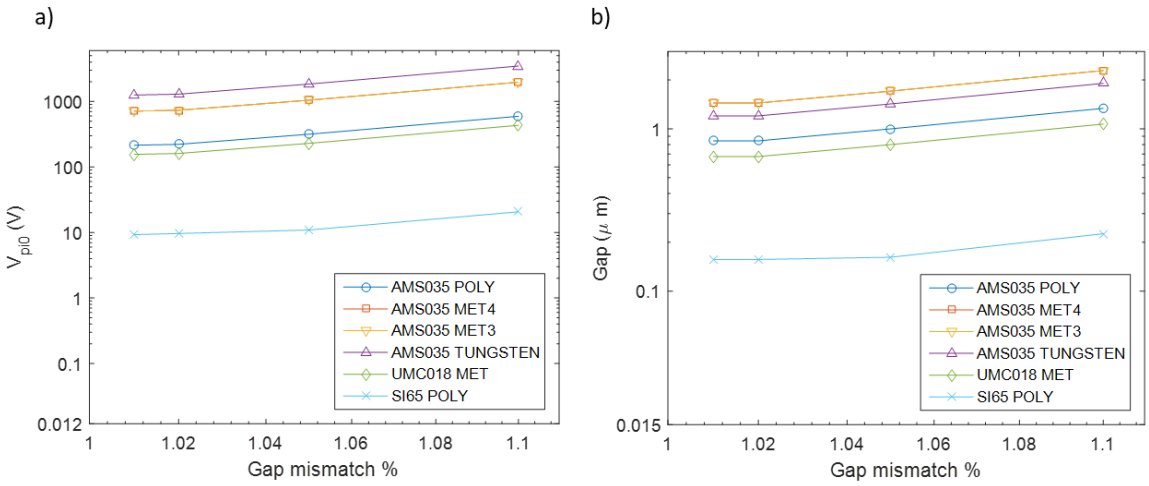

Figure 4-6: a) Bias voltage needed and b) gap distance required for a 10-MHz frequency resonator as a function of gap mismatch for the technologies considered in 4.2.

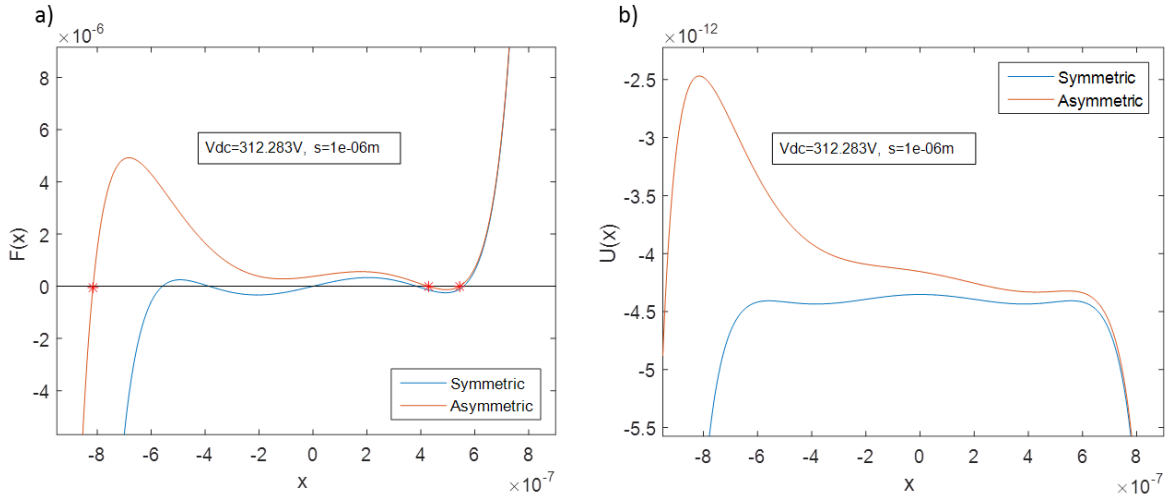

Figure 4-7: Comparison between the symmetric and asymmetric case in a) the force function and in b) the potential function for a gap of $1\mu m$ and a DC voltage given by $V_{DC} = 0.1 \cdot V_{pi0} + 0.9 \cdot V_{piw}$.

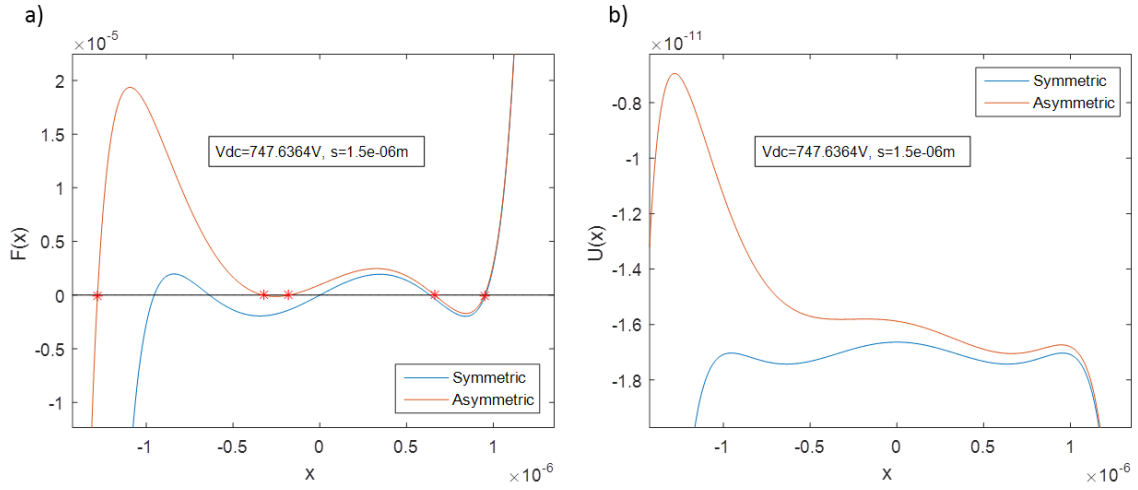

Figure 4-8: Comparison between the symmetric and asymmetric case in a) the force function and in b) the potential function for a gap of $1.5\mu m$ and a DC voltage given by $V_{DC} = 0.1 \cdot V_{pi0} + 0.9 \cdot V_{piw}$.

4.4 Nondimensional analysis and frequency response

Considering the natural frequency of the resonator ω_0 (namely $\sqrt{k_1/m_{\text{eff}}}$), defining the new time variable $\tau = t\omega_0$ and following the procedure explained in [26], the relation between the t- derivatives and τ-derivatives are found to be:

$$\begin{aligned}\dot{x} &= \frac{dx}{dt} = \frac{dx}{d\tau}\frac{d\tau}{dt} = x'\omega_0 \\ \ddot{x} &= \frac{d\dot{x}}{dt} = \frac{d\left(x'\omega_0\right)}{d\tau}\frac{d\tau}{dt} = x''\omega_0^2.\end{aligned} \tag{4.27}$$

Using these relations, and considering the variable $\hat{x} = \frac{x}{s}$, the equation of the system with topology I (equation (4.2)), where the term of square sine has been neglected (since the AC excitation amplitude is considered to be far smaller than the DC bias voltage), can be written as

$$\begin{aligned}&\hat{x}'' + \frac{\gamma}{m_{\text{eff}}\omega_0}\hat{x}' + \frac{k_1}{m_{\text{eff}}\omega_0^2}\hat{x} + \frac{k_3 s^2}{m_{\text{eff}}\omega_0^2}\hat{x}^3 = \frac{\epsilon_0 t_h l}{2}V_{DC}^2\frac{1}{m_{\text{eff}}\omega_0^2 s^3}\left(\frac{1}{\left(1-\hat{x}\right)^2} - \frac{1}{\left(1+\hat{x}\right)^2}\right) \\ &+\frac{\epsilon_0 t_h l}{2}\left(-2V_{DC}V_{AC}\sin\left(\Omega\tau\right)\right)\frac{1}{m_{\text{eff}}\omega_0^2 s^3}\left(\frac{1}{\left(1-\hat{x}\right)^2}\right)\end{aligned} \tag{4.28}$$

where $\Omega = \frac{\omega}{\omega_0}$. Thus, defining the dimensionless parameters

- $\delta = \frac{\gamma}{m_{\text{eff}}\omega_0} = \frac{\left(\frac{m_{\text{eff}}\omega_0}{Q}\right)}{m_{\text{eff}}\omega_0} = \frac{1}{Q}$;
- $\beta = \frac{k_1}{m_{\text{eff}}\omega_0^2} = 1$;
- $\alpha = \frac{k_3 s^2}{m_{\text{eff}}\omega_0^2} = \frac{k_3 s^2}{k_1} = \frac{12.272}{16}\left(\frac{s}{w}\right)^2$;
- $\mu = \frac{\epsilon_0 t_h l}{m_{\text{eff}}\omega_0^2 s^3}$

the nondimensional equation of the system is found to be

$$\hat{x}'' + \beta\hat{x} + \alpha\hat{x}^3 + \delta\hat{x}' = \mu_1\left(\frac{1}{\left(1-\hat{x}\right)^2} - \frac{1}{\left(1+\hat{x}\right)^2}\right) - \mu_2\frac{\cos\left(\Omega\tau\right)}{\left(1-\hat{x}\right)^2} \tag{4.29}$$

where, $\mu_1 = \frac{1}{2}\mu V_{DC}^2$, and $\mu_2 = \mu V_{DC}V_{AC}$. The potential distribution along the position of the equation (4.29) shows two minimums (as it is required in order to achieve homoclinic chaotic motion) for a range of values of the μ_1 parameter between μ_{1min} and μ_{1max}. These boundary values of μ_1 for bistability correspond to $\mu_{1min} = \mu V_{pi0}$ and $\mu_{1max} = \mu V_{piw}$, and

from the definitions of the voltage boundary values V_{pi0}, V_{piw} given respectively in (4.12), and (4.13) ,

- $\mu_{1min} = \dfrac{1}{2}\dfrac{\epsilon_0 t_h l}{m_{\text{eff}}\omega_0^2 s^3}\dfrac{k_1 s^3}{2\epsilon t_h l} = \dfrac{1}{4}$ (dimensionless and constant)

- $\mu_{1max} = \dfrac{1}{2}\dfrac{\epsilon_0 t_h l}{m_{\text{eff}}\omega_0^2 s^3}\dfrac{2\left(k_3 s^2 + k_1\right)^3}{27\epsilon t_h l s k_3^2} = \dfrac{\left(k_3 s^2 + k_1\right)^3}{27 k_1 s^4 k_3^2} = \dfrac{\left(12.272 \cdot \left(\dfrac{s}{w}\right)^2 + 16\right)^3}{27 \cdot (12.272)^2 \cdot 16 \cdot \left(\dfrac{s}{w}\right)^4}$ (dimensionless, function of (s/w) and existing only if the geometric condition for bistability, $s > 1.615w$ is verified)

This nondimensional equation allows the characterization of all-the cc-beam resonators (in any available technology) with a given ratio between s and w. Moreover, since the ω_0 has been used in the procedure to obtain the nondimensional equation, no matter the desired frequency. Writing the linear and nonlinear stiffness in the electrical domain together with the linear and nonlinear stiffness in mechanical domain, and neglecting the higher to 3 terms of the power series expansion, equation (4.29) can be expressed as:

$$\hat{x}'' + \delta\hat{x}' = \left(-\beta + 2\mu V_{DC}^2\right)\hat{x} + \left(-\alpha + 4\mu V_{DC}^2\right)\hat{x}^3 - V_{DC}V_{AC}\sin(\Omega\tau)\,\mu\frac{1}{(1-\hat{x})^2} \tag{4.30}$$

With the definitions $V = -V_{DC}V_{AC}$, $\phi_1 = \left(-\beta + 2\mu V_{DC}^2\right)$, $\phi_3 = \left(-\alpha + 4\mu V_{DC}^2\right)$ last equation is expressed as:

$$\hat{x}'' + \delta\hat{x}' = \phi_1\hat{x} + \phi_3\hat{x}^3 + V\cos(\Omega\tau)\,\mu\frac{1}{(1-\hat{x})^2} \tag{4.31}$$

Solving equation (4.31) using the multiple scales method, a relation for the frequency response fo the resonator as a function of the system parameters is obtained [28], [50]:

$$\left(\frac{a\Delta\Omega}{4} - \frac{\gamma_1 z^3}{4\Omega_0}\right)^2 + \delta^2\left(\frac{-\gamma_1 a^3}{16\Omega_0^2} + \frac{a\delta^2}{128\Omega_0^2} + \frac{a\Delta\Omega}{16\Omega_0} + \frac{a}{8}\right)^2 - \left(\frac{\delta^2}{128\Omega_0^3} + \frac{1}{8\Omega_0}\right)^2 K^2 = 0 \tag{4.32}$$

where $\gamma_1 = \dfrac{1}{8}\left(3\phi_3 - \dfrac{10k_2^2}{3\Omega_0^2}\right)$, $\quad k_2 = 3\sqrt{|\phi_1\phi_3|}$. $\quad \Omega_0 = \sqrt{|2\phi_1|}$, $\quad A = V\mu$ and
$K = A\left(2\sqrt{\left|\dfrac{\phi_1}{\phi_3}\right|} - 3\dfrac{\phi_1}{\phi_3} + 4\dfrac{\phi_1}{\phi_3}\sqrt{\left|\dfrac{\phi_1}{\phi_3}\right|} + 1\right)$

Figures 4-9, and 4-10 represent the frequency response of MEM systems (from equation (4.32)) with different dimensional parameters, in agreement with section 3.1.10.

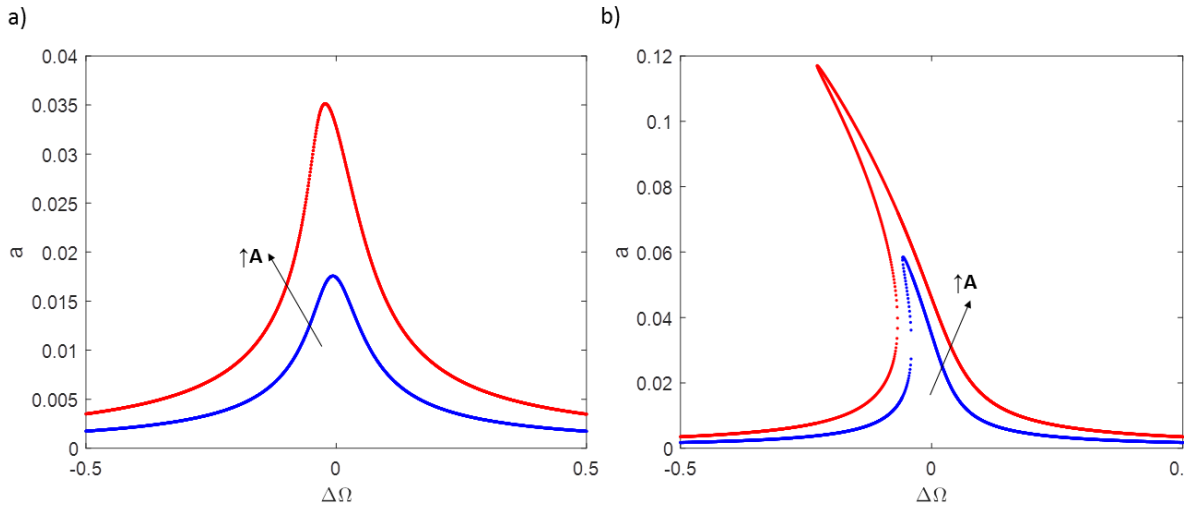

Figure 4-9: Frequency response of the resonator with $\beta = 12$, $\mu = 0.338$, a)$\delta = 0.1$ and b) $\delta = 0.03$.

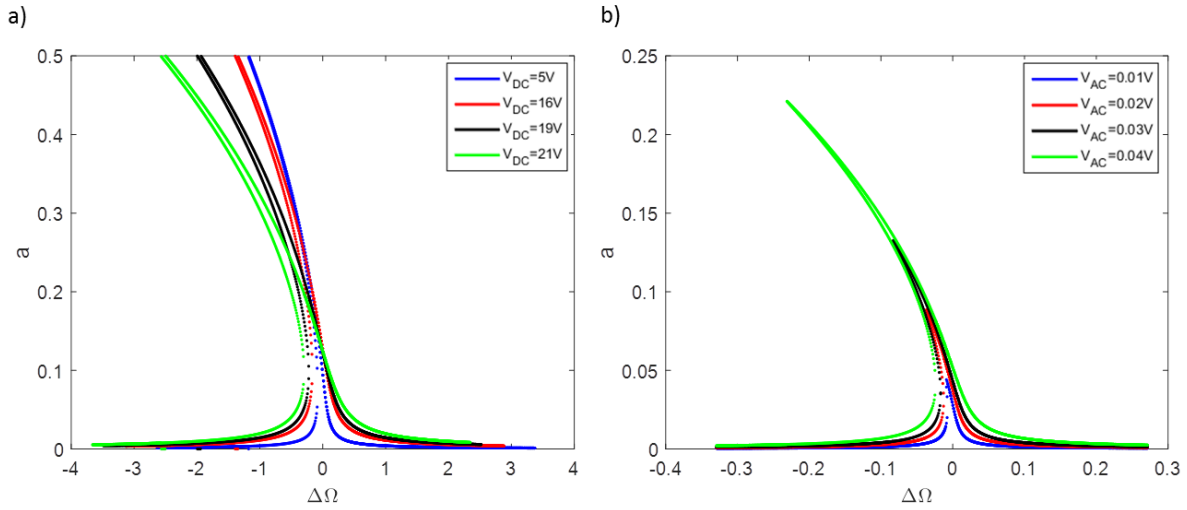

Figure 4-10: Frequency response of 1MHz resonator designed with AMS 035 technology for a) $V_{AC} = 0.3$ V and different bias voltages and b)$V_{DC} = 5$V and different excitation amplitudes.

4.5 Melnikov analysis

As introduced in section 2.4, the Melnikov method has been used in several references to establish a necessary condition for chaotic motion based on the existence of transverse

homoclinic orbits in the Poincare map [55]. The Melnikov function gives a measure of the leading order distance between the stable and unstable manifolds for the complete system (with non-null dissipative and forcing terms)[21]. The Melnikov criterion gives a necessary but not sufficient condition for occurrence of homoclinic chaotic behavior, and is based on the intersection of system response with the homoclinic orbit [29]. With the definition of all its parameters, equation (4.31) is written now as

$$\begin{aligned} \hat{x}' &= \hat{u} \\ \hat{u}' &= \phi_1 \hat{x} + \phi_3 \hat{x}^3 + \epsilon \left(\overline{\delta} \hat{u} + \overline{\mu} \sin(\Omega \tau) V \frac{1}{(1-\hat{x})^2} \right) \end{aligned} \tag{4.33}$$

where $\delta = \epsilon \overline{\delta}$ and $\mu = \epsilon \overline{\mu}$. The potential function can be approximated to $U(x) = \frac{1}{2}\phi_1 x^2 + \frac{1}{4}\phi_3 x^4$. From the definition (given in [55]) of the homoclinic orbit given in equation (2.38):

$$\begin{aligned} \Gamma_{\pm}^0(t) &= \left(\hat{x}^0(t), \hat{u}^0(t) \right) = \\ & \left(\pm \sqrt{-\frac{2\phi_1}{\phi_3}} \operatorname{sech}\left(\sqrt{-\phi_1} t \right), \mp \sqrt{\frac{2\phi_1^2}{\phi_3}} \operatorname{sech}\left(\sqrt{-\phi_1} t \right) \tanh\left(\sqrt{-\phi_1} t \right) \right) \end{aligned} \tag{4.34}$$

and with $\Gamma_{\pm}^0(t) = \left(\hat{x}^0(t), \hat{u}^0(t) \right)$, the Melnikov function is given by

$$M(\tau_0) = \int_{-\infty}^{\infty} f\left(\Gamma_+^0(\tau) \right) \wedge g\left(\Gamma_+^0(\tau), \tau + \tau_0 \right) d\tau \tag{4.35}$$

namely:

$$M(\tau_0) = \int_{-\infty}^{\infty} \hat{u}^0(\tau) \left(-\delta \hat{u}^0(\tau) + V \sin\left(\Omega(\tau + \tau_0) \right) \mu \frac{1}{\left(1 + \hat{x}^0(\tau)\right)^2} \right) d\tau \tag{4.36}$$

Defining $x_e = \sqrt{-\frac{2\phi_1}{\phi_3}}$ as the positive root of the potential function ($U(x)$), and $K = -\phi_1$, and following the procedure detailed in [26], the Melnikov criterion is found to be:

$$\left| \frac{\delta \sqrt{K} x_e^2}{3V\mu} \right| \leq \left| \frac{x_e \pi \frac{\Omega}{\sqrt{K}}}{\sqrt{\left(1 - (x_e)^2\right)}} \frac{\sinh\left(\frac{\Omega}{\sqrt{K}} \left(-\arccos(x_e) \right) \right)}{\sinh\left(\frac{\Omega}{\sqrt{K}} \pi \right)} \right| \tag{4.37}$$

References [28] and [29] consider, two critical amplitudes for the chaotic motion prediction as an improvement of the Melnikov method. In these references, based on the intersection of the steady state of the system with the homoclinic orbit, two effective criteria depending on the relative value of the damping ratio were established. For a resonator with a high damping ratio the chaotic motion occurs where the corresponding maximum velocity approaches to the homoclinic orbit velocity. On the other hand, a resonator with low damping ratio becomes chaotic where its vibration amplitude approaches the homoclinic orbit amplitude. The two critical amplitudes considered in [28] and [29] are

$$a_{cr1} = \frac{\phi_1}{\Omega\sqrt{2\left(-\phi_3\right)}} \tag{4.38}$$

and

$$a_{cr2} = \sqrt{\frac{-\phi_1}{2\phi_3}} \tag{4.39}$$

If the right hand side term of equation (4.37) minus the left hand side term of the equation is labeled as Melnikov points, figure 4-11 depicts the value of the Melnikov points for different values of the AC excitation amplitude, providing for different values of frequency a minimum AC amplitude which fulfills the necessary but not sufficient Melnikov criterion for chaos. In figure 4-11, these minimum values of AC excitation amplitude are also compared with those provided by the criterion proposed in [28] and [29].

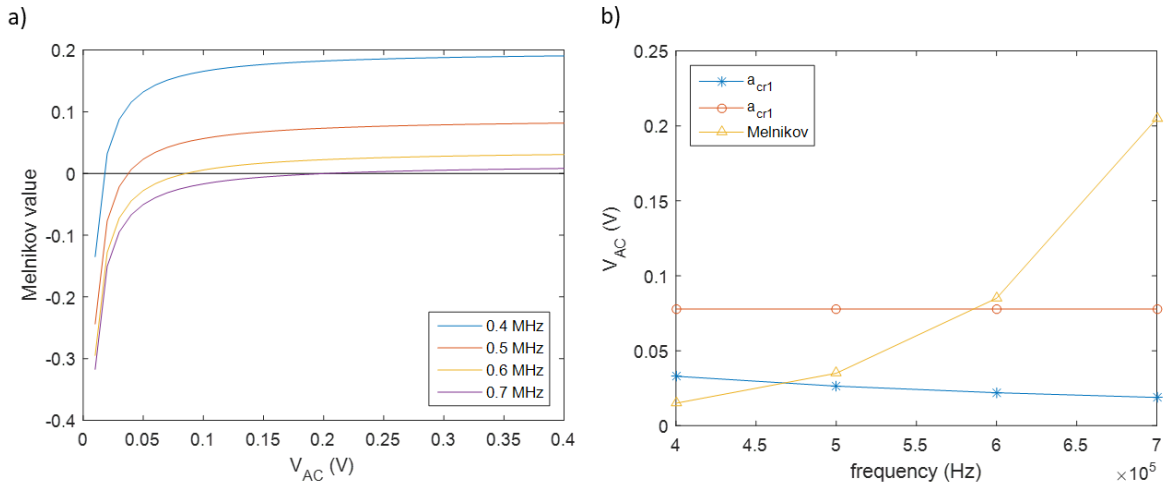

Figure 4-11: a) Representation of the Melnikov points for different values of driving frequency and of AC excitation amplitude, using the parameter values corresponding to a 1MHz polysilicon resonator designed in AMS 035, under a DC bias of $V_{DC} = 20.7V$ and b) comparison between the minumum AC excitation amplitude obtained from the Melnikov method and from the critical amplitudes (equations (4.38) and (4.39)) given in [28] and [29].

4.6 Chaotic behavior in 1WP MEMS resonators: a critical revision

Numerical simulations of the Duffing oscillator with single-well potential, reported in literature (as well as in section 2.3.2), show various types of nonlinear dynamic behaviors: symmetry breakings, hysteresis, period doubling bifurcations and, finally, chaotic motion [64], [65]. However, chaotic motion obtained under these conditions (in-well chaos) as the completion of a period doubling route is described as weak in contrast to cross-well Duffing chaos, considered as robust [54], [62]. This weak nature can be observed, among others, through the chaotic signal spectrum bandwidth that is significantly narrower than the bandwidth exhibited by a cross-well chaotic signal. In this sense, cross-well chaos is desired instead of in-well chaos in practical applications as random number generation or chaos-based secure communications. On the other hand, single-well based chaos in a Duffing system is achieved for relative high actuation amplitudes [64], [65] in comparison with the Duffing chaos based on two-well potential (for comparison, see figures 2-7a) and 2-4b)). This fact may compromise the stability in the case of MEMS resonators due to the parametric

excitation in the electrostatic actuation. Given the similarity between the electrostatically actuated MEMS motion and the Duffing oscillator, the last results suggest a priori the unsuitability of in-well chaotic operation.

Furthermore, a fundamental issue from a useful perspective is that single-well chaotic behavior in electrostatically actuated MEMS resonators is provided for a narrow range of system parameters to allow a practical implementation by means of any physical device. This fact is verified in several works that analyze chaos behavior in MEMS resonators [24], [25], [115] as depicted in table 4.1. The actuation voltage range ratio has been obtained as the ratio between the range of the excitation voltage amplitudes that provide chaotic behavior and the lower absolute value of this range. It is important to remark that none of these works reports experimental measurements.

The works in [24] and [25], provide numerical simulations of the transition to chaos in an electrostatic clamped-clamped microbeam through period doubling route under superharmonic excitations. A bias voltage slightly higher than DC-symmetry breaking (that indicates the presence of nonlinearities), but lower than the pull-in voltage is applied; from this, following period doubling bifurcations and by superharmonic frequencies, in-well chaos is found for a voltage range of only few millivolts. A similar performance is found in [25] and [115] where the path of symmetry breakings and period doubling bifurcations in torsional mirror resonators is followed. Single-well potential chaos is attained again only for an actuation voltage range of few millivolts or even less. On the other hand, non-planar motion has been recently proposed in [30] as a novel way to achieve extensive chaotic behavior in contrast to nonextensive chaotic behavior attained through period-doubling bifurcations as commented earlier. Such performance is observed by modeling the non-planar motion of a silicon nanowire. Unfortunately, non-planar movement exhibits a challenging capacitive readout given the small variation of the resonator-driver capacitance caused by the torsional NEMS oscillation (in contrast to lateral displacement) making the use of capacitive transduction impractical. Therefore, different readout techniques like the integration of piezoresistive layers or the use of off-chip and bulky optical readout systems among other techniques must be considered at the expense of increasing fabrication cost and complexity.

Table 4.1: Summary of works reporting on single-well potential based chaotic behavior in simple resonant structures under electrostatic actuation.

Reference	[25]	[25]	[24]	[115]	[30]
Resonator	Cantilever	Torsional mirror	CC-beam	Torsional mirror	Nanowire
In-plane actuation?	Yes	Yes	Yes	No	No
Actuation voltage range ratio (%)	0.016	0.003	0.016	0.01	< 0.5

4.7 Numerical results of 2WP cc-beams

To illustrate the practical limits and the design procedure in fabricating chaotic generators based on in-plane electrostatically actuated cc-beam resonators, the main parameters corresponding to various top-down CMOS technology approaches (which have previously demonstrated the capability in fabricating these types of MEMS structures) have been derived (table 4.2). For comparison purposes, a target resonance frequency of 1 MHz has been considered. The bias boundary values numerically obtained when the electrostatic force is considered to be concentrated at the middle point of the beam span are compared with those (denoted by $V\mathrm{q}_{pi0}$ and $V\mathrm{q}_{piw}$) obtained when the load is approximated to be uniformly distributed along the beam.

Table 4.2: Design parameter values for two-well potential operation in 1 MHz cc-beam resonators implemented in various CMOS-MEMS technology approaches. The gap s is chosen to establish a relative DC voltage range of 10% .

Technology	$E\,(GPa)$	$\rho\,(kg/m^3)$	$w\,(nm)$	$t_h\,(nm)$	$l\,(\mu m)$	$s\,(nm)$	$C_0\,(aF)$
AMS 035 POLYSILICON	160	2330	350	282	54.601	842.22	161.87
AMS 035 METAL 4	131	3000	600	850	63.839	1443.8	332.77
AMS 035 METAL 3	131	3000	600	640	63.839	1443.8	250.56
AMS 035 TUNGSTEN	411	19300	500	800	48.7	1203.2	286.71
UMC 018 METAL	131	3000	280	580	43.611	673.78	332.39
SI 65 nm POLYSILICON	160	2330	65	100	23.53	180[1]	115.74
Technology	$V_{pi0}\,(V)$	$V_{piw}\,(V)$	$\eta\,(nC/m)$	$V\mathrm{q}_{pi0}\,(V)$	$V\mathrm{q}_{piw}\,(V)$	$\eta_q\,(nC/m)$	V_{piw}/V_{pi0}
AMS 035 POLYSILICON	20.411	22.452	3.923	28.866	31.753	5.5479	1.1
AMS 035 METAL 4	68.064	74.871	15.688	96.258	105.88	22.186	1.1
AMS 035 METAL 3	68.064	74.871	11.812	96.258	105.88	16.704	1.1
AMS 035 TUNGSTEN	119.89	131.88	28.569	169.55	186.5	40.402	1.1
UMC 018 METAL	14.823	16.305	7.3126	20.963	23.059	10.342	1.1
SI 65 nm POLYSILICON	0.87	1.03	0.559	1.229	1.452	0.79	1.1814

In order to limit the required bias voltage, one possible solution that would be explored is the use of a nanometric CMOS technology. The smaller size implies a reduction of the needed bias voltages (even to extremely low values); however, the electromechanical

[1]Minimum gap distance allowed by this technology

coupling also decreases around two orders of magnitude with respect to submicrometric CMOS technologies, potentially compromising the signal capacitive readout, and even more when on-chip CMOS circuitry is not feasible in the nanometric CMOS technology.

Numerical simulation results are presented below as an example of cross-well chaotic response of a cc-beam resonator. The parameters used are based on a polysilicon beam fabricated in the AMS 035 CMOS technology as in [44]. The resonator is arranged according to Topology I, with dimensions given in the first row of table 4.2. At room conditions operation ($P = 1$atm and $T = 300$ K) the resonator exhibits a quality factor (Q) of 165. The parameters of the motional equation, obtained from equations (3.11), (3.24), (3.9) and (3.10) are: $m_{\text{eff}} = 4.82\times10^{15}kg$, $\gamma = 1.83\times10^{10}Ns/m$, $k_1 = 0.19N/m$, $k_3 = 1.19\times10^{12}N/m^3$, and a fundamental in-plane resonance frequency of 1 MHz. To ensure a DC voltage operation range of 10%, the gap has been set in this case to 842 nm obtaining pull-in voltages of $V_{pi0} = 20.41V$ and $V_{piw} = 22.44V$, respectively, in agreement with 4.2. Figure 4-12 show numerically obtained bifurcation diagrams where, for different values of DC voltage and AC excitation amplitude, the position of the Poicare points are plotted. The regions of the parameter space where chaotic behavior is found agree with the predictions of the Melnikov method.

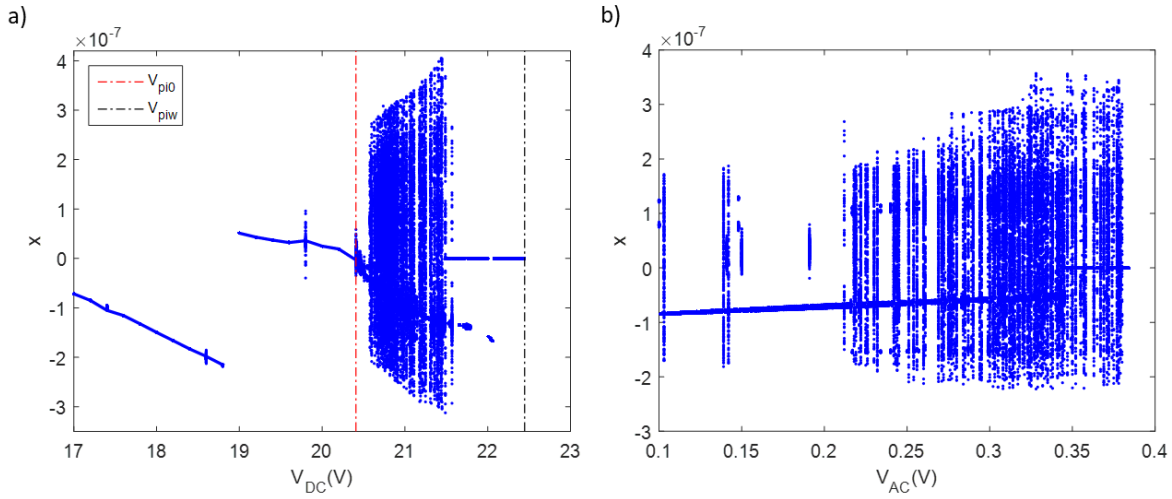

Figure 4-12: Bifurcation diagrams based on the position of the Poincare points for the 1MHz-designed AMS 035 polysilicon resonator under a) $V_{AC} = 0.3V$and a variation of the DC voltage and under b) a $V_{DC} = 20.7V$ and a variation of the AC excitation amplitude.

For a DC bias voltage of 20.7 V the potential well bottom is located at $x = \pm93nm$ and cross-well chaotic behavior is observed for an excitation voltage of $V_{AC} = 0.3V$ as shown in

figure 4-13. It is important to remark that cross-well chaos can be achieved for relatively small excitation voltages in contrast to the DC voltage required for in-well chaos (single-well potential) as detailed in section (4.6). On the other hand, due to the relative large gap distance used to enable double-well potential, the magnitude of the capacitive current generated in the resonator-driver is relative low, in the nanoampere range, as depicted in figure 4-14. This low current together with the relative high frequency make the readout system to be critical. In this sense, the use of on-chip CMOS circuitry allows high-sensitivity readout as demonstrated in previous works [44], [45]. A positive value of the maximal Lyapunov exponent is obtained with the Wolf algorithm (see section 2.5.3 for details), as shown in figure 4-15. Such results imply the presence of sustained chaos in the output time series. Appendix A introduces a method based on fuzzy logic and artificial neural networks to search the operation conditions to optimize the chaotic response.

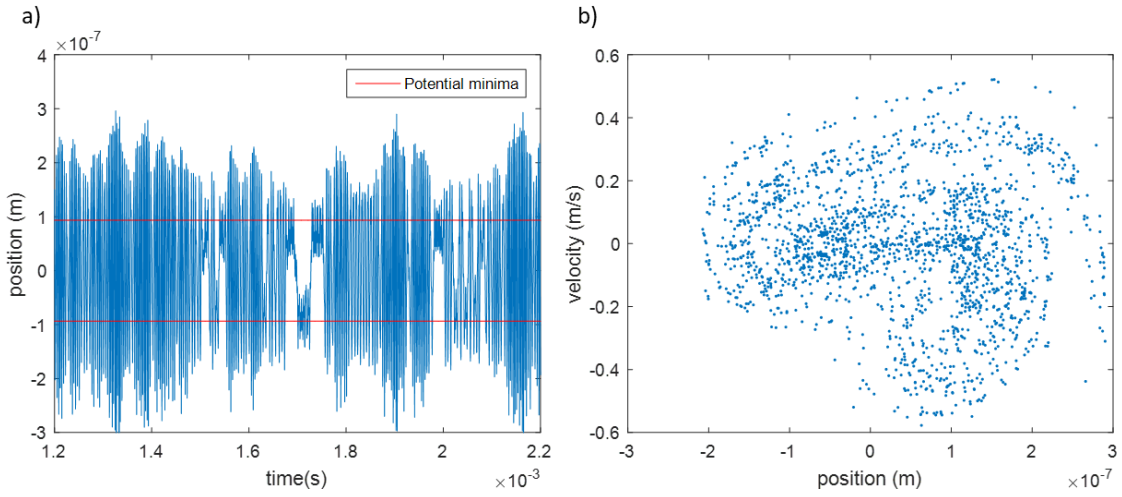

Figure 4-13: a) Time series waveform and b) Poincare map for $V_{DC} = 20.7V$, $V_{AC} = 0.3V$ and superharmonic excitation $f = f_0/2 = 500$kHz, showing the typical shape of chaotic dynamics.

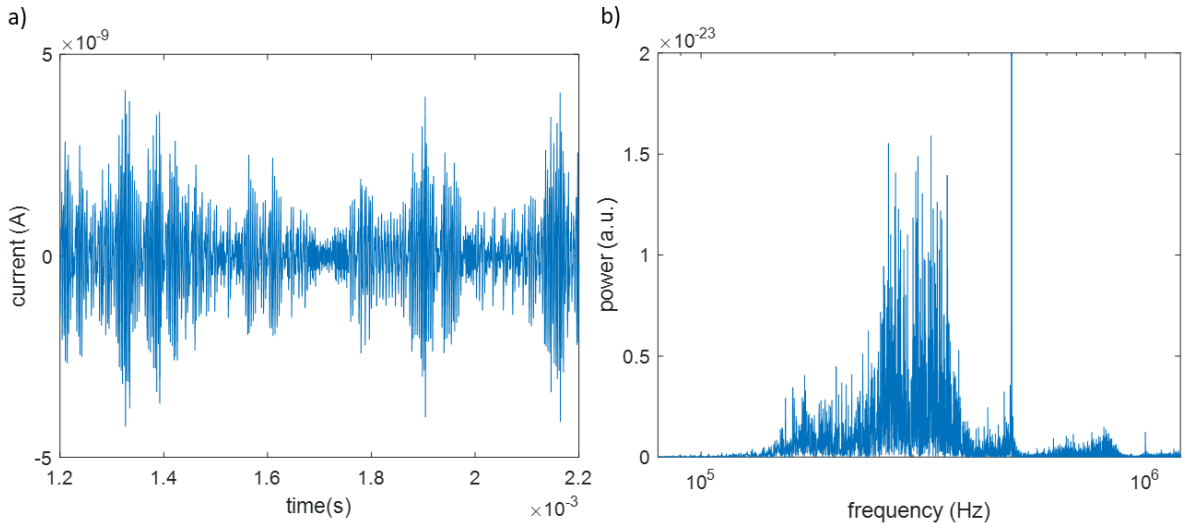

Figure 4-14: a) Capacitive current generated and b) spectrum corresponding to the chaotic signal depicted in figure 4-13.

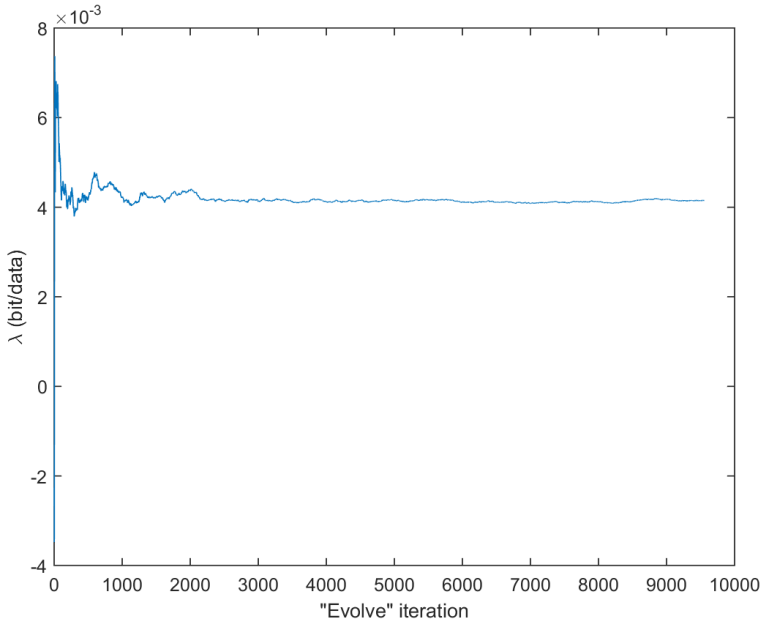

Figure 4-15: Maximal Layapunov exponent, numerically obtained with Wolf algorithm from time-series corresponding to the chaotic signal depicted in figure 4-13.

Finally, in order to demonstrate the potential use of the chaotic signal as true random number generator, the levels of the position have been classified in a 8-bit quantification as depicted in figure 4-16. The probability of every position is evenly distributed for a wide range of positions. In this way, instance, the generation of 7-bit random numbers is found

to be feasible.

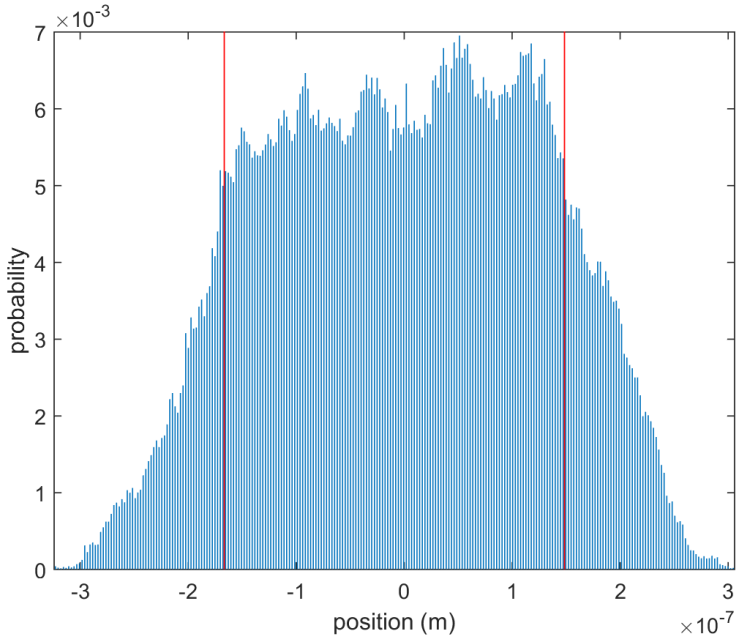

Figure 4-16: Histogram of different position levels for the chaotic signal time-series given in figure 4-13a).

4.8 Discussion and conclusions

The chaotic behavior of MEMS structures constitutes an exotic field exhibiting a considerable potential. It is important to emphasize that, up to date, no experimental results of chaotic motion were reported on simple structures like cc-beams. Chaotic behavior has been only experimentally observed for relatively large and complex structures using non-overlapping comb fingers as driver electrodes working in the kHz range. In this chapter, the possibility of obtaining chaotic behavior with a MEMS simple resonator (cc-beam and cantilever) placed in-plane has been evaluated from two approaches. The first approach was oriented to explore the one-well chaotic behavior of simple and in-plane oscillators (cc-beams or cantilevers) as culmination of period doubling route. An exhaustive revision of the works found in the literature indicates the unfeasibility of the in-well chaotic behavior since the extremely narrow range of the actuations voltages that disables chaotic performance in real systems. In addition, numerical simulations of the Duffing system (performed in section 2.3.2) shown the need of great excitation amplitudes, and a weakness of the chaotic response in comparison with the homoclinic chaos. These results discourage definitively

the practical exploitation of in-well chaos using the proposed approach. In the second approach, the reproduction of the well known 2WP Duffing chaotic attractor with a beam MEMS resonator has been analyzed. This chaotic behavior is found to be robust, broad banded, stationary and provided by a wide range of parameters. In fact, two-well Duffing chaos is the most widely used among most chaotic oscillators references. In any case, it is important to mention inconsistencies found in some previous works ([26], [27], [116]). As we remark in the first section, in a cc- beam resonator the effective mass, linear and nonlinear stiffness and the capacitance for zero displacement parameters are not independent. Solving the system of equations to size the microresonator considered in [26] reveals a set of values for these parameters that are fully incompatible. The given capacitance for zero displacement takes an unusually high value of $C_0 = 0.94pF$ for a simple cc-beam resonator ($C_0 \times s = 1.875 \times 10^{18} Fm$ and $s = 2\mu$m). Assuming a Young modulus of $E = 160$ GPa for the silicon cc-beam resonator and by the equations intended for k_1, k_3 and C_0 the microresonator dimensions are found to be: $w = 506nm$, $l = 344\mu$m and $t = 616\mu$m. The aspect ratio t_h/w obtained from such values ($\sim 10^3$) is absolutely unfeasible for any MEMS fabrication technology. In fact, the maximum t_h/w ratio reported up to now is less than 100 [117]. In addition, a mass density value of $122kg/m^3$ is also derived from last parameters, which is an unrealistic value for common MEMS materials.

To summarize, taking a first approximation of a simple lumped model to easily get the essential nonlinear performance of beam-shaped resonators, both the technological (material and aspect ratios) and electrical (voltage values) requirements for the generation of a double-well potential distribution (which enables its operation as cross-well based chaotic generator in an extensive and robust way) have been determined. In contrast to typical applications (sensors, RF oscillators, etc.), a relatively large gap is required making the capacitive readout a key issue. In this way, the resonator width minimization becomes mandatory if high frequency operation is desired, since the required bias voltage value scales linearly with the resonance frequency. These results are given for some CMOS technologies (which have been reported in literature to be used for MEMS resonator fabrication) to illustrate the order of magnitude of the polarization voltages depending on the required operating frequency and the approximated real resonator dimensions.

Chapter 5

Nonlinear macro-model for cc-beam microresonators

In chapter 4, the design and operating conditions for cross-well motion (based on bistability) have been reported and numerically reproduced to obtain rich and sustained chaotic behavior. Bistability (two-well potential distribution) can be seen as the first step to attain the chaotic behavior in MEMS resonators, having also some other applications, like threshold switches, memory cells, relays, valves etc. [118]. Up to now, all the analytic procedure relies on the parallel plate approximation, namely the conception of that all the beam is sliding as a solid without deformation and that it keeps always a perfect parallel orientation with respect to the electrodes. However, bistable behavior requires relative large beam displacements making the resonator to electrode parallel plate approximation ([21], [26]) inaccurate for its design, especially in narrow beams. In addition, the fringing field effects and residual stress (second order nonlinear effects) may modify significantly the resonator-electrode capacitance and the resonance frequency respectively [119] and, in consequence, must be taken into account for a more realistic and reliable modeling.

In this chapter a nonlinear compact model with accurate near-real resonator deflection profile based on finite difference method is developed. The finite difference method provides a good accuracy with low computational cost. The model includes the mechanical stiffness cubic nonlinearity term, the intrinsic electrostatic nonlinearities, the fringing field contributions and the residual fabrication stress [114], [120]. Since only time-derivatives equations are used, the model can be embedded within common electrical simulators for system level

simulations into the IC design flow (see appendix B for more details). Finally, the model has been applied to predict the design parameters and biasing conditions to achieve two-well potential distribution (or bistable behavior) in a narrow cc-beam resonator reported in references [109], [121]. Moreover, the accuracy of the model has been validated through extensive FEM simulations and experimental data.

5.1 Near real deflection profile

Consider the Topology I exposed in chapter 4 because of the advantages it provides: as explained in section 4.2, this topology reduces the parasitic feedthrough current and uses independent AC and DC voltage sources (more suitable for operating as a self-sustained oscillator [45]).

The beam parallel plane deformation is found to be not realistic enough, especially for large displacements of the middle point. Thus, the deflection profile of the electrostatically actuated cc-beam is considered in order to obtain an improved model. The electrostatic actuation can understood as a distributed phenomenon along the span that causes the beam deformation and at the same time is affected by it. Despite the fact that the distributed load caused by the electrostatic actuation is not uniform, especially for large deformations, the cc-beam is considered to be under a uniform load (q) accordingly to [78] (the deflection profile in this case is obtained as equation (3.12)). If the electrostatic coupling is not applied over the whole beam length, the elastic equation of the deflection profile is given by [78]:

$$\omega_q(x,y)=\begin{cases}\dfrac{y^2}{6EI}\left(3M_A+R_Ay\right) & 0\le y<\dfrac{l-l_c}{2}\\ \dfrac{-1}{24EI}\left(q\left(y-\dfrac{l-l_c}{2}\right)^4-4R_Ay^3-12M_Ay^2\right) & \dfrac{l-l_c}{2}\le y<\dfrac{l+l_c}{2}\\ \dfrac{1}{6EI}\left(3\left(M_B+lR_B\right)y^2-R_By^3+l^2\left(3M_B+lR_B\right)\right.\\ \quad\left.-3\left(2M_B+lR_B\right)ly\right) & \dfrac{l+l_c}{2}\le y<l\end{cases} \tag{5.1}$$

where $M_{A,B}$ and$R_{A,B}$ are respectively the reaction forces and momentums in the clamped ends of the beam given by equations (5.2). The effective coupling length is l_c considering a symmetrical disposition of the electrode with respect to the beam.

$$M_A = M_B = -\frac{ql_c}{24l}\left(-l_c^2 + 3l^2\right); \quad R_A = R_B = \frac{ql_c}{2} \tag{5.2}$$

The maximum deflection occurs at the beam center ($\omega_q(l/2)$), whose displacement corresponds to the x parameter ($x = \omega_q(l/2)$), and is used to find the normalized deflection profile for the cc-beam (5.3) (for the case of a uniform load applied to the whole beam span), that is, the deflection at each position in terms of such maximum. The expression obtained is independent of the load value.

$$\omega_q(x, y) = \frac{384x}{l^4}\left(-\frac{l}{12}y^3 + \frac{1}{24}y^4 + \frac{l^2}{24}y^2\right) \tag{5.3}$$

Moreover, following what is exposed in section 3.1.1, the equation of the first mode shape of a cc-beam is [58]:

$$u_1(x, y) = xC_1\left[\sinh(\beta_1 \cdot y/l) - \sin(\beta_1 \cdot y/l) + \alpha_1\left(\cosh(\beta_1 \cdot y/l) - \cos(\beta_1 \cdot y/l)\right)\right] \tag{5.4}$$

where $\alpha_1 = (\sinh\beta_1 - \sin\beta_1)/(\cos\beta_1 - \cosh\beta_1)$, β_1 is the eigenvalue for the fundamental vibration mode ($\beta_1 = k_n$) , and C_1 is a constant obtained by imposing that $\frac{u_1(l/2)}{x} = 1$ ($C_1 = 1/\left[\sinh(\beta_1/2) - \sin(\beta_1/2) + \alpha_1\left(\cosh(\beta_1/2) - \cos(\beta_1/2)\right)\right]$), and$x$ is the maximum deflection (at $y = l/2$). The beam deflection under a punctual force in the x-direction (F_x) applied at the center is found [78] to follow the polynomial equation (3.8). Following the same procedure as the one for equation (5.3), equation (3.8) can be expressed in terms of the maximum deflection point (and independent of the force value) as

$$\omega_F(x, y) = -\frac{48xy^2}{l^3}\left(\frac{y}{3} - \frac{l}{4}\right) \tag{5.5}$$

In figure 5-1a) the deflection profile obtained by FEM simulations of a cc-beam under electrostatic force is compared respectively with the shape of the deflection profile caused by either an uniformly distributed load (equation (5.3)) or lumped load applied to the center of the beam (equation (5.5)), and with the first mode shape of a cc-beam (equation (5.4)). Equations (5.3), (5.4) and (5.5) are plotted in figure 5-1a) for the x value corresponding to the maximum deflection point given by FEM simulations. It is interesting to notice the good agreement between all these curves, and between these curves and the FEM obtained points. Given the accuracy of the deflection profile given by the curve (5.3), it is used as an

approximation of the real deflection profile. Moreover, it presents practical advantages: it is defined along the whole beam span (in contrast with equation (5.5) which is only defined for $y \in [0, l/2]$), and it is a polynomial function (so it is simpler to operate with than the mode shape equation (5.4)).

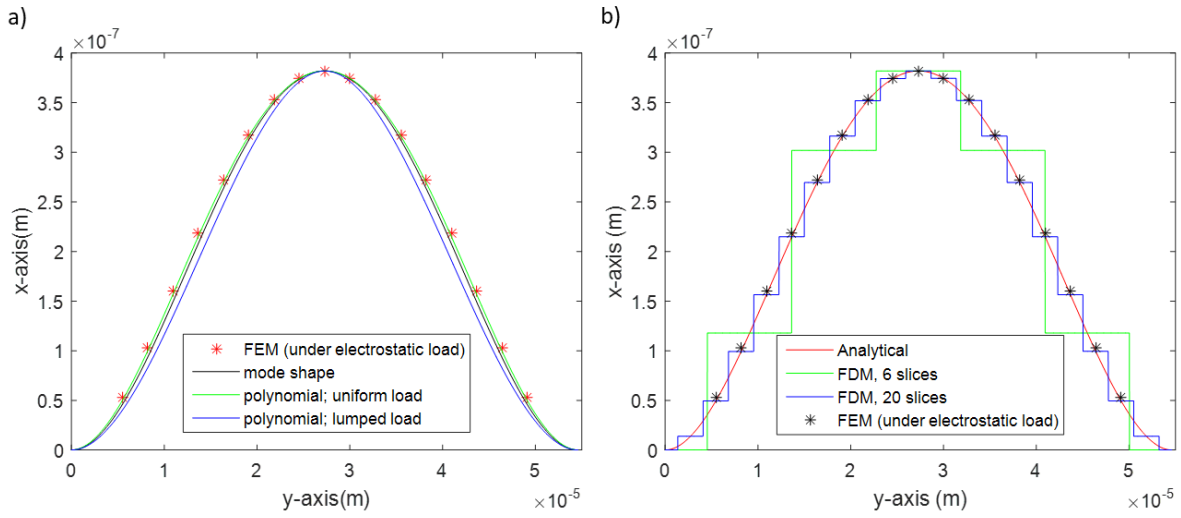

Figure 5-1: a) Elatic deflection profiles comparison between the mode shape equation (5.4), the deflection under uniform load (polynomial equation (5.3)), the deflection under lumped and centered load (polynomial equation (5.5)) and the deflection profile provided by FEM simulation. b)Analytical (equation (5.3)) and FEM-obtained deflection profile, and the corresponding finite difference method (FDM) profile for $N = 6$ slices and $N = 20$ slices. Both figures refer to an AMS 035 polysilicon cc-beam resonator whose dimensions are given in the first row of table 4.2 under a electrostatic load provided by a bias voltage of 34V.

As exposed in section 3.1.5, the electrostatic force acting on the beam is found as the negative gradient of the energy stored between the beam and each electrode, thus in the defined 1 DOF it is proportional to the x-derivative of the capacitance. The differential beam-electrode capacitance can be accurately approximated for the equation (5.6) as a function of the beam deflection (x) at the middle point and the position (y) on the beam.

$$dC\left(x,y\right) = \frac{\epsilon_0 t_h dy}{s - \omega_q\left(x,y\right)} \tag{5.6}$$

The whole dynamic equation of the electromechanical system, posed as the dynamic equilibrium over the point $y = l/2$, can be expressed in the terms previously introduced, as

an improvement of equation (4.2) :

$$\begin{aligned} & m_{\text{eff}}\ddot{x} + \gamma\dot{x} = -\left(k_{1\sigma}x + k_{3\sigma}x^3\right) \\ + \quad & \frac{1}{2}\epsilon_0 t_h k_{\text{FF}} \int_0^l \left(\frac{\left(V_{AC}\cos\left(\omega t\right) - V_{DC}\right)^2}{\left(s - \omega_q\left(x,y\right)\right)^2} - \frac{V_{DC}^2}{\left(s + \omega_q\left(x,y\right)\right)^2} \right) \left(\frac{\partial \omega_q\left(x,y\right)}{\partial x} \right) dy \end{aligned} \quad (5.7)$$

where $k_{1\sigma}$,$k_{3\sigma}$ are the linear and nonlinear stiffness coefficients that depend, a priori, on the residual fabrication stress, and k_{FF} is the fringing field term, which provides a contribution to the coupling capacitance between the beam and the electrodes. These effects, the residual fabrication stress and the fringing field contribution to the coupling capacitance, and their influence on the parameters of the dynamic equation will be analyzed in following sections. The electrostatic force can be numerically approximated by integrating the differential capacitance along the beam length, and subsequently by deriving it with respect to the x variable. However, this numerical procedure results to be highly time-consuming and unfeasible in an electrical simulator. To conduct the described electromechanical system within IC design tools, only time derivatives can be contained in the model.

From the assimilation of the dynamic equation to the classic Duffing equation with parametric excitation, and given the solution of the undamped and unforced Duffing equation based on Jacobi elliptic function explained in section 2.2.2, the resonance frequency of the system is found to present amplitude dependence on the nonlinear stiffness, following a function that can be assimilated to equation (2.40). The effect of the nonlinear stiffness on the resonance frequency and its dependence on the oscillation amplitude is illustrated by numerical simulations. In these simulations a control parameter a is introduced to modify the nonlinear stiffness when numerically solving the undamped and unforced Duffing system ($m_{\text{eff}}\ddot{x} + k_1 x + a k_3 x^3 = 0$) using dimensions and parameters corresponding to a 1MHz AMS 035 polysilicon cc-beam resonator (dimensions given in the first row of table 4.2). The maximum power frequencies (namely the resonance frequencies) for each oscillation amplitude are represented in figure 5-2a). Those frequencies are compared and mainly agree with the analytically obtained ones from equation (2.40). Numerical simulations reported in figure 5-2a) show that the influence of the nonlinear stiffness on the resonance frequency is only important for oscillations whose values are significant fractions of the gap parameter. However, in practice, the oscillation amplitude is limited by more critical effects like the pull-in effect. With this results, we can forecast that for the usual small oscillation amplitudes the

nonlinear stiffness will have a negligible effect on the resonance frequency.

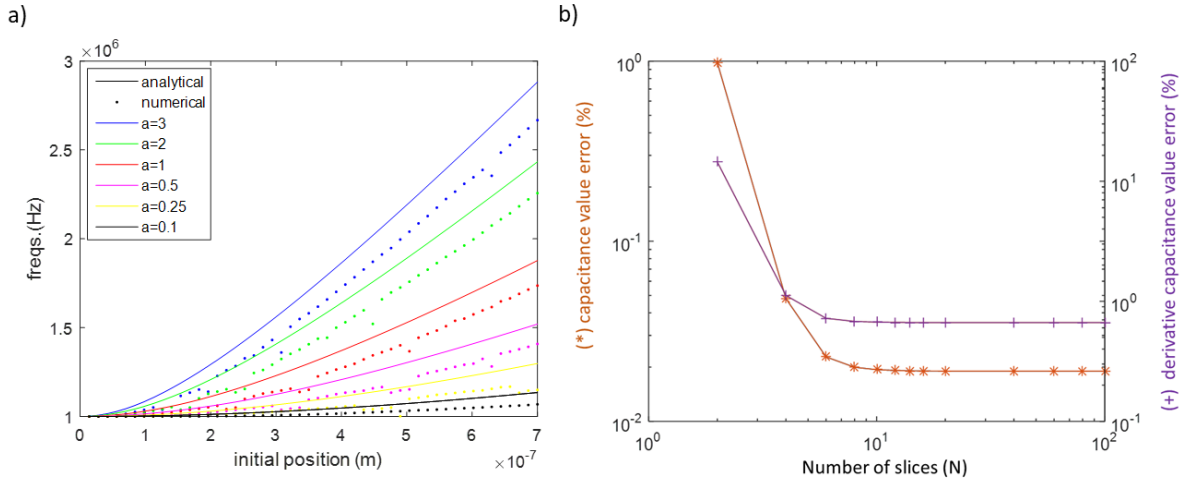

Figure 5-2: a) Numerically and analytically obtained resonance frequency for each oscillation amplitude value, and for different values of a constant (a) which modifies the nonlinear stiffness. b) Average error between FEM simulations and the proposed model (based on FMD) for the values of capacitance (left) and its x-derivative (right) as a function of the number (N) of slices. In both figures the cc-beam resonator dimensions are the same and given in the first row of table 4.2.

5.2 Model based on finite difference method

Given the need of simplifying the numerical process to obtain the electromechanical system dynamical response without loss of accuracy, a method based on finite differences is applied, and the system equations are adapted, including the nonlinear contributions. As in [122] the finite difference method is applied to calculate the capacitance and the electrostatic force acting on the beam resonator. The total capacitance between the beam and each electrode is calculated by slicing the beam along its length (y direction) and by considering each one of the N slices as a parallel plane capacitor with a displacement given by the elastic profile curve, approximated by the equation of the uniformly loaded cc-beam (equation (5.3)). This conception, in which each slice has a length of $\Delta y = \dfrac{l}{N}$ is depicted in figure 5-1b) for two different number of slices; the total capacitance is obtained as:

$$C = \epsilon_0 t_h \Delta y \sum_{n=1}^{N} \frac{1}{(s - xP_n)} + Cc \tag{5.8}$$

with P_n being the normalized displacement of each slice (from equation (5.3), the displacement of the n-th slice is given by $\omega_q(x, \Delta y \cdot n) = x \cdot P_n$), and the C_c term is an offset value of the capacitance which does not depend on the beam deformation . This C_c parameter has no influence on the electrostatic force because it does not appear in the x derivative function of the capacitance position, which is found to be

$$\frac{\partial C}{\partial x} = \epsilon_0 t_h \Delta y \sum_{n=1}^{N} \frac{P_n}{(s - xP_n)^2} \tag{5.9}$$

The finite difference method accuracy is good enough as deduced from the results in figure 5-2b). In addition, the accuracy reaches a value close to its maximum for a relatively low number of slices ($N \sim 10$). Taking a higher N value raises the computational cost without a significant accuracy benefit. The system dynamic equation (5.7) can be now adapted to the finite difference method approach by reformulating the electrostatic forcing term:

$$\begin{aligned} m_{\text{eff}}\ddot{x} + \gamma\dot{x} &= -\left(k_{1\sigma}x + k_{3\sigma}x^3\right) \\ + \quad \frac{\epsilon_0 l t_h k_{\text{FF}}}{2N} &\sum_{n=1}^{N} \left(\frac{(V_{AC}cos(\omega t) - V_{DC})^2}{(s - xP_n)^2} - \frac{V_{DC}^2}{(s + xP_n)^2} \right) P_n \end{aligned} \tag{5.10}$$

and in the same way as in section 4.2.1, by developing the static forcing term in power series, and regrouping in powers of x

$$\begin{aligned} & m_{\text{eff}}\ddot{x} + \gamma\dot{x}\left(k_{1\sigma} - V_{DC}^2 \frac{2k_{\text{FF}}\epsilon_0 t_h l}{N s^3} \sum_{n=1}^{N} P_n^2\right) x + \left(k_{3\sigma} - V_{DC}^2 \frac{4k_{\text{FF}}\epsilon_0 t_h l}{N s^5} \sum_{n=1}^{N} P_n^4\right) x^3 \\ = \quad & \frac{\epsilon_0 l t_h k_{\text{FF}}}{2N} \sum_{n=1}^{N} \left(\frac{(V_{AC}cos(\omega t))^2 - 2V_{AC}V_{DC}cos(\omega t)}{(s - xP_n)^2} \right) P_n \end{aligned} \tag{5.11}$$

In practice, the higher-order terms of the power series development can be neglected. The motional capacitive current generated in each beam-electrode interface is expressed as

$$i_c = V_{DC}\frac{\partial C(t)}{\partial t} = -\frac{V_{DC}\epsilon_0 t_h l k_{\text{FF}}}{N} \sum_{n=1}^{N} \frac{P_n}{(s + xP_n)^2}\dot{x} \tag{5.12}$$

5.3 Analysis of model accuracy and parameter fitting

The accuracy of the nonlinear model based on the finite difference method is proved in this section from FEM simulations and experimental measurements. In addition, the model is applied to obtain an accurate analytical expression for the pull-in voltage in electrostatically actuated cc-beam resonators.

5.3.1 Pull-in analysis

Neglecting fringing field effect and residual fabrication stress and considering in this case a one-electrode system, the pull-in voltage is derived from the static terms in equation

$$m_{\text{eff}}\ddot{x} + \gamma\dot{x} = -\left(k_1 x + k_3 x^3\right) + \frac{\epsilon_0 t_h l}{2N}\sum_{n=1}^{N}\frac{\left(V_{AC}cos\left(\omega t\right) - V_{DC}\right)^2}{\left(s - xP_n\right)^2}P_n \tag{5.13}$$

when the mechanical term and electrostatic term take the same value,

$$V_{pi} = \sqrt{\frac{2\left(k_1 x_r + k_3 x_r^3\right)}{\epsilon_0 t_h \dfrac{l}{N}\displaystyle\sum_{n=1}^{N}\frac{P_n}{\left(s - P_n x_r\right)^2}}} \tag{5.14}$$

with x_r being the static equilibrium point whose equilibrium become instable i.e. where the pull in effect arises. Although equation (5.14) depends on the number of slices considered, the accuracy does not improve for $N > 10$ as shown in figure 5-3a). For the resonator parameters indicated in the first row of table 4.2 (1MHz polysilicon resonator of AMS 035), pull-in is analytically obtained for a voltage of 34.78 V corresponding to a nominal displacement of 500.5 nm. FEM simulations with COMSOL have been performed to validate the model. The simulator provides, for each voltage, the equilibrium position values (corresponding to the deformation displacement of the central point of the beam) that can be stable, unstable or non-existent. The top of the curve corresponds to the boundary bias voltage between the stable and unstable solutions, and represents the pull-in position and bias voltage. In this case, the pull-in (depicted in figure 5-3b)) is obtained with COMSOL for a voltage of 35.69 V and a nominal displacement of 492 nm. Thus, the model error is found to be bounded to 2.7%, corroborating the validity of the proposed finite difference method, and providing a breakthrough in terms of accuracy over the parallel plate approximation.

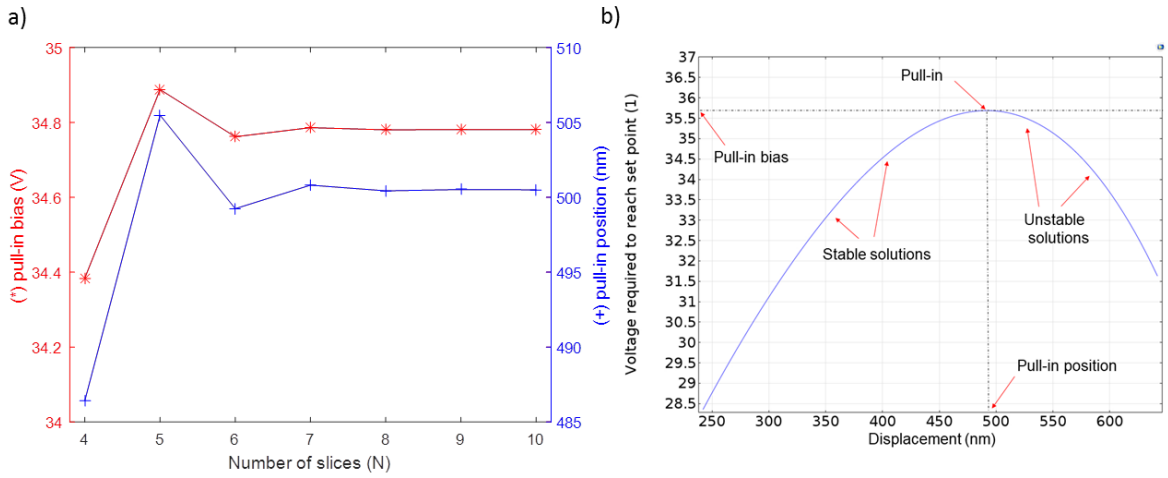

Figure 5-3: Pull-in calculation using a) the analytical model as a function of the number (N) of slices, and b) using FEM analysis with COMSOL. In both figures the cc-beam resonator dimensions are provided in the first row of table 4.2.

5.3.2 Fringing field effect

An accurate beam-electrode capacitance estimation requires considering the fringing field effect, especially in narrow beam resonators, where this phenomenon is accentuated. Several models for this effect have been published (e.g. [119], [123] and [124]). Amongst all the equations in literature for the fringing field effect, the function with best fitting with our FEM simulations and experimental data is equation (5.15), an expression obtained from a semi-empirical formulation [114] that depends only on geometric parameters and on a dimensionless fringing field factor (α_{FF}):

$$k_{\mathrm{FF}} = \left[1 + \alpha_{\mathrm{FF}} \left(\frac{s}{t_h}\right) \left(\frac{w}{s}\right)^{0.222}\right] \tag{5.15}$$

Extensive 3D-FEM simulations were carried out for various cc-beam dimensions and aspect ratios to prove the accuracy of equation (5.15) and to determine the fringing field factor (α_{FF}). The computed capacitance values between the electrode and the non-deformed beam were compared to the theoretical capacitance value. As expected, the FEM computed capacitance value increases exponentially due to the fringing field as the electrostatic coupling volume increases until a maximum saturation value. Such capacitance value includes the overall fringing field contribution and can be used to determine the value of the dimensionless parameter α_{FF} in the fringing field analytical expression (5.15). Table 5.1 summarizes

Table 5.1: Beam-electrode static capacitance and α_{FF} parameter obtained from COMSOL, considering two 1 MHz designed cc-beams with technologies described in table 4.2.

Technol.	FEM C_0 (fF)	FEM dC/dx (nF/m) (average)	α_{FF}
AMS 035 μm POLYSILICON	0.578	0.207	0.329
UMC 018 μm METAL	0.674	0.414	0.249

the FEM simulations results considering two cc-beam dimensions according to two commercial CMOS technologies. The fringing field constant is obtained from the derivative of the capacitance with respect the x parameter to avoid the undesired contribution of offset parasitic capacitances, which are constant and independent on the position (and in consequence have no effect on the driving force). Values between 0.25-0.35 have been revealed as good approximation for the fringing field parameter.

5.3.3 Residual fabrication stress

The residual fabrication stress, present commonly in many MEMS structures, may induce a variation of its resonance frequency. This can be attributed to a beam stiffness change, assuming that its mass and volume remain constant. Cc-beam structural mechanics FEM simulations have been performed to find an analytical expression of the residual stress influence on the beam linear and nonlinear stiffness coefficients. As expected, a residual stress value increase results in a stiffness linear term increase according to the expressions found in the literature as in [120],

$$k_{1\sigma} = k_1 \left(1 + \frac{\sigma_{\mathrm{eff}} l^2}{\eta E w^2} \right) \tag{5.16}$$

where σ_{eff} is the residual stress value and η is a constant coefficient depending on the different vibration modes profile shape (i.e. independent on either the dimensional parameters or the fabrication technology [125]). For the fundamental mode of a cc-beam, a value $\eta = 3.39$ has been found and corroborated with FEM simulations. On the other hand, the cubic nonlinear stiffness term value remains practically unchanged by the residual stress (table 5.2), corroborating the results also found in [60] and [126]. Therefore, the approximation $k_{3\sigma} \sim k_3$ seems appropriate even for large stress factor variations. These considerations are consistent with equation (2.17), where the axial force only affects the linear stiffness.

Table 5.2: Cc-beam linear and nonlinear stiffness values obtained from FEM simulations for various dimensions and residual stress values, with and without the Poisson effect.

	$k_1\,(Nm^{-1})$ / $k_3\,(Nm^{-3})$		
	AMS 035		UMC 018
Layer	Metal	Poly Si	Metal
$l\,(\mu m)$	18	54.6	13.8
$t_h\,(nm)$	850	282	580
$w\,(nm)$	600	350	280
(no Poisson effect)			
$\sigma_{\text{eff}} = 0$MPa	$65.27/1.17 \cdot 10^{14}$	$0.194/8.08 \cdot 10^{11}$	$10.11/7.33 \cdot 10^{13}$
(with Poisson effect)			
$\sigma_{\text{eff}} = 0$MPa	$65.12/1.15 \cdot 10^{14}$	$0.194/8.06 \cdot 10^{11}$	$10.11/7.25 \cdot 10^{13}$
$\sigma_{\text{eff}} = 10$MPa	$66.48/1.15 \cdot 10^{14}$	$0.278/8.06 \cdot 10^{11}$	$10.67/7.25 \cdot 10^{13}$
$\sigma_{\text{eff}} = 50$MPa	$71.9/1.15 \cdot 10^{14}$	$0.615/8.05 \cdot 10^{11}$	$12.93/7.24 \cdot 10^{13}$
$\sigma_{\text{eff}} = 100$MPa	$78.66/1.15 \cdot 10^{14}$	$1.026/8.05 \cdot 10^{11}$	$15.72/7.23 \cdot 10^{13}$
$\sigma_{\text{eff}} = 500$MPa	$132.1/1.13 \cdot 10^{14}$	$4.166/8.03 \cdot 10^{11}$	$37.58/7.18 \cdot 10^{13}$
$\sigma_{\text{eff}} = 1$GPa	$197.64/1.12 \cdot 10^{14}$	$7.973/8.01 \cdot 10^{11}$	$64.09/7.14 \cdot 10^{13}$
$\sigma_{\text{eff}} = 5$GPa	$696.6/1.04 \cdot 10^{14}$	$3.768/7.95 \cdot 10^{11}$	$265.68/6.92 \cdot 10^{13}$

5.3.4 Poisson effect

The Poisson ratio effect on the cc-beam mechanics has been also analyzed from FEM simulations. A variation of only 0.2% and 1% in the values of the linear and cubic stiffness coefficients respectively were obtained (see table 5.2, where, as an example, the case corresponding to $\sigma_{\text{eff}} = 0$ is reported with and without considering the Poisson effect). Therefore, to simplify the analytical expressions derived, the Poisson contribution has not been considered in the nonlinear model.

5.3.5 Analytical and experimental frequency response

The bias voltage applied symmetrically to the structure modifies the effective beam stiffness. Such spring softening effect has been used in several works to tune the system resonance frequency (e.g. [21], [26] and[18]). In general, the bias voltage could tune either the linear and nonlinear mechanical stiffness terms in equation (5.10). From the Jacobi frequency equation (2.40) provided in section 2.2.2 and in [56], a general equation has been found

including the fringing field and the residual stress parameter.

$$f_j = \frac{\sqrt{\frac{1}{m_{\text{eff}}}\left(\left(k_{1\sigma} + X^2 k_3\right) - \left(\frac{2\epsilon_0\, t_h\, l\, k_{\text{FF}}}{s^3 N}\sum_{n=1}^{N} P_n^2 + X^2\frac{4\epsilon_0\, t_h\, l\, k_{\text{FF}}}{s^5 N}\sum_{n=1}^{N} P_n^4\right) V_{DC}^2\right)}}{4K\left(\frac{bX^2}{2\left(a+bX^2\right)}\right)} \tag{5.17}$$

where $a = \frac{1}{m_{\text{eff}}}\left(k_{1\sigma} - V_{DC}^2\frac{2k_{\text{FF}}\epsilon_0 t_h l}{N s^3}\sum_{n=1}^{N} P_n^2\right)$, $b = \frac{1}{m_{\text{eff}}}\left(k_3 - V_{DC}^2\frac{4k_{\text{FF}}\epsilon_0 t_h l}{N s^5}\sum_{n=1}^{N} P_n^4\right)$ and X represents a system amplitude response characteristic value derived from equation (2.39) making the analytical expression to agree with the amplitude dependent peak resonant frequency in section 2.2.2 and [127]. Experimental measurements on fabricated CMOS cc-beam resonators (figure 5-4) were performed to obtain the resonance frequency value as a function of the bias voltage (V_{DC}) for various electrostatic actuation forces (V_{AC}). Figure 5-4b) results show that the natural frequency (denoted by $f_{0\sigma_{\text{eff}}}$, affected by the residual stress and corresponding to the case $V_{DC} = 0$), and the resonance frequencies of the biased cc-beam do not present a significant variation for various values of excitation amplitude, meaning that X^2 term in equation (5.17) can be neglected. Indeed, oscillations of small amplitude around the non-deformed position present a frequency response whose resonance frequency can be approximated to:

$$f_r = \underbrace{\frac{1}{2\pi}\sqrt{\frac{k_{1\sigma}}{m_{\text{eff}}}}}_{f_{0\sigma_{\text{eff}}}}\sqrt{1 - \frac{2V_{DC}^2\epsilon_0 t_h l k_{\text{FF}}}{s^3 N k_{1\sigma}}\sum_{n=1}^{N} P_n^2} \tag{5.18}$$

Specifically the cc-beam resonator used for experimental measurements depicted in figure 5-4 corresponds with a C1 resonator of the Run 2015 set (see chapter 6 for details) with dimensions specified in the first column of table 6.1 and in the first column of table 6.2. The analytical curve is obtained from equation (5.18). The increase in the measured natural frequency (to 2.2 MHz) with respect to the designed one (0.75 MHz) is found to be due to the residual stress. Using equations (5.16) and (5.18) the residual stress and the fringing field parameter for this device were found to be respectively 224 MPa and ~ 0.2.

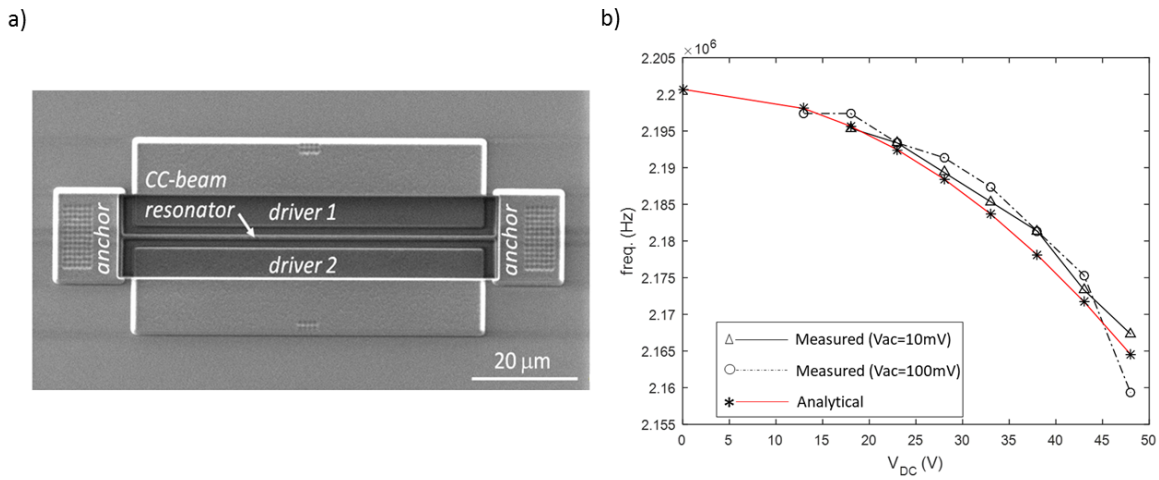

Figure 5-4: a) SEM image of a fabricated CMOS-MEMS cc-beam resonator. b) Experimental dependence of the resonance frequency with the applied bias voltage for a designed metal 0.75-MHz cc-beam resonator.

5.4 Conditions for bistability

The model has been implemented in Verilog-A for electromechanical simulations using Spectre within the CADENCE IC design framework (appendix B). The implemented Verilog-A nonlinear model can be used to determine a DC sweep and operating point, transient, small signal (AC) and large signal (PSS), among others, and simulations of electrical and non-electrical variables like resonator position or velocity. As an example, results in figure B-2 show the DC bias range required to generate a double-well potential distribution ($V_{pi0} < V_{DC} < V_{piw}$). The fringing field effect is clearly remarkable; it can be seen that considering this effect is a must for a successful design. The DC biasing conditions to enable a double-well potential distribution set a minimum ratio between the gap (s) and beam width (w) as reported in chapter 4. In this section, such design procedure is adapted to the finite difference method based on equation (5.10), and considering the fringing field and fabrication stress.

In order to obtain a negative linear effective stiffness and a positive nonlinear effective stiffness, the following inequalities for the DC biasing voltage are obtained

$$\sqrt{\frac{k_{1\sigma} N s^3}{2\epsilon_0 t_h l k_{\mathrm{FF}} \sum_{n=1}^{N} P_n^2}} < V_{DC} < \sqrt{\frac{k_3 N s^5}{4\epsilon_0 t_h l k_{\mathrm{FF}} \sum_{n=1}^{N} P_n^4}} \tag{5.19}$$

Given the k_1 and k_3 definitions (equations (3.9) (3.10)), the cc-beam-electrode gap distance condition in terms of the beam width is obtained from last inequality (5.19):

$$s > w \sqrt{2\frac{16}{12.272}\frac{\sum_{n=1}^{N} P_n^4}{\sum_{n=1}^{N} P_n^2}\left(1+\frac{\sigma_{\text{eff}} l^2}{\eta E_T w^2}\right)} \tag{5.20}$$

This updated equation considers both an accurate deflection profile of the beam and the residual stress factor in contrast to previous works ([26] and [38], for instance). Conceiving the model as a 1-DOF system, the potential function $U(x, V_{DC})$ is expressed as the integral along x of the static terms in equation (5.10), having included the fringing field and residual stress factors:

$$U(x, V_{DC}) = \frac{1}{2}k_{1\sigma}x^2 + \frac{1}{4}k_3 x^4 - V_{DC}^2 \frac{\epsilon_0 t_h l k_{\text{FF}}}{2N}\sum_{n=1}^{N}\left(\frac{1}{(s-xP_n)}+\frac{1}{(s+xP_n)}\right) \tag{5.21}$$

From the potential function, specifically by solving the system ($\frac{\partial U(x, V_{DC})}{\partial x} = 0$, $\frac{\partial^2 U(x, V_{DC})}{\partial x^2} = 0$) the singular points and their stability boundaries can be obtained. From these equations, the nontrivial singular points exist only if the geometric condition (5.20) is verified. When this condition is attained, by increasing the bias voltage, the system is made to undergo a supercritical Pitchfork bifurcation, which will provide two stable nontrivial points between bias boundaries named V_{pi0} and V_{piw}. Such singular points represent the corresponding position and bias voltage boundary values for which a two-well potential distribution takes place. Adapting the procedure explained in chapter 4 to the finite difference method addressed in this chapter and including both fringing field and residual stress, the analytical expressions for the lower bias boundary value (equation (5.22)) and the required beam length (equation (5.23)) for the design resonance frequency are obtained.

$$V_{pi0} = \sqrt{\frac{k_{1\sigma} N s^3}{2\epsilon_0 l t_h\, k_{\text{FF}} \sum_{n=1}^{N} P_n^2}} \tag{5.22}$$

$$l = \sqrt{\frac{\sigma_{\text{eff}} k_n^4 + \sqrt{\sigma_{\text{eff}}^2 k_n^8 + 12 E w^2 k_n^4 f_{0\sigma_{\text{eff}}}^2 \pi^2 \eta^2 \rho}}{6 f_{0\sigma_{\text{eff}}}^2 \pi^2 \eta \rho}} \tag{5.23}$$

Figure 5-5 shows the cc-beam design rule to enable the existence of two-well potential distribution for various slices numbers and three residual stress values. In the case of no stress, a value $s/w = 1.39$ is found to be lower than the oner reported for the parallel plate approximation of the beam-electrode system (s/w=1.615) as reported in chapter 4 and [38]. In a recent work ([50]) a slightly higher value of $s/w = 1.43$ is obtained considering an approximated beam deflection based on its resonance mode shape in contrast to this thesis where the static deflection function is considered, being more appropriate for the static analysis.

Like in previous equations derived in this thesis, the value from equation (5.20) depends on the number of slices considered (N). In this case for a reasonable low value of $N > 4$ the design condition factor converges to a stable value, as shown in figure 5-5. In contrast to the results obtained in chapter 4, here the residual stress effect sets the design condition in equation (5.20) to depend on the beam dimensions. In addition, the voltage boundary values for bistability (V_{pi0} and V_{piw}) grow no longer linear with the cc-beam resonance frequency. Table 5.3 summarizes the design and biasing conditions for bistability provided by the model for a designed and fabricated 1-MHz metal cc-beam resonator corresponding to a C4 resonator of the Run 2015 set (used in experimental measurements which will be widely explained in chapter 6, and whose dimensions are exposed in table 6.2) under various assumptions, and compares those results with the ones given by the parallel plate approximation (considering in this case a uniformly distributed force). Specifically, the used resonator for the experimental measurements related in table 5.3 is C4(16)-k15[1] under a temperature of 110°C. The reported results, which include experimental measurements, clearly indicate again the need of considering both fringing field effects and residual stress for a successful cc-beam design.

[1]This nomenclature for specifying the resonator, chip and generation of fabricated sets is explained in appendix C.

Table 5.3: Comparative of DC biasing margins to achieve 2WP, the required gap value ($s_{\min}$ given by equation (5.20)) and the natural resonance frequency, considering the dimensions of the C4 design in table 6.2 with and without residual fabrication stress. The fringing field and the total stress parameters were experimentally found to be 0.355 and 41 MPa respectively.

Metal C4	Parallel plate	Finite difference model			Experimental
		$\alpha_{\text{FF}} = 0$	$\alpha_{\text{FF}} = 0.335$	$\alpha_{\text{FF}} = 0.335$	$\alpha_{\text{FF}} = 0.335$
		$\sigma_L = 0$ Pa	$\sigma_L = 0$ Pa	$\sigma_L = 41$ MPa	$\sigma_L = 41$ MPa
V_{pi0} (V)	163.031	180.843	140.532	202.39	194
V_{pi0} (V)	221.58	269.52	209.44	237.31	–
$s_{\min}$ (μm)	0.969	0.832	0.832	1.198	–
f_0 (MHz)	1	1	1	1.421	1.42

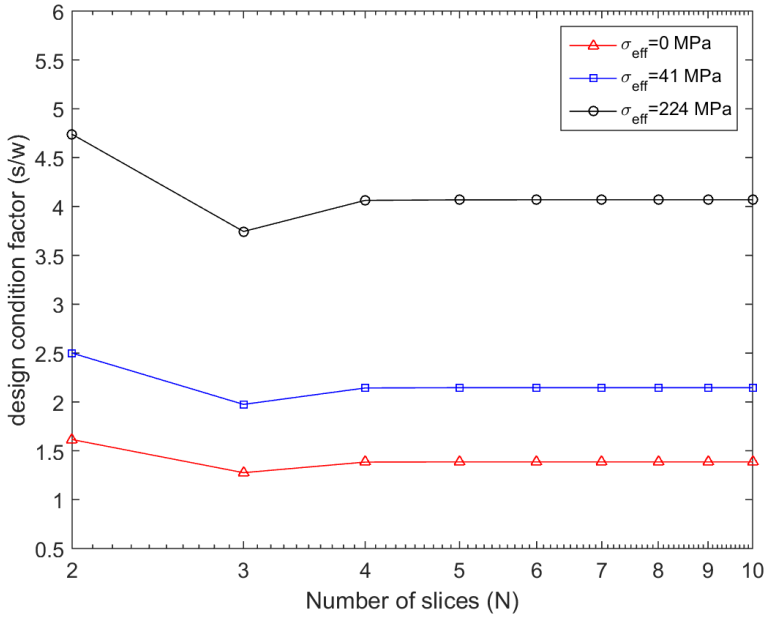

Figure 5-5: Minimum design condition factor s/w ratio enabling two-potential distribution as a function of the number of slices (N) for three stress parameter values. The values corresponding to the nonzero stress parameters (whose stationary values were found to be respectively ~ 4.07 and ~ 2.15) are calculated for the C1 design in table 6.2. In the case of zero stress the design condition value (1.386) is independent on the dimensions.

Experimental measurements, reported in table 5.3 (and, afterwards, in chapter 6), on fabricated devices revealed positive residual stress parameter values indicating the presence of tensile load, which induces an increase of the resonance frequency. In this case, to keep a desired value of the resonance frequency, larger beam lengths are required. On the other hand, the tensile residual stress involves the need of increasing the gap (s) to attain the

geometric condition for the two-well potential distribution. High values of the gap parameter imply high values of the required bias voltages to reach the bistability. However, one of the design requirements is keeping low values of the bias voltage. The design natural frequency of the beam can be optimized to provide the minimum values for the needed bias voltage. Knowing that the natural frequency of the beam for small amplitude oscillations can be approximated to the square root of the quotient between the total effective linear stiffness and the effective mass (equation (5.18)) [56], figure 5-6a) depicts the lowest bias boundary values obtained for the minimum s value attaining the geometric condition (equation (5.20)) for different values of σ_{eff}, as a function of the desired natural frequency. Notice that in the case of $\sigma_{\text{eff}} \neq 0$, for each specific natural frequency (which implies a value of length (l) accordingly to equation (5.23)) a required minimum gap value $s_{\min}$ is obtained, and this minimum gap value is used to obtain the 2WP lower bias boundary value for the minimum gap attaining the geometric condition ($V_{pi0}\,(s_{\min})$). Each curve shows an optimal natural frequency in terms of the needed bias voltage. The optimal design frequency, which minimizes the needed bias voltage to achieve a two-well potential distribution, set the beam length according to equation (5.23).

Given the common experimental values for the residual stress (see section 6.2.4), even for the optimal design frequency, the biasing corresponding to the minimum gap attaining the geometric condition is quite high. Moreover, it is important to take into account that the minimum value of gap attaining the geometric condition corresponds to the situation in which the double-well potential distribution arises, and for this value of gap V_{pi0} and V_{piw} have very close values to each other. The margin between the lower and the upper bias boundary values that provide the double-well potential distribution grows with the gap (s) (as shown in figure 5-6b)), and specifically a margin of 10% between V_{pi0} and V_{piw} is desired. The curves shown in figures 5-6a) and b) are calculated for the parameter values corresponding to the Metal4 layer of the AMS 035 technology detailed in table 4.2 ($w = 600$nm, $t_h = 850$nm); in the specific case of figure 5-6b), the bias boundary values for bistability are calculated with the obtained optimal value of frequency (and, consequently of l, which results to be, in this case $l = 71\mu$m) for a given value of σ_{eff} ($\sigma_{\text{eff}} = 0.1623$ GPa is the residual stress average value of the Run 2015 set, as it will be pointed in chapter 6).

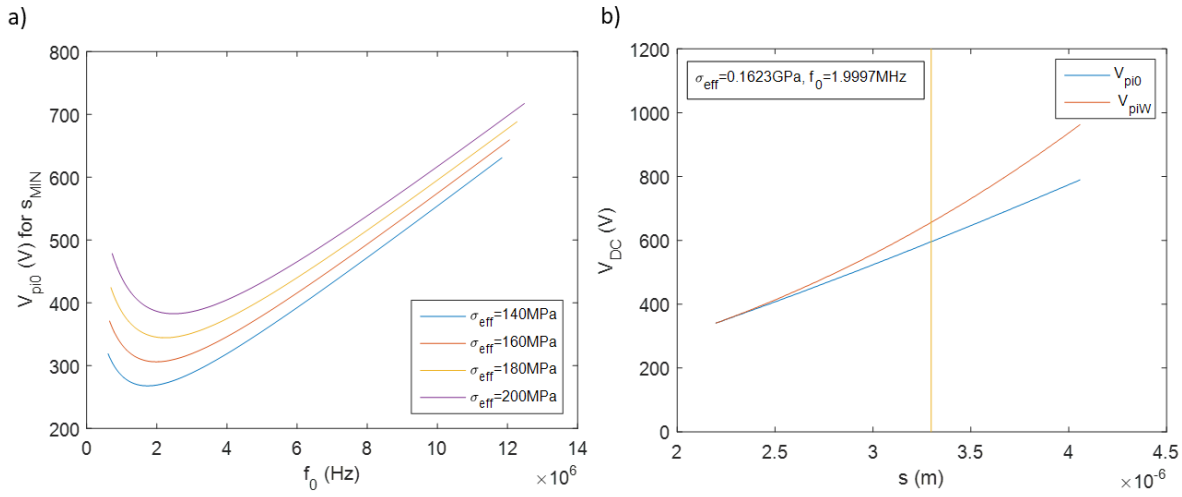

Figure 5-6: a) Lower bias boundary values to achieve bistability for the minimum gap attaining the geometric condition (5.20) for different values of the residual stress, as function of the design natural frequency. b)Plot of the bias boundary values which provide two-well potential distribution as a function of the gap parameter (s), for a given value of residual stress. The vertical line points the gap value for which a margin of 10% between the V_{pi0} and V_{piw} is attained ($s = 3.3$ μm, in this case).

Figure 5-7 summarizes the effect of the residual stress on different design and operating parameters, within the allowance of the condition of bistability. A growing residual stress value implies the need of a bigger gap, an increase of the resonance frequency and of the absolute values of the bias boundary values for bistability as well as a reduction of the margin between them. The numerical calculations of the parameters depicted are obtained from the same dimensions as the ones used in figure 5-6 ($l = 71\mu$m, $w = 600$nm, $t_h = 850$nm), which happens to correspond with the dimension of the C3 resonator of the Run 2017 set (see table 6.6).

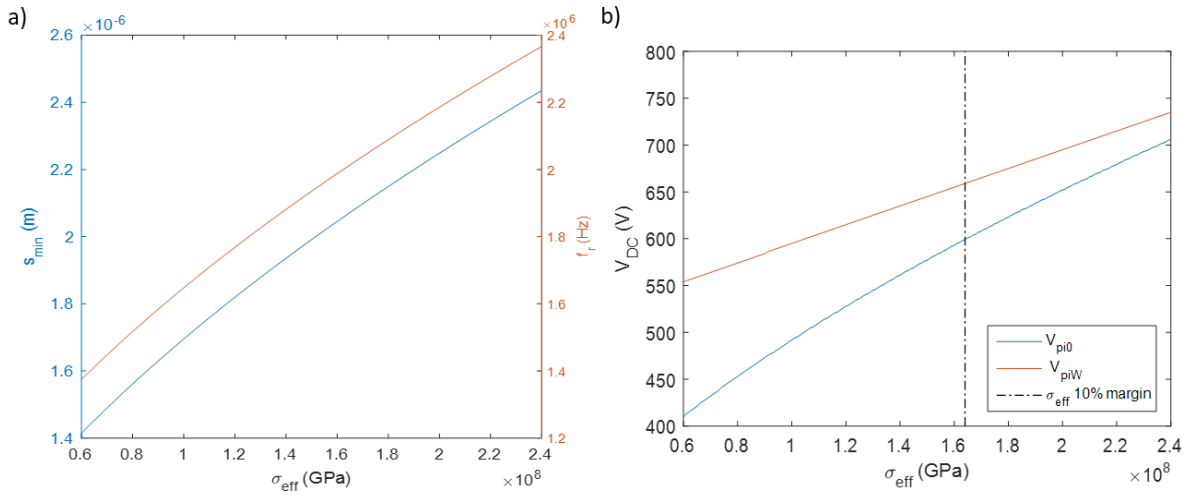

Figure 5-7: a) Variation of the minimum gap attaining the condition for bistability and of the resonance frequency as function of the possible value of the residual stress σ_{eff}. b) Bias boundary values for a constant gap ($s = 3.3$ μm) and different values of the residual stress.

5.5 Thermal effect

To improve the features of the bistable system in terms of the bias voltage requirements (and of geometric design condition), the thermal effect can be used to provoke a variation in the Young modulus ([128] and [129]) as well as a generation of an internal stress according to

$$E_T = E\left(1 + TCE\left(T - T_0\right)\right);\ \sigma_T = -\alpha_T\left(T - T_0\right)E_T \tag{5.24}$$

with T_0 being the initial temperature, TCE the Temperature Coefficient of Young modulus, and α_T the thermal expansion coefficient (that must be determined experimentally). Typically, the thermal expansion coefficient α_T has a positive value, which means that operating the beam under rising temperatures causes a growing of the compressive stress that stands against the tensile residual stress. Thus, the total stress denoted as σ_L is defined as the sum of the residual stress σ_{eff} and the thermal stress σ_T. The new geometric condition that enables 2WP is obtained by considering σ_L and E_T instead of σ_{eff} and E (equation (5.25)). In the same way, a redefinition of the equations of the effective mechanical linear stiffness (equation (5.26)) and of the lower bias boundary value (equation (5.27)) are obtained:

$$\frac{s}{w}\Big|_{\min} = \sqrt{2\frac{16}{12.272}\frac{\sum_{n=1}^{N} P_n^4}{\sum_{n=1}^{N} P_n^2}\left(1+\frac{\sigma_L l^2}{\eta E_T w^2}\right)}, \tag{5.25}$$

$$k_{1\sigma_L} = k_1\left(1+\frac{\sigma_L l^2}{\eta E w^2}\right), \tag{5.26}$$

and

$$V_{pi0} = \sqrt{\frac{k_{1\sigma_L} N s^3}{2\,\epsilon_0\, l\, t_h\, k_{\mathrm{FF}} \sum_{n=1}^{N} P_n^2}} \tag{5.27}$$

Equations (5.25), (5.26) and (5.27) indicate that thermal effect makes the beam less stiff, allowing that smaller gaps fulfill the design condition and, in consequence, lower bias voltages are needed to attain bistability. The effect of the temperature on the measurement of a fabricated resonator (with a given value for the gap parameter (s)) is the reduction of the absolute values of the bias boundaries for bistability (V_{pi0} and V_{piw}), and an enlargement of the V_{piw}/V_{pi0} ratio, as shown in figure 5-8. These effects can be deduced from the facts that a growing $s/s_{\min}$ ratio implies an increase of the V_{piw}/V_{pi0} ratio and that a decrease of the total stress value implies that V_{pi0} will be lower. The calculations of figure 5-8 have been performed using the cc-beam dimensions proper to the C4 resonator of the Run 2015 set (see table 6.2).

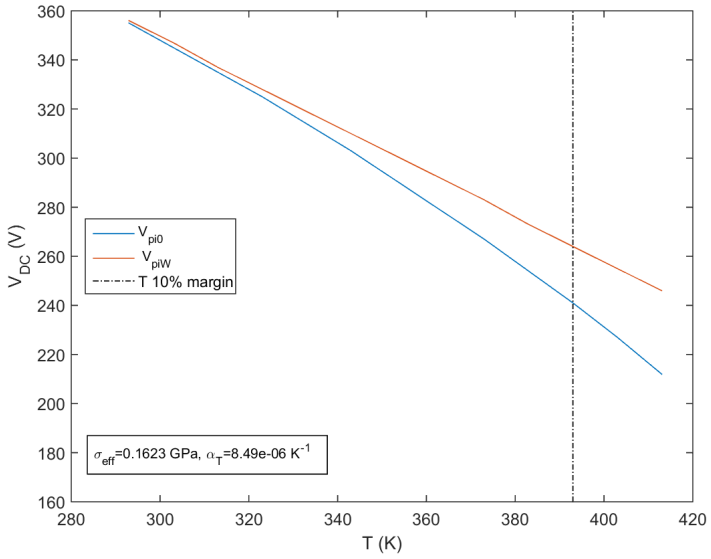

Figure 5-8: Bias boundary values (V_{pi0} and V_{piw}) as a function of the temperature under which the 1MHz metal resonator is subjected, for given values of σ_{eff} and α_T. The vertical line points the gap value for which a margin of 10% between the V_{pi0} and V_{piw} is attained.

5.6 Melnikov method adjustment

The Melnikov function has been adapted to the finite difference equation (5.10) which models the system addressed in this chapter. Following the process described in [26] to obtain a nondimensional version of equation (5.10), having the definitions of the dimensional parameters of equation (5.10), and knowing that within the frame of the current accurate model the resonance frequency value is given by $\omega_0 = \sqrt{\dfrac{k_{1\sigma_L}}{m_{\text{eff}}}}$, the parameters of the nondimensional equation are defined as $\hat{x} = \dfrac{x}{s}$; $\Omega = \dfrac{\omega}{\omega_0}$; $\beta = \dfrac{k_1}{m_{\text{eff}}\omega_0^2} = 1$; $\alpha = \dfrac{k_3 s^2}{m_{\text{eff}}\omega_0^2} = \dfrac{k_3 s^2}{k_{1\sigma_L}} = \dfrac{12.272}{16}\left(\dfrac{s}{w}\right)^2\left(1+\dfrac{\sigma_L l^2}{\eta E w^2}\right)^{-1}$, $\delta = \dfrac{\gamma}{m_{\text{eff}}\omega_0} = \dfrac{\left(\dfrac{m_{\text{eff}}\omega_0}{Q}\right)}{m_{\text{eff}}\omega_0} = \dfrac{1}{Q}$ and $\mu = k_{\text{FF}}\dfrac{\epsilon_0 t_h l}{m_{\text{eff}}\omega_0^2 N s^3}$. Denoting $V = -V_{DC}V_{AC}$, $\phi_1 = \left(-\beta + 2\mu V_{DC}^2\sum_{n=1}^{N} P_n^2\right)$, $\phi_3 = \left(-\alpha + 4\mu V_{DC}^2\sum_{n=1}^{N} P_n^4\right)$, the nondimensional equation of the electromechanical system is approximated to

$$\hat{x}'' + \delta\hat{x}' = \phi_1\hat{x} + \phi_3\hat{x}^3 + V\sin(\Omega\tau)\,\mu\sum_{n=1}^{N}\frac{P_n}{(1-\hat{x}P_n)^2} \tag{5.28}$$

The equation (5.28), can be expressed as the system

$$\begin{aligned}\hat{x}' &= \hat{u} \\ \hat{u}' &= \phi_1\hat{x} + \phi_3\hat{x}^3 + \epsilon\left(\delta\hat{u} + V\mu sin\left(\Omega\tau\right)\sum_{n=1}^{N}\frac{P_n}{\left(1-\hat{x}P_n\right)^2}\right)\end{aligned} \tag{5.29}$$

where ϵ is a smal perturbationl parameter. If $\Gamma_{\pm}^{0}\left(t\right) = \left(\hat{x}^0\left(t\right), \hat{u}^0\left(t\right)\right)$ is considered to be the homoclinic orbit defined in [55] as equation (4.34), accordingly to [55] the Melnikov function given by equation (4.35) can be expressed as:

$$M\left(\tau_0\right) = \int_{-\infty}^{\infty}\hat{u}^0\left(\tau\right)\left(-\delta\hat{u}^0\left(\tau\right) + V\mu\sin\left(\Omega\left(\tau+\tau_0\right)\right)\sum_{n=1}^{N}\frac{P_n}{\left(1+\hat{x}^0\left(\tau\right)P_n\right)^2}\right)d\tau \tag{5.30}$$

This integral can be separated in two terms

$$M\left(\tau_0\right) = \underbrace{\int_{-\infty}^{\infty} -\left(\hat{u}^0\left(\tau\right)\right)^2\delta d\tau}_{I_1} + \underbrace{\int_{-\infty}^{\infty}\hat{u}^0\left(\tau\right)V\mu\sin\left(\Omega\left(\tau+\tau_0\right)\right)\sum_{n=1}^{N}\frac{P_n}{\left(1+\hat{x}^0\left(\tau\right)P_n\right)^2}d\tau}_{I_2} \tag{5.31}$$

and, if $x_e = \sqrt{-\frac{2\phi_1}{\phi_3}}$ is defined as the positive solution of the potential function $U\left(x\right) = 0$ and $K = \phi_1$, the first term I_1 has a solution given by [26]:

$$I_1 = \int_{-\infty}^{\infty} -\left(\hat{u}^0\left(\tau\right)\right)^2\delta d\tau = -\frac{2}{3}\delta\sqrt{K}x_e^2 \tag{5.32}$$

As stated in [26],

$$\int_{-\infty}^{\infty}\hat{u}^0\left(t\right)\frac{\sin\left(\omega\left(t+t_0\right)\right)}{\left(1+\hat{x}^0\left(t\right)\right)^2}dt = x_e\frac{2\pi\frac{\omega}{\sqrt{K}}}{\sqrt{\left(1-x_e^2\right)}}\cos\left(\omega t_0\right)\frac{\sinh\left(\frac{\omega}{\sqrt{K}}\left(-\arccos\left(x_e\right)\right)\right)}{\sinh\left(\frac{\omega}{\sqrt{K}}\pi\right)} \tag{5.33}$$

From this previous result, I_2 can be solved as

$$
\begin{aligned}
I_2 &= \int_{-\infty}^{\infty} \hat{u}^0(\tau) V\mu \sin(\Omega(\tau+\tau_0)) \sum_{n=1}^{N} \frac{P_n}{(1+\hat{x}^0(\tau) P_n)^2} d\tau \\
&= V\mu \sum_{n=1}^{N} \frac{P_n^2 x_e 2\pi \frac{\Omega}{\sqrt{K}}}{\sqrt{(1-(P_n x_e)^2)}} \cos(\Omega\tau_0) \frac{\sinh\left(\frac{\Omega}{\sqrt{K}}(-\arccos(P_n x_e))\right)}{\sinh\left(\frac{\Omega}{\sqrt{K}}\pi\right)}
\end{aligned}
\tag{5.34}
$$

and then, the whole Melnikov function is found to be

$$
\begin{aligned}
&M(\tau_0) = I_1 + I_2 = -\frac{2}{3}\delta\sqrt{K}x_e^2 + \\
&V\mu \sum_{n=1}^{N} \frac{P_n^2 x_e 2\pi \frac{\Omega}{\sqrt{K}}}{\sqrt{(1-(P_n x_e)^2)}} \cos(\Omega\tau_0) \frac{\sinh\left(\frac{\Omega}{\sqrt{K}}(-\arccos(P_n x_e))\right)}{\sinh\left(\frac{\Omega}{\sqrt{K}}\pi\right)}
\end{aligned}
\tag{5.35}
$$

which must be equal to 0 for some τ_0, so the next condition must be attained:

$$
\frac{2}{3}\delta\sqrt{K}x_e^2 \leq V\mu \left| \sum_{n=1}^{N} \left[\frac{P_n^2 x_e 2\pi \frac{\Omega}{\sqrt{K}}}{\sqrt{(1-(P_n x_e)^2)}} \frac{\sinh\left(\frac{\Omega}{\sqrt{K}}(-\arccos(P_n x_e))\right)}{\sinh\left(\frac{\Omega}{\sqrt{K}}\pi\right)} \right] \right| \tag{5.36}
$$

Finally, the Melnikov criterion can be obtained

$$
\left| \sum_{n=1}^{N} \left[\frac{P_n^2 x_e \pi \frac{\Omega}{\sqrt{K}}}{\sqrt{(1-(P_n x_e)^2)}} \frac{\sinh\left(\frac{\Omega}{\sqrt{K}}(-\arccos(P_n x_e))\right)}{\sinh\left(\frac{\Omega}{\sqrt{K}}\pi\right)} \right] \right| - \frac{\delta\sqrt{K}x_e^2}{3V\mu} \geq 0 \tag{5.37}
$$

Taking as variable parameters the frequency and amplitude (expressed in dBm referenced to 50Ω) of the AC excitation and the bias voltage, the Melnikov method shows regions of this parameter space where chaotic motion based on two-well potential distribution may arise. The left hand side of the inequation (5.37) is renamed as "Melnikov value" in figure 5-9,

which for two given values of excitation amplitude represents the results of the Melnikov analysis evaluation for different combinations of bias voltage and driving frequency (the used nondimensional parameters have been obtained from the dimensions corresponding to the C4 resonator of the Run 2015 set, shown in table 6.2, and from the experimental values of σ_L and α_{FF} of the specific resonator C4(17)-k15 under an operating temperature of 120°C). As introduced in chapter 4, references [28] and [29] consider, wihtin the situation of the two-well potential distribution, two critical amplitudes (equations (4.38) and (4.39)) as improvements of the accuracy of the Melnikov method in the case of high and low damping ratios respectively. However, numerical simulations revealed that those critical amplitudes represent an improvement of the Melnikov mehtod accuracy only for great bias voltage closer to the the upper bias boundary value (static pull-in voltage) than to the lower bias boundary value, for the parallel plane approximation used in [28] and [29]. With the finite difference method addressed in this chapter, the Melnikov method provides still a better performance of the chaotic behavior prediction, when comparing all the amplitude prediction values with the numerical results. As an example to illustrate this asseveration, figure 5-10 shows the Poincare positions from the numerical solving of the differential equation (5.10) under constant values of bias voltage and driving frequency, and for different values of excitation amplitude: while the Melnikov method reports a possible chaotic behavior (which can be only transient chaos) for an amplitude greater than -6.2 dBm, the critical amplitudes a_{cr1} and a_{cr2} establish respectively the prediction of the boundary for chaotic behavior in -17.4 dBm and -10.9 dBm.

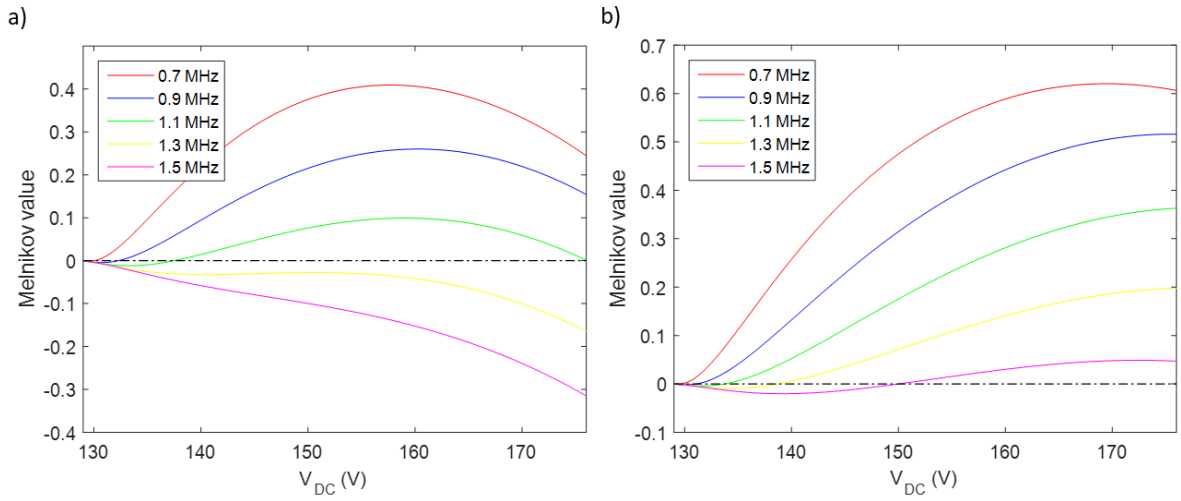

Figure 5-9: Numerical Melnikov values for a) 5 dBm and b) 10 dBm values for the AC excitatation amplitudes. Zero or positive Melnikov values indicate that the Melnikov criterion for homoclinic chaotic behavior is verified.

5.7 Numerical simulations of chaotic motion

Numerical simulations of chaotic time series and Poincare map, as the dynamical response of the complete system described in this chapter, are reported in figure 5-11 and in figure 5-12 using the dimensions corresponding to the C4 resonator of the Run 2015 set (see table 6.2) and the experimental values of σ_L and α_{FF} of the specific resonator C4(17)-k15 under an operating temperature of 120°C. The used values of bias voltage and excitation amplitude and frequency verify the Melnikov criterion for chaotic motion. Previously, the bifurcation diagram plotted in figure 5-10 depicts the numerically obtained Poincare positions (for constant values of bias voltage and excitation frequency) as a function of the AC, to explore the values of excitation amplitude which provide chaotic numerical response. The signal output reported in figure 5-12 is obtained from the expression of the generated capacitive current provided by the model (equation (5.12)), neglecting its parasitic component and multiplying each frequency component by the gain of the transimpedance amplifier at its corresponding frequency. Finally, the Wolf algorithm provides the maximal Lyapunov exponent of the time series depicted in figure 5-11 and represents it in figure 5-13, where its positive and finite value is demonstration of the presence of chaos.

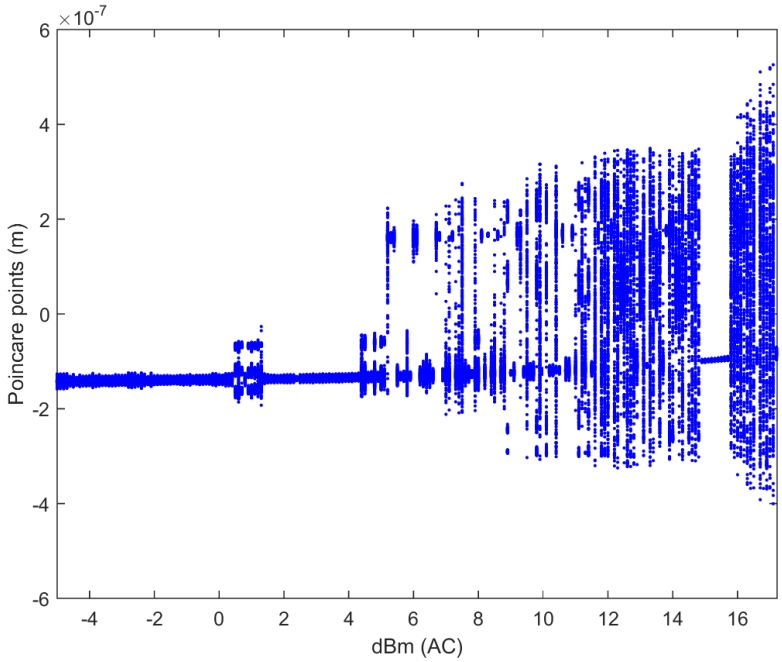

Figure 5-10: Numerical bifurcation diagram based on Poincare points, for a bias voltage of 135 V and a driving frequency of 0.7 MHz.

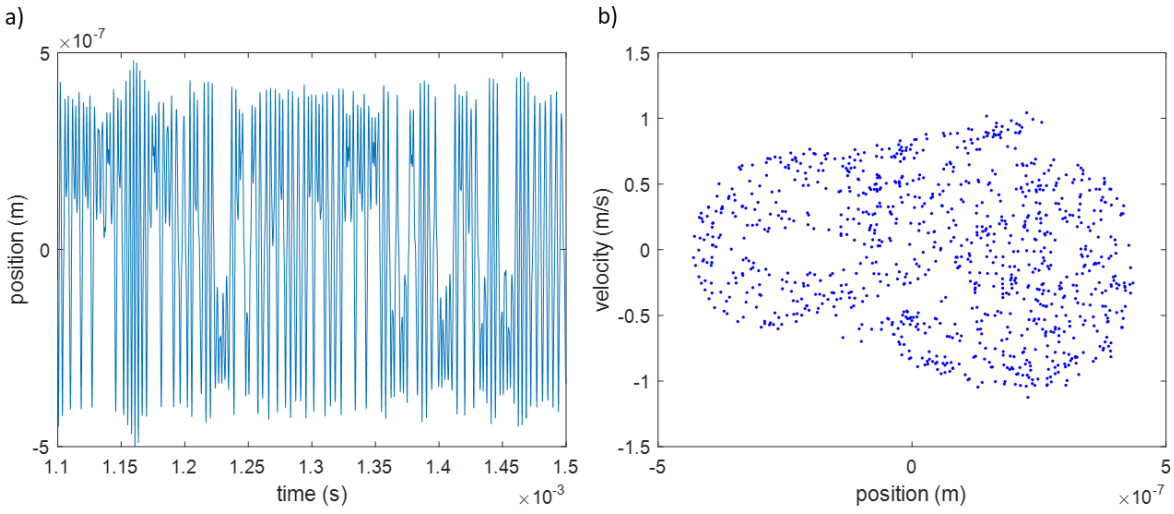

Figure 5-11: Numerically obtained a)time series and b) Poincare map, for a bias voltage of 135 V, 11 dBm of excitation amplitude and a driving frequency of 0.7 MHz.

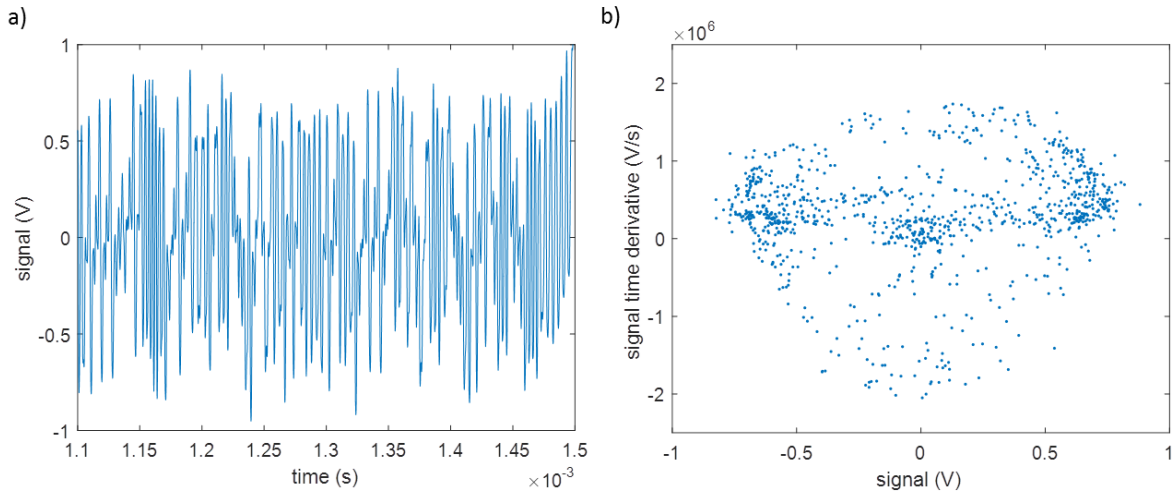

Figure 5-12: Numerical simulations of a) time series and b) Poincare map corresponding to the generated output signal obtained from the amplification of the generated capacitive current through an approximation of the G_{TIA} transimpedance amplifier of the circuit, for a bias voltage of 135 V, 11 dBm of excitation amplitude and a driving frequency of 0.7 MHz.

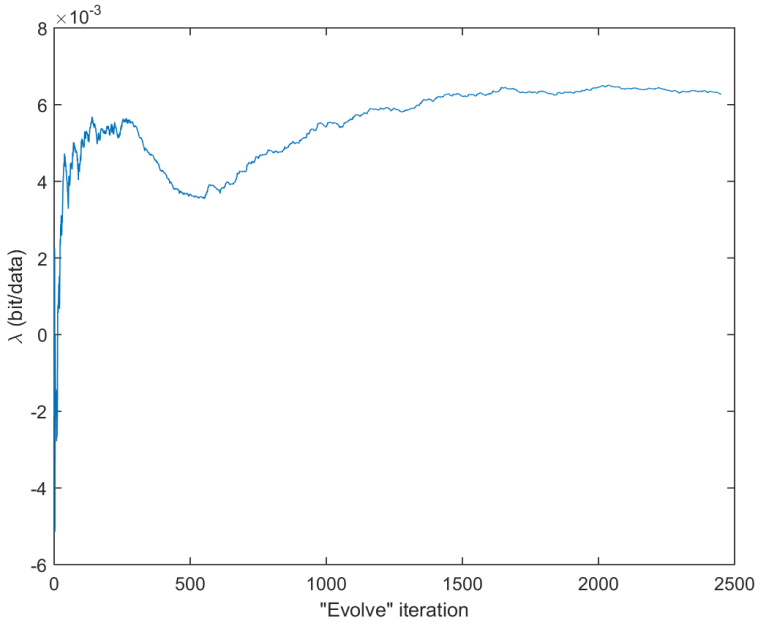

Figure 5-13: Maximal Lyapunov exponent, numerically obtained with Wolf algorithm from chaotic time series depicted in figure 5-11.

5.8 Discussion and conclusions

A compact model for electrostatic cc-beam resonators (easily implementable as a Verilog-A module for system level electrical simulations) has been developed, considering a near-real deflection profile (in the form of a finite difference method) and the second order nonlinear effects (fringing field contribution to the coupling capacitance, residual stress and the thermal effect). To test the accuracy of the model, and to obtain the values of the parameters corresponding to the underlying nonlinear effects, extensive FEM simulations and experimental measurements have been effectuated. The residual stress is found to affect the linear mechanical stiffness while the nonlinear stiffness is practically unaffected by the residual stress; the Poisson effect has no appreciable influence on the stiffness variation caused by the residual stress. The developed model has been used to derive the conditions to achieve bistability (i.e two-well potential distributions): dimensional design rule and the needed bias voltage for bistability are found to depend on the residual stress and on some dimensional parameters; the needed bias voltage for bistability grows no longer linearly with the frequency but for each value of the residual stress there is an optimal value of the frequency. The residual stress implies the need of greater gap to attain the design condition for two-well potential distribution, and a decrease of the ratio between the upper and the lower bias boundary values. In the same way as in the parallel plate approximation, in order to minimize the required bas voltage, the resonators must be designed with the minimum width (w) available by each technology. The thermal effect can be used to compensate the residual stress. In this way smaller gaps fulfill the design condition (s/w) and lower bias voltages are needed. A greater temperature than the one of room conditions, makes the beam less stiff, implies a decrease of the absolute value of the bias boundary values for bistability and provokes an enlargement of the ratio V_{piw}/V_{pi0}.

Chapter 6

Experimental results: bistability and chaos

This chapter presents the experimental measurements and validation of the nonlinear model introduced in chapter 5. The model considers a near real deflection profile for the cc-beam and the second order nonlinear effects, namely the thermal effect, the fabrication residual stress, and the contribution of the fringing field to the coupling capacitance between the beam and the electrodes. Several monolithically integrated cc-beam resonators in the MHz frequency range have been fabricated with the AMS 035 CMOS technology (in two sets of fabrication). These fabricated devices have been used to experimentally demonstrate the bistable operation and, eventually the extensive, robust and nontransient chaotic behavior for the first time in a cc-beam resonator. In this sense, such results provide a breakthrough in the field, with respect to the existing works reported in literature.

6.1 Experimental setup

Several cc-beam resonators have been designed and fabricated in AMS 035 technology. Topology I (explained in section 4.2.1) used in the design allows two basic setups which are schematically depicted in figure 6-1. In both setups the bias voltage V_{MEMS} is applied to the beam in order to enable the generation of the motional capacitive current and to tune the linear and nonlinear stiffness of the beam. In Setup#1, the AC excitation (V_{AC}) is performed in the driving electrode (where a bias V_{D1} voltage is applied to compensate the readout circuit gate voltage $V_{D2} = 2V$ which is applied to the readout electrode).

Given that there is no direct coupling between the electrode where the AC exctiation is applied (D1) and the readout electrode (D2), this setup minimizes the generation of the parasitic feedthrough current (see section 4.2), and the generated capacitive current can be approximated to equation (5.12), with $V_{DC} = V_{\text{MEMS}} - V_{D2}$. On the other hand, in Setup#2, the AC excitation (V_{AC}) is applied to the beam, together with the V_{MEMS} bias voltage by means of a bias tee and the V_{D1} bias voltage is also applied to the upper driver to compensate the gate voltage at the lower driver. In this way, besides the motional component proper to equation (5.12), now the generated capacitive current also has the parasitic component. The total generated capacitive current can be expressed as equation (6.1).

$$i_c = \epsilon_0 t_h \frac{l}{N} k_{FF} \left((V_{DC} + V_{AC}\cos(\omega t)) \sum_{n=1}^{N} \frac{-P_n}{(s + xP_n)^2} \dot{x} - (\omega V_{AC} \sin(\omega t)) \left(\sum_{n=1}^{N} \frac{1}{(s + xP_n)} + C_c \right) \right) \tag{6.1}$$

The first term of equation (6.1) corresponds with the motional component while the second term is the parasitic current caused by the sinusoidal nature of the applied AC voltage.

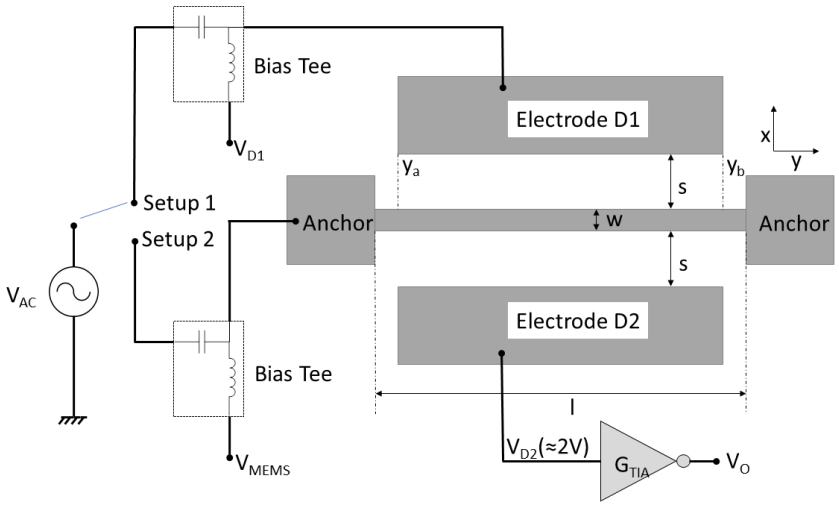

Figure 6-1: Schematic the electrostatically actuated bistable cc-beam showing the two basic setups used in this chapter.

6.1.1 Transimpedance amplifier circuit

The CMOS readout circuit consists in a transimpedance amplifier which detects and converts the capacitive current into a voltage. Figure 6-2 depicts the scheme of the readout CMOS circuitry monolithically integrated with resonator on the fabricated chips. The transimpedance amplifier (TIA) is constituted by three main modules: the front-end preamplifier (UGB module), the voltage amplifier (CA module), and the 50-Ω output buffer (B50) [130].

- UGB, front-end-preamplifier: integrates (through the C_I, parasitic capacitance at the sense node) the capacitive current from the resonator, and the resulting V_{in} voltage is detected by means of its readout preamplifier, which in this case is a unity gain buffer. The parasitic capacitance at the sense node is found to be the sum of the input capacitance of the circuit (C_G), the resonator-substrate capacitance (C_{SB}), the connexion to the circuit capacitance (C_{CB}), and the capacitance of the bias element (C_{bias}). All these capacitances were minimized in order to maximize the sensitivity of the readout. In order to keep the large impedance at the sense node (and, consequently a low input-referred noise) a pseudo resistor (specifically, a PMOS transistor working at the sub-threshold region with an extremely high resistance) is used as the bias. Therefore, with the aim to reduce the parasitic capacitance associated to the bias element (C_{bias}) a resistance R_{bias} was connected between V_{in} and V_{01} (namely the input and the output of the front-end preamplifier).

- CA, voltage amplifier: this amplifier is based on a cascode with cascode-load configuration. Given the high gain of this amplifier, the stage is also self-polarized by means of a PMOS pseudo resistor and AC coupled with the front-end-preamplifier in order to assure the correct biasing at the input node. The intrinsic gain is reduced by using the AC coupling given the capacitance divider produced between it and the input capacitance of the cascode amplifier.

- B50, 50-Ω output buffer: An output buffer stage is added to drive the 50-Ω input impedance of the RF measurement instruments. Is based on two source follower stages. In order to reduce its power consumption the output is AC coupled to an external instrument by means of an external capacitance.

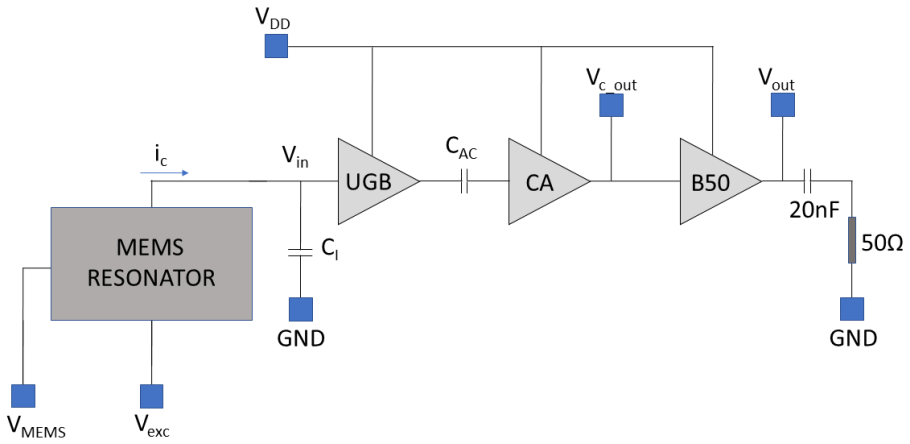

Figure 6-2: Electrical scheme of the CMOS readout circuitry UGBCA50, connected to the MEMS resonator, in the same IC CMOS chip.

The whole circuit is addressed as UGBCA50. For the electrical characterization of the resonators, with a 2-driver configuration corresponding to Topology I (see section 4.2), five input/output pads (called respectively V_{DD}, V_{MEMS}, V_{exc}, V_{out} and GND) are used, and an additional pad has been included to allow the access at the output node of the cascode amplifier ($V_{\mathrm{c\ out}}$). The input pads V_{MEMS} and V_{exc} access respectively to the cc-beam resonator and to the D1 electrode, while the V_{DD} pad corresponds to the supply voltage of the CMOS circuitry and the GND pads are grounded. The V_{out} pad provides the output signal of the readout circuitry. An optical image of the whole area is shown in figure 6-3.

6.1.2 Laboratory measurement setup

Once the fabrication and releasing process is finished, every chip is stuck and bonded to a socked and mounted on a PCB. This PCB is placed into a climatic chamber to set and control the temperature and humidity conditions: the study of the thermal effect implies the test of the system response under different temperatures. Notice that for experimental measurements below 100°C, a relative humidity of 20% is used. Different DC sources (Agilent E3631/3 B and Keithley 2410) provide the bias voltages specified in the electrical scheme depicted in figure 6-2. The AC excitation is supplied by a function generator (AWG 2021) or a network analyzer (Agilent E5062A) which, from the output signal (V_{out}) provides

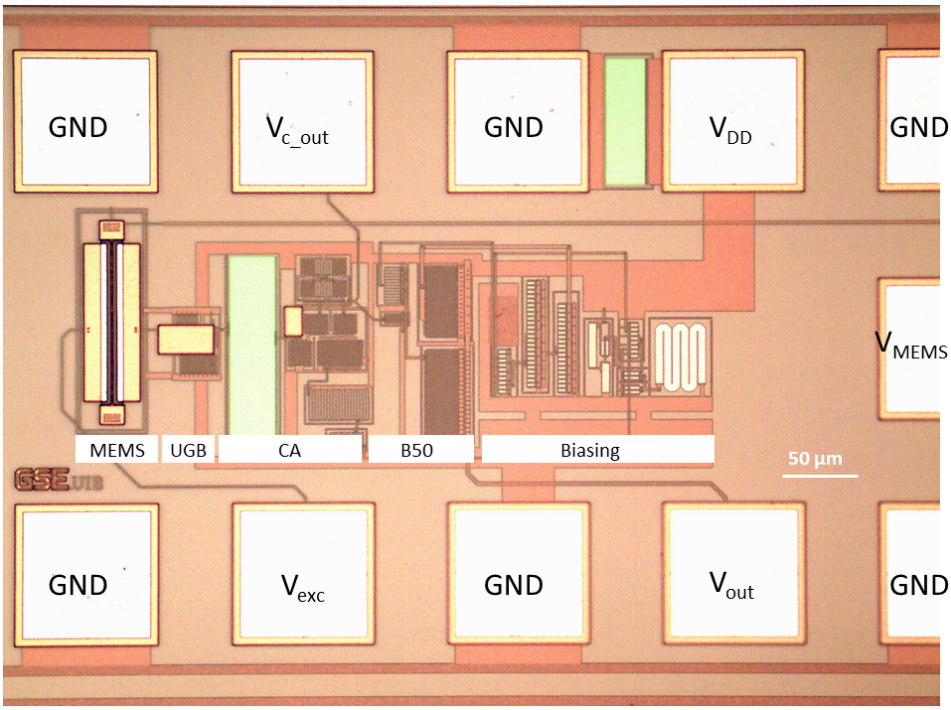

Figure 6-3: Optical image of the CMOS-MEMS design fabricated in AMS 035 technology, with the MEMS area connected to the readout circuitry (UGBCA50).

the S_{21} transmission parameter. The scheme of this configuration is shown in figure 6-4. The output signal V_{out} is also applied to a spectrum analyzer (Agilent E4407B) and/or to an oscilloscope (TDS 640A) to acquire the spectrum or the time series of the signal respectivley. Finally, all the standalone instrumentation and the measurement data is remotely managed by a computer through GPIB or RS-232.

6.2 Experimental validation of the nonlinear model

A symmetrical application of the bias voltage generates a stiffness in the electrical domain that tunes linear and nonlinear stiffness of system, accordingly to [21] and [56], and to chapters 4 and 5. Besides the dependence on the linear stiffness, the resonance frequency of the nonlinear electromechanical oscillator is known to exhibit amplitude dependence on the nonlinear stiffness, thus, for small oscillation amplitudes, the resonance frequency can be approximated to depend only on the linear stiffness either in mechanical or electrostatic domain (equation (6.2)). The thermal terms, (E_T and σ_L) defined in chapter 5, are included to the equation to model the thermal effect on the frequency response. To indicate the

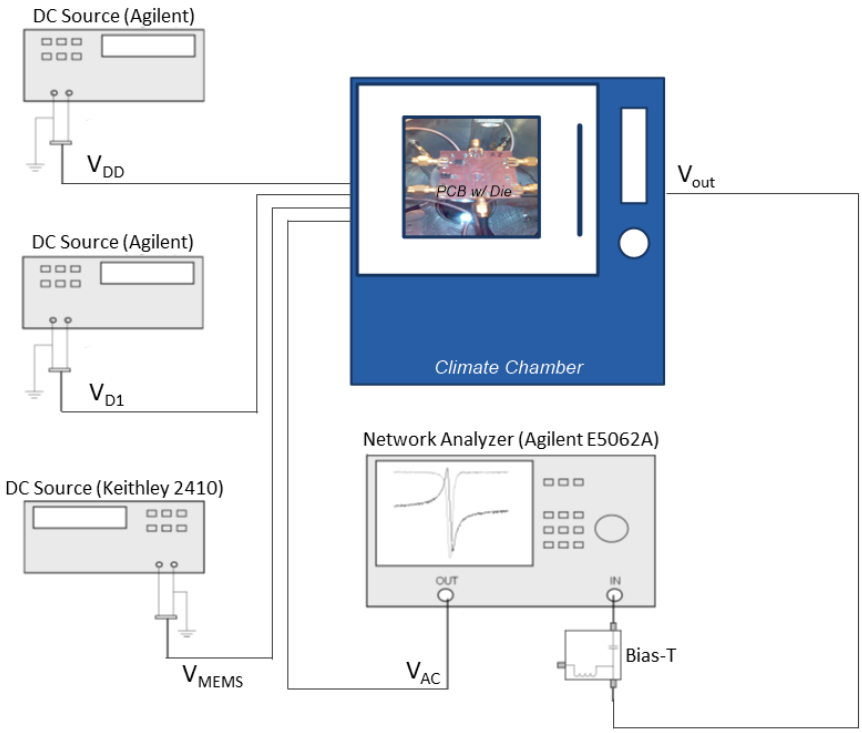

Figure 6-4: Scheme of the experimental setup used for measurements.

influence of the thermal effect, the resonance frequency is denoted by f_{rT}.

$$f_{rT} = \frac{1}{2\pi\sqrt{m_{\text{eff}}}}\sqrt{\frac{16E_T t_h w^3}{l^3}\left(1+\frac{\sigma_L l^2}{\eta E_T w^2}\right) - \frac{k_{\text{FF}} 2\,\epsilon_0\, l\, t_h}{N s^3} V_{DC}^2 \sum_{n=1}^{N} P_n^2} \tag{6.2}$$

Equation (6.2) implies a linear relation between f_{rT}^2 and V_{DC}^2. The procedure to validate the nonlinear model consists firstly in checking that the experimental points (V_{DC}, f_{rT}) fit the shape of the function (6.2). Then from each experimental curve the values of the second order parameters (i.e. fringing fields constant, residual stress and thermal expansion coefficient) are obtained and checked to remain in similar values.

6.2.1 Designs and experimental measurements

As wider explained in chapter 3, the commercial CMOS technology used for the designs and fabrication is the C35 process family from "Austria Micro Systems", a 3.3V 0.35μm CMOS technology which provides provides 4 layers of metal and 2 layers of polysilicon, as well as the tungsten VIA. Table 6.1 relates the dimensions and main mechanical parameters of

each structural layer in the AMS 035 CMOS technology, available for the cc-beam resonators mechanization.

Table 6.1: Dimensions and parameters of the AMS 035 CMOS technology.

AMS 035 Tech.	Metal 4	Metal 3	Tungsten	Polysilicon
E (GPa)	131	131	411	160
ρ (kg/m^3)	3000	3000	19300	2330
w (μm)	0.6	0.6	0.5	0.35
t_h (μm)	0.85	0.64	1	0.282

Two generations of devices have been designed, fabricated and measured with the aim of validating the nonlinear macro-model developed in chapter 5, establishing the limits for the second order parameter values.

6.2.2 First generation set of prototypes

The first generation of designed and fabricated devices corresponds to the Run 2015 set. Table 6.2 summarizes the dimensions of the fabricated resonators corresponding to this first generation, whose desing in Cadence is shown in figure C-1 (appendix C). Figure 6-5 shows an optical image of a C4 resonator corresponding to the Run 2015 set.

Table 6.2: Desing parameters of the fabricated resonators corresponding to the Run 2015 set.

	Metal 4				Polysilicon	
Parameters	C1	C2	C3	C4	C5	C6
l (μm)	73.75	63.85	52.1	63.85	54.6	63
w (μm)	0.60	0.6	0.6	0.6	0.35	0.35
s (μm)	1.72	1.5	1.45	2.07	0.9	0.9
freq. (MHz)	0.75	1	1.5	1	1	0.75

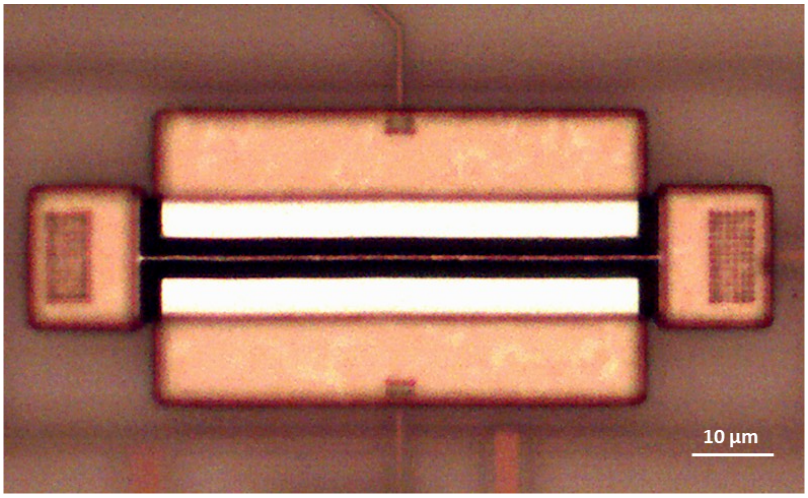

Figure 6-5: Optical image of a fabricated C4 resonator corresponding to the Run 2015 set.

Extensive experimental measurements of the frequency response of the fabricated CMOS cc-beam resonators have been performed under different thermal and biasing conditions. The Setup#1 (see figure 6-1) is used in this experimental procedure to reduce the parasitic feedthrough current, allowing an accurate measurement of the system frequency response. Figure 6-6a) shows that the power of the primary resonance peak grows with the applied bias voltage, as does the attenuation of the antiresonance, while the primary resonance frequency is decreasing. On the other hand, in figure 6-6b) the shapes of the experimental resonance frequency dependence on the bias voltage show a very good agreement with the theoretical curves provided by equation (6.2), demonstrating the accuracy of the approach, and fulfilling the first step to the model validation by means of experimental data. Moreover, such experimental data have been used to find second order parameters as well as the respective V_{pi0} values (these values of bias voltage correspond with the lower bias boundary value if the geometric condition (s/w) for bistability is attained, otherwise they imply the collapse of the towards one of the electrodes beam because of the pull-in effect). The average value of the fringing field constant is obtained from the slope of each curve $f_{rT}^2 = m \cdot V_{DC}^2 + n$. From equation (6.2), the slope m (which can be numerically obtained from the experimental points) is found to be

$$m = -k_{\mathrm{FF}} \frac{\epsilon_0 l t_h}{2\pi^2 m_{\mathrm{eff}} N s^3} \sum_{n=1}^{N} P_n^2 \tag{6.3}$$

and from this expression and the definition of k_{FF} , given in equation (5.15), the α_{FF} con-

stant can be calculated. From the natural frequency at room temperature, the equation of $k_{1\sigma T}$ (5.26) provides the value of the residual stress (σ_{eff}) not modified by the thermal effect. The experimental V_{pi0} values are obtained as the intersection of the curves of equation (6.2) given by the experimental points with the $f_{rT} = 0$ axis; Finally the thermal constant α_T is obtained from the variation of the natural frequency ($f_{rT}\,(V_{DC} = 0)$) caused by the change in the temperature: given the respective definitions of E_T, and σ_T (provided by (5.24)) and equation (6.2) for $V_{DC} = 0$, the α_T with best fitting of the experimental curve is numerically obtained, as shown in figure 6-7. All these values are summarized in tables 6.3, 6.4 and 6.5, as well as the minimum gap value attaining the geometric condition for bistablility and its associated lower bias boundary value V_{pi0} when the resonator is subjected to the room temperature (RT=20°C by default) and when the resonator is subjected to an "operational temperature" (OT=120°C by default). The second order nonlinear parameters are shown in figures 6-12 and 6-13. The reasonable similarity (keeping in mind the fabrication tolerances and the uncertainties in the chemical attack releasing procedure) between the respective values of all these parameters corresponding to the different experimentally measured devices belonging to the Run 2015 set, constitutes a prove of the models accuracy.

The results tables include the wet etching time using the different wet etchants explained in section 3.2.3; in these tables the acronym HMS stands for the home-made hydrofluoric solution.

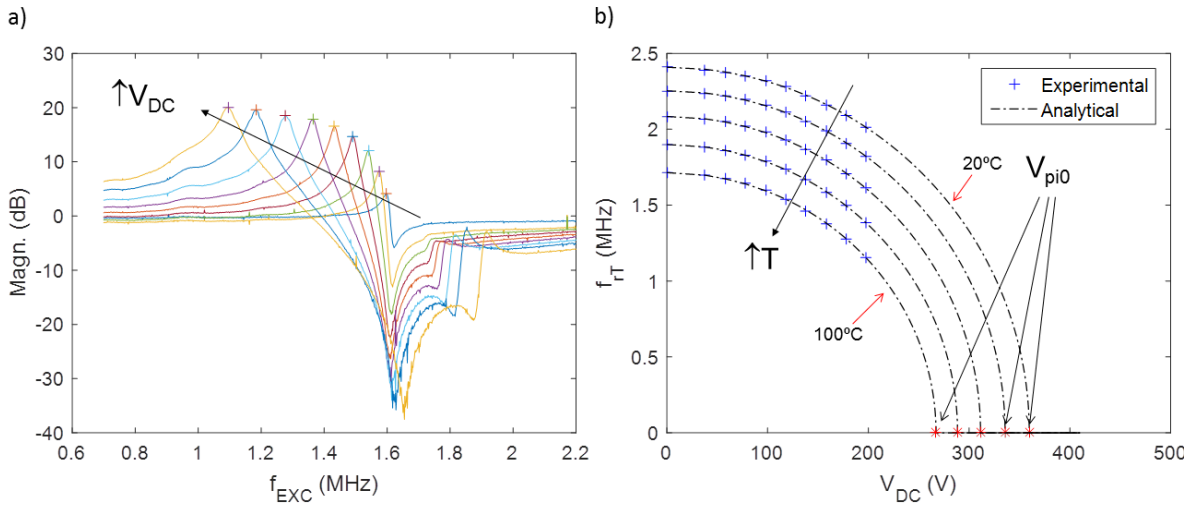

Figure 6-6: From resonator C4(15)-k15 a) experimental frequency response of a metal 4 (aluminium and titanium nitride) cc-beam resonator for a temperature of 110°C under different bias voltage values; b)representation of the experimental maximum response power frequency of this metal 4 cc-beam resonator with respect to the applied bias voltage for different temperature values (20°C, 40°C, 60°C, 80°C and 100°C), and their respective theoretical counterparts (in dotted lines).

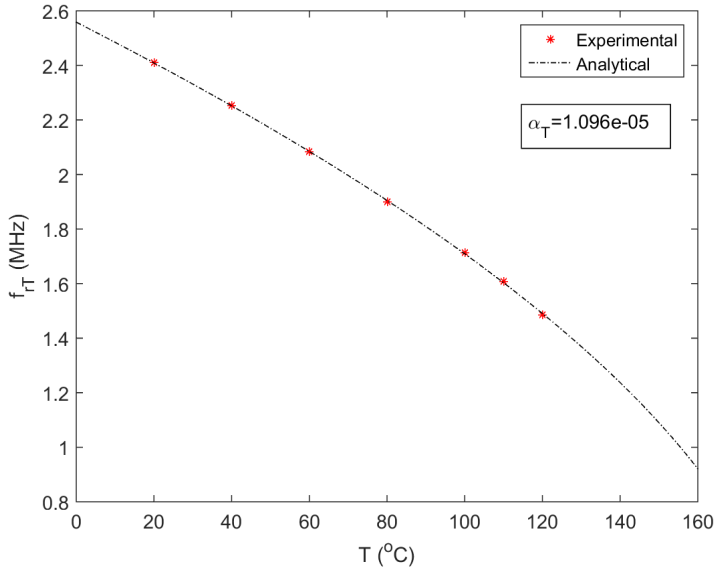

Figure 6-7: Experimental natural frequencies ($f_{rT}\,(V_{DC}=0)$) values for different temperatures, and the analytical fitting function from which the value of the α_T constant is obatined, from the resonator C4(15)-k15.

Table 6.3: Experimentally measured parameters corresponding to Metal 4 resonators belonging to the Run 2015 set.(* OT=130°C ,** OT=110°C).

METAL4 Run2015	Chip4 C1	Chip4 C4	Chip14 C4	Chip15 C4
Wet etching time	10' (HMS)	10' (HMS)	10' (HMS)	10' (HMS)
f_0 (MHz) at RT	1.919	2.232	2.223	2.409
σ_{eff} (GPa)	0.163	0.156	0.155	0.1885
α_T (K^{-1})	8.71e-06	8.99e-06	9.73e-06	1.096e-05
α_{FF} (∅)	0.172	0.150	0.265	0.235
s_{min} (μm) at RT	2.130	1.857	1.850	2.005
V_{pi0} (V) at RT	232.17	339.59	328.15	359.69
s_{min} (μm) at OT	1.298*	1.247	1.128	1.355**
V_{pi0} (V) at OT	152.58*	236.33	206.17	265.27**

Table 6.4: Experimentally measured parameters corresponding to Metal 4 resonators belonging to the Run 2015 set. (* OT=130°C ,** OT=110°C).

METAL4 Run2015	Chip16 C4	Chip17 C4	Chip34 C4	Chip43 C4
Wet etching time	10' (HMS)	20' (HMS)	10' (Silox)	20' (ALPAD)
f_0 (MHz) at RT	2.31	1.951	2.143	1.886
σ_{eff} (GPa)	0.170	0.110	0.141	0.100
α_T (K^{-1})	1.13e-05	8.35e-06	9.76e-06	5.84e-06
α_{FF} (∅)	0.236	0.652	0.2638	0.382
s_{min} (μm) at RT	—	1.623	—	1.569
V_{pi0} (V) at RT	—	241.35	—	248.12
s_{min} (μm) at OT	1.209**	0.918	1.040	1.122*
V_{pi0} (V) at OT	228.65**	136.83	215.37	182.02*

Table 6.5: Experimentally measured parameters corresponding to Metal 4 resonators belonging to the Run 2015 set. (* OT=130°C ,*** RT=25°C).

METAL4 Run2015	Chip52 C4	Chip53 C4	Chip57 C4	Chip59 C4
Wet etching time	10' (HMS)	10' (HMS)	10' (Silox)	10' (Silox)
f_0 (MHz) at RT	1.857	1.681	2.169	1.982
σ_{eff} (GPa)	0.096	0.0716	0.145	0.115
α_T (K^{-1})	3.49e-06	4.55e-06	9.07e-06	8.74e-06
α_{FF} ($\emptyset$)	0.519	0.689	0.310	0.227
s_{min} (μm) at RT	1.5450	1.3985	1.8049***	1.649***
V_{pi0} (V) at RT	248.60	203.26	307.48***	294.96***
s_{min} (μm) at OT	1.288*	—	1.168	0.944
V_{pi0} (V) at OT	196.39*	—	209.90	182.31

These experimental results provided the information about the order of magnitude of the residual stress generated from the fabrication procedure. Given the experimental values of the fabrication residual stress, although the geometric condition for bistability is attained by the most of the resonators at room temperature, the desired margin of 10% between the upper and the lower bias boundary value does not occur at room temperature. In practical application, driving the resonator into the bistable regime is not recommended without a margin wide enough, because it would eventually lead to the resonator collapse as a consequence of the pull in effect. Thus, for the resonators belonging to the Run 2015 set, the operating temperature must be applied in order to compensate the tensile residual stress before the bistable region is reached.

6.2.3 Second generation set of prototypes

The second generation of designed and fabricated cc-beam resonators corresponds to the Run 2017 set. This second generation has been designed to include new prototypes to explore the feasibility of the two-well potential distribution at room temperature (RT) with a sufficient margin between the bias boundary values for bistability. In addition, other designs are included in Run 2017 set to test their functionality and to measure their features.

Table 6.6 summarizes the dimensions of the fabricated resonators corresponding to the Run 2017 set, whose design screen in Cadence is shown in figure C-2 (appendix C). As developed in chapter 5, the ensurement of a big enough margin between bias boundary

values for bistability involves the use of big gaps, and consequently big values of bias voltage are needed. Some of the prototypes have been designed following the frequency optimization of the needed bias voltage explained in chapter 5 (resonators denoted whose frequency is remarked with (opt)) while the other ones have a given frequency , but in any case the second order nonlinear effects must be taken into account. For this reason, a previous estimation (experimental measurements of the Run 2015 devices) of the parameters corresponding to these second order effects is needed. The further experimental measurements of the Run 2017 devices provide the actual values of these second order effect parameters, and indicate whether there is a big variation of them between fabrication sets. The whole Run 2017 is designed considering a thermal constant and a fringing field constant given from an average of the α_T and α_{FF} respectively measured from the resonators belonging to the Run 2015 set, namely $\alpha_T = 9.605e-6K^{-1}$ and $\alpha_{\mathrm{FF}} = 0.2$. Most of the resonators in Run 2017 are designed considering a 100% of an average value σ_{eff} of the Run 2015 set ($\sigma_{\mathrm{eff}} = 0.1623$ GPa), however some of them have been designed considering a 50% of this value. As an exception of the general criterion, the C4 has been designed with the optimal frequency to minimize the bias voltage under an operating temperature (OT) of 100°C (and under the effect of the corresponding thermal stress). Finally, using the VIA tungsten layer (see section3.2) some resonators have been designed. Since the residual stress is a priori unknown, 3 of the 4 tungsten resonators have been designed neglecting the residual stress, and the 4th one has been designed considering a 50% of the average residual stress of the Metal 4 resonators of the Run 2015 set.

Table 6.6: Desing parameters of the fabricated resonators corresponding to the Run 2017 set.

		σ_{eff} (Gpa)	margin	T (°C)	l (μm)	s (μm)	freq. (MHz)	V_{pi0} (V)	V_{piw} (V)
C1	Metal 4	0	—	—	63.85	2.07	1	355	—
C2		0.1623	10%	RT	50.9	2.55	3	624	688
C3		0.1623	10%	RT	71	3.3	2 (opt)	594	654
C4		0.064 (σ_L)	10%	100°C	111	3.3	0.8 (opt)	238	263
C5		0.1623	5%	RT	71	2.9	2 (opt)	496	522
C6	Metal 3	0.1623	10%	RT	58.65	2.55	3	595	656
C7		0.1623	10%	RT	73	3.375	1.93 (opt)	562.5	620
C8		0.0812	10%	RT	103	3.5	0.97 (opt)	400	—
C9	Tungsten	0	10%	RT	48.7	1.125	1	156.1	173.0
C10		0	10%	RT	34.4	1.125	2	312.1	346.0
C11		0	5%	RT	48.7	0.975	1	127.0	133.6
C12		0.0812	10%	RT	55.825	1.45	1	224.5	246.9

Metal resonators

The experimental results obtained from the measurement of the Metal 4 resonators corresponding to the Run 2017 set are sumarized in table 6.7. As expected, the increase of the gap parameter (s) in the new designs of Run 2017, with the aim of enforce the dimensional condition to allow bistability, implies an increase of the needed bias voltage. In this way the high voltages needed to achieve bistability in the Metal 4 resonators of the Run 2017 set are the counterpart to the bigger margins (V_{piw} to V_{pi0}) that is needed to assume.

Although the values of the σ_{eff} coefficient provided by experimental measurements are in the same order of magnitude as the estimated residual stress (the σ_{eff} average value from the experimental measurements of the resonators belonging to the Run 2015 set), they are greater than it, and in general, greater than expected. The increase of these values with respect to the estimated one is not very pronounced (from approx. 5% to approx. 15%). However the residual stress has a great influende on the s_{min} parameter and on the needed bias voltage (see figure 5-7, which depicts specifically the numerically obtained values of the bias boundary values for bistability for a resonator with dimensions corresponding to the C3 resonator of the Run 2017 set). Thus, for the σ_{eff} coefficients obtained from the experimental measures, the margin between V_{pi0} and V_{piw} will be slightly smaller than the

10% at room temperature. Figure 6-8 depicts the experimental frequency response and the resonance frequency of a Metal 4 resonator (C3) corresponding to the Run 2017 set under different temperature and bias conditions, while figure 6-9 shows an optical image of a Metal 4 resonator (C4) corresponding to such a run.

Table 6.7: Experimentally measured parameters corresponding to Metal 4 resonators belonging to the Run 2017 set. (* OT=100°C ,** OT=140°C).

METAL4 Run2017	Chip6 C2	Chip7 C5	Chip8 C3	Chip8 C4	Chip17 C3	Chip17 C4
Wet etching time	10' (Silox)	15' (Silox)	30' (Silox)	30' (Silox)	15' (Silox)	15' (Silox)
f_0 (MHz) at RT	3.076	2.14	2.09	1.25	2.123	1.281
σ_{eff} (GPa)	0.174	0.191	0.180	0.172	0.187	0.182
α_T (K^{-1})	8.724e-06	8.92e-06	9.21e-06	7.58e-06	9.80e-06	9.09e-06
α_{FF} (∅)	0.237	0.197	0.242	0.266	0.226	0.404
s (μm)	2.55	2.9	3.3	3.3	3.3	3.3
s_{min} (μm) at RT	1.627	—	2.151	3.143	2.185	3.221
V_{pi0} (V) at RT	762.51	–	597.19	350.64	688.65	433.92
s_{min} (μm) at OT	1.193	1.715*	1.256**	2.215	1.479	2.416
V_{pi0} (V) at OT	450.57	412.58*	373.82**	245.70	378.67	242.52

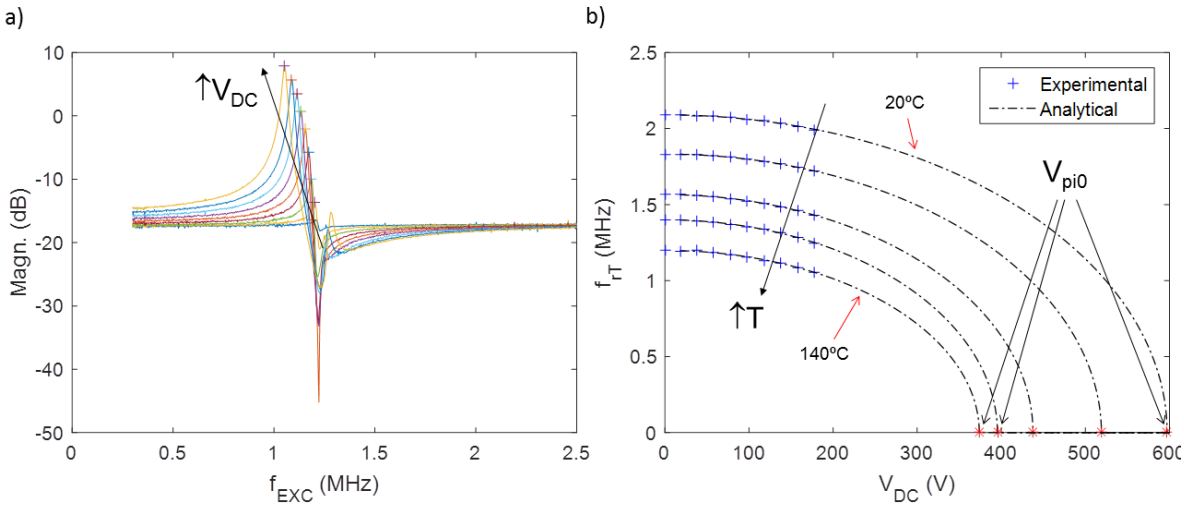

Figure 6-8: From resonator C3(8)-k17 a) experimental frequency response of metal cc-beam resonator for a temperature of 140°C under different bias voltage values; b)representation of the experimental maximum response power frequency of this metal cc-beam resonator with respect to the applied bias voltage for different temperature values (20°C, 60°C, 100°C, 120°C and 140°C), and their respective theoretical counterparts (in dotted lines).

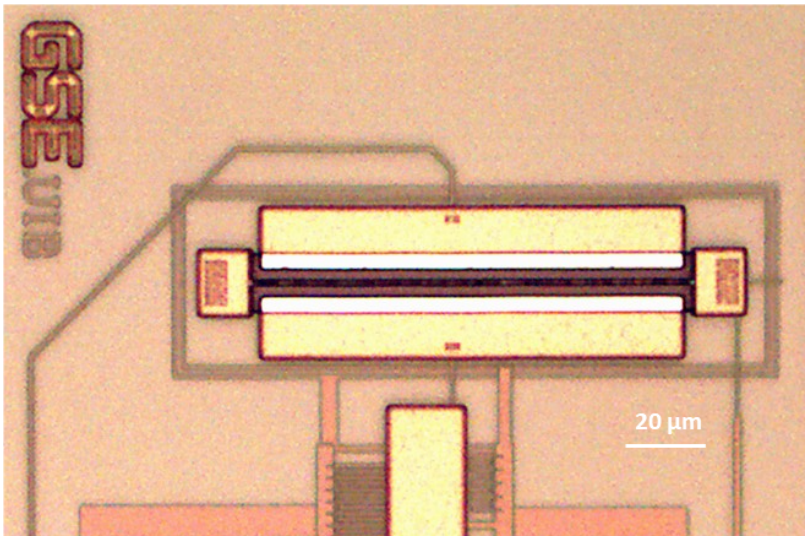

Figure 6-9: Optical image of a Metal 4 resonator (C4) belonging to the Run 2017 set.

Tungsten resonators

The experimental results of the measured tungsten resonators (summarized in tables 6.8 and 6.9) revealed an average residual stress coefficient of $\sigma_{\text{eff}} \sim 0.74$ GPa , more than 4.5 times the average value of the residual stress coefficient used as reference in the design estimations (moreover, notice that 3 of the 4 tungsten resonators have been designed without considering the residual stress). Another important fact is that the variation of the natural frequency with the temperature is not as pronounced as in the Metal 4 cases (the average tungsten α_T parameter represents approximately the 30% of the average Metal 4 α_T value). Low dependence of the frequency on temperature is considered an advantageous feature for a resonator performance. However in this case, the small values of α_T coefficient prevent the thermal effect from successfully compensating the huge residual stress. These circumstances make the fabricated tungsten resonators unable to meet the dimension condition for bistability at any temperature that the climatic chamber is capable to reach. The solutions for further designs, in order to overcome the issues of the tungsten fabricated resonators, would involve a much greater gap parameter (which would imply much greater bias voltages) or a fabrication procedure which ensures a reduction of the residual stress. Figure 6-10 depicts the experimental frequency response and the resonance frequency of a tungsten resonator (C11) corresponding to the Run 2017 set under different temperature and bias conditions, while figure 6-11 shows an optical image of a tungsten resonator (C9) corresponding to such

a run.

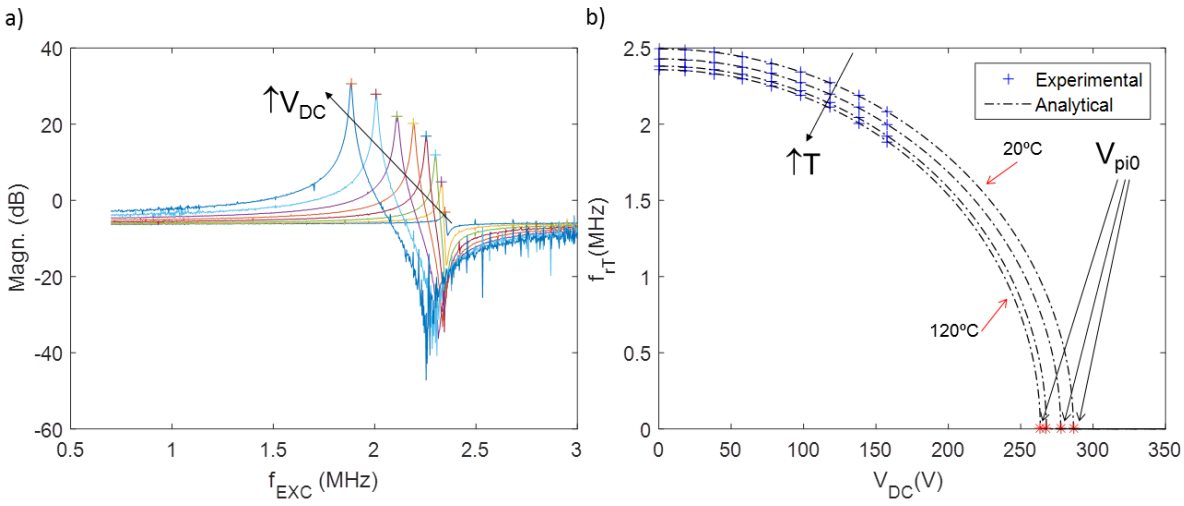

Figure 6-10: From C11(7)-k17 a) experimental frequency response of a tungsten cc-beam resonator for a temperature of 120°C under different bias voltage values; b)representation of the experimental maximum response power frequency of this tungsten cc-beam resonator with respect to the applied bias voltage for different temperature values (20°C, 60°C, 100°C and 120°C), and their respective theoretical counterparts (in dotted lines).

Table 6.8: Experimentally measured parameters corresponding to tungsten resonators belonging to the Run 2017 set.

TUNGSTEN Run2017	Chip2 C9	Chip2 C10	Chip2 C11	Chip2 C12
Wet etching time	10' (Silox)	10' (Silox)	10' (Silox)	10' (Silox)
f_0 (MHz) at RT	2.412	3.697	2.437	2.105
σ_{eff} (GPa)	0.708	0.707	0.725	0.743
α_T (K^{-1})	2.66e-06	2.94e-06	2.28e-06	2.58e-06
α_{FF} ($\emptyset$)	0.481	0.475	0.446	0.394
s (μm)	1.125	1.125	0.975	1.45
s_{min} (μm) at RT	1.672	1.279	1.689	1.917
V_{pi0} (V) at RT	339.87	523.61	280.83	441.78
s_{min} (μm) at OT	1.571	1.202	1.601	1.793
V_{pi0} (V) at OT	320.59	485.31	272.07	402.51

Table 6.9: Experimentally measured parameters corresponding to tungsten resonators belonging to the Run 2017 set.

TUNGSTEN Run2017	Chip7 C11	Chip7 C12	Chip8 C10	Chip8 C11
Wet etching time	15' (Silox)	15' (Silox)	30' (Silox)	30' (Silox)
f_0 (MHz) at RT	2.494	2.135	3.766	2.486
σ_{eff} (GPa)	0.767	0.768	0.745	0.760
α_T (K^{-1})	2.45e-06	2.19e-06	3.66e-06	2.83e-06
α_{FF} ($\emptyset$)	0.554	0.459	0.701	0.704
s (μm)	0.975	1.45	1.125	0.975
s_{min} (μm) at RT	1.729	1.945	1.303	1.723
V_{pi0} (V) at RT	286.36	433.12	502.30	272.23
s_{min} (μm) at OT	1.634	1.846	1.209	1.613
V_{pi0} (V) at OT	263.52	407.98	452.33	251.12

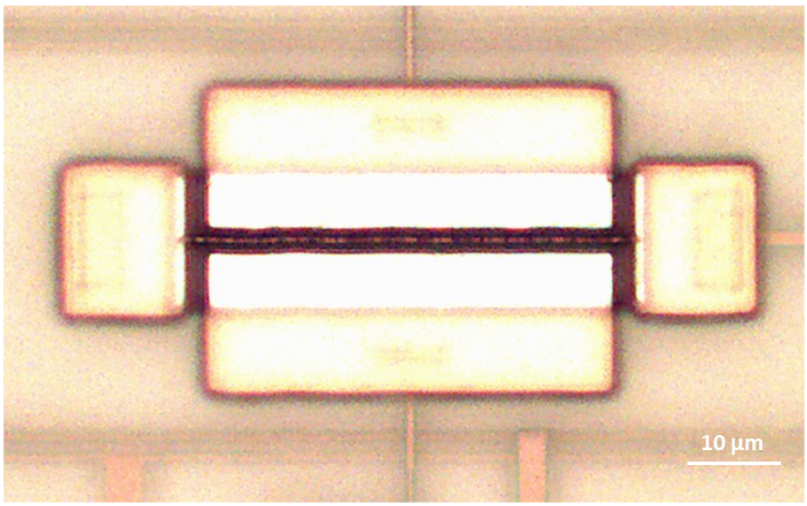

Figure 6-11: Optical image of a tungsten resonator (C9) belonging to the Run 2017 set.

Using the measured average values for the nonlinear second order effects, table 6.10 shows the optimal dimensional values to enable the two-well potential distribution with a tungsten device. As explained in chapter 5, the minimum gap value attaining the dimensional condition for bistability (s_{min}) under each temperature provides coincident values of bias boundary values for bistability; greater values of gap are needed to ensure the 10% of margin and the enormous bias voltages required discourages the implementation of this approach.

Table 6.10: Numerical estimation of the dimensional and biasing conditions for bistability following the optimization process described in chapter 5. The averaged values of the second order parameters ($\sigma_{\text{eff}} = 0.7404$ GPa, $\alpha_T = 2.699 \cdot 10^{-6} K^{-1}$, $\alpha_{\text{FF}} = 0.45$), have been used in the calculation.

T	l (μm)	f_0 (MHz)	s_{min} (μm)	$V_{pi0}(V)$ for s_{min}	$s_{10\%}$ (μm)	$V_{pi0}(V)$ for $s_{10\%}$	$V_{piw}(V)$ for $s_{10\%}$
20°C	52	2.279	1.801	618.4	2.871	1153	1269
100°C	55	2.023	1.789	544.3	2.859	1019	1122
120°C	56	1.953	1.790	525.8	2.850	979	1077

6.2.4 Experimental second order parameters comparison

The second order parameters σ_{eff} and α_T of the Metal 4 resonators of the Run 2017 set are found to be quite similar to the ones corresponding to the Metal 4 resonators of the Run 2015 set, as depicted in figure 6-12 and 6-13. However, as it has been mentioned in section 6.2.3, the residual stress coefficient has been found to be slightly higher in the resonators of the Run 2017 (even if the values of this coefficient of both runs are in the same order of magnitude). Conversely, the tungsten resonators present their own values of σ_{eff} and α_T, which are quite distant from the metal 4 values, as depicted in 6-12. In general, the average values of σ_{eff}, and α_T parameters corresponding to Metal 4 and tungsten can be respectively observed. Nevertheless, some points of α_T corresponding to the Metal 4 resonators of the Run 2015 set are particularly low and may be considered as outliers (figure 6-12b). The α_{FF} values (which are, a priori, independent on the material), present a greater dispersion (figure 6-13). However, and except for some spurious values corresponding to Metal 4 resonators of the Run 2015 set, a tendency to an average value (≈ 0.23) for the Metal 4 resonators, while the tungsten resonators present higher and more scattered values of α_{FF}. Regardless, a general average value can be obtained and considered. The respective variations of the experimentally obtained constant values (i.e. the respective variations inside the sets of metal 4 σ_{eff}, of tungsten σ_{eff}, metal 4 α_T, of tungsten α_T and of α_{FF}) can be explained to be caused by several factors:

- The presence of fabrication tolerances in the dimensional parameters of the resonator, which can reach up to 10% in the worst cases.
- The lack of uniformity of the chemical attack corresponding to the wet etching process.

- The possible lack of uniformity of the cross section of the beam along the span.

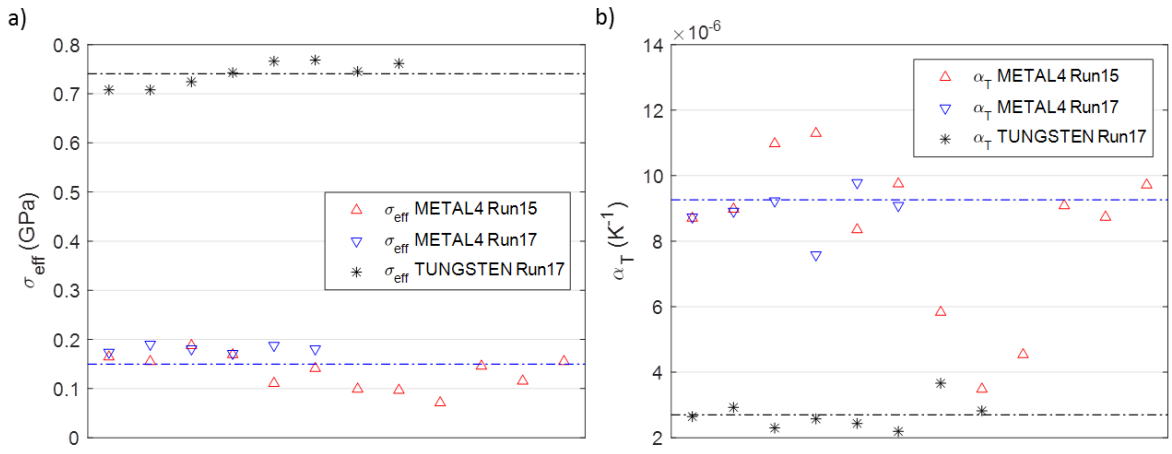

Figure 6-12: Experimental σ_{eff} and α_T parameter values. The respective average values ($\sigma_{\text{eff}} = 0.1499$ GPa for Metal 4 and $\sigma_{\text{eff}} = 0.7404$ GPa for tungsten, $\alpha_T = 9.261 \cdot 10^{-6}\, K^{-1}$ for Metal 4 and $\alpha_T = 2.699 \cdot 10^{-6}\, K^{-1}$ for tungsten) are indicated by dashed lines.

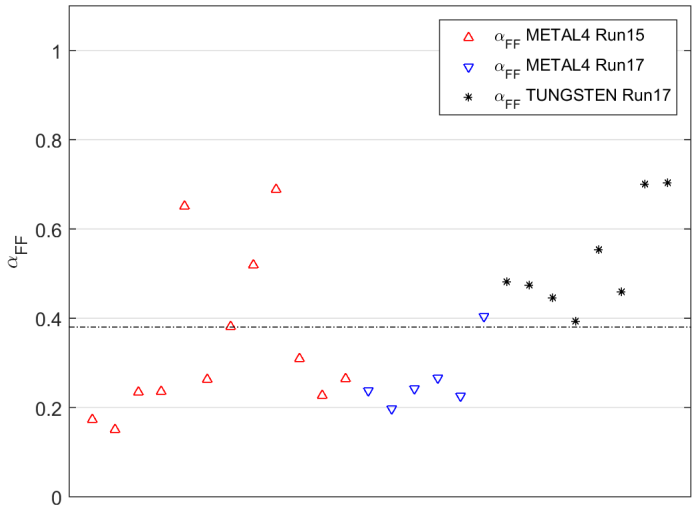

Figure 6-13: Experimental α_{FF} parameter values. The average value ($\alpha_{\text{FF}} = 0.38$) is indicated by dashed lines.

6.3 Experimental validation of bistability

If the ratio s/w condition is attained for a given temperature, the increasing bias voltage makes the system follow a supercritical Pitchfork bifurcation, which will provide two stable nontrivial points (corresponding to the symmetrically located minima of the potential function) between the bias boundary values V_{pi0} and V_{piw} (see figure 6-14). Following this Pitchfork bifurcation when the growing bias voltage reaches V_{pi0} the nondeformed position ($x = 0$) becomes unstable, and the oscillation of the beam takes place around the new nontrivial stable positions, as is proper of homoclinic structures.

6.3.1 Experimental bistability measurement

The change of the point around which the oscillation takes place produces a change of the coupling capacitance between the beam and the readout electrode which can be sensed by a network analyzer as a shift of the S_{21} scattering parameter of the CMOS-MEMS system. The network analyzer must be set up to provide a constant value of the excitation frequency, corresponding to a higher value than the natural frequency in each temperature because, otherwise, at some point in the process of increasing DC (and consequently decreasing the resonance frequency) the excitation frequency would be equal to the resonance frequency, placing the system in a dangerous condition of falling into pull-in collapse. In order to maximize the sensitivity of the experimental detection procedure, the configuration denominated as Setup#2 in figure 6-1 has been implemented; this setup allows the possibility of sensing the variation in the parasitic current produced by the oscillation around a nontrivial equilibrium point, besides the variation of the motional current due to the same reason. Since the oscillation of the beam has small amplitude, in this case the parasitic component dominates over the motional component; moreover, from equation (6.1) it can be seen that a variation of the point around which the oscillation takes place has more influence on the parasitic component than on the motional component. The variation of the experimental S_{21} magnitude, depicted in figure 6-15a), implies the presence of the two-well potential distribution, and may be compared with the analytical pitchfork bifurcation expressed in terms of the normalized capacitance corresponding to the singular points of the potential function.

While the applied bias voltage is being increased, once the proper value has been reached

($V_{pi0} < V_{DC} < V_{piw}$), the experimental points may move towards both potential wells because of some slight asymmetries induced by the V_{D1} voltage. For instance, in figure 6-15a), the points with positive values are obtained with $V_{D1} = 4V$, while those with negative values correspond to $V_{D1} = 2V$. Those asymmetries produce the margin between the upper trajectory and the lower trajectory of the experimental data shown in figure 6-15a). When the asymmetry produced by the V_{D1} voltage is performed with a time square signal, the snap-though motion is clearly observed in the time domain for biasing voltages higher than V_{pi0}. Figure 6-15b) shows the time history of the system transmission response (S_{21}) experimentally measured (also, using Setup#2) with a network analyzer when the cc-beam resonator is excited by a squared signal at 4 Hz through the V_{D1} node. Bistability is observed from the snap-through motion attained when the system exhibits two-well potential (for $V_{\text{MEMS}} = 203V$ in this case). This plot compares the variation of the position caused by the effect of the changing asymmetry when we are outside the bistable region ($V_{\text{MEMS}} = 160V$) and when we are inside it ($V_{\text{MEMS}} = 203V$): the variation of 2V of the asymmetry in the single potential well region provokes just a slight deformation, while in the bistable region generates a big variation. It is needed to note that the results of bistability, reported in figures 6-15a) and b) have been obtained under an operating temperature of 120°C. Specifically figures 6-15a) and b) correspond to experimental measurements of the resonator C4(16)-k15. Bistability has been also measured with metal resonators belonging to the Run 2017 set: figure 6-16 shows the experimental bifurcation to the bistable state of C3(8)-k17, under an operating temperature of 140°C.

Numerical studies reported in section 5.5 indicate that the application of higher temperature increases the margin between V_{pi0} and V_{piw} for the same s/w ratio (see figure 5-8), and moreover the absolute values of these bias boundary values is decreased, moving the system away from the danger of pull-in collapse; thus the use of high temperatures is recommended.

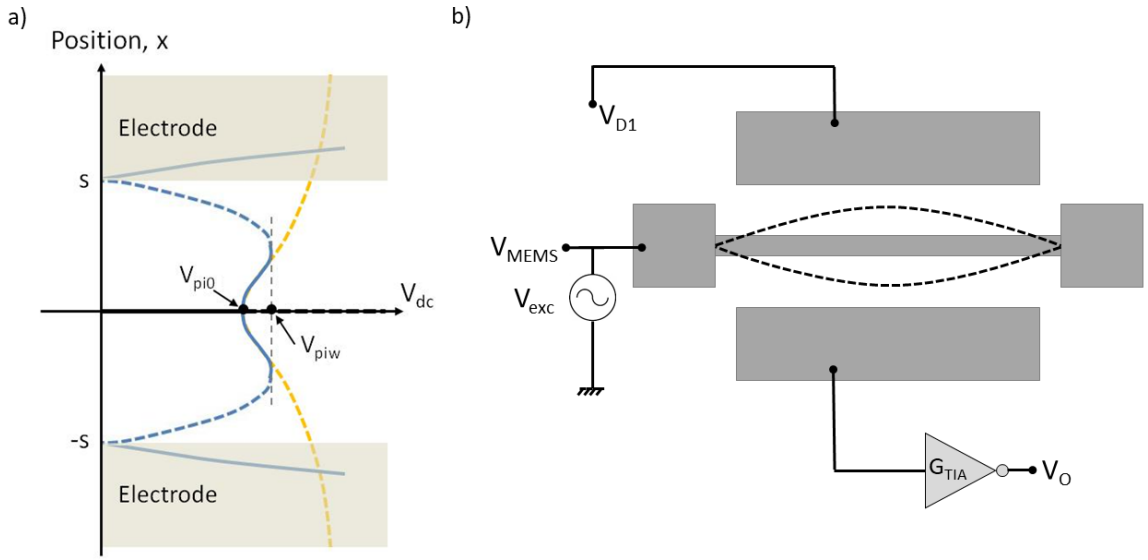

Figure 6-14: Schematic representation of a) the supercritical Pitchfork bifurcation of the equilibrium points in the 2WP distribution and b) the nontrivial equilibrium deformations of the cc-beam resonator.

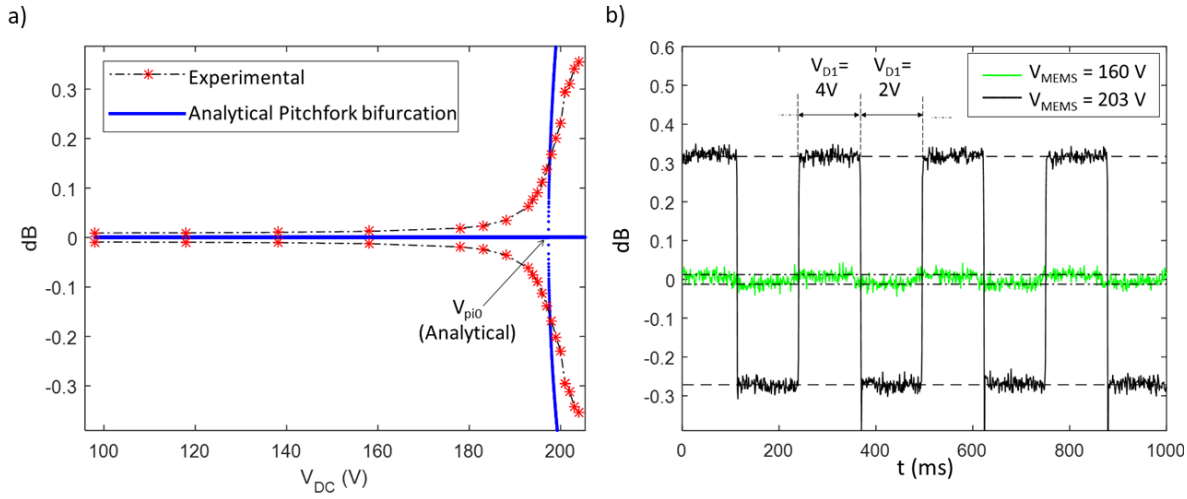

Figure 6-15: a) Experimental (from the Metal 4 resonator C4(16)-k15) and numerical Pitchfork bifurcation. b) Experimental time history of the system transmission response inside and outside of the bistable regime.

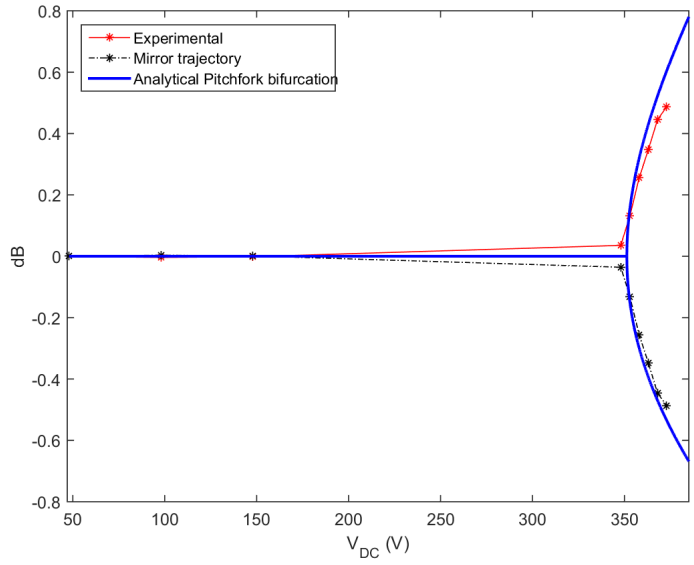

Figure 6-16: Experimental (from the Metal 4 resonator C3(8)-k17) and numerical Pitchfork bifurcation.

6.3.2 Capacitive coupling analysis

The experimentally obtained coupling levels between the cc-beam resonator and the readout driver can be used to estimate the value of the offset capacitance C_k defined as the total capacitance contribution which does not depend on the beam deformation $C_k = k_{\mathrm{FF}} C_c$. Given the small oscillation amplitudes, when using the Setup#2 for the measurement of the bistable behavior, the parasitic component of the capacitive current is far bigger than the motional component, which can be neglected, thus the capacitive current can be approximated to

$$i_c \approx -\omega V_{AC} \sin(\omega t) \left(k_{\mathrm{FF}} \frac{\epsilon_0 t_h l}{N} \sum_{n=1}^{N} \frac{1}{(s + P_n x)} + C_k \right) \tag{6.4}$$

The transimpedance gain, whose value for each input frequency is known, can be expressed as

$$G_{\mathrm{TIA}}(\omega) = \frac{V_{\mathrm{o\ rms}}}{i_{\mathrm{c\ rms}}} \tag{6.5}$$

while the coupling level measured in the network analyzer is the relation between the system input and output signals in the form

$$S_{21} = 20 \log_{10} \left(\frac{V_{\text{o rms}}}{V_{\text{AC rms}}} \right). \tag{6.6}$$

In this way, the transimpedance gain can be approximated to

$$G_{\text{TIA}}(\omega) \approx \frac{10^{\frac{S_{21}}{20}}}{2\pi f_{\text{exc}} \left(k_{\text{FF}} \frac{\epsilon_0 t_h l}{N} \sum_{n=1}^{N} \frac{1}{(s + P_n x)} + C_k \right)} \tag{6.7}$$

Considering the coupling level S_{21} corresponding to the bias voltages that provides a single potential well and negligible displacement ($x \approx 0$), the offset component of the capacitance C_k can be estimated following equation (6.8). The values of this parameter, corresponding to several measured devices are shown in the last row of table 6.11 represented in figure 6-17. All the estimated C_k values are of the same order of magnitude and, as has been pointed in section 6.2.4, their apparent disparity can be explained by the fabrication tolerances and uncertainty in the releasing process.

$$C_k \approx \left(\frac{10^{\frac{S_{21}}{20}}}{2\pi f_{\text{exc}} G_{\text{TIA}}(\omega)} - k_{\text{FF}} \frac{\epsilon_0 t_h l}{s} \right) \tag{6.8}$$

The total experimental capacitance at zero displacement can be approximated with the expression

$$C_{0\_\text{exptl}} \approx \frac{10^{\frac{S_{21}}{20}}}{2\pi f_{\text{exc}} G_{\text{TIA}}} \tag{6.9}$$

The comparison between the total experimental capacitance values at zero displacement (equation (6.9)) and the theoretical C_0 values (equation (3.29)) is shown in table 6.11. These estimation procedure can only be done if the the value of the transimpedance gain of the whole TIA amplifier is well known. However, in most of the effectuated experimental measurements of bistability, an additional capacitance have been added to the $V_{\text{c out}}$ output, with the aim of limit the gain of the amplifier and avoid the saturation of the output signal. When this capacitance is added, the transimpedance gain is minor than the nominal of the UGBCA50 circuit (for the usual frequency ranges), but its exact value is unknown. The measurements of the devices listed in table 6.11 (and whose estimated C_k values are depicted in figure 6-17) have been effectuated without having added this additional capacitance to the $V_{\text{c out}}$ node. In this way the value of the transimpedance gain of the whole TIA amplifier

is well known, and tabulated to depend on the frequency of the input signal.

Table 6.11: Comparison between the experimental and theoretical capacitive coupling level

	Chip15 C4	Chip16 C4	Chip17 C4	Chip59 C4
Experimental S_{21}	11.2566	11.0981	10.0438	8.8711
Experimental C_0 (F)	9.33e-16	9.16e-16	7.37e-16	6.44e-16
Theoretical C_0 (F)	2.32e-16	2.32e-16	2.32e-16	2.32e-16
Estimated C_k (F)	6.00e-16	5.83e-16	2.25e-16	3.13e-16

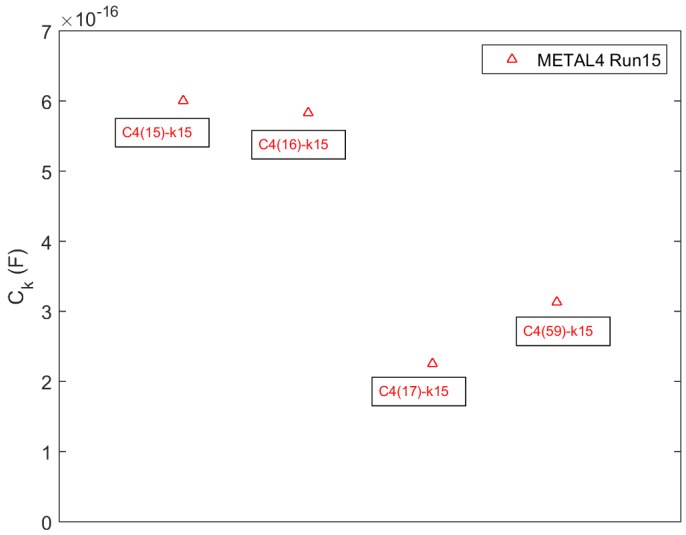

Figure 6-17: Estimation of the offset capacitance component C_k obtained from the low biased S_{21} coupling level measurements.

6.4 Experimental demonstration of chaotic motion

This section reports the experimental measurement of extensive and sustained homoclinic chaotic response obtained for the first time from fabricated cc-beams resonators in the range of the MHz. The procedure of chaotic behavior seeking requires the application of specific biasing conditions for each resonator under test. In this case, the procedure with the specific resonator C4(17)-k15 is reported.

For a bias voltage beyond the lower bias boundary value, once the bistable region has been reached, the analytic equation (6.2) provides no real frequency; however numerical sim-

ulations of the complete system for a frequency sweep provide a new resonance frequency which grows again with the applied bias voltage until the upper bias boundary value (V_{piw}), from which the collapse of the beam caused by the pull-in effect would occur. The growth of the resonance frequency in the bistable region has been also experimentally observed (assuming the pull-in danger when the frequency sweep makes the system undergo thought its resonance frequency at so high bias voltages), and compared with the numerically obtained one in figure 6-18)a). The experimental frequencies start to grow with the bias voltage for a DC value smaller than the analytically expected value from equation (6.2)(V_{pi0}); the assumption that the linear stiffness (either in mechanical and electrical domain) dominates in the frequency over the other nonlinear stiffness terms becomes non acceptable when the linear stiffness becomes suffciently small. The result is that the system steps into the bistable region and the corresponding homoclinic structure arises for lower DC values than theoretically expected. This effect can also be seen in the experimental coupling bifurcation diagram, figure 6-18b).

From the conducted experiment for bistable behavior of the system, referred in previous section and effectuated with the specific resonator under test (figure 6-18), it is known that for a bias voltage greater than approx $V_{DC} = 121.5V$ the system exhibit a two-well potential distribution and, with this condition, it is susceptible to provide chaotic response.

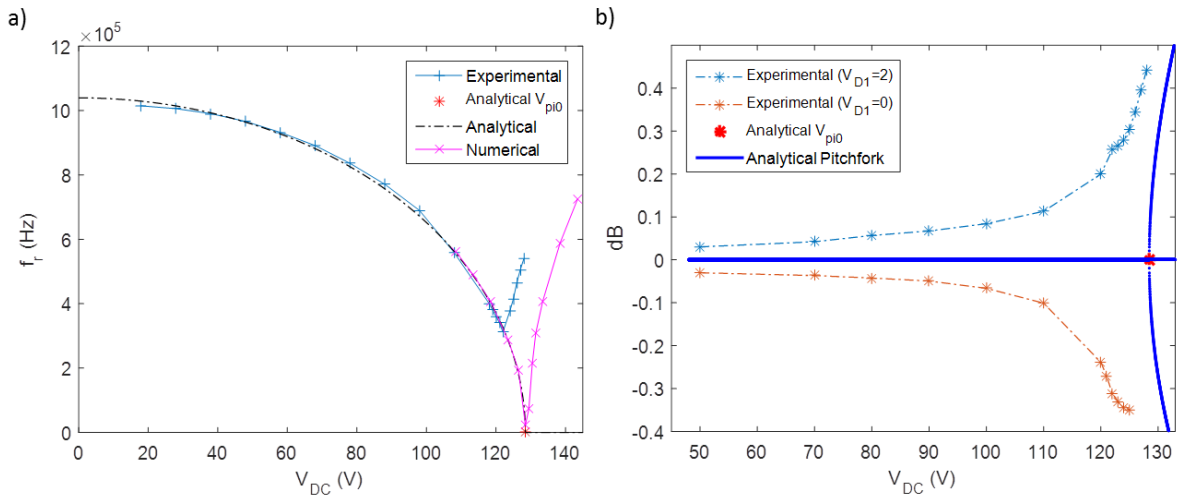

Figure 6-18: a) Experimental and numerical resonance frequency as a function of the bias voltage, and b) experimental bistability and numerical pitchfork bifurcation. Both plots refer data obtained under a temperature of 120°C.

The fact that the homoclinic structure appears for a lower bias voltage than the analytically predicted one prevents the correct application of the formulated procedure of the Melnikov method. A further correction of the Melnikov method taking into account this situation would be needed. The experimental output is a voltage signal. In the experimental procedure the Setup#1 is used in order to minimize the parasitic capacitive current. To find the generation of chaotic behavior, the bias voltage is set in a value which implies the two-potential well distribution, and then the nonlinear and chaotic behavior are tracked by sweeping the excitation amplitude and frequency. When the proper excitation frequency is found, the presence of nonlinear effects impose their influence and by increasing the excitation amplitude the system eventually exhibits extensive chaotic behavior (figures 6-21, and 6-23). The nonlinear behavior corresponding to the period doubling bifurcation has been also measured and reported in figures 6-19 and 6-20.

Experimental chaos is found to be more evasive than in numerical simulations, but finally it was obtained. Another control variable that can also be modified during the chaotic behavior search process is V_{D1}. All the experimental measurements of period doubling bifurcation and chaotic response have been performed under an operating temperature of 120°C. Besides the signal time series, the obtained chaotic behavior is also represented with its Poincare map (figures 6-21b), and 6-23b)), showing a typical shape of the chaotic series, which may be compared with the numerically obtained one, in figure 5-12. All the experimentally obtained signals are filtered in order to remove the high frequency noise. After this filtering, the maximal Lyapunov exponent of the time series depicted in figures 6-21a), and 6-23a) have been calculated by means of the algorithm introduced by Wolf et.al in [77] and successively improved until the implementation of the latest version for the Matlab environment in 2016 (see section 2.5.3). The positive and finite value of the maximal Lyapunov exponent given by the Wolf algorithm, and shown in figures 6-22 and 6-24 corroborates the presence of extensive chaotic essence in the measured time series. Finally, figure 6-25 shows the lab experimental setup, in a moment where a chaotic response was experimentally measured.

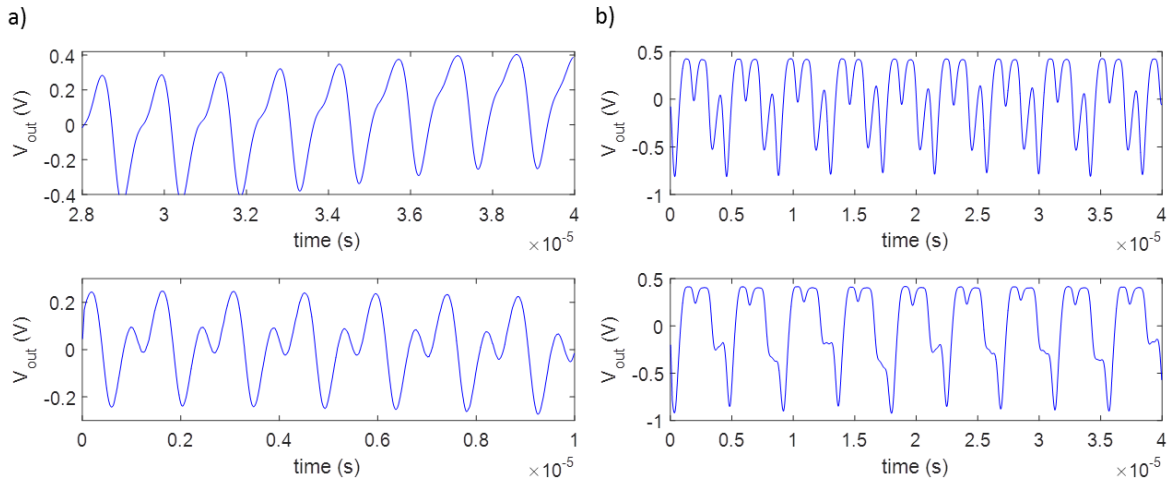

Figure 6-19: Experimental time series of the system showing nonlinear behavior and period doubling bifurcation. The parameter values are a) (up) $V_{\text{MEMS}} = 127$ V, $V_{D1} = 2.9$ V, $f_{\text{exc}} = 1.387$ MHz and $V_{AC} = 15.05$ dBm (bottom) $V_{\text{MEMS}} = 127$(V), $V_{D1} = 4$ (V), $f_{\text{exc}} = 1.38$ MHz and $V_{AC} = 18.3$ dBm and b) (up) $V_{\text{MEMS}} = 127$ V, $V_{D1} = 4$ V, $f_{\text{exc}} = 1.42$ MHz and $V_{AC} = 15.05$ dBm (bottom) $V_{\text{MEMS}} = 127$(V), $V_{D1} = 2.8$ (V), $f_{\text{exc}} = 1.38$ MHz and $V_{AC} = 15.05$ dBm.

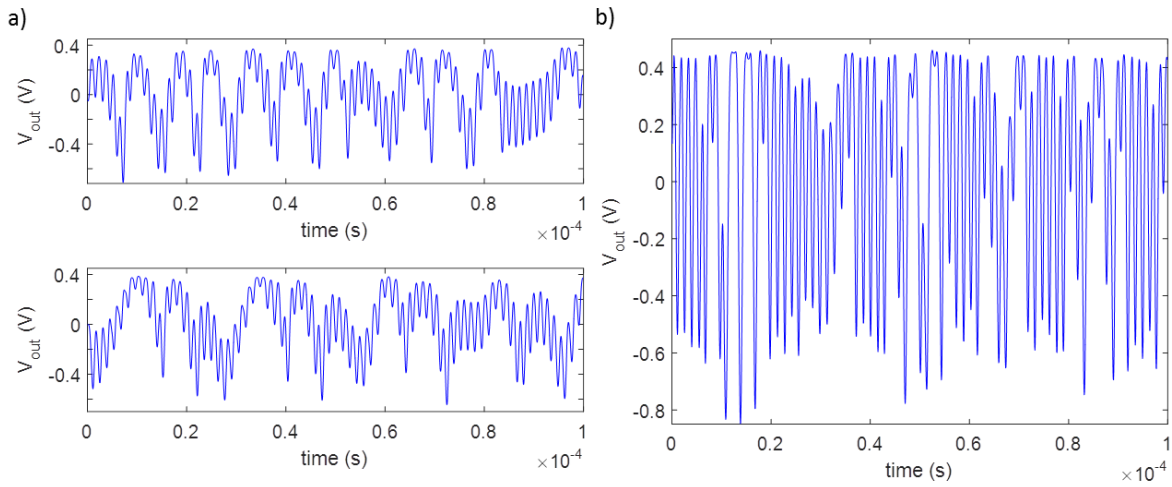

Figure 6-20: Experimental time series of the system showing nonlinear behavior and period doubling bifurcation. The parameter values are a) (up) $V_{\text{MEMS}} = 126$ V, $V_{D1} = 4$ V, $f_{\text{exc}} = 1.415$ MHz and $V_{AC} = 15.05$ dBm (bottom) $V_{\text{MEMS}} = 128$(V), $V_{D1} = 4$ (V), $f_{\text{exc}} = 1.43$ MHz and $V_{AC} = 15.05$ dBm and b) $V_{\text{MEMS}} = 127$ V, $V_{D1} = 4$ V, $f_{\text{exc}} = 1.386$ MHz and $V_{AC} = 15.05$ dBm.

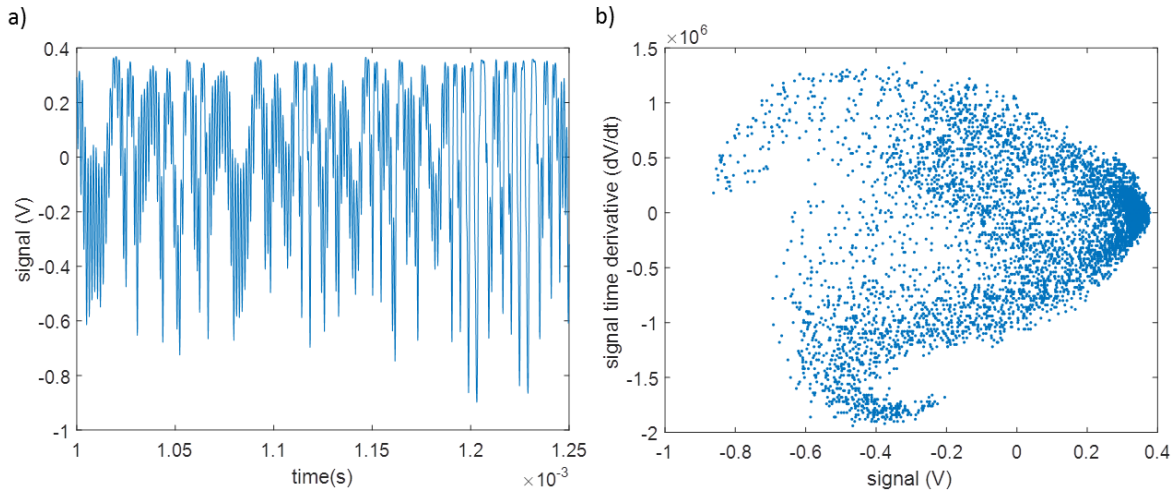

Figure 6-21: Experimental chaotic time series a) and Poincare map b) for $V_{\mathrm{MEMS}} = 128$ V, $V_{D1} = 3.24$ V, an excitation amplitude of 15.05 dBm and a driving frequency of 1.39 MHz

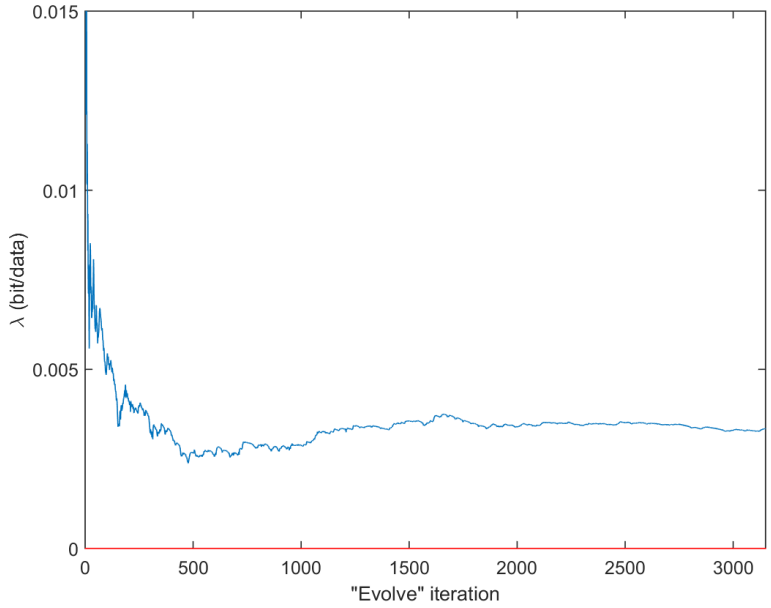

Figure 6-22: Maximal lyapunov exponent, numerically obtained with Wolf algorithm from the chaotic time series depiced in figure 6-21.

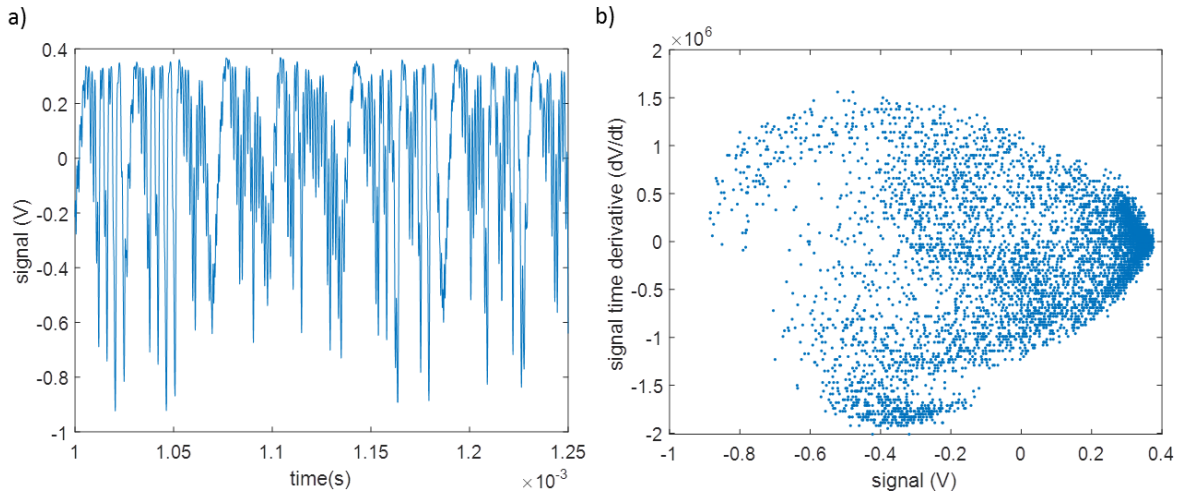

Figure 6-23: Experimental chaotic time series a) and Poincare map b) for $V_{\mathrm{MEMS}} = 128$ V, $V_{D1} = 3.72$ V, an excitation amplitude of 15.05 dBm and a driving frequency of 1.39 MHz.

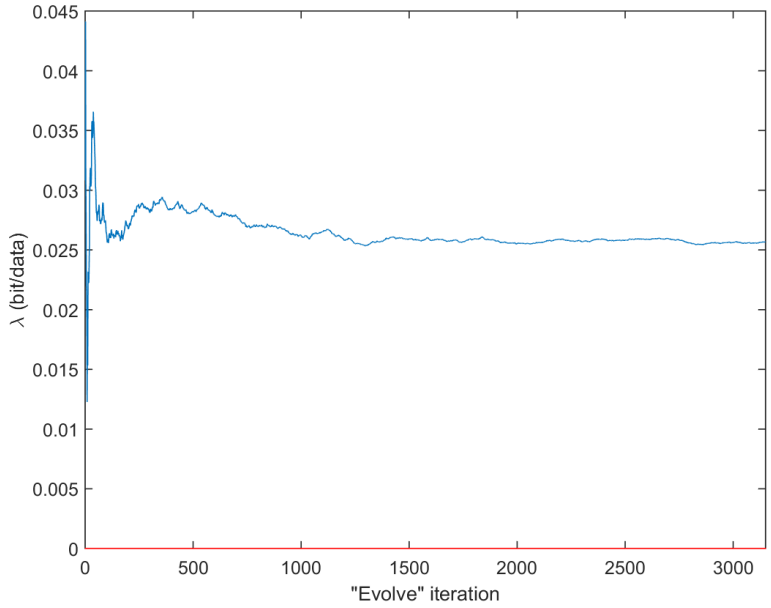

Figure 6-24: Maximal lyapunov exponent, numerically obtained with Wolf algorithm from the chaotic time series depiced in figure 6-23 .

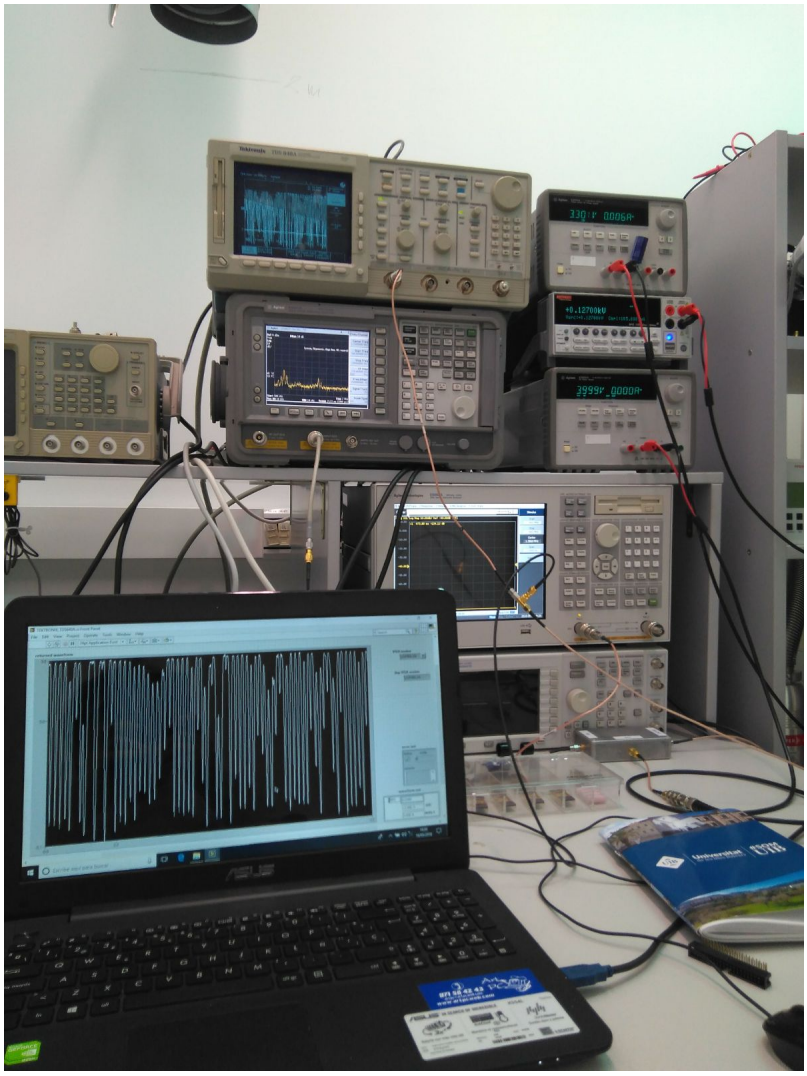

Figure 6-25: Photograph of the lab facilities, and of the experimental detection of chaotic behavior in MEMS resonator.

6.5 Discussion and conclusions

The first conclusions of this chapter is the verification of the hypothesis formulated in previous chapters, especially in chapter 5. The nonlinear model based on the finite difference method from a near real deflection profile and taking into account the second order nonlinear effects has been experimentally proved to be accurate enough. To reach this conclusion, the experimental variation of resonance frequency with the bias voltage and temperature has been observed to have the shape predicted by the model equations, and the experimental values of the second order constants have been seen to keep respectively similar enough

values between them. The experimental measurements have been performed on devices fabricated in two different generations (Run 2015 and 2017 sets). The slight differences between the values of the constants of the second-order non-linear effects can be explained from the tolerances of the nominal fabrication process and chemical attack for the release of the structure. However, in the specific case of the residual stress, as stated in chapter 5, its variation has a great influence on the results and produces a large divergence on the bias voltage values needed to obtain two-well potential distribution.

On the other hand, the second order parameter values of the tungsten resonators have been experimentally obtained. The measured average value of the tungsten residual stress disables the achievement of the bistability at reasonable values of temperature and/or bias voltage.

The bistable behavior reported in this chapter has been experimentally measured for the first time in straight and non axially forced cc-beam resonators. The measured bistable behaviors have been experimentally obtained for the bias voltage predicted by the nonlinear model (as function of the respective values of the second order effects constants) in several fabricated devices. The homoclinic structure has been found to arise for a bias voltage slightly lower than the predicted one, because in practice the resonance frequency does not reach the zero value with the growing bias voltage, but starts to grow again from a small but greater than zero value. Furthermore, from the situation of bistability, generated in a fabricated device, extensive chaotic motion, based on the homoclinic structure proper of the achieved two-well potential distribution, has been experimentally measured for the first time in a cc-beam resonator providing, in addition, important improvements in terms of frequency (MHz range) and bandwidth with respect to the previous experimental works reported in literature. The chaotic nature of the measured signals have been verified by means of a numerically obtained positive and finite value of the maximal Lyapunov exponent from a trustworthy algorithm.

Chapter 7

Conclusions and future work

7.1 Final conclusions

The research developed in the frame of the CRIPTOMEMS and KEYNEMS projects provides interesting and novel results which forecast promising further applications in several fields. From the analytical study of the nonlinear behavior of electrostatically actuated MEMS resonators, the goal has been the exploitation of such nonlinearities to achieve bistability and chaotic response of the system. Because of the inherent benefits in terms of scalability, frequency, simplicity and fabrication reliability, the elected structure has been the straight and non-axially forced cc-beam with in plane resonance. The strategy has been a previous obtaining of the conditions for the reproduction of the Duffing-Ueda strange attractor based on the homoclinic structure, namely the 2WP distribution or bistability.

A first study has been performed to explore the viability of using beam-shaped microstructures as chaotic signal generators. This first analysis has been performed on the parallel plate approximation, since it is the most common analysis found in literature, and accurate enough for small oscillations amplitudes. Within this framework, and from the demonstrated stiffness tuning capability of the symmetrical application of a bias voltage, a geometric design condition (which involves a minimum ratio between the electrode-beam gap and the beam width) to allow the generation of two-well potential distribution has been stated. This gap/width ratio has been found to be the factor which the ratio between the upper and lower bias boundary values for bistability depends on. The design criterion has been the minimization of the bias voltage needed to achieve bistability while enabling a margin of 10% between the upper and lower bias boundary values for bistability. This

criterion implies the use of the minimum beam width allowed by the considered technology. The requirement of 10% of margin between bias boundary values sets the needed gap value. The beam length is found to depend on the desired natural frequency, and a linear dependence between the needed bias voltage for bistability and the design frequency has been proven. Within this approximation, numerical simulations of the nonlinear response of a 1MHz-designed cc-beam with dimensions corresponding to a 350 nm-width polysilicon resonator beam have been performed, obtaining extensive chaotic response, analyzed with Melnikov method, and corroborated with a positive and finite value of the maximal Lyapunov exponent. Besides the analysis of the conditions to obtain chaotic behavior based on 2WP, the possibility of chaos based on 1WP has been explored, through the analytical and numerical study of the Duffing equation and an exhaustive revision of the literature. The lack of robustness of the chaotic behavior, the narrow range of the system parameters that provide it and the need of large excitation amplitudes discourage this approach.

A later analysis has gone beyond the parallel plate approximation. In this case we have developed a model based on a FDM from a near real deflection profile, which considers a set of nonlinear effects whose influence is lower than the main terms in model equation but that cannot be neglected for a proper design and analysis procedure. These second order effects are the fabrication residual stress, the contribution of the fringing fields, and the thermal effect. FEM simulations and experimental measurements have been used to determine the proper expressions to include these effects into the model. The tensile fabrication residual stress is found to provoke an increase of the linear stiffness while the nonlinear stiffness remains practically unaffected. The fringing fields effect implies a contribution to the coupling capacitance between the beam and the electrodes that increases the electrostatic force. The growing temperature is known to make the beam less stiff, through a decrease of the Youngs modulus, and the appearance of an internal compressive stress that stands against the fabrication residual stress. The considerations previously made for the parallel plate approximation have been adapted to the more accurate FDM approach. The accuracy of this electromechanical model has been tested by comparing its predictions with the results provided by COMSOL FEM simulations. Moreover, since only time derivatives are included in the model, it can be implemented in an analog hardware description language (AHDL) enabling system level electrical simulations.

With the accurate new model, the minimum gap/width ratio required to attain bista-

bility is no longer a constant, but depends on the residual stress and on the geometric parameters. In addition, the residual stress makes the needed bias voltage for bistability grow no longer linearly with the design natural frequency. In contrast, for each value of the residual stress there is an optimal frequency that minimizes the needed bias voltage to achieve the two-well potential distribution. In order to ensure the attainment of the geometric condition for bistabiliy or in any case, enlarge the margin between the bias boundary values, the thermal effect is applied to compensate the residual stress effect. Using this complete model, numerical simulations of the homoclinic chaotic response of a 600 nm-width 1MHz metal designed device are reported and checked with the maximal Lyapunov exponent criterion. The chaotic behavior is found to arise for a set of parameters for which the Melnikov criterion (properly adapted to the model based on finite difference method and considering the second order effects) predicts the possibility of chaotic response. Experimental results from fabricated metal and tungsten resonators with the AMS 035 technology have proved the accuracy of the complete FDM-based model, and provided the experimental values for the constants of the second order nonlinear effects. The tungsten resonators have been found to be unfeasible for its performance as 2WP systems under reasonable values of bias voltage and temperature, because of the presence of great values of residual stress.

Finally, for the first time, the bistable behavior and chaotic signal generation with simple and straight metal cc-beam resonator in the range of MHz has been experimentally measured. Extensive experimental homoclinic chaotic motion has been obtained from the bistable cc-beam resonator and validated by means of a positive Lyapunov exponent.

7.2 Future work

This work has contributed to the development of chaotic resonators by means of a low-cost CMOS-MEMS platform. The next step is to extend the experimental measures to new designs. The release and experimental corroboration of the correct performance of the polysilicon resonators is particularly promising, since they are supposed to provide a great improvement in terms of the needed bias voltage and because of the possibility of bistable and chaotic response at room temperature with a wide bias margin. In addition, new prototypes like curved beams and non-interdigitated comb drives have been included in a new set of fabricated devices (see figure 7-1). Through their experimental measurements, new

functionalities and features can be explored and compared with those of the cc-beam resonators. Finally, from the experimentally obtaining of the chaotic behavior, its application in secure communication purposes becomes available.

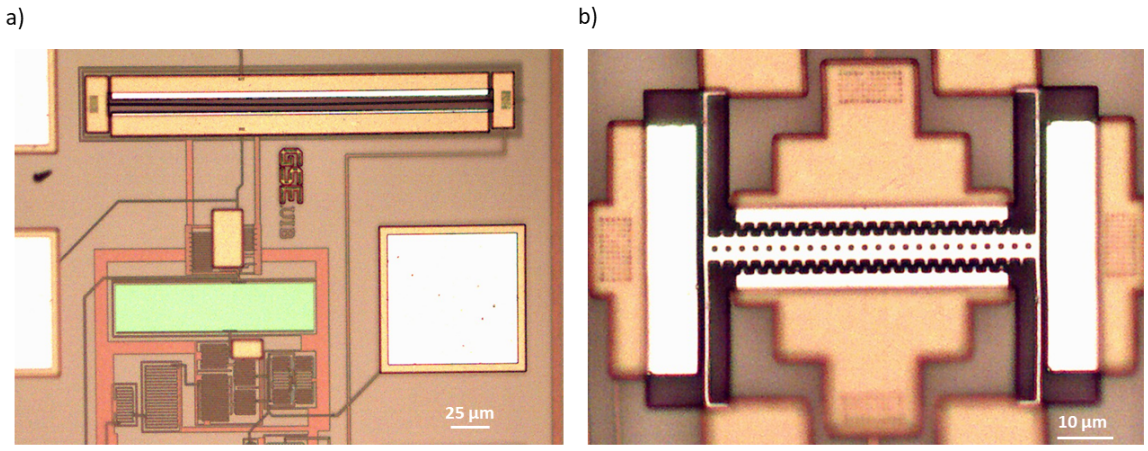

Figure 7-1: Optical images of a) Metal 3 arched beam and b) Metal 4 non-interdigitated comb drives resonator.

7.2.1 Application of chaotic systems in secure communications

The chaotic systems provide rich and complex possibilities for signal generation, with wide applicability in signal processing and communications. The apparent erratic essence (noise-like) but deterministic, with wide bandwidth in the frequency domain, of the chaotic signals allows its application in secure communication purposes, and more specifically in the field of cryptography. On the other hand, one of the most interesting properties of the chaotic signals is their capability of synchronization between pairs of chaotic transmitters [34]. A review of the chaotic synchronization and cryptography theory is exposed in Appendix D.

The great dependence on initial conditions exhibited by chaotic systems allows several parameters to be used as encryption key in a further cryptographic system based on chaotic MEMS [131]. The use of hardware-based cryptography, itself, is supposed to provide benefits in terms of frequency and speed on the traditional software cryptographic techniques. Moreover, the approach based on the dependence on a non-measurable physical parameter, provides an important added value.

Appendix A

MEMS chaotic response improvement with ANN and Fuzzy Control

Fuzzy logic has been revealed to be a powerful method to control different kind of plants. Its application in the control of nonlinear, subject to noise, or partially unknown systems is particularly useful. The use of fuzzy-logic controllers in chaotic systems reported in literature are focused on control and suppression of the chaotic response, which is considered to be undesirable. Thus, in [132] a fuzzy controller obtained from a knowledge base formed by fuzzy sets and inference matrix is used to perturb a variable of the Chua circuit and stabilize the chaotic output. Meanwhile, in [133] Gaussian membership based fuzzy models are used to estimate the unknown parameters and functions needed to build a controller that is proved, by means of the Lyapunov stability theory, to be useful to control a Duffing system. Concerning to the dynamics of MEMS, fuzzy systems have been designed in [26], [134] and [135] to mimic ideal controllers based on the Sliding Mode Control, i.e. feedback controllers which cause the state trajectory to reach a sliding surface and behaving as a stable trajectory. In such references, the fuzzy control is used to convert chaotic oscillations into desired regular ones, exhibiting a periodic behavior.

On the other hand, the ANNs are found to be a very powerful and efficient method for modeling purposes, due to their learning and generalization capabilities. They learn dependences between input-output dataset in the training procedure, adjusting the network

parameters (neuron connection weights and neuron transfer functions or thresholds). Once properly trained, the ANN provides quickly accurate output values from input vectors (that should belong to the same range as the training data, but may not be included in the training set) even without the knowledge of the modeled physical process [136].

A.1 Fuzzy-neural controller

Within the assumption made in chapter 4 (the parallel plate approximation and without considering the second order effects), let the dimensionless equation of the system be defined as

$$\hat{x}'' + \beta\hat{x} + \alpha\hat{x}^3 + \delta\hat{x}' = \mu_1\left(\frac{1}{(1-\hat{x})^2} - \frac{1}{(1+\hat{x})^2}\right) - \mu_2\frac{\cos(\Omega\tau)}{(1-\hat{x})^2} + \mu_3\frac{\cos(\Omega\tau)^2}{(1-\hat{x})^2} \tag{A.1}$$

where the dimensionless parameters β, α, δ are defined in section 4.4, and for this approach are found to be either constant or depend only on the ratio s/w. On the other hand, lets define $\mu_1 = \frac{1}{2}\mu V_{DC}^2$, $\mu_2 = \mu V_{DC}V_{AC}$, $\mu_3 = \frac{1}{2}\mu V_{AC}^2$, with $\mu = \frac{\epsilon_0 t_h l}{m_{\text{eff}}\omega_0^2 s^3}$. As it has been explained in chapter 4, the potential function of the system described by equation (A.1) exhibits two minima for a bias voltage range defined between the bias boundary values V_{pi0} and V_{piw}, namely in the range of μ_1 values between $\mu_{1\text{min}}$ and $\mu_{1\text{max}}$. In section 4.4 it has been stated that these boundary μ_1 values are respectively a constant ($\mu_{1\text{min}} = 0.25$) and an expression which depend only on the s/w ratio:

$$\mu_{1\text{max}} = \left(12.272\left(\frac{s}{w}\right)^2 + 16\right)^3\left(27\cdot(12.272)^2\cdot 16\left(\frac{s}{w}\right)^4\right)^{-1} \tag{A.2}$$

It is important to remember that this upper boundary value for bistability ($\mu_{1\text{max}}$) only exists if the two-well potential distribution has been reached, this is to say, if the dimensional condition for bistability $s > 1.615$ is attained. Consider a 1MHz -polysilicon resonator with a gap value that allows a 10% of margin between the bias boundary values for bistability (V_{pi0} and V_{piw}), with dimensions given in the first row of table 4.2 ($l = 54.6\mu$m , $w =$ 350nm, $t_h =$ 282nm, and $s =$ 842nm) and a quality factor $Q = 165$; the values of the dimensionless parameters results to be $\alpha = 4.44$, $\beta = 1$ (constant value for all resonators), $\delta = 6.061\cdot 10^{-3}$, $\mu_{1\text{min}} = 0.25$ (constant value for all resonators) and $\mu_{1\text{max}} = 0.3025$. Even

when the conditions to achieve robust and extensive chaotic response in nonlinear MEMS oscillators are verified, the attainment of the proper parameters which provide chaotic dynamics behavior (since it is highly sensitive to parameter variation) is not immediate. Instead of the large amount of time consuming numerical simulations that are needed to find the robust chaotic behavior (which is desired for its further applications) a new control method is proposed. This proposed new approach consists in the application of a fuzzy controller for the MEMS system that performs a search of the conditions of maximum richness in the chaotic behavior of the plant system (MEMS) within the design dimensions and biasing conditions that assure a two-well potential distribution. This search is executed by means of iterations that involve the change of an operating parameter and the measure of dynamic features in the output signal on a time window. The spectrum bandwidth parameter of the MEMS dynamics time-series is taken as a metric of the nonlinear and chaotic behavior of the system. In order to enable its further application in an experimental setting, the bandwidth is measured from the number of points (n) in the periodogram with a higher power than a boundary value (for instance 10% of the maximum power), which can be directly obtained from a spectrum analyzer.

Artificial neural networks are proposed to be combined with this control application due to their powerful capability to be also adapted to a nonlinear, noisy, or even partially unknown plant; moreover, ANNs are easily implementable over, for instance, a microcontroller or FPGA [137]. The scheme of the whole system is depicted in figure A-1. An artificial neural network is trained to provide a crisp control function, given by a control surface (obtained by fuzzy reasoning), which relates the input bandwidth parameter n_k (which would be obtained from a spectrum analyzer (S.A.)) of the nonlinear signal generated by the MEMS system and the actual value of the μ_{1k} parameter (namely the dimensionless value of the actual DC voltage term in the system) to a normalized output control value a_k falling between -1 and 1. The subscript k represents the k-th iteration of the control procedure. The control output value a_k is adjusted to the dimensional value by an amplification block (K) and applied directly to the MEMS system as a variation of the DC voltage value. This amplification block must have the parameters corresponding to the technology of the MEMS system, as well as the iteration number k and the first DC value applied.

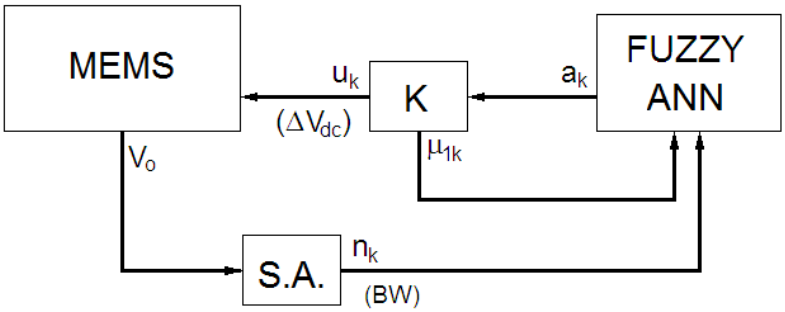

Figure A-1: Scheme of the proposed fuzzy control system implemented with ANN.

The control surface is designed to be stable and to be useful to maximize the chaotic response, knowing the high variance of the dynamical behavior with small changes in the parameters (that can be caused by fabrication tolerances). Since the control surface is obtained from the normalized parameters proper to the dimensionless equation of the MEMS system, equation (A.1), the same control surface is valid for any cc-beams resonator dimensions, and for different fabrication technologies, while having the same s/w ratio. In this sense, to apply the control system to cc-beam devices built with different dimensions, or in different technologies, only the amplification block K has to be modified.

To build the fuzzy-based control surface, several steps in fuzzy reasoning are performed [138]. First of all, state and control variables are identified and the membership functions of the several linguistic labels for each variable are constructed (figure A-2). In the present case, the bandwidth quantification (n) and the μ_1 parameter are identified as state variables and the normalized output (a), as control variable. After that, an implication matrix between the linguistic labels is defined (table A.1). The singleton function of the actual state variable values as fuzzification and the Mamdami function as fuzzy implication function are used (see [138] for wider explanation of fuzzy reasoning). For each pair of inputs, the union (maximum function) of the intersections between the output membership function and the minimum of the input singletons is obtained. Consequently, the defuzzified value is obtained as the centroid of this area. For each pair of inputs, a single defuzzified value is obtained and the whole set of defuzzified values can be represented as the mesh of the control surface (figure A-4). It is preferable to control the normalized bias input parameter rather than the normalized excitation amplitude, because the margin between the bias boundary values (given by V_{pi0} and V_{piw}) is better known and wider than the margin of the AC amplitude

(bounded by the dynamic pull-in effect). The avoidance of DC values upper than the pull-in limits is needed, so the fuzzy implication matrix between linguistic variables must ensure a negative increment of the control variable for the linguistic variable corresponding to values of μ_1 close to the upper limit. Furthermore, to avoid the creation of infinite loops, the control surface must have a non symmetric transition from positive to negative output sign. After defining the fuzzy sets of the linguistic variables and the fuzzy implication matrix, the control surface is obtained. The membership functions and, in consequence, the control surface, may be customized to fulfill the stability requirements and may be optimized to allow a faster convergence.

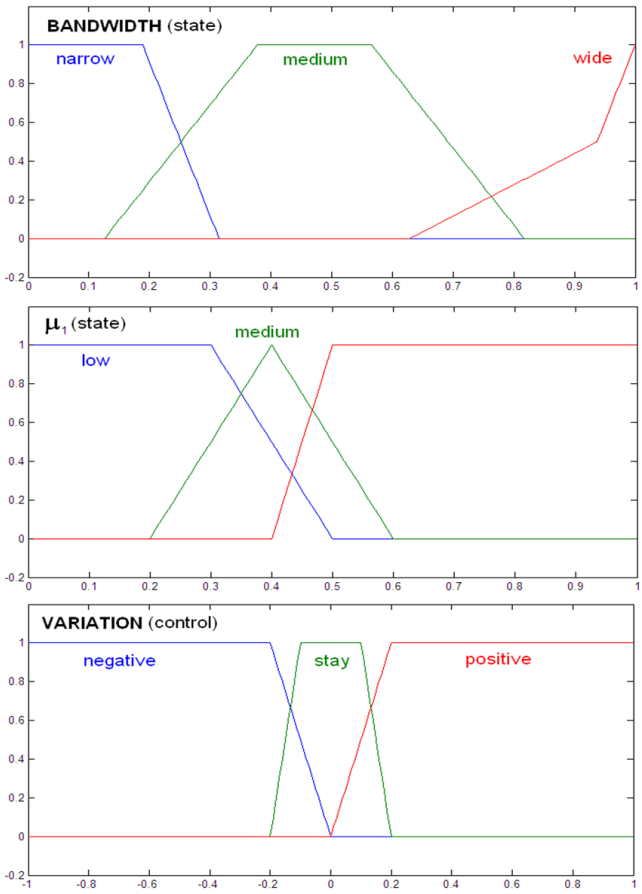

Figure A-2: Membership functions of the different variables to the respective linguistic labels.

Table A.1: Fuzzy implication matrix between the linguistic labels.

	μ_1 low (ML)	μ_1 medium (MM)	μ_1 high (MH)
Bandwidth narrow (BWN)	variation positive (VP)	variation positive (VP)	variation negative (VN)
Bandwidth medium (BWM)	varition positive (VP)	variation positive (VP)	variation negative (VN)
Bandwidth wide (BWW)	stay (VS)	stay (VS)	stay (VS)

A.2 Analytical study of the control convergence

The MEMS system (expressed for instance in equation (A.1) or (4.33)) can be view as an equation in the form $\dot{\bar{x}} = f(\bar{x}, t)$, and moreover, considering the definition of the driving force (equation (3.34)) with constant V_{AC} and taking V_{DC} as the control variable, the MEMS system equation has the form of $\dot{\bar{x}} = f(\bar{x}, t, V_{DC})$. The function of the number of points in the periodogram with a significant power (n_k) has the form of $n_k = g(\bar{x}, V_{DC} + u_{k-1})$, where u_k is the output of the whole control system (both n_k and u_k refer the k-th iteration), and g is, a priori, an unknown function. N_d is considered the minimum acceptable measure value for the bandwidth, i.e. the lower bound of the iteration procedure goal. If the error function of each iteration is defined as $e_k = H[N_d - n_k - 1]$, where $H[x]$ is the Heavyside function and a Lyapunov candidate function that verifies the conditions of the Lyapunov stability for discrete-time systems [139] is found, the convergence to zero of the error function is assured. In summary, given a system described as $x_{k+1} = h(x_k)$, for an equilibrium point $x = x_{st}$, and a neighborhood U of such a point, a generic discrete-time Lyapunov candidate function $V(x)$ must verify:

- $V(x) \geq 0 \forall x \in U$ and $V(x_{st}) = 0$
- $\Delta V(x) = V(h(x)) - V(x) \leq 0 \forall x \in U$
- The equilibrium point $x = x_{st}$ is G_0-asymptotically stable, with $G_0 = \{x \in U : V(x) = 0\}$

to ensure that the equilibrium point is stable in the terms of Lyapunov along the neighborhood. Then a discrete-time Lyapunov candidate function has been found as

$$V_k = e_k u_k^2 \tag{A.3}$$

Ensuring that u_k can only be zero if e_k is zero, the value of the function V_k is zero if and only if e_k is zero; otherwise V_k is always positive. The variation between iterations of this Lyapunov candidate function is

$$V_k - V_{k-1} = e_k u_k^2 - e_{k-1} u_{k-1}^2 \tag{A.4}$$

Following with the premise that if e_k is zero then u_k is zero, $e_{k-1} = 0$ implies $e_k = u_k = 0$, and in this case $V_k - V_{k-1} = 0$. For $e_{k-1} > 0$, e_k any of the following situations can occur:

- $e_k = 0$ and thus $V_k - V_{k-1} = -u_{k-1}^2 < 0$
- $e_k > 0$ and thus $V_k - V_{k-1} = u_k^2 - u_{k-1}^2$, in consequence the only condition that is needed to be ensured is $|u_k| < |u_{k-1}|$

The last condition to be fulfilled is that $e = 0$ must be G_0- assimptotically stable. Let the sets G_0 and B_θ be defined to be respectively $G_0 = \{e \in \mathbb{R} : V(e) = 0\}$, and $B_\theta = \{x \in \mathbb{R} : |x| < \theta\}$, with θ an arbitrary real positive number while h^+ is defined to be the set of the functions $h^+ = \{h^p, p \in \mathbb{N}\}$, with h being the iteration function ($h_{e_k} = e_{k+1}$). The condition of G_0- assimptotic stablility of the $e = 0$ point implies that $\forall \epsilon > 0 \exists \delta > 0 : h^+(B_\delta \cap G_0) \subset B_\epsilon$, and there have to exist a $\delta > 0$ such that $\lim_{p \to \infty} h^p(e) = 0 \forall e \in (G_0 \cap B_\delta)$. It is straightforward to see that, since $G_0 = \{0\}$ these latter two conditions are fully satisfied and, in consequence the zero error is stable in terms of Lyapunov criteria. In summary, in order to verify the analytical conditions that assure the error function convergence to zero, the control system output must be zero only once the procedure goal is reached, and its absolute value must decrease in each iteration.

A.3 Results and simulations

The disposed setup (figure A-1) allows the fulfillment of the requirements for zero error convergence. The condition of zero output control value for all the bandwidth inputs higher than the boundary value N_d is imposed by the control surface. The condition $|u_k| < |u_{k-1}|$ is imposed by means of a cycle divider, in the block K, that performs an amplification given by a q^{-k} factor with k the iteration number and q a real positive number: in this case the actual output value of the k iteration is $\frac{u_k}{q^k}$ and the condition to be fulfilled is

that $\left|\frac{u_k}{q^k}\right| < \left|\frac{u_{k-1}}{q^{k-1}}\right|$ which in the worst case implies $\left|\frac{\max(u)}{q^k}\right| < \left|\frac{\min(u)}{q^{k-1}}\right|$, and last expression implies $\frac{|\max(u)|}{|\min(u)|} < q$, the q value must higher than the ratio max/min nonzero output absolute value of the control surface. From this condition a compromise solution is needed: the control surface must be smooth enough to be able to be obtained by the fuzzy inference procedure, but on the other hand a small ratio of the max/min nonzero output of the control surface is required because otherwise the output value of the control system would decrease quickly and an increasing number of iterations would be needed to reach the goal of the control system. After the definition of the control surface, an artificial neural network is defined in Matlab environment and trained with the input output values of the control surface (figure A-3). Numerical simulations with the parameters corresponding to a 1MHz natural frequency polysilicon cc-beam resonator (designed in AMS 035 technology with the parameters given in the first row of table 4.2) were performed, using the control system designed to verify the exposed convergence conditions, with the aim to corroborate its capability in leading to a desired chaotic response. The control surface used is shown in figure A-4. In each iteration the output of the control system is applied to the input parameters of the next simulation. The spectral representation of the MEMS system dynamic response time series shows a significant increase of the bandwidth in a few iterations, as it is shown in figure A-5. A further analysis of the position time series of the MEMS system confirms that, while the response after the first iteration corresponds to a linear behavior, the dynamics of the system after the third iteration of the control system corresponds to a robust cross-well chaotic behavior, as can be deduced from the typical chaotic shape of the Poincare map, and a finite and positive maximal Lyapunov exponent. An analysis of the numerical simulations indicates that the stability conditions obtained in section A.2 are sufficient but not necessary to achieve the system convergence to the desired rich and complex chaotic stationary response. However, the implementation of a control system that verifies such conditions guarantees mathematically the convergence.

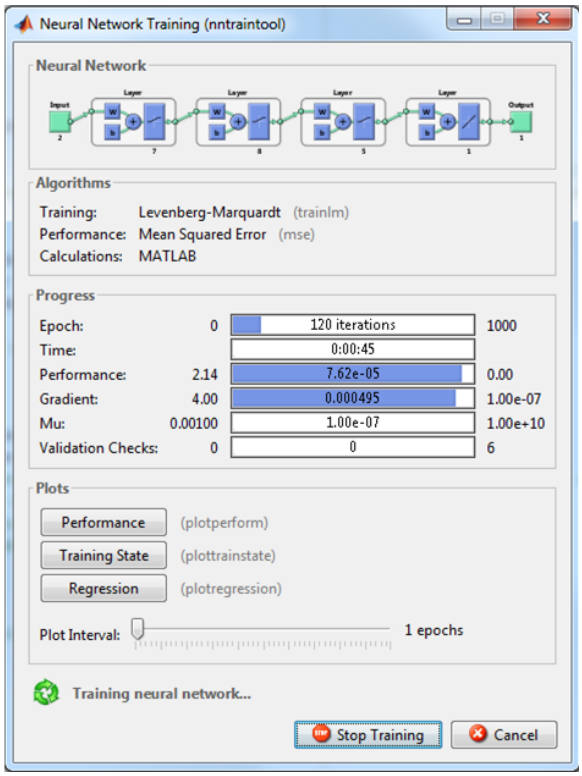

Figure A-3: Matlab ANN toolbox interface, plotted during the training process.

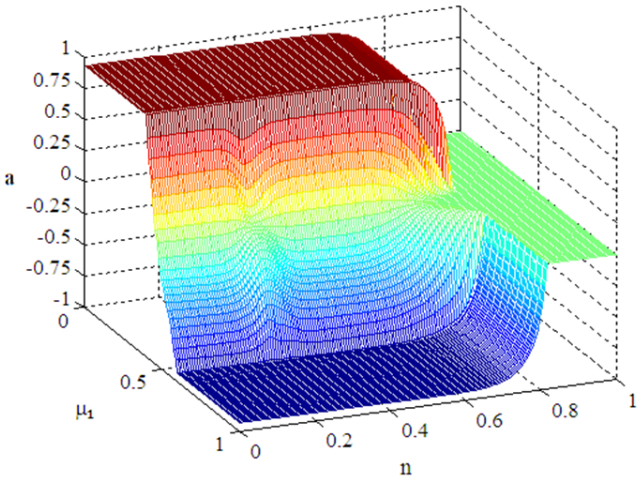

Figure A-4: Control surface designed to test the effectiveness of the control system; z axis represents the normalized response of the control systems, x axis the normalized actual μ_1 value) and the y axis normalized actual bandwidth measure.

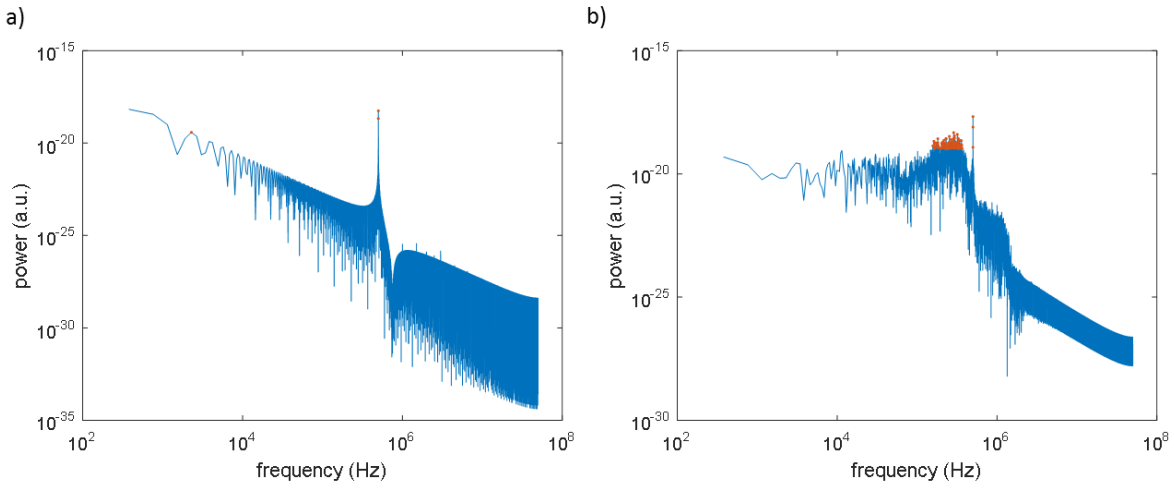

Figure A-5: Signal spectrum representation after a) 1 iteration, and b)4 iterations. In the present case, the amplification block K provides $u_k \approx 0.072\,(a_k)^{1/2}$.

A.4 Conclusions

A control method, combining fuzzy logic and artificial neural networks, to improve the chaotic response richness of a nonlinear submicrometric electromechanical resonator is developed for the first time as a way to optimize the MEMS performance in secure communication applications (for instance). The stability requirements and the conditions (a decreasing absolute value in the control output and null output value only when the goal is achieved) for the convergence to the desired chaotic dynamics have been analytically determined, and applied to simulate the response of a cc-beam resonator designed in a CMOS technology. The application of the fuzzy-ANN based control method presents several advantages such as the applicability in nonlinear plants, and the adaptability to different types of plant technology. Moreover, since the presented control system performs an automatic search for the parameters that provide a wide band chaotic response, the actual values of these parameters are no needed, and in consequence the control system can be applied in further experimental applications, in which, due to the hypersensitivity of chaotic behaviour, small parameter variations due to fabrication tolerances may invalidate the previous simulation-based chaos search results. The input-output dataset provided by the fuzzy control surface in this approach is smooth enough to allow the ANN to achieve, after the training procedure, almost perfect adjustment.

Appendix B

Model integration in Verilog-A for system level electrical simulations

Analog hardware description languages (AHDL) allow the description of multi-domain systems like MEMS within EDA tools [140]. Therefore, system level electrical simulations of MEMS together with CMOS circuitry can be carried out using an electrical simulator. A Verilog-A compact macro-model using the description provided in chapter 5 has been developed and allows electromechanical simulations in an analog circuit design environment like Virtuoso (CADENCE). The beam-driver model is defined as a three-port system: the two electrodes and the beam structures. Each port is bi-directional to allow current in any direction depending on the configuration used to actuate the beam and to perform the electrical readout. The main Verilog-A macro-model features are:

- Nonlinear model.
- Accurate deflection profile of the beam.
- Fringing field factor (α_{FF}).
- Residual fabrication stress contribution to the stiffness (σ_{eff}).
- 3 bidirectional electrical ports: electrode 1 ($D1$), electrode 2 ($D2$) and beam (B).
- 2 mechanical output ports: nominal displacement (Z) and velocity (V_b).
- Number of beam slices (N) as an input parameter.

All the macro-model input parameters related to the beam-driver system geometrical dimensions (thickness, length, width and gap), the structural material mechanical properties (E,ρ), the dielectric constant, Q-factor, number of slices, fringing field factor and residual fabrication stress can be set by the user. This macro-model, whose symbol in CADENCE environment is shown in figure B-1, is suited for all type of analyses including AC, DC, transient, noise, PSS, parametric, etc.

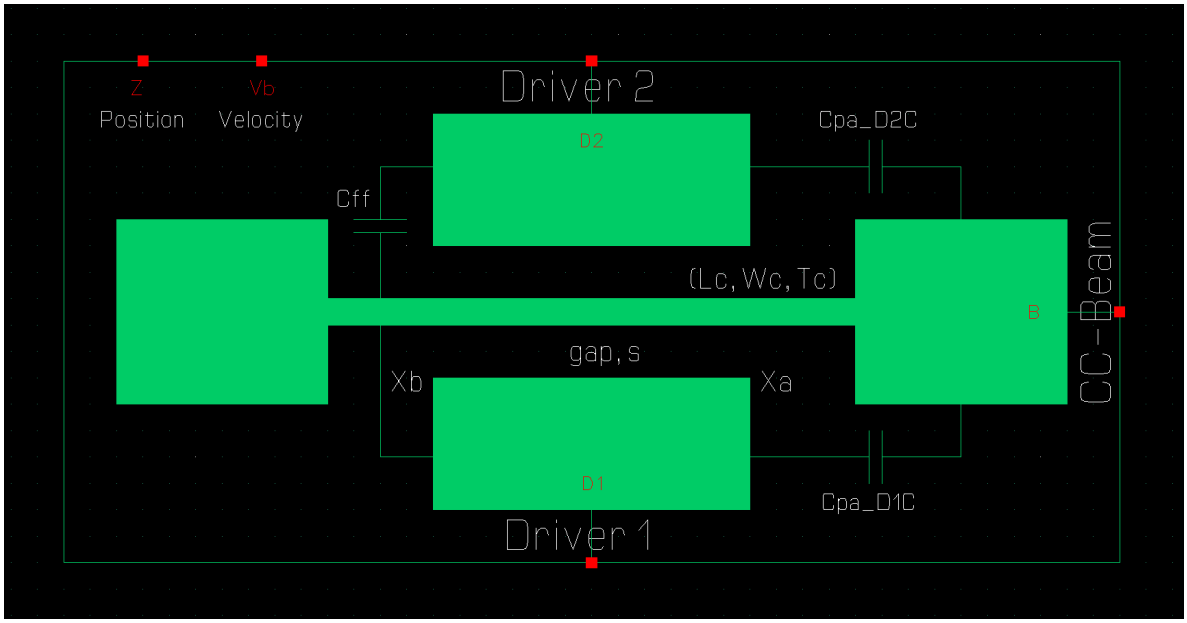

Figure B-1: Plot of the Verilog-A macro-model symbol in CADENCE environment.

The Verilog-A model has been applied to analyze the conditions that enable bistability behavior in a cc-beam resonator with the parameters specified in previous sections for C4 resonator of the Run 2015 set (a AMS 035 metal fabricated resonator with dimensions $l = 63.85\mu$m, $w = 600$nm, $t_h = 850$nm, and $s = 2.07\mu$m) intended to act as a chaotic signal generator (figure B-2). These dimensions ensure the attainment of design condition to allow the two-well potential distribution in a cc-beam within the model based on finite difference method and taking into account the influence of the fabrication residual stress (equation (5.20)), for the σ_{eff} values considered in figure 5-4 (chapter 5). The results in figure B-2 agree with those shown in table 5.3 (chapter 5).

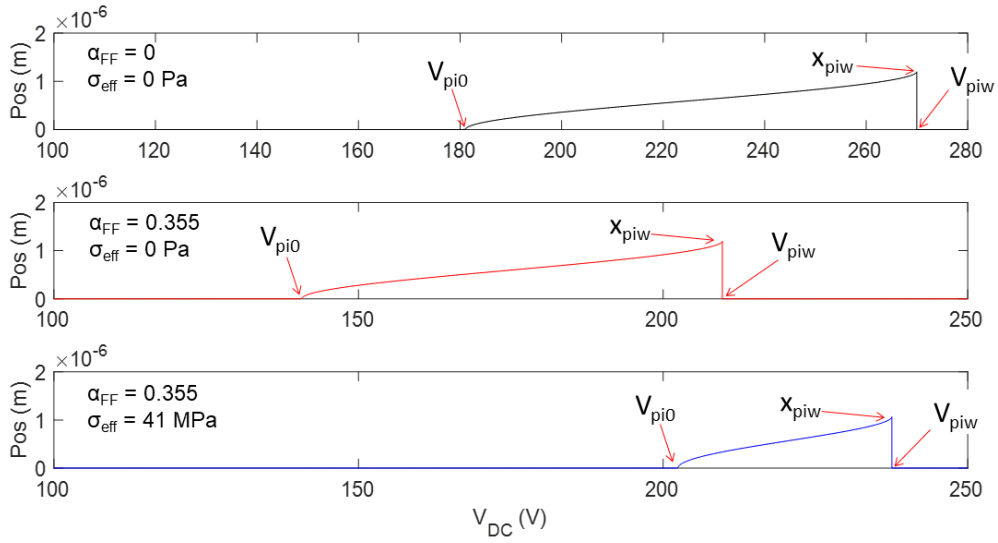

Figure B-2: Equilibrium position results obtained from a DC analysis using Spectre simulator in CADENCE framework, for various values of the fringing field constant, and the fabrication residual stress parameter.

Appendix C

Runs description

The complete layout of the two generations of chips designed and fabricated in the framework of this thesis are summarized in this appendix.

C.1 First generation: Run 2015 set

The Run 2015 set, labeled as Keyset15, was fabricated in November 2015. The resonators (cc-beams) corresponding to the KEYNEMS project are C1 to C4 (Metal 4 resonators) and C5, C6 (polysilicon resonators). The complete chip dimensions are 3.65×1.84 mm.

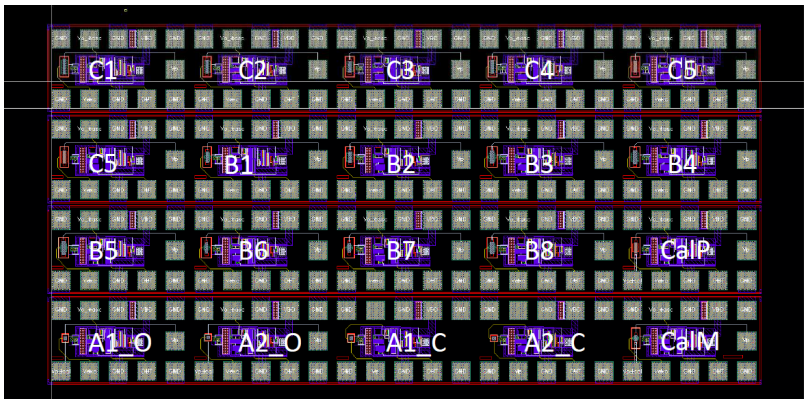

Figure C-1: Cadence screen of the Run 2015 design.

C.2 Second generation: Run 2017 set

The Run 2017 set, labeled as Keyset17, was fabricated in November 2015, The resonators (cc-beams) corresponding to the KEYNEMS project are C1 to C5 (Metal 4 resonators),

C6 to C8 (Metal 3 resonators), C9 to C12 (tungsten resonators), C13 to C15 (polysilicon resonators), and two additional curved cc-beams C16 (Metal 3) and C17 (polysilicon). The complete chip dimensions are 4.35×3.42 mm.

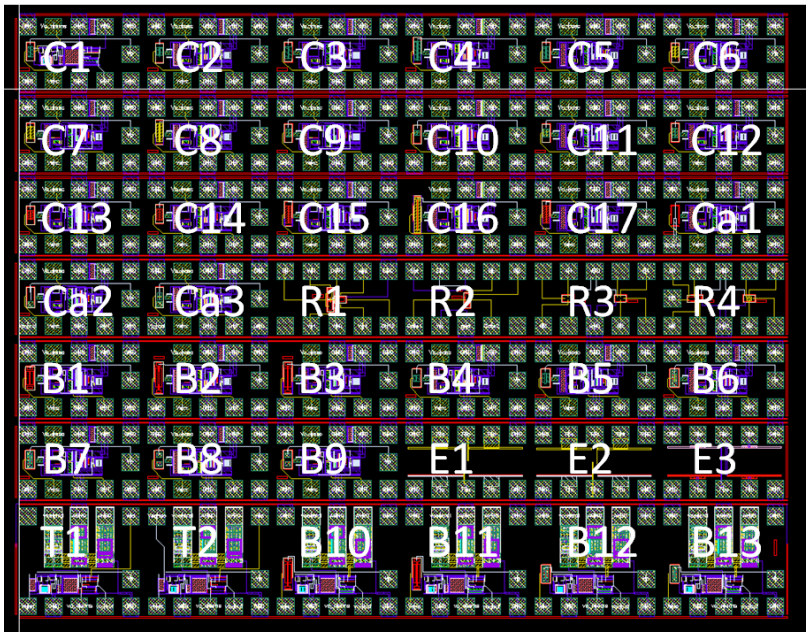

Figure C-2: Cadence screen of the Run 2017 design.

C.3 Resonators designation code

With the aim of simplifying the designation of the resonators, belonging to the several chips fabricated in each generation, the nomenclature used in this thesis is the following: Cx(y)-kz, where x stands for the resonator number, y stands for the chip number and z can be 15 (corresponding to the Run 2015 set) or 17 (corresponding to the Run 2017 set). As an example C4(1)-k15 refers to the C4 resonator of the chip 1, corresponding to the Run 2015 set.

Appendix D

Theoretical approach to chaotic synchronization and cryptography

Cryptography, a subfield of cryptology, deals with the construction of protocols, methods and algorithms to achieve information security goals, typically on a mathematical basis [141]. By definition, and encrypted signal is understood as the codified signal which cannot be interpreted without a processing depending on a key (parameter containing the secret information which allows the interpretation of the message). The different approaches for secure communication cryptographic schemes are classified by the essence of the key and by the used methods of encryption and decryption. All the chaos-based procedures for secure communications applications follow a common scheme (figure D-1): a valuable message is protected by means of a chaotic encryption, sent through a non-secure channel, and will be only able to be decrypted if the encryption key is known.

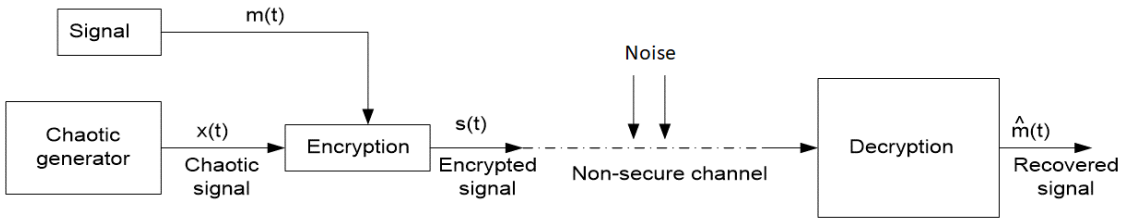

Figure D-1: Common scheme of the cryptographic systems.

D.1 Theoretical approach to the synchronization between chaotic systems

The property of synchronization between two identical chaotic systems was first reported by [33], and [142]. Most of the approaches to the synchronization between chaotic systems use the mastes-slave (or drive-response) formalism. In this way, the idea of synchronization consists in the use of an output signal from the master system to control the slave system so that the output signal of the slave system tends asymptotically to the output signal of the master system [143]. Consider the chaotic system described by

$$\dot{x} = Ax + f(x) \tag{D.1}$$

and

$$\dot{y} = By + g(y) + u \tag{D.2}$$

with $x, y \in \mathbb{R}^n$ being the state vectors of the systems; A,B $n \times n$ system parameter matrices, and $f, g : \mathbb{R}^n \longrightarrow \mathbb{R}^n$ the respective nonlinear functions of each system. Consider the system described by equation (D.1) as the master system, and the system described by equation (D.2) as the slave system. In the equation of the slave system there is an additional term: $u \in \mathbb{R}^n$ is a control vector or controller of the slave system. In this way, the problem of the synchronization consists in designing a controller u which ensures the asymptotic convergence of the output signals of both systems. The synchronization error vector is defined as

$$e = y - x \tag{D.3}$$

with $e \in \mathbb{R}^n$. The synchronization error dynamics can be expressed, in the general case as

$$\dot{e} = By - Ax + (g(y) - f(x)) + u \tag{D.4}$$

The asymptotic convergence of the output signals of both systems implies $\lim_{t\to\infty} \|e(t)\| = 0$; the stability theory of Lyapunov can be used to demonstrate and ensure this convergence. A candidate Lyapunov function (V) is defined as a scalar function ($V : \mathbb{R}^n \longrightarrow \mathbb{R}$) , locally (in 0) definite positive (i.e. exists U, neighborhood of 0 such that $V(0) = 0$ and $V(x) > 0 \forall x \in U \backslash \{0\}$) which can be used to prove the stability of a dynamic system [144].

Using this definition, the stability theorem of Lyapunov is announced:

Theorem 2. *Let x=0 be an equilibrium point of the autonomous system* $\dot{x} = f(x)$*, and let* $V(x)$ *be a candidate Lyapunov function whose time derivative function is given by*

$$\dot{V}(x) = \frac{\partial V(x)}{\partial x}\frac{dx}{dt} = \nabla V(x)\,\dot{x} = \nabla V(x)\,f(x), \tag{D.5}$$

if the function $\dot{V}(x)$ *is locally semidefinite negative (i.e. exists U, neighborhood of 0 such that* $\dot{V}(x) \leq 0 \forall x \in U$ *then the system presents a stable equilibrium in U. If the function* $\dot{V}(x)$ *is locally definite negative (i.e. exists U, neighborhood of 0 such that verifies strictly that* $V(x) < 0 \forall x \in U \backslash \{0\}$ *), the equilibrium is locally attractive. Finally if the candidate Lyapunov function is definite positive over all the domain, and its time derivative is globally definite negative (*$\dot{V}(x) < 0 \forall x \in \mathbb{R}^n \backslash \{0\}$*), the equilibrium is globally attractive.*

There is no general method for building or finding a candidate Lyapunov function, which is able to demonstrate the stability of a given equilibrium point. However, it is important to notice that the stability theorem of Lyapunov (theorem 2) provide sufficient but non necessary conditions for the demonstration of an equilibrium stability, thus the impossibility of finding a proper Lyapunov function to prove the stability of an equilibrium point does not imply the instability of this equilibrium point.

To test the stability of the state $e = 0$ of the synchronization error system (D.4) consider a candidate Lyapunov function given by $V(e) = e^T P e$, with P being a definite positive matrix[1], then $V(e)$ will be a positive definite function by construction. If a controller u is defined to provide an error which verifies

$$\dot{V}(e) = \frac{dV(e)}{dt} = -e^T Q e \tag{D.6}$$

with Q being a definite positive matrix, then it can be assured that $V(e)$ is a definite negative function. In this way, the stability theorem of Lyapunov guarantees that the error function dynamics is globally exponentially stable stable, and that the condition $\lim_{t\to\infty} \|e(t)\| = 0$ is verified for all initial condition $e(0) \in \mathbb{R}^n$.

[1] a positive definite matrix M has, amongst others,these equivalent definitions:

- The determinants of all the principal minors are positive.
- All the eigenvalues of M are positive.
- $z^T M z > 0 \forall z \in \mathbb{C}^n$ such that $z \neq 0$.

D.1.1 Synchronization of Lorenz systems

In [34] and [145], the synchronization between chaotic Lorenz systems is experimentally demonstrated as well as its application in the duty of encryption and decryption. The Lorenz system, which can be physically implemented as a circuit, is mathematically described as the following equation, obtained from the electric parameters of the circuit [146]:

$$\begin{aligned} \dot{u} &= \sigma\,(v-u) \\ \dot{v} &= ru - v - 20uw \\ \dot{w} &= 5uv - bw \end{aligned} \tag{D.7}$$

For some set of parameter values, the Lorenz system exhibit chaotic behavior. Moreover, the synchronization between pairs of Lorenz systems present a surprising robustness over noise and (more important), over the useful signal which can be encrypted inside the chaotic output of the master system.

Consider a pair of identical Lorenz system, where one of them works as master system, and the other one as the slave system. Figure D-2 shows the scheme of the synchronization between the two Lorenz systems. The output signal of the master system, obtained from its first channel, is introduced in the second and third channel of the slave system and its output signal is compared with the one of the master system to obtain the error signal.

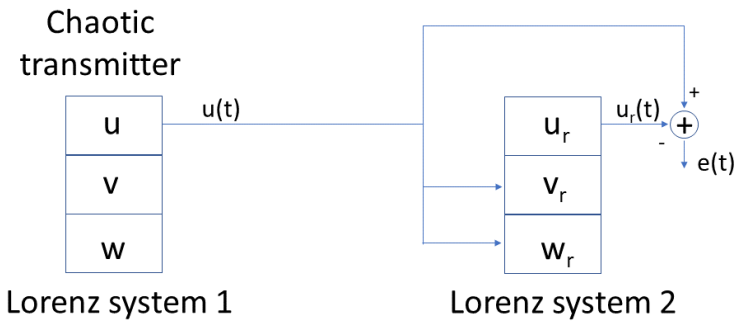

Figure D-2: Scheme of the synchronization between two identical Lorenz systems [34].

Assuming that both systems are identical, the equations of the slave system are found

to be:

$$\begin{aligned} \dot{u}_s &= \sigma\left(v_r - u_s\right) \\ \dot{v}_s &= ru - v_s - 20uw_s \\ \dot{w}_s &= 5uv_s - bw_s \end{aligned} \tag{D.8}$$

with (u_s, v_s, w_s) the vector of state variables of the slave system. The error vector is defined as:

$$\begin{aligned} e_1 &= u - u_s \\ e_2 &= v - v_s \\ e_3 &= w - w_s \end{aligned} \tag{D.9}$$

and its dynamics are governed by:

$$\begin{aligned} \dot{e}_1 &= \sigma\left(e_2 - e_2\right) \\ \dot{e}_2 &= -e_2 - 20u\left(t\right)e_3 \\ e_3 &= 5u\left(t\right)e_2 - be_3 \end{aligned} \tag{D.10}$$

The synchronization procedure consists, then, in the stabilization of the error vector dynamics in the state $e = \vec{0}$. In this case, the dynamics of the error vector is found to be asymptoticly stable, the state $e = \vec{0}$ is globally attractive. It can be demonstrated with the Lyapunov function:

$$V\left(e,t\right) = \frac{1}{2}\left(\frac{1}{\sigma}e_1^2 + e_2^2 + 4e_3^2\right), \tag{D.11}$$

which verifies the condition of being definite positive in the origin, and its time derivative function:

$$\dot{V}\left(e,t\right) = \frac{1}{\sigma}e_1\dot{e}_1 + e_2\dot{e}_2 + 4e_3\dot{e}_3 = -\left(e_1 - \frac{1}{2}e_2\right)^2 - \frac{3}{4}e_2^2 - 4be_3^2 \tag{D.12}$$

is globally definite negative. In this way, the stability theorem of Lyapunov guarantees that $e\left(t\right) \longrightarrow \vec{0}$ when $t \longrightarrow \infty$, i.e. synchronization would take place.

The demonstrated capability of autosynchronization can be applied in the definition of

a whole cryptographic system based on the chaotic behavior of Lorenz systems. Figure D-3 represents the scheme of the cryptographic system: a useful signal $m(t)$ is masked by the chaotic signal $u(t)$ generated in the master system, generating the $s(t)$ signal. The power of the useful signal is significantly lower than the power of the chaotic signal. The $s(t)$ signal will be emitted and used by the slave system to reproduce the chaotic signal, and this reproduction of the master chaotic signal is not affected or disturbed either by noise or by the useful signal carried by the $s(t)$ signal. In this way, the subtraction of the generated chaotic signal in the slave system $u_r(t)$ from the transmitted $s(t)$ provide a good approximation to the useful signal ($\hat{m}(t) \approx m(t)$). Figure D-4 represents the Lorenz system 3D trajectory obtained from the master system (u, v, w) and the one obtained from the slave system (u_r, v_r, w_r) from the whole numerically implemented Lorenz cryptographic system. Moreover, figure D-5 depicts the original and the recovered useful signal, encrypted and decrypted by the Lorenz cryptographic system.

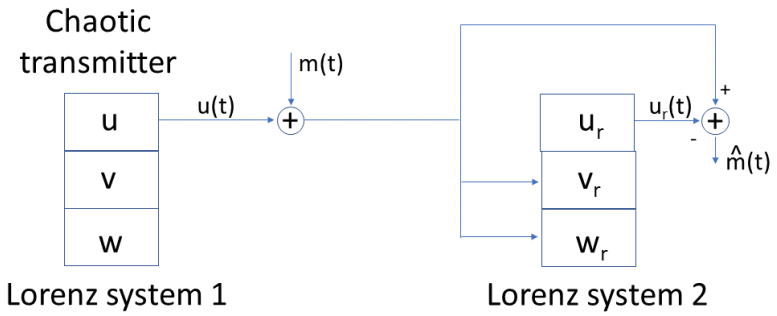

Figure D-3: Scheme of the cryptographic system based on Lorenz systems [34].

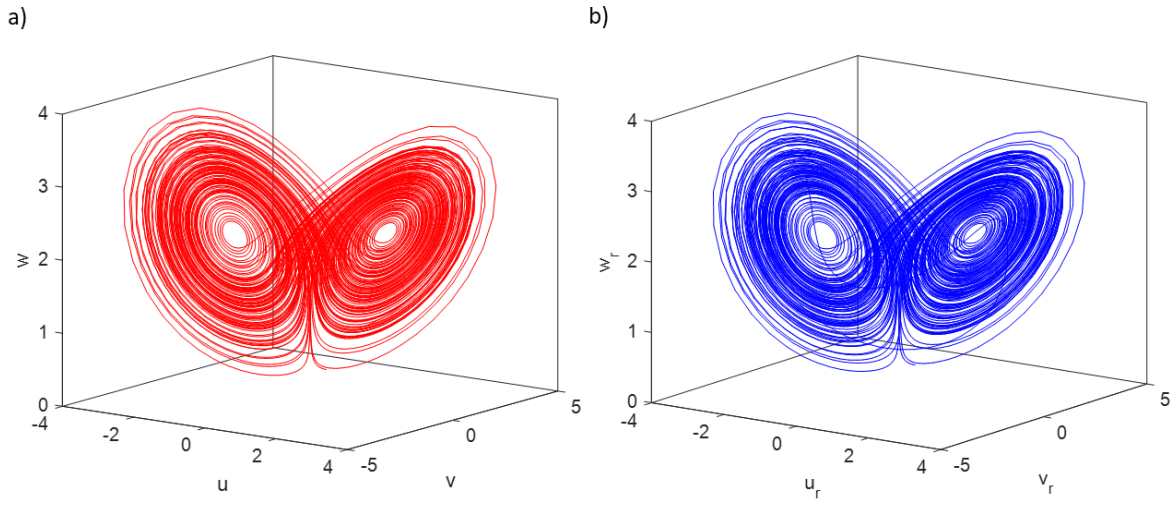

Figure D-4: Original (a)) and recovered (b)) 3D chaotic trajectories of the Lorenz systems in the cryptographic scheme depicted in figure D-3.

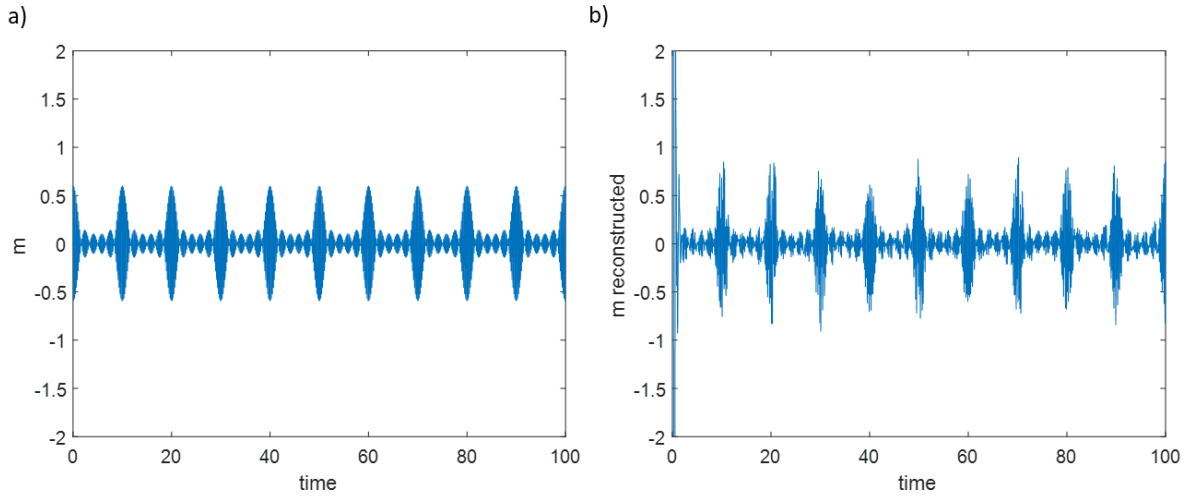

Figure D-5: Time series of the original and the recovered useful signal using the cryptographic scheme depicted in figure D-3.

It is interesting to note that this idea is not restricted to just the Lorenz circuit, but has wider potential [34]. For example, Kocarev et al. have also demonstrated the masking concept into chaotic signal, by using Chua‘ s circuit [147]. In consequence , this scheme must also be tested in the Duffing system.

D.1.2 Synchronization of Duffing systems

In [143], the problem of synchronize two chaotic Duffing systems is tackled. Considering a master system whose dynamics is governed by the equations

$$\begin{aligned} \dot{x}_1 &= x_2 \\ \dot{x}_2 &= -\delta x_2 + \beta x_1 - \alpha x_1^3 + \Phi \cos(\omega t) \end{aligned} \tag{D.13}$$

and an slave system, which is suppose to be defined by identical parameters than the master system:

$$\begin{aligned} \dot{y}_1 &= y_2 + u_1(t) \\ \dot{y}_2 &= -\delta y_2 + \beta y_1 - \alpha y_1^3 + \Phi \cos(\omega t) + u_2(t) \end{aligned} \tag{D.14}$$

with $u^T = [u_1, u_2]$ being the controller (not necessarily linear) that must be designed to provoke an asymptotic convergence to zero of the error function defined as

$$\begin{aligned} e_1 &= y_1 - x_1 \\ e_2 &= y_2 - x_2 \end{aligned} \tag{D.15}$$

and whose dynamics is governed by

$$\begin{aligned} \dot{e}_1 &= e_2 + u_1(t) \\ \dot{e}_2 &= -\delta e_2 + \beta e_1 - \alpha\left(y_1^3 - x_1^3\right) + u_2(t) \end{aligned} \tag{D.16}$$

The controller proposed by [143] is

$$\begin{aligned} u_1(t) &= -e_2 - \epsilon e_1 \\ u_2(t) &= -\beta e_1 + \alpha\left(y_1^3 - x_1^3\right) + (\delta - \epsilon)\epsilon_2 \end{aligned} \tag{D.17}$$

with $\epsilon > 0$, in this way, the equation governing the error vector dynamics become

$$\begin{aligned} \dot{e}_1 &= -\epsilon e_1 \\ \dot{e}_2 &= -\epsilon e_2 \end{aligned} \tag{D.18}$$

The Lyapunov function given by

$$V(e) = \frac{1}{2}\left(e_1^2 + e_2^2\right) \tag{D.19}$$

is considered; this function is clearly a positive definite function, because it is generated from $V(e) = e^T P e$, with $P = \begin{bmatrix} 1/2 & 0 \\ 0 & 1/2 \end{bmatrix}$ definite positive matrix (the determinants of all its principal minors are positive, and hence it verifies that $z^T M z > 0 \forall z \in \mathbb{C}^n$ such that $z \neq 0$). Moreover the function (D.19) has a time derivative function given by

$$\dot{V}(e) = e_1\dot{e}_1 + e_2\dot{e}_2 = -\epsilon\left(e_1^2 - e_2^2\right) \tag{D.20}$$

which is clearly definite negative. Then the stability theorem of Lyapunov assures that the behavior of the error vector is exponentially stable toward the $\vec{0}$ value, in a global way.

The property of the synchronization between Duffing systems has been used to synchronize the chaotic behavior of MEMS systems in [18]. The synchronization procedure consists in the use of a controller in the acceleration component of the slave system y_2 consisting in a negative gain for the error signal between the position signals of both systems as shown in figure D-6. This approach is the first proposal of synchronization between two MEMS devices. The master system is defined as:

$$\begin{aligned} \dot{x}_1 &= x_2 \\ \dot{x}_2 &= q_0\left(Gx - k_1 x_1 - k_3 x_1^3 - c x_2\right) \\ Gx &= \left(V_1 + V_a \sin(t)\right)^2 f(x_1) - \left(V_2 - V_a \sin(t)\right)^2 f(-x_1) \end{aligned} \tag{D.21}$$

and the slave system:

$$\begin{aligned} \dot{y}_1 &= y_2 \\ \dot{y}_2 &= q_0\left(Gy - k_1 y_1 - k_3 y_1^3 - c y_2 + u\right) \\ Gy &= \left(V_1 + V_a \sin(t)\right)^2 f(y_1) - \left(V_2 - V_a \sin(t)\right)^2 f(-y_1) \end{aligned} \tag{D.22}$$

$$u = p(x_1 - y_1) \tag{D.23}$$

where k_1 and k_3 are the linear and nonlinear stiffness respectively, c is the damping term, and $f(x)$ is a function of the position component x which models the half of the x-derivative of the capacitance. In this case both systems are supposed to be identical.

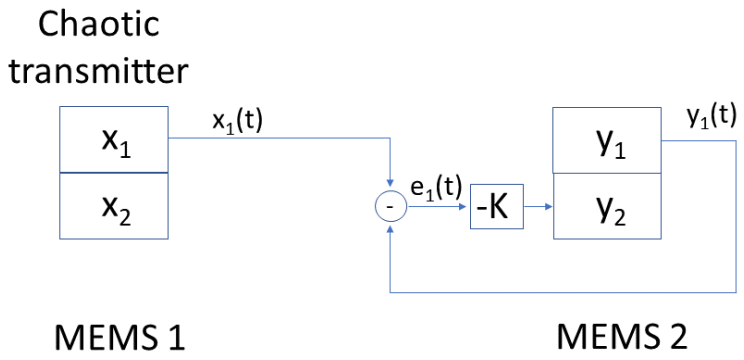

Figure D-6: Scheme of the synchronization two MEM systems proposed in [18].

Reference [18] reports a successful numerical synchronization between a pair of matched chaotic MEMS.

D.2 Chaotic masking cryptography in Duffing systems

The syncrhonization between pairs of chaotic Duffing systems is only possible in absence of perturbations (namely noise or useful signal), otherwise the slave system reproduces its whole $s(t)$ input signal. In this way the cryptographic scheme based on chaotic masking does not provide the desired results, and the recovery of the useful signal is not available. However, reference [148] proposes an approximation to perform the synchronization between chaotic Duffing systems based on "H_∞" approach, which is supposed to result more robust over external perturbations. Consider a Duffing master system defined by equation (D.13), while the slave system is governed by:

$$\begin{aligned} \dot{z}_1 &= z_2 + u_1(t) + d_1(t) \\ \dot{z}_2 &= -\delta z_2 + \beta z_1 - \alpha z_1^3 + \Phi\cos(\omega t) + u_2(t) + d_2(t) \end{aligned} \tag{D.24}$$

with $u(t)^T = [u_1, u_2]$ being the controller vector, and $d(t)^T = [d_1(t), d_2(t)]$ the vector of external disturbances. With this situation, the dynamics of the error vector can be written

as

$$\begin{aligned} \dot{e}_1 &= e_2 + u_1(t) + d_1(t) \\ \dot{e}_2 &= -\delta e_2 + \beta e_1 - \alpha\left(z_1^3 - x_1^3\right) + u_2(t) + d_2(t) \end{aligned} \tag{D.25}$$

and in matricial form

$$\dot{e} = Ae + g(t) + u(t) + d(t) \tag{D.26}$$

with

$$A = \begin{bmatrix} 0 & 1 \\ -\beta & -\delta \end{bmatrix}; \quad g(t) = \begin{bmatrix} 0 \\ -\alpha\left(z_1^3 - x_1^3\right) \end{bmatrix} \tag{D.27}$$

Following the calculation of the method H_∞, the system presents H_∞ synchronization si the error function $\vec{e}(t)$ satisfies

$$\int_0^\infty e^T(t)\, Qe(t)\, dt < \xi^2 \int_0^\infty d^T(t)\, d(t)\, dt \tag{D.28}$$

with $\xi > 0$ being the H_∞ norm bound (or disturbance attenuation level) and Q is a positive and symmetric matrix. With these definitions [148] enunciates and demonstrates :

Theorem 3. *For given $\xi > 0$ and $Q = Q^T$, if there exists $X = X^T > 0$ and Y such that*

$$\begin{bmatrix} AX + XA^T + Y + Y^T & I & X \\ I & -\xi^2 I & 0 \\ X & 0 & -Q^{-1} \end{bmatrix} < 0 \tag{D.29}$$

where A is the matrix of the linear factor of the error dynamics (equation (D.26)*), then H_∞ synchronization of the chaotic signals, with ξ level of attenuation is obtained under the controller*

$$u(t) = YX^{-1}e(t) - g(t) \tag{D.30}$$

Moreover, a corollary announced and demonstrated by reference [148], shows that using the system of controllers defined by theorem 3, asymptotic synchronization between chaotic Duffing systems in the absence of external disturbance is also obtained.

On the other hand in [149] the synchronization between MEMS chaotic output signals in the presence of parametric uncertainties and/or disturbances has been analytically achieved,

and demonstrated from the Lyapunov stability theory. The nonlinear dynamics of the master system is defined as

$$\dot{\vec{x}} = \vec{F}(\vec{x})\,\vec{\alpha} + \vec{f}(t, \vec{x}) \tag{D.31}$$

which is susceptible of reporting chaotic behavior, and a second nonlinear system is defined as

$$\dot{\vec{y}} = \vec{G}(\vec{y})\,\vec{\beta} + \vec{g}(t, \vec{y}) + \vec{h}(\vec{y})\,u \tag{D.32}$$

which acts as slave system; $\vec{x}, \vec{y} \in \mathbb{R}^2$ are bounded state vectors, $\vec{\alpha} = (\alpha_1, \alpha_2, \ldots, \alpha_n)^T$, and $\vec{\beta} = (\beta_1, \beta_2, \ldots, \beta_p)^T$ are vectors of parameters corresponding to each equation ($\vec{\beta} \in \mathbb{R}^2$ is the vector of uncertain parameters, or subjected to disturbances, belonging to the slave system) , u is a scalar control function and

$$\vec{F}(\vec{x}) = \begin{bmatrix} 0 & 0 & \ldots & 0 \\ F_{21}(\vec{x}) & F_{22}(\vec{x}) & \ldots & F_{2n}(\vec{x}) \end{bmatrix} = \begin{bmatrix} 0 \\ \vec{F_2} \end{bmatrix} \tag{D.33}$$

$$\vec{G}(\vec{y}) = \begin{bmatrix} 0 & 0 & \ldots & 0 \\ G_{21}(\vec{y}) & G_{22}(\vec{y}) & \ldots & G_{2p}(\vec{y}) \end{bmatrix} = \begin{bmatrix} 0 \\ \vec{G_2} \end{bmatrix} \tag{D.34}$$

$$\vec{f}(t, \vec{x}) = \begin{bmatrix} x_2 \\ f(t, \vec{x}) \end{bmatrix}; \quad \vec{g}(t, \vec{y}) = \begin{bmatrix} y_2 \\ g(t, \vec{y}) \end{bmatrix}; \quad \vec{h}(t, \vec{y}) = \begin{bmatrix} 0 \\ h_2(\vec{y}) \end{bmatrix} \tag{D.35}$$

It can be observed that equations (D.31) and (D.32) have the typical form of the Duffing equation and of the MEMS resonators with electrostatic actuation, and that the controller term in the slave system is only applied to the acceleration component of the system. The functions $f(t, \vec{x})$ and $g(t, \vec{y})$ represent the excitation functions in each system, while h_2 is defined as $h_2 = \dfrac{1}{(1-y)^2}$, considering y to be the dimensionless position (adimensionalized with the gap parameter). Given four positive constants ($\mu_1, \mu_2, \mu_3, \mu_4 > 0$), if the control term is defined as

$$u = h_2^{-1}(\vec{y}) \left(-\vec{G_2}\hat{\beta} + F_2\hat{\alpha} - g(t, \vec{y}) + f(t, \vec{x}) - \mu_2^{-1}(\mu_1 e_1 + \mu_2 e_2) - \mu_2^{-1}\mu_1 e_2 \right) \tag{D.36}$$

while the parameters are updated according to the laws

$$\begin{aligned}\dot{\hat{\alpha}} &= -\mu_3\left(\mu_1 e_1 + \mu_2 e_2\right)\mu_2 \vec{F}_2^T \\ \dot{\hat{\beta}} &= -\mu_4\left(\mu_1 e_1 + \mu_2 e_2\right)\mu_2 \vec{G}_2^T \end{aligned} \tag{D.37}$$

and $\vec{e} = \vec{x} - \vec{y} = (e_1 e_2)^T$ is the error vector, then the slave system synchronizes globally and asymptotically with the master system. This statement can be proved using the Lyapunov stability theory. The main drawback of this synchronization scheme to be used in secure communication purposes is that the controller, which has to be be implemented by circuitry (and in this way it can be replied), depends on the parameters of both systems, thus it depend also on the encryption key. In this way, the encryption key remains exposed.

D.3 Cryptographic method based on initial conditions modulations

The technique of encryption by modulation is based on the introduction of the useful message in the parameters of the system dynamics. Specifically, the encryption can be performed when the information affects the initial conditions of the master system. It can be mathematically demonstrated that under specific circumstances the synchronization error vector dynamics depends on the initial conditions of the systems. Following the formulation of [131], with the Duffing master system dynamics described by

$$\begin{aligned}\dot{x}_1 &= x_2 \\ \dot{x}_2 &= -\alpha x_1^3 - \delta x_2 + \Phi\cos\left(x_3\right) \\ \dot{x}_3 &= 1 \end{aligned} \tag{D.38}$$

and the slave system dynamics described by

$$\begin{aligned}\dot{y}_1 &= y_2 \\ \dot{y}_2 &= -\alpha y_1^3 - \delta y_2 + \Phi\cos\left(y_3\right) \\ \dot{y}_3 &= 1 \end{aligned} \tag{D.39}$$

Those systems present a synchronization error which can be expressed as

$$x_2(t_0) - y_2(t_0) = -\delta \int_0^{t_0} (x_2(t) - y_2(t))\, dt + 2\Phi \sin(\psi) \sin(t_0 + \Omega) + C_1 \qquad \text{(D.40)}$$

with C_1 being a integration constant, $\psi = \dfrac{x_3(0) - y_3(0)}{2}$ (x_3, y_3 are constants) and $\Omega = \psi + y_3(0) + \dfrac{\pi}{2}$. When t tends to infinity, equation (D.40), stays in a stationary state dominated by the second term [150]. This second term depends on the initial conditions of both systems: if $x_3 - y_3 = 2n\pi$ where n is an integer, the error function will tend to zero, while if $x_3 - y_3 = 2(n-1)\pi$, the error will stay at its maximum stationary state. The synchronization, then is made to depend on the initial conditions of the systems. The communication system is designed by choosing two sets of initial conditions, to represent the binary values 0 and 1 whether synchronization takes place or not. Once the values for the initial conditions in the slave system have been established, to represent a 0 bit the initial conditions in the master system that allow the synchronization are imposed, and to represent a 1 bit the initial conditions in the master system that prevent the synchronization are imposed (or vice versa, only a criterion is needed). For instance, if an initial value $y3 = 0$ is fixed in the slave system, following the previous criterion a 0 bit is obtained from an input $m = x_3(0) = 2\pi$ and a 1 bit is obtained from an input $m = x_3(0) = \pi$. In this way, a binary word of 4 bits [0,1,0,1] is transmitted by the initial conditions $m = [2\pi, \pi, 2\pi\pi]$ imposed at the master system by means of resets with a frequency f_1 (which has not to correspond to any frequency proper to the chaotic response) and recovered in the slave system as the error signal of the synchronization between it and the master system output: a period $T_1 = \dfrac{1}{f_1}$ of synchronization equals to a logical 0, and a period T_1 of no synchronization corresponds to a logical 1.

D.4 Requirements for secure communications based on chaotic MEMS

The engineering problem of the secure communications based on chaotic MEMS consists basically in the use of the generated chaotic signal to encrypt the useful signal, and decrypt the unintelligible signal by means of another chaotic MEMS, which have to synchronize with the first one. The synchronization must be conditioned to the identity of an unclonable

parameter (the encryption key) of both MEMS (the transmitter and the receiver). In summary, the design constraints of the cryptographic system based on chaotic MEMS are:

1. The useful signal must be placed, in frequency domain, into the bandwidth of the chaotic signal used to encrypt, in order to prevent the possibility of its interception by filtering.

2. The chaotic behavior must be sensitive to small variations of the parameter taken as the encryption key, because otherwise it would be possible to decrypt the useful signal without the encryption key.

3. The chaotic behavior must be robust (non sensitive) to the variations of the other physical parameters due to fabrication tolerances, because otherwise the recovering of the useful signal would be impossible, even possessing the encryption key.

4. The designed controllers, which will be implemented in the circuitry, must not depend on any parameter related to the encryption key, because otherwise, it would be exposed and will be easily duplicable, and only reproducing the circuitry the decryption would be available.

5. The synchronization between the generated chaotic signals by both generators must be attained in a robust way regarding to external perturbations (like the useful signal).

6. The controllers, which belong to the slave system must be able to be implemented, this is to say, they must refer to variables that can be accessed. For instance, there is no way to introduce a control signal to the velocity channel of the slave system. Mainly, the available access to the system variables is through the bias voltage and the AC excitation, which directly influence the acceleration channel of the electromechanical system.

7. In order to obtain a robust synchronization, it is necessary to have a feedback that keeps the error variable stable to avoid divergent behaviors.

The fulfillment of all these requirements when designing a complete cryptographic system based on the chaotic behavior of MEMS constitutes a challenge for future work. However, the steps to overcome the first and main obstacle (the achievement of robust and stationary

chaotic behavior in MEMS resonators with sufficient performance to be used in applications of cryptography) have been done in the current dissertation.

Bibliography

[1] R. O. Topaloglu, "More than Moore Technologies for Next Generation Computer Design," *Springer-Verlag New York*, 2015.

[2] R. Feynman, "There's Plenty of Room at the Bottom," *Engineering and Science*, vol. 23, pp. 22–36, 1960.

[3] H. Nathanson, W. Newell, R. Wickstrom, and J. Davis, "The resonant gate transistor," *IEEE Transactions on Electron Devices*, vol. 14, no. 3, pp. 117–133, 1967. [Online]. Available: http://ieeexplore.ieee.org/lpdocs/epic03/wrapper.htm?arnumber=1474635

[4] W. C. Tang, T. C. H. Nguyen, and R. T. Howe, "Laterally Driven Polysilicon Resonant Microstructures," *Sensors and Actuators*, vol. 20, no. 1-2, pp. 25–32, 1989.

[5] C. T. Nguyen, "Frequency-selective MEMS for miniaturized low-power communication devices," *IEEE Transactions on Microwave Theory and Techniques*, vol. 47, no. 8, pp. 1486–1503, 1999.

[6] S. Lee, M. U. Demirci, and C. T. C. Nguyen, "A 10MHz Micromechanical Resonator Pierce Oscillator for Communications," *11th International Conference on Solid-State Sensors and Actuators*, 2010.

[7] K. H. L. Chau, S. R. Lewis, Y. Zhao, R. T. Howe, S. F. Bart, and R. G. Marcheselli, "An integrated force-balanced capacitive accelerometer for low-g applications," *Sensors and Actuators A*, vol. 54, pp. 472–76, 1996.

[8] R. Bashir, "BioMEMS: state-of-the-art in detection, opportunities and prospects," *Advanced Drug Delivery Reviews*, vol. 56, pp. 1565–1586, 2004.

[9] C. L. Goldsmith, A. Malczewski, Z. . Yao, S. Chen, J. Ehmke, and D. H. Hinzel, "RF MEMS variable capacitors for tunable filters," *International Journal of RF and Microwave Computer-Aided Engineering*, vol. 9, no. 4, pp. 362–374, 1999.

[10] H. T. Jiang, Y. Wang, J. Yeh, and N. Tien, "On-chip spiral inductors suspended over deep copper-lined cavities," *IEEE Transactions on Microwave Theory and Techniques*, vol. 48, no. 12, pp. 2415–23, 2000.

[11] E. R. Brown, "RF-MEMS switches for reconfigurable integrated circuits," *IEEE Transactions on Microwave Theory and Techniques*, vol. 46, no. 11, pp. 1868–1880, 1998.

[12] C. T. Nguyen, "MEMS Technologies and Devices for Single-Chip RF Front-Ends," *Int. Conf. on Ceramic Interconnect and Ceramic Microsystems Technologies (CICMT), Tech. Dig*, 2006.

[13] T. Y. J. Alligood, K.T. Sauer, "Chaos, an Introduction to Dynamical Systems," *Springer-Verlag, New York, USA*, 1997.

[14] J. Sprott, "Chaos and Time-Series Analysis," *Oxford University Press*, 2010.

[15] M. T. Rosenstein, J. J. Collins, and C. J. De Luca, "A practical method for calculating largest Lyapunov exponents from small data sets," *Nonlinear Phenomena*, vol. 65, no. 1, pp. 117–134, 1993.

[16] F. Moon, "Chaos and fractal dynamics," *John Wiley and Sons*, 1997.

[17] S. Strogratz, "Nonlinear dynamics and chaos," *Perseus Books, Reading, Massachusetts*, 1994.

[18] Y. Wang, S. Adams, J. Thorp, N. MacDonald, P. Hartwell, and F. Bertsch, "Chaos in MEMS, parameter estimation and its potential application," *IEEE Transactions on Circuits and Systems I: Fundamental Theory and Applications*, vol. 45, no. 10, pp. 1013–1020, 1998.

[19] K. Shaw, Z. Zhang, and N. MacDonald, "SCREAM I: A single mask, single crystal silicon process for microelectromechanical structures," *MEMS 1993*, pp. 115–160, 1993.

[20] B.E. DeMartini, H.E. Butterfield, J. Moehlis and K. Turner, "Prediction and validation of chaotic behavior in an electrostatically actuated microelectromechanical oscillator," *Transducers and Eurosensors*, no. 805, pp. 1697–1700.

[21] B. E. DeMartini, H. E. Butterfield, J. Moehlis, and K. L. Turner, "Chaos for a microelectromechanical oscillator governed by the nonlinear mathieu equation," *Journal of Microelectromechanical Systems*, vol. 16, no. 6, pp. 1314–1323, 2007.

[22] J. Guckenheimer and P. Holmes, "Nonlinear Oscillations, Dynamical Systems, and Bifurcations of Vector Fields," *Springer-Verlag*, 1983.

[23] S. Liu, A. Davidson, and Q. Lin, "Simulation studies on nonlinear dynamics and chaos in a MEMS cantilever control system," *Journal of Micromechanics and Microengineering*, vol. 14, no. 7, pp. 1064–1073, 2004.

[24] S. K. De and N. R. Aluru, "Complex oscillations and chaos in electrostatic microelectromechanical systems under superharmonic excitations," *Physical Review Letters*, vol. 94, no. 20, pp. 1–4, 2005.

[25] S. De and N. Aluru, "Complex nonlinear oscillations in electrostatically actuated microstructures," *Microelectromechanical Systems, Journal of*, vol. 15, no. 2, pp. 355–369, 2006. [Online]. Available: http://ieeexplore.ieee.org/xpls/abs_all.jsp?arnumber=1618721

[26] H. S. Haghighi and A. H. D. Markazi, "Chaos prediction and control in MEMS resonators," *Communications in Nonlinear Science and Numerical Simulation*, vol. 15, no. 10, pp. 3091–3099, 2010. [Online]. Available: http://dx.doi.org/10.1016/j.cnsns.2009.10.002

[27] M. S. Siewe and U. H. Hegazy, "Homoclinic bifurcation and chaos control in MEMS resonators," *Applied Mathematical Modelling*, vol. 35, no. 12, pp. 5533–5552, 2011. [Online]. Available: http://dx.doi.org/10.1016/j.apm.2011.05.021

[28] E. Maani Miandoab, H. N. Pishkenari, A. Yousefi-Koma, and F. Tajaddodianfar, "Chaos prediction in MEMS-NEMS resonators," *International Journal of Engineering Science*, vol. 82, pp. 74–83, 2014. [Online]. Available: http://dx.doi.org/10.1016/j.ijengsci.2014.05.007

[29] E. M. Miandoab, A. Yousefi-Koma, H. N. Pishkenari, and F. Tajaddodianfar, "Study of nonlinear dynamics and chaos in MEMS/NEMS resonators," *Communications in Nonlinear Science and Numerical Simulation*, vol. 22, no. 1-3, pp. 611–622, 2015. [Online]. Available: http://dx.doi.org/10.1016/j.cnsns.2014.07.007

[30] Q. Chen, L. Huang, Y. C. Lai, C. Grebogi, and D. Dietz, "Extensively chaotic motion in electrostatically driven nanowires and applications," *Nano Letters*, vol. 10, no. 2, pp. 406–413, 2010.

[31] S. Hu and A. Raman, "Chaos in atomic force microscopy," *Physical Review Letters*, vol. 96, no. 3, pp. 1–4, 2006.

[32] F. Jamitzky, M. Stark, W. Bunk, W. M. Heckl, and R. W. Stark, "Chaos in dynamic atomic force microscopy," *Nanotechnology*, vol. 17, no. 7, 2006.

[33] L. M. Pecora and T. L. Carroll, "Synchronization in chaotic systems." *Physical Review Letters*, vol. 64, no. 8, pp. 821–824, 1990.

[34] K. M. Cuomo, V. a. Oppenheim, and S. H. Strogatz, "Synchronization of Lorentz-based chaotic circuits with application to communications," *IEEE Transactions on Circuits and Systems II*, vol. 40, no. 10, pp. 626–633, 1993.

[35] J. P. Goedgebuer, P. Levy, L. Larger, C. C. Chen, and W. T. Rhodes, "Optical communication with synchronized hyperchaos generated electrooptically," *IEEE Journal of Quantum Electronics*, vol. 38, no. 9, pp. 1178–1183, 2002.

[36] É. Genin, L. Larger, J. P. Goedgebuer, M. W. Lee, R. Ferriére, and X. Bavard, "Chaotic Oscillations of the Optical Phase for Multigigahertz-Bandwidth Secure Communications," *IEEE Journal of Quantum Electronics*, vol. 40, no. 3, pp. 294–298, 2004.

[37] L. Larger, J. P. Goedgebbuer, and F. Delorme, "Optical encryption system using hyperchaos generated by an optoelectronic wavelength oscillator," *Phys.Rev.E.*, vol. 57, no. 6, pp. 6618–24, 1998.

[38] J. Han, Q. Zhang, and W. Wang, "Design considerations on large amplitude vibration of a doubly clamped microresonator with two symmetrically located electrodes,"

Communications in Nonlinear Science and Numerical Simulation, vol. 22, no. 1-3, pp. 492–510, 2015. [Online]. Available: http://dx.doi.org/10.1016/j.cnsns.2014.08.011

[39] D. S. Nguyen, E. Halvorsen, E. Halvorsen, and C. P. Le, "Experimental Validation of Damping Model for a MEMS Bistable Electrostatic Energy Harvester," *PowerMEMS. Journal of Physics: Conference Series 557*, 2014.

[40] A. Ramini, M. L. F. Bellaredj, M. A. Al Hafiz, and M. I. Younis, "Experimental investigation of snap-through motion of in-plane MEMS shallow arches under electrostatic excitation," *Journal of Micromechanics and Microengineering*, vol. 26, no. 1, p. 015012, 2016. [Online]. Available: http://stacks.iop.org/0960-1317/26/i=1/a=015012?key=crossref.f2ca3e7683fe99e9c837f4e4dc8afd44

[41] M. Taher A. Saif, "On a tunable bistable MEMS-theory and experiment," *Journal of Microelectromechanical Systems*, vol. 9, no. 2, pp. 157–170, 2000. [Online]. Available: http://ieeexplore.ieee.org/lpdocs/epic03/wrapper.htm?arnumber=846696

[42] N. Krakover and S. Krylov, "Bistable Cantilevers Actuated by Fringing Electrostatic Fields," *Journal of Vibration and Acoustics*, vol. 139, no. 4, 2017.

[43] N. Krakover, B. R. Hic, and S. Krylov, "Resonant pressure sensing using a micromechanical cantilever actuated by fringing electrostatic fields," *Proceedings of the IEEE International Conference on Micro Electro Mechanical Systems (MEMS)*, vol. 2018-January, pp. 846–849, 2018.

[44] A. Uranga, J. Verd, E. Marigó, J. Giner, J. L. Muñóz-Gamarra, and N. Barniol, "Exploitation of non-linearities in CMOS-NEMS electrostatic resonators for mechanical memories," *Sensors and Actuators, A: Physical*, vol. 197, pp. 88–95, 2013.

[45] J. Verd, A. Uranga, G. Abadal, J. L. Teva, F. Torres, J. López, F. Pérez-Murano, J. Esteve, and N. Barniol, "Monolithic CMOS MEMS oscillator circuit for sensing in the attogram range," *IEEE Electron Device Letters*, vol. 29, no. 2, pp. 146–148, 2008.

[46] C. C. Lo, F. Chen, and G. K. Fedder, "Integrated HF CMOS-MEMS square-frame resonators with on-chip electronics and electrothermal narrow gap mechanism," *Proceedings of the conference on tech digest of IEEE transducers 2005*, vol. 2, 2005.

[47] W. Chen, W. Fang, and S. Li, "A generalized CMOS-MEMS platform for micromechanical resonators monolithically integrated with circuits," *J Micromech Microeng*, vol. 21, 2011.

[48] M. Younis, "MEMS Linear and Nonlinear Statics and Dynamics," *Springer*, 2010.

[49] M. I. Younis, E. M. Abdel-Rahman, and A. Nayfeh, "A reduced-order model for electrically actuated microbeam-based MEMS," *Journal of Microelectromechanical Systems*, vol. 12, no. 5, pp. 672–680, 2003.

[50] E. M. Miandoab, H. N. Pishkenari, and A. Yousefi-Koma, "Nonlinear dynamics of nano-resonators: an analytical approach," *Microsystem Technologies*, vol. 22, no. 9, pp. 2259–2271, 2016.

[51] M. Kovacic, I. Brennan, "The Duffing Equation," *John Wiley and Sons*, 2011.

[52] F. Moon and P. Holmes, "A magnetostatic strange attractor," *Journal of Sound and Vibration*, vol. 35, pp. 285–96, 1979.

[53] H. Yabuno, "Free vibration of a Duffing oscillator with viscous damping," *I.Kovacic, M.Brennan. "The Duffing Equation". John Willey and Sons*, 2011.

[54] S. Lenci and G. Rega, "Forced harmonic vibration in a Duffing oscillator with negative linear stiffness and linear viscous damping," *I.Kovacic, M.Brennan. The Duffing Equation. John Wiley and Sons*, 2011.

[55] J. García-Margallo and J. Bejarano, "Melnikov ' S Method for Non-Linear Oscillators With Non-Linear Excitations," *Journal of Sound and Vibration*, vol. 212, pp. 311–319, 1998.

[56] L. Cveticanin, "Analysis techniques for the various forms of the Duffing equation," *I.Kovacic, M.Brennan. "The Duffing Equation". John Willey and Sons*, 2011.

[57] L. Landau and E. Lifshitz, "Mechanics," *3rd Edn Oxford,Butterworth-Heinemann, UK*, 1999.

[58] V. Kaajakari, "Practical MEMS," *Small Gear Publishing*, 2009.

[59] V. Kaajakari, T. Mattila, A. Oja, and H. Seppä, "Nonlinear Limits for Single Crystal Silicon Microresonators," *Journal of microelectromechanical systems*, vol. 13, no. 5, pp. 715–724, 2004.

[60] L. C. Shao, M. Palaniapan, W. W. Tan, and L. Khine, "Nonlinearity in micromechanical freefree beam resonators: modeling and experimental verification," *Journal of Micromechanics and Microengineering*, vol. 18, no. 2, p. 025017, 2008. [Online]. Available: http://stacks.iop.org/0960-1317/18/i=2/a=025017?key=crossref.56cc679147568c65477263d6fbf71526

[61] J. Thompson and H. Stewart, "Nonliear dynamics and chaos," *John Wiley and Sons*, 1986.

[62] W. Szemplińska-Stupnicka, A. Zubrzycki, and E. Tyrkiel, "Properties of chaotic and regular boundary crisis in dissipative driven nonlinear oscillators," *Nonlinear Dynamics*, vol. 19, no. 1, pp. 19–36, 1999.

[63] G. Baker and J. Gollup, "Chaotic dynamics, an introduction," *Cambridge University Press*, 2011.

[64] U. Parlitz and W. Lauterborn, "Superstructure in the bifurcation set of the Duffing equation," *Physics Letters*, vol. 107A, no. 8, pp. 351–355, 1985.

[65] U. Parlitz, "Common dynamical features of periodically driven strictly dissipative oscillators," *International Journal of Bifurcation and Chaos*, vol. 3, no. 3, pp. 703–715, 1993.

[66] B. DeMartini, "Development of Nonlinear and Coupled Microelectromechanical Oscillators for Sensing Applications," *PhD Thesis, University of Californa, Santa Barbara*, 2008.

[67] H. Kantz and T. Schreiber, "Nonlinear Time Series Analysis," *Cambridge Nonlinear Science Series, Cambridge University Press*, 1999.

[68] J. Eckmann and D. Ruelle, "Ergodic theory of chaos and strange attractors," *Reviews of Modern Physics*, vol. 57, no. 3, pp. 1115–1115, 1985.

[69] J. Agnelli and A. Barrea, "Reconstrucción de Atractores," *Revista de Educación Matemática*, vol. 21, pp. 18–32, 2006.

[70] M. Tarnopolski, "On the fractal dimension of the Duffing attractor," *Physics Letters A*, vol. 97, no. 6, pp. 224–226, 2013.

[71] J. P. Huke, "Embedding Nonlinear Dynamical Systems: A Guide to Takens' Theorem," *Secretary*, no. March, p. 30, 2006.

[72] H. D. Abarbanel, R. Brown, J. J. Sidorowich, and L. S. Tsimring, "The analysis of observed chaotic data in physical systems," pp. 1331–1392, 1993.

[73] H. Whitney, "Differentiable manifolds," *Annals of Mathematics*, vol. 37, pp. 648–80, 1936.

[74] T. Sauer, J. A. Yorke, and M. Casdagli, "Embedology," *Journal of Statistical Physics*, vol. 65, p. 579616, 1991.

[75] G. Soler, "Estudio asintótico de órbitas no recurrentes," *Proceedings of XVIII CEDYA- VIII CMA*, 2003.

[76] E. Lorenz, "Deterministic nonperiodic flow," *Journal of the Atmosferic Science*, vol. 20, p. 13041, 1963.

[77] A. Wolf, J. B. Swift, H. L. Swinney, and J. A. Vastano, "Determining Lyapunov Exponents from a Time-Series," pp. 285–317, 1985.

[78] R. Craig, "Mechanics of Materials," *John Wiley and Sons*, 1996.

[79] M. Agarwal, H. Mehta, and R. Candler, "Impact of miniaturization on the current handling of electrostatic MEMS resonators," *IEEE 20th International Conference MEMS 2007*, 2007.

[80] R. J. Roark, W. C. Young, and R. Plunkett, *Formulas for Stress and Strain*, 1976, vol. 43, no. 3.

[81] A. Bouchami and F. Nabki, "Non-Linear Modeling of MEMS-Based Oscillators using an Analog Hardware Description Language," *2014 Ieee 12Th International New Circuits and Systems Conference (Newcas)*, no. 4, pp. 257–260, 2014.

[82] G. Rezazadeh, M. Fathalilou, K. Shirazi, and S. Talebian, "A novel relation between pull-in voltage of the lumped and distributed models in electrostatically-actuated microbeams," *2009 Proceedings of the 5th International Conference on Perspective Technologies and Methods in MEMS Design, MEMSTECH 2009*, pp. 22–24, 2009.

[83] K. L. Ekinci, Y. T. Yang, and M. L. Roukes, "Ultimate limits to inertial mass sensing based upon nanoelectromechanical systems," *Journal of Applied Physics*, vol. 95, no. 5, pp. 2682–2689, 2004.

[84] K. Y. Yasumura, T. D. Stowe, E. M. Chow, T. Pfafman, T. W. Kenny, B. C. Stipe, and D. Rugar, "Quality factors in micron- and submicron-thick cantilevers," *Journal of Microelectromechanical Systems*, vol. 9, no. 1, pp. 117–125, 2000.

[85] G. Sobreviela, "CMOS-MEMS para aplicaciones de RF: Osciladores," *PhD Thesis, Universitat Autònoma de Barcelona*, 2016.

[86] J. Verd, "Monolithic CMOS-MEMS Resonant Beams for Ultrasensitive Mass Detection," *PhD Thesis, Universitat Autònoma de Barcelona*, 2016.

[87] T. HAC, "Equivalent circuit representation of electromechanical trans- ducers: I.Lumped-parameter systems," *Micromechanics Microengineering*, vol. 6, pp. 157–176, 1996.

[88] C.-C. Nguyen, "Micromechanical resonators for oscillators and filters," *1995 IEEE Ultrasonics Symposium. Proceedings. An International Symposium*, vol. 1, pp. 489–499, 1995.

[89] K. L. Ekinci and M. L. Roukes, "Nanoelectromechanical systems," *Review of Scientific Instruments*, vol. 76, no. 061101, 2005.

[90] M. L. Ekinci, "Electromechanical Transducers at the Nanoscale," *Actuation and Sensing of Motion in Nanoelectromechanical Systems (NEMS)*, vol. 1, pp. 786–97, 2005.

[91] O. Brand, "Microsensor integration into systems-on-chip," *Proceedings of the IEEE*, vol. 94, no. 6, 2006.

[92] G. K. Fedder, R. T. Howe, T. J. K. Liu, and E. P. Quévy, "Technologies for cofabricating MEMS and electronics," *Proceedings of the IEEE*, vol. 96, no. 2, pp. 306–322, 2008.

[93] J. Smith, S. Montague, J. Sniegowski, J. Murray, and P. McWhorter, "Embedded micromechanical devices for the monolithic integration of MEMS with CMOS," *Poceedings of IEEE IEDM'95*, pp. 609–612, 1995.

[94] J. Yasaitis, M. Judy, T. Brosnihan, P. Garone, N. Pokrovskiy, D. Sniderman, R. Limb, S. Howe, B. Boser, M. Palaniapan, X. Jiang, and S. Bhave, "A modular process for integrating thick polysilicon MEMS devices with sub-micron CMOS," *Proceedings of SPIE*, vol. 4979, pp. 145–54, 2003.

[95] K. H. L. Chau, S. R. Lewis, Y. Zhao, R. T. Howe, S. F. Bart, and R. G. Marcheselli, "An integrated force-balanced capacitive accelerometer for low-g applications," *Sensors and Actuators A*, vol. 54, pp. 472–76, 1996.

[96] C. Hierold, "Intelligent CMOS sensors," *Proceedings of IEEE MEMS 2000*, pp. 1–6, 2000.

[97] G. K. Fedder, S. Santhanam, M. L. Reed, S. C. Eagle, D. F. Guillou, M. S. Lu, and L. R. Carley, "Laminated high-aspect-ratio microstructures in a conventional CMOS process," *Sensors and Actuators A*, vol. 57, pp. 103–10, 1996.

[98] T. Ishihara, K. Suzuki, S. Suwazono, M. Hirata, and H. Tanigawa, "CMOS integrated silicon pressure sensor," *Journal of Solid-State Circuits*, vol. SSC-2, no. 2, pp. 151–55, 1987.

[99] A. Uranga, J. Verd, and N. Barniol, "CMOS-MEMS resonators: From devices to applications," *Microelectronic Engineering*, vol. 132, pp. 58–73, 2014. [Online]. Available: http://dx.doi.org/10.1016/j.mee.2014.08.015

[100] J. Verd, A. Uranga, J. Teva, J. López, F. Torres, J. Esteve, G. Abadal, F. Pérez-Murano, and N. Barniol, "Integrated CMOS MEMS with on-chip readout electronics for high-frequency applications," *IEEE Electron Device Letters*, vol. 27, no. 6, pp. 495–597, 2006.

[101] M. Riverola, "Micro and Nano-Electro-Mechanical Devices in the CMOS Back End and their Applications," *PhD Thesis, Universitat Autònoma de Barcelona*, 2017.

[102] A. Uranga, J. Teva, J. Verd, J. L. López, F. Torres, G. Abadal, N. Barniol, J. Esteve, F. Pérez-Murano, I. Circuits, and I. C. Systems Society, "CMOS integrated MEMS resonator for RF applications," *ISCAS 2006: 2006 IEEE International Symposium on Circuits and Systems*, pp. 2301–2304, 2006. [Online]. Available: http://www.scopus.com/inward/record.url?eid=2-s2.0-34547354309&partnerID=40&md5=74d4b292ffd7e2143ffbc31a2ad85e00

[103] J. Verd, A. Uranga, J. Segura, and N. Barniol, "A 3V CMOS-MEMS oscillator in 0.35μm CMOS technology," *2013 Transducers and Eurosensors XXVII: The 17th International Conference on Solid-State Sensors, Actuators and Microsystems, TRANSDUCERS and EUROSENSORS 2013*, no. June, pp. 806–809, 2013.

[104] M. Riverola, G. Sobreviela, F. Torres, A. Uranga, and N. Barniol, "A monolithically integrated torsional CMOS-MEMS relay," *Journal of Micromechanics and Microengineering*, vol. 26, no. 11, 2016.

[105] C. L. Dai, "A maskless wet etching silicon dioxide post-CMOS process and its application," *Microelectronic Engineering*, vol. 83, no. 11-12, pp. 2543–2550, 2006.

[106] M. Riverola, G. Vidal-Álvarez, F. Torres, and N. Barniol, "CMOS-NEM relay based on tungsten VIA layer," *Proceedings of IEEE Sensors*, vol. 2014-December, no. December, pp. 162–165, 2014.

[107] M. Riverola, G. Vidal-Álvarez, G. Sobreviela, A. Uranga, F. Torres, and N. Barniol, "Dynamic Properties of Three-Terminal Tungsten CMOS-NEM Relays Under Nonlinear Tapping Mode," *IEEE Sensors Journal*, vol. 16, no. 13, pp. 5283–5291, 2016.

[108] W. Zhang, R. Baskaran, and K. Turner, "Tuning the dynamic behavior of parametric resonance in a micromechanical oscillator," *Applied Physics Letters*, vol. 82, no. 1, pp. 130–132, 2003.

[109] R. M. C. Mestrom, R. H. B. Fey, J. T. M. van Beek, K. L. Phan, and H. Nijmeijer, "Modelling the dynamics of a MEMS resonator: Simulations and experiments," *Sensors and Actuators, A: Physical*, vol. 142, no. 1, pp. 306–315, 2008.

[110] C. L. Olson and M. Olson, "Dynamical symmetry breaking and chaos in Duffing's equation," *American Journal of Physics*, vol. 59, no. 10, pp. 908–911, 1991.

[111] B. E. DeMartini, J. F. Rhoads, K. L. Turner, S. W. Shaw, and J. Moehlis, "Linear and nonlinear tuning of parametrically excited MEMS oscillators," *Journal of Microelectromechanical Systems*, vol. 16, no. 2, pp. 310–318, 2007.

[112] L. A. Rocha, E. Cretu, and R. F. Wolffenbuttel, "Analysis and analytical modeling of static pull-in with application to MEMS-based voltage reference and process monitoring," *Journal of Microelectromechanical Systems*, vol. 13, no. 2, pp. 342–354, 2004.

[113] X. L. Feng, M. H. Matheny, C. A. Zorman, M. Mehregany, and M. L. Roukes, "Low voltage nanoelectromechanical switches based on silicon carbide nanowires," *Nano Letters*, vol. 10, no. 8, pp. 2891–2896, 2010.

[114] J. Teva, G. Abadal, Z. J. Davis, J. Verd, X. Borrisé, A. Boisen, F. Pérez-Murano, and N. Barniol, "On the electromechanical modelling of a resonating nano-cantilever-based transducer," *Ultramicroscopy*, vol. 100, no. 3-4, pp. 225–232, 2004.

[115] R. Shabani, S. Tariverdilo, G. Rezazadeh, and A. P. Agdam, "Nonlinear vibrations and chaos in electrostatic torsional actuators," *Nonlinear Analysis: Real World Applications*, vol. 12, no. 6, pp. 3572–3584, 2011. [Online]. Available: http://dx.doi.org/10.1016/j.nonrwa.2011.06.016

[116] W. M. Zhang, O. Tabata, T. Tsuchiya, and G. Meng, "Noise-induced chaos in the electrostatically actuated MEMS resonators," *Physics Letters, Section A: General, Atomic and Solid State Physics*, vol. 375, no. 32, pp. 2903–2910, 2011. [Online]. Available: http://dx.doi.org/10.1016/j.physleta.2011.06.020

[117] A. Zeniou, K. Ellinas, A. Olziersky, and E. Gogolides, "Ultra-high aspect ratio Si nanowires fabricated with plasma etching: Plasma processing, mechanical stability analysis against adhesion and capillary forces and oleophobicity," *Nanotechnology*, vol. 25, no. 3, 2014.

[118] J. Qiu, J. H. Lang, and A. H. Slocum, "A curved-beam bistable mechanism," *Journal of Microelectromechanical Systems*, vol. 13, no. 2, pp. 137–146, 2004.

[119] R. C. Batra, M. Porfiri, and D. Spinello, "Electromechanical model of electrically actuated narrow microbeams," *Journal of Microelectromechanical Systems*, vol. 15, no. 5, pp. 1175–1189, 2006.

[120] F. Nabki, P. V. Cicek, T. A. Dusatko, and M. N. El-Gamal, "Low-stress CMOS-compatible silicon carbide surface-micromachining technology-Part II: Beam resonators for MEMS above IC," *Journal of Microelectromechanical Systems*, vol. 20, no. 3, pp. 730–744, 2011.

[121] R. M. C. Mestrom, R. H. B. Fey, K. L. Phan, and H. Nijmeijer, "Simulations and experiments of hardening and softening resonances in a clamped-clamped beam MEMS resonator," *Sensors and Actuators, A: Physical*, vol. 162, no. 2, pp. 225–234, 2010. [Online]. Available: http://dx.doi.org/10.1016/j.sna.2010.04.020

[122] T. Veijola and T. Mattila, "Modeling of nonlinear micromechanical resonators and their simulation with the harmonic-balance method," *International Journal of RF and Microwave Computer-Aided Engineering*, vol. 11, no. 5, pp. 310–321, 2001.

[123] T. Sakurai and K. Tamaru, "Simple Formulas for Two- and Three-Dimensional Capacitances ," *IEEE Transactions on electron devices*, vol. ED-30, no. 6, pp. 183–185, 1983.

[124] N. P. van der Meijis and J. T. Fokkema, "VLSI circuit reconstruction from mask topology," *Integration, the VLSI Journal*, vol. 2, pp. 85–119, 1984.

[125] H. A. Tilmans, M. Elwenspoek, and J. H. J. Fluitman, "Micro resonant force gauges," *Sensors and Actuators Al*, vol. 30, pp. 35–53, 1992.

[126] K. B. Lee, A. P. Pisano, and L. Lin, "Nonlinear Behaviors of a Comb Drive Actuator under Electrically Induced Tensile and Compressive Stresses," *Journal of Micromechanics and Microengineering*, vol. 17, no. 3, pp. 557–566, 2007. [Online]. Available: http://stacks.iop.org/0960-1317/17/557

[127] L. Landau and E. Lifshitz, "Mechanics," *Oxford, UK*, 1999.

[128] M. McCarthy, N. Tiliakos, V. Modi, and L. G. Fr??chette, "Thermal buckling of eccentric microfabricated nickel beams as temperature regulated nonlinear actuators for flow control," *Sensors and Actuators, A: Physical*, vol. 134, no. 1, pp. 37–46, 2007.

[129] R. Melamud, M. Hopcroft, C. Jha, B. Kim, S. Chandorkar, R. Candler, and T. W. Kenny, "Effects of stress on the temperature coefficient of frequency in double clamped resonators," *Digest of Technical Papers - International Conference on Solid State Sensors and Actuators and Microsystems, TRANSDUCERS '05*, vol. 1, pp. 392–395, 2005.

[130] J. Verd, A. Uranga, J. Teva, G. Abadal, F. Torres, N. Barniol, F. Perez-Murano, J. Esteve, and Ieee, "CMOS cantilever-based oscillator for attogram mass sensing," *2007 Ieee International Symposium on Circuits and Systems, Vols 1-11*, no. C I, pp. 3319–3322, 2007.

[131] B. Jovic, "Synchronization Techniques for Chaotic Communication Systems," *Signals and Communication Technology, Springer*, 2011.

[132] O. Calvo and J. Cartwright, "Fuzzy Control of Chaos," *International Journal of Bifurcation and Chaos*, vol. 08, no. 08, pp. 1743–1747, 1998.

[133] L. Chen, G. Chen, and Y. Lee, "Fuzzy modeling and adaptive control of uncertain chaotic systems," *Information Sciences*, vol. 121, pp. 27–37, 1999.

[134] A. Poursamad and A. H. Davaie-Markazi, "Robust adaptive fuzzy control of unknown chaotic systems," *Applied Soft Computing*, vol. 9, no. 3, pp. 970–976, 2009. [Online]. Available: http://www.sciencedirect.com/science/article/pii/S1568494608001774

[135] S. Zhankui and K. Sun, "Nonlinear and chaos control of a micro-electro-mechanical system by using second-order fast terminal sliding mode control," *Communications in Nonlinear Science and Numerical Simulation*, vol. 18, no. 9, pp. 2540–2548, 2013. [Online]. Available: http://dx.doi.org/10.1016/j.cnsns.2013.01.002

[136] Z. Marinkovic, V. Markovic, and A. Caddemi, "Artificial neural networks in small signal and noise modeling of microwave transistors," *Artificial Neural Networks, Nova Science Publishers*, 2011.

[137] J. R. Tripathy, H. K. Tripathy, and S. S. Nayak, "Artificial Neural Network Implementation in Microchip PIC 18F45J10 8-Bit Microcontroller ," *International Journal of Engineering and Advanced Technology*, vol. 30, 2014.

[138] J. S. R. Jang and C. T. Sun, "Neuro-Fuzzy modeling and Control," *Proceedings of the IEEE*, vol. 83, no. 3, pp. 378–406, 1995.

[139] A. Iggidr and M. Bensoubaya, "Stability of Discrete-time Systems: New Criteria and Applications to Control Problems," *Institut National de Recherche en Informatique et en Automatique*, 1996.

[140] A. Bouchami and F. Nabki, "Non-linear modeling of MEMS-based oscillators using an analog hardware description language," *New Circuits and Systems Conference (NEWCAS), 2014 IEEE 12th International*, no. 4, pp. 257–260, 2014.

[141] R. Maes, "Physically Unclonable Functions: Constructions, Properties and Applications," *PhD Thesis, Katholieke Universiteit Leuven*, 2012.

[142] K. Lakshmanan, M. Murali, "Chaos in Nonlinear Oscillators: Controlling and Synchronizations," *World Scientific, Singapore*, 1996.

[143] V. Suresh, R. Sundarapandian, "Global Chaos Synchronization of Chaotic Systems by Nonlinear Control with Applications to 2-Dimensional Chaotic Systems," *International Journal of Computational and Applied Mathematics*, vol. 5, no. 3, pp. 325–333, 2010.

[144] W. Hahn, "Stability of Motion," *Springer-Verlag, New York, USA*, 1967.

[145] K. M. Cuomo and A. V. Oppenheim, "Chaotic signals and systems for communications," pp. 137–140, 1993.

[146] M. S. H. Thompson, J, "Nonlinear Dynamics and Chaos," *John Willey and Sons*, 1986.

[147] U. Parlitz, L. O. Chua, and L. Kocarev, "Experimental demonstration of secure communications via chaotic synchronization," pp. 709–713, 1992. [Online]. Available: http://www.physik3.gwdg.de/ ulli/pdf/KHECP92.pdf%5Cnpapers3://publication/uuid/0FD8DA33-44AE-4ED8-8DF6-9F8D7AD53567

[148] C. K. Ahn, "A new chaos synchronization method for Duffing oscillator," *IEICE Electronics Express*, vol. 6, no. 18, pp. 1355–1360, 2009.

[149] A. Jimenez-Triana, Z. Guchuan, and L. Saydy, "Chaos synchronization of an electrostatic MEMS resonator in the presence of parametric uncertainties," *American Control Conference (ACC), 2011*, no. 1, pp. 5115–5120, 2011.

[150] B. Jovic, S. Berber, and C. P. Unsworth, "A novel mathematical analysis for predicting master-slave synchronization for the simplest quadratic chaotic flow and Ueda chaotic systems with application to communications," *Physica D*, vol. 213, no. 1, pp. 31–50, 2006.